Acta Pharmacologica Sinica (2012) 33: 1–2
© 2012 CPS and SIMM All rights reserved 1671-4083/12 $32.00
www.nature.com/aps

Research Highlight

A hearty solution for acute myeloid leukemia

Yi-ju HUNG[1], H Eugene LIU[2, 3, *]

Acta Pharmacologica Sinica (2012) 33: 1–2; doi: 10.1038/aps.2011.197

The process of developing novel anticancer agents has become more costly and lengthy than ever[1]. In addition, agents that target *de novo* pathway not only put the patients to unpredictable toxicity but also increase the risk in drug development[2]. Therefore, re-discovering the potential of decade-old drugs for novel anticancer therapeutics provides a new route for drug development. Thalidomide, rapamycin, and azacitidine exemplify the potential of this approach and many more, such as metformin, and valproic acid are in the process of validating their role as new anticancer agents[3, 4]. Now we have two more members to join the rank. Cardiac glycosides, which have been used to treat cardiac failure for decades, recently emerge as potential anti-cancer agents[5]. A recent work by TAILLER *et al* took advantage of high thorough-put screening of 1040 FDA approved agents for antileukemic activity and identified ouabain and zinc pyrithione, which have been used in the past for treating heart failure and dermatologic diseases respectively, as novel antileukemic agents[6] . They found that these agents induced apoptosis of various leukemic cells through the inhibition of NF-κB pathway. Although these two agents induce apoptosis of leukemic cells through common downstream signal pathway, how they differ in upstream remains elusive. For clarity of discussion, we here focus on the potential of cardiac glycosides.

The notion of using cardiac glycosides for its potential anticancer activity has been around for several decades, due to observation that breast cancer patients with digitalis therapy tends to have lower recurrence[7, 8]. Some even suggests that the association of high plasma level of digitoxin with reduced risks for cancer[9]. Using cardiac glycosides for anticancer treatment has a sound mechanistic basis. First, essentially all types of cancer cells have aberrant metabolisms (called Warburg effect) that can be differentiated from normal cells, making cancer metabolism an ideal target for drug development. Second, the toxicity of cardiac glycosides has been well characterized. Thus, the toxicity and cost might be more predictable for the development of this class of drugs. There have been several clinical trials testing the potential of cardiac glycosides, alone or in combination with chemotherapy, for various cancers[10, 11].

Ouabain binds and suppresses Na$^+$/K$^+$-ATPase, which subsequently leads to apoptosis through depolarization of mitochondria (Figure 1). This mechanism of action is analogous to "mitochondrial priming" of cancer cells by

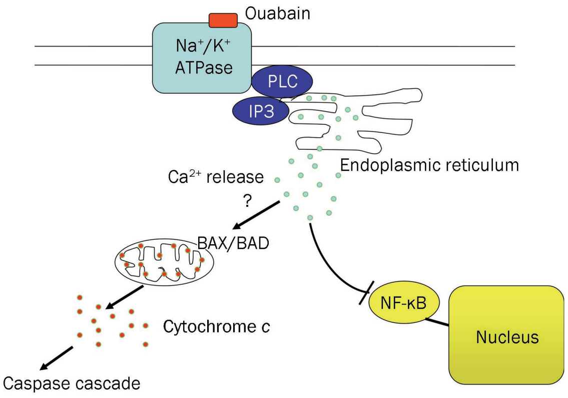

Figure 1. Proposed mechanisms that induce apoptosis in leukemic cells by cardiac glycosides (ouabain). Binding of ouabain to NA$^+$/K$^+$-ATPase activates phospholipase C (PLC) and inositol-1,4,5-triphosphate (IP3), the latter subsequently binds to IP3 receptor of endoplasmic reticulum, releasing calcium ions into cytoplasm. Increased intracellular calcium ions might induce the apoptosis through inhibition of NF-κB-mediated signal transduction and depolarization of mitochondrial outer membrane.

---

[1] *Department of Pathology, Koo's Foundation Sun Yat-Sen Cancer Center, Taipei, Taiwan, China;* [2] *Graduate Institute of Clinical Medicine, Taipei Medical University, Taipei, Taiwan, China;* [3] *Division of Hematology and Oncology, Department of Medicine, Wan Fang Hospital, Taipei Medical University, Taipei, Taiwan, China*
Correspondence: Prof H Eugene LIU
(liuxx086@tmu.edu.tw)

BH3 peptides, which induced permeabilization of mitochondrial outer membrane, prompted release of cytochrome *c* into cytoplasm, and activated programmed cell death[12]. The degree of depolarization of mitochondria in cancer cells was correlated with sensitivity to chemotherapeutic agents.

More relevant to its clinical utility is the finding that primary CD34(+) blasts in acute myeloid leukemia (AML) were more sensitive to ouabain treatment than CD34(–) blasts. In contrast, CD34(+) and CD34(–) cells from healthy donors were insensitive to ouabain. The preferential sensitivity of CD34(+) leukemic blasts is consistent with known differential activation of NF-κB in CD34(+) leukemic cells, but not in unstimulated normal CD34(+) cells[13]. Therefore, through inhibition of NF-κB, ouabain may selectively eliminate CD34(+) leukemic blasts without detrimental effects to normal hematopoietic progenitors. Another plausible explanation might be that CD34(+) leukemic cells might have higher Na^+/K^+-ATPase activity, making them sensitive to ouabain. Furthermore, as leukemic blasts are often quiescent and resistant to cytotoxic chemotherapy, ouabain may be used to prime leukemic blasts to enhance chemosensitivity.

However, the application of ouabain to clinical use deserves a note of caution. This drug was dropped out of favor for clinical use for several reasons. First, its bioavailability is poor, compared with other cardiac glycoside, *eg* digoxin. So it has to be parenterally given, which limits its clinical utility. Second, the activity of ouabain on Na/K ATPase might be dose-dependent. Since endogenous ouabain-like substance is also present in human body at pico-to-nanomolar ranges, suggesting that the level of endogenous ouabain in leukemic patients might be too low to affect NF-κB and that frequent infusion of exogenous ouabain to maintain plasma concentration high enough might be needed to sustain the inhibition of NF-κB[14, 15]. If so, systemic toxicity might be the limiting factor for its use especially in the elderly patients which constitute the bulk of leukemic patients. Yet, developing semi-synthetic glycosides for cancer therapy has been gaining ground in recent years. A notable agent is UNBS1450 (Unibioscreen), a semi-synthetic cardenolide, which has been tested for various cancers in a phase I trial since 2008. This agent has been shown to deactivate NF-κB in both lung cancer and leukemic cells *in vitro* at nanomolar levels[16]. Furthermore, the sensitivity to UNBS1450 appears to correlate with the expression of Na^+/K^+-ATPase level, implicating that Na/K-ATPase might also be a biomarker for selecting patients for future clinical trials. The findings by Tailler et al highlight the complexity of cancer biology and the potential of using high-throughput screening to discover new application of old drugs for anti-drug discovery, which might some day become a hearty solution for acute myeloid leukemia.

---

1 Sukhai MA, Spagnuolo PA, Weir S, Kasper J, Patton L, Schimmer AD. New sources of drugs for hematologic malignancies. Blood 2011; 117: 6747–55.
2 Suntharalingam G, Perry MR, Ward S, Brett SJ, Castello-Cortes A, Brunner MD, *et al*. Cytokine storm in a phase 1 trial of the anti-CD28 monoclonal antibody TGN1412. New Engl J Med 2006; 355: 1018–28.
3 Sahra IB, Marchand-Brustel YL, Tanti J-F, Bost F. Metformin in cancer therapy: a new perspective for old antidiabetic drug? Mol Cancer Ther 2010; 9: 1092–9.
4 Stamatopoulos B, Meuleman N, De Bruyn C, Mineur P, Martiat P, Bron D, *et al*. Antileukemic activity of valproic acid in chronic lymphocytic leukemia B cells defined by microarray analysis. Leukemia 2009; 23: 2281–9.
5 Prassas I, Diamandis EP. Novel therapeutic applications of cardiac glycosides. Nature Rev Drug Discovery 2008; 7: 926–35.
6 Tailler M, Senovilla L, Lainey E, Thepot S, Metivier D, Sebert M, *et al*. Antineoplastic activity of ouabain and pyrithione zinc in acute myeloid leukemia. Oncogene 2011. doi: 10.1038/onc.2011.521
7 Stenkvist B. Is digitalis a therapy for breast cancer? Oncol Rep 1999; 6: 493–6.
8 Stenkvist B, Pengtsson E, Dahlgvist B, Eriksson O, Jarkrans T, Nordin B. Cardiac glycosides and breast cancer, revisited. New Engl J Med 1982; 306: 484.
9 Haux J, Klepp O, Spigset O, Tretli S. Digitoxin medication and cancer; case control and internal dose-response studies. BMC Cancer 2001; 1: 11.
10 Mekhail T, Kaur H, Ganapathi R, Budd GT, Elson P, Bukowski RM. Phase 1 trial of Anvirzel in patients with refractory solid tumors. Invest New Drugs 2006; 24: 423–7.
11 Kahn MI, Taft B, Rasku MA, Laber D, Chesney J. A phase 2 trial of biochemotherapy with cisplatin, vinblastine, dacarbazine, interleukin-2, interferon, and digoxin in melanoma patients. ASCO Chicago 2007.
12 Chonghaile TN, Sarosiek KA, Vo TT, Ryan JA, Tammareddi A, Moore VDG, *et al*. Pretreatment mitochondrial primng correlates with clinical response to cytotoxic chemotherapy. Science 2011; 334: 1129–33.
13 Guzman ML, Neering SL, Upchurch D, Grimes B, Howard DS, Rizzieri DA, *et al*. Nuclear factor-kappaB is constitutively activated in primitive human acute myelogenous leukemia. Blood 2001; 98: 2301–7.
14 Selden R, Smith TW, Findley W. Ouabain pharmacokinetics in dog and man: determination by radioimmunoassay. Circulation 1972; 45: 1176–82.
15 Gottlieb SS, Rogowski AC, Weinberg W, Krichten CM, Hamilton BP, Hamlyn JM. Elevated concentrations of endogenous ouabain in patients with congestive heart failure. Circulation 1992; 86: 420–5.
16 Juncker T, Cerella C, Teiten M-H, Morceau F, Schumacher M, Ghelfi J, *et al*. UNBS1450, a steroid cardiac glycoside inducing apoptotic cell death in human leukemia cells. Biochem Pharmacol 2011; 81: 13–23.

Acta Pharmacologica Sinica (2012) 33: 3–4
© 2012 CPS and SIMM All rights reserved 1671-4083/12 $32.00
www.nature.com/aps

Research Highlight

A novel tumor suppressor miRNA miR-520e contributes to suppression of hepatoma

Bo-an LI*

Acta Pharmacologica Sinica (2012) 33: 3–4; doi: 10.1038/aps.2011.198

Hepatocellular carcinoma (HCC), one of the most common cancers worldwide, represents the third cause of cancer-related death[1]. Curative options for HCC are limited and exclusively available for patients carrying an early stage HCC. In advanced stages, traditional chemotherapy proved to be only marginally effective or even toxic. Thus, the identification of new treatment options is needed. New targets for non-conventional treatment will necessarily take advantage of progresses on the molecular pathogenesis of HCC[2].

MicroRNAs (miRNAs) are short non-coding RNAs 19–25 nucleotides in length, which negatively regulate gene expression by pairing with complementary sequences within the 3′-untranslated regions (UTRs) of targeted transcripts at the post-transcriptional and/or translational level[3, 4]. miRNAs expression is frequently deregulated in many types of human cancers, and plays critical roles in tumorigenesis, which functions either as tumor suppressors or as oncogenes. In the recent years, several studies have revealed that the expression of miRNAs is deregulated in human HCC in comparison with matched non-neoplastic tissue[5]. More and more miRNAs involved in hepatocarcinogenesis were identified in HCC tissues. Xu *et al* indicated that miR-195 may suppress tumorigenicity and regulate G_1/S transition of HCC cells by repressing Rb-E2F signaling involving targeting multiple molecules, such as cyclin D1, CDK6, and E2F3[6]. Liang *et al* reported that miR-125b was able to suppress tumor growth in hepatic carcinogenesis through the suppression of oncogene LIN28B expression[7]. miR-637 acts as a tumor suppressor, through the suppressive effect on HCC mediated by disruption of Stat3 activation[8]. miR-99a acts as a prospective prognosis predictor of HCC and potential tumor suppressor for HCC therapeutics, which induces cell cycle arrest by directly targeting IGF-1R and mTOR[9]. Thus, those miRNAs may function in a network in hepatocarcinogenesis.

In a recent issue of *Oncogene*, Zhang's group identified a novel tumor suppressor miRNA miR-520e in hepatoma cells. Zhang and colleagues demonstrated that the miR-520e was dramatically decreased in the examined hepatoma cells and clinical hepatocellular carcinoma (HCC) tissues[10]. In cancer, aberrant DNA hypermethylation of tumor suppressor genes, global genomic DNA hypomethylation and disruption of the histone modification patterns are the main epigenetic alterations, which have consequently been widely studied. Some miRNAs are downregulated in cancer and act as bona fide tumor suppressor genes, and this knowledge led to the proposal of the hypothesis that miRNAs could be silenced by epigenetic mechanisms[11]. The miR-520e gene is located in 19q13.42 and is reported to be in chromosome 19 miRNA cluster (C19MC), the largest human miRNA gene cluster discovered so far. Their finding presented important information for the identification of potential mechanism of down-regulation of miR-520e. The silencing of miR-520e was attributed to the methylation status of CpG islands, which are localized in the region of miR-520e promoter. Next, the paper used MTT assay, EdU assay, colony formation assay and analysis of tumorigenicity in nude mice to examine the potential role of miR-520e in tumorigenesis. They found that miR-520e suppresses growth of hepatoma cells *in vitro* and *in vivo*. Then, they revealed that NF-κB-inducing kinase (NIK) was a direct target gene of miR-520e. The NIK is a member of mitogen-activated protein kinase kinase kinase (MAP3K) family. NIK is usually constitutively and rapidly degraded by its TRAF3-mediated recruitment to TRAF2, which recruits cIAPs 1 and 2. NIK ubiquitination by these cIAPs promotes its proteosomal degradation. Stabilized NIK phosphorylates IKKα homodimers, which in turn phosphorylate p100 on its C-terminus, resulting in p100 ubiquitination and partial proteolytic processing by the proteosome to p52. The activated p52 then activates transcription when it associates with its binding partner (pri-

---

State Key Laboratory of Cellular Stress Biology, School of Life Sciences, Xiamen University, Xiamen 361005, China
Correspondence: Prof Bo-an LI
(bali@xmu.edu.cn)

marily RelB). Usually, NIK has a vital role in the alternative NF-κB activation pathway[12, 13]. However, in this study they observed that NIK was able to activate NF-κB/p65 via ERK1/2 signaling. Taken together, the finding suggests that miR-520e suppresses hepatoma cell growth through NIK/p-ERK1/2/NF-κB signaling pathway. Finally, they observed that the growth of tumor could be efficiently inhibited by direct injection with miR-520e in mice, suggesting that miR-520e might be a novel candidate for HCC therapy.

As the important roles of miRNAs in cancer are gradually revealed, their potential applications as useful and effective targets have generated great interest in cancer gene therapy strategies, as well as diagnosis, classification, prognosis and risk factor evaluations. In cell culture and xenograft mice models, the miRNA could cause tumor regression. One of the major problems of miRNA therapy is the delivery to only a restricted number of cells, which will certainly limit the therapeutic efficacy and provide only partial knock-down[14]. Thus, additional work needs to be carried out to improve the delivery of miRNA including novel chemical modifications of miRNA targeting molecules, development of novel devices for sustained delivery of therapeutics and engineering of novel viral vectors. The current large number of intense research and development activities in the area of miRNA therapy will further strengthen the possibilities of affecting modern medicine.

---

1 Parkin DM, Bray F, Ferlay J, Pisani P. Global cancer statistics, 2002. CA Cancer J Clin 2005; 55: 74–108.

2 Gramantieri L, Fornari F, Callegari E, Sabbioni S, Lanza G, Croce CM, *et al*. MicroRNA involvement in hepatocellular carcinoma. J Cell Mol Med 2008; 12: 2189–204.

3 Bartel DP. MicroRNAs: target recognition and regulatory functions. Cell 2009; 136: 215–33.

4 Bartel DP, Chen CZ. Micromanagers of gene expression: the potentially widespread influence of metazoan microRNAs. Nat Rev Genet 2004; 5: 396–400.

5 Murakami Y, Yasuda T, Saigo K, Urashima T, Toyoda H, Okanoue T, *et al*. Comprehensive analysis of microRNA expression patterns in hepatocellular carcinoma and non-tumorous tissues. Oncogene 2006; 25: 2537–45.

6 Xu T, Zhu Y, Xiong Y, Ge YY, Yun JP, Zhuang SM. MicroRNA-195 suppresses tumorigenicity and regulates G_1/S transition of human hepatocellular carcinoma cells. Hepatology 2009; 50: 113–21.

7 Liang L, Wong CM, Ying Q, Fan DN, Huang S, Ding J, *et al*. MicroRNA-125b suppressesed human liver cancer cell proliferation and metastasis by directly targeting oncogene LIN28B2. Hepatology 2010; 52: 1731–40.

8 Zhang JF, He ML, Fu WM, Wang H, Chen LZ, Zhu X, *et al*. Primate-specific microRNA-637 inhibits tumorigenesis in hepatocellular carcinoma by disrupting signal transducer and activator of transcription 3 signaling. Hepatology 2011; 54: 2137–48.

9 Li D, Liu X, Lin L, Hou J, Li N, Wang C, *et al*. MicroRNA-99a inhibits hepatocellular carcinoma growth and correlates with prognosis of patients with hepatocellular carcinoma. J Biol Chem 2011; 286: 36677–85.

10 Zhang S, Shan C, Kong G, Du Y, Ye L, Zhang X. MicroRNA-520e suppresses growth of hepatoma cells by targeting the NF-kappaB-inducing kinase (NIK). Oncogene 2011. doi: 10.1038/onc.2011.523.

11 Lujambio A, Esteller M. CpG island hypermethylation of tumor suppressor microRNAs in human cancer. Cell Cycle 2007; 6: 1455–9.

12 Dhawan P, Richmond A. A novel NF-kappa B-inducing kinase-MAPK signaling pathway up-regulates NF-kappa B activity in melanoma cells. J Biol Chem 2002; 277: 7920–8.

13 Foehr ED, Bohuslav J, Chen LF, DeNoronha C, Geleziunas R, Lin X, *et al*. The NF-kappa B-inducing kinase induces PC12 cell differentiation and prevents apoptosis. J Biol Chem 2000; 275: 34021–4.

14 Davidson BL, Harper SQ. Viral delivery of recombinant short hairpin RNAs. Methods Enzymol 2005; 392: 145–73.

Acta Pharmacologica Sinica (2012) 33: 5–10
© 2012 CPS and SIMM All rights reserved 1671-4083/12 $32.00
www.nature.com/aps

Review

Chronic intermittent hypoxia-induced deficits in synaptic plasticity and neurocognitive functions: a role for brain-derived neurotrophic factor

Hui XIE, Wing-ho YUNG*

School of Biomedical Sciences, Faculty of Medicine, The Chinese University of Hong Kong, Hong Kong, China

Obstructive sleep apnea (OSA) is well known for its metabolic as well as neurobehavioral consequences. Chronic intermittent hypoxia (IH) is a major component of OSA. In recent years, substantial advances have been made in elucidating the cellular and molecular mechanisms underlying the effect of chronic IH on neurocognitive functions, many of which are based on studies in animal models. A number of hypotheses have been put forward to explain chronic IH-induced neurological dysfunctions. Among these, the roles of oxidative stress and apoptosis-related neural injury are widely accepted. Here, focusing on results derived from animal studies, we highlight a possible role of reduced expression of brain-derived neurotrophic factor (BDNF) in causing impairment in long-term synaptic plasticity and neurocognitive functions during chronic IH. The possible relationship between BDNF and previous findings on this subject will be elucidated.

Keywords: obstructive sleep apnea; intermittent hypoxia; synaptic plasticity; long-term potentiation; brain-derived neurotrophic factor

Acta Pharmacologica Sinica (2012) 33: 5–10; doi: 10.1038/aps.2011.184

Introduction

Obstructive sleep apnea (OSA), a very common breathing and sleep disorder, is associated with intermittent hypoxia (IH) resulting from upper airway obstruction of structural or neural causes[1, 2]. The most distinct features of OSA are episodes of oxyhemoglobin desaturations, which are terminated by brief periods of microarousals that could lead to sleep deprivation, fragmentation and alteration in sleep pattern[3]. During OSA, arterial O_2 saturation could drop to very low level (50%–60%) within every cycle. This problem is alarmingly common and likely to be over-looked by the general population. The prevalence in men and women have been estimated to be 24% and 9% respectively if we only assess the frequency of increased obstructive events during sleep[4]. A large variety of problems are associated with OSA, including cardiovascular morbidity, hypertension, obesity, dyslipidemia, insulin resistance, and neurocognitive malfunctions[5, 6]. Because of the prevalence of OSA, there is a substantial cost that the society has to pay for their treatment, and also the failure in their diagnosis. In addition, OSA incurs society costs in the form of reduced work efficiency, occupational and motor vehicle accidents, decreased quality of life and morbidity. Statistical analysis confirmed that treatment reduces the medical cost of OSA[7], highlighting the significance and impact of improving available treatment strategies.

OSA and neurological functions

It is well known that OSA is not just a breathing disorder with metabolic consequences. The cyclic hypoxia and sleep fragmentation could lead to impaired brain functions which severely degrade performance in daily lives and work, and is one of the major causes of sleepiness and concentration-deficit related traffic accidents. It is well known that OSA results in cognitive deficits including decreased attention and vigilance, phonological problem, irritability, impairment in executive functions and long-term memory[8–15]. However, very little is known about the detailed events happening in the central nervous system in OSA subjects, and the relative roles of sleep fragmentation and intermittent hypoxia. Furthermore, although surgery and continuous positive airway pressure (CPAP) are useful treatments for OSA, whether long-term changes happening in the brain could be reverted is not known. These are important questions to be addressed and the answers are just beginning to be unraveled.

---

* To whom correspondence should be addressed.
E-mail whyung@cuhk.edu.hk

Received 2011-11-28 Accepted 2011-12-12

Chronic IH-induced impairment in memory and neuroplasticity

There are a large number of studies in human OSA subjects to investigate the origin of the neurocognitive problems, many of which are based on brain imaging. Techniques such as structural magnetic resonance imaging and proton magnetic resonance spectroscopy revealed significant changes in various brain regions and metabolism in OSA patients[15]. It should be pointed out that, because of the simultaneous occurrence of intermittent hypoxemia and sleep fragmentation in OSA, dissecting the influences of these two factors on cognitive functions, and what aspects of cognition, are difficult in human subjects. Understandably, these techniques are limited in providing mechanistic explanation of the pathological events at the cellular level. On the other hand, based on animal models, attempts and significant advances have been made in the last decade in unveiling the relationship between OSA and cognitive dysfunction and the underlying mechanisms.

To assess the neurobehavioral effects of episodic hypoxia in the absence of sleep fragmentation, Gozal and colleagues in early years established an animal model to study the anatomical and behavioral correlates of chronic episodic hypoxia in the rat[11, 13]. They established that exposure to IH during sleep cycle of adult rats is associated with significant spatial learning deficits as well as increased neuronal loss within susceptible brain regions such as the hippocampus and cortex. Subsequent studies have confirmed that chronic IH treatment, as well as sleep fragmentation, as models of OSA, could impair spatial memory functions of rodents to different degrees, as measured by the conventional water maze tests[16–22].

There are a number of factors and pathways that have been proposed to account for the effects of OSA-associated IH and sleep disturbance on neurocognitive functions. An early notion asserted that episodes of hypoxia could trigger apoptosis programs in neurons in areas including the hippocampus and cortex, and could lead to cytoarchitectural disorganization[11, 16]. In fact, apoptosis in the hippocampal CA1 region could be detected as early as 1–2 d in the IH-treated rats, preceding the appearance of memory deficits[11]. Consistent with this idea, a significant number of hippocampal slices obtained from the hypoxic animals failed to exhibit tetanus-induced potentiation of populations spikes, measured at 15 min post-stimulation[23]. The effects on the conventional early phase (*ie* up to 1 h) and late-phase (longer than 3 h) long-term potentiation (LTP) were however not addressed in this study.

The relatively mild degree of apoptosis detected in the brains of the IH animals[11] raises the question of whether apoptosis could explain the neurocognitive malfunctions of the animals. In fact, it is possible that chronic IH can cause a general compromise of oxidative phosphorylation and consequently poor maintenance of ion gradients of neurons. In other words, the physiological function of the neurons may be compromised before explicit apoptosis. There were few attempts to examine the direct effects of chronic IH on the excitability of hippocampal neurons, and their synaptic transmission, in the animal model of OSA. Nevertheless, it has been shown that in the developing nervous system, IH will affect neuronal excitability and its maturation by altering the expression of Na channels and ion transporters[24, 25]. In the adult mice, we also found that chronic IH decreases membrane input resistance and excitability of hippocampal CA1 neurons[26].

The reasons for the compromised neuronal function or apoptosis in the hippocampus or other brain areas are not entirely known. However, it is highly probable that oxidative stress plays a significant role (reviewed by WANG *et al*[27]). Thus, it has been well established that there are increased expressions of oxidative stress markers found in the brains of rodents subjected to IH treatment[28–30]. Administration of antioxidants[28] or over-expressing superoxide dismutase[30] attenuated reactive oxygen species (ROS) production and apoptosis in chronic IH-treated animals. More recent evidence supports a specific role of NADPH oxidase in IH-induced oxidative stress[31, 32]. However, up to now, the source and mechanism of ROS generation and its impact on neurocognitive deficits in IH are not entirely clear.

There exist other possible mechanisms by which IH could affect the hippocampus and therefore learning and memory behaviours. For example, FUNG *et al*[33] suggested that intermittent hypoxia produces abnormally high level of glutamate and causes excitotoxicity in hippocampal neurons. LI *et al*[34] concluded from their study that intermittent hypoxia in the rat is associated with an increased expression of iNOS which may play a critical role in IH-mediated neurobehavioural deficits. Furthermore, inflammation, which has been shown to play important roles in mediating the peripheral effects of IH[35], may contribute to neural injury in the brain[36].

It is well known that the hippocampal circuit is critical for the formation of spatial memory. However, a causal relationship between chronic IH and hippocampal synaptic plasticity has not been established until very recently. In a recent study based on a mouse model of OSA, we showed for the first time that there was a significant decrease in early phase long-term potentiation (E-LTP) in the hippocampi of both 7-d and 14-d IH-treated mice, while there was no apparent effect on the 3-d IH group[26]. This result provides an explanation for the well-documented memory deficits associated with OSA and its models. Of importance, it was demonstrated that not only the conventional E-LTP was impaired by IH, but the late-phase LTP (L-LTP), which better correlates with the formation of long-term memory, was also impaired and to a more significant extent. However, whether those factors that have been proposed to contribute to cognitive dysfunction, namely oxidative stress, apoptosis, decreased neuronal excitability, excitotoxicity, inflammatory response *etc*, is a cause of impaired LTP has not been demonstrated.

Critical role of decreased BDNF expression in chronic intermittent hypoxia

Brain-derived neurotrophic factor (BDNF), as a member of the neurotrophin family, plays key roles in neuronal survival and differentiation during development[37–39]. BDNF is also known to be expressed and released in an activity-dependent manner in the central nervous system and can acutely modulate synaptic transmission and plasticity[40–43]. In a previous study, we and co-workers reported that BDNF is critical in the expression of L-LTP in the hippocampus suggesting that it is a key protein in long-term memory formation[44]. Consistent with this idea, a single amino acid polymorphism in the BDNF gene has been shown to affect the cortical morphology and memory in human[45, 46]. In addition, the conversion of proBDNF to mature form of BDNF is tightly regulated by central tissue plasminogen activator (tPA) which catalyses the conversion of plasminogen to plasmin. Plasmin then cleaves proBDNF to mature BDNF.

In our study on the chronic IH mouse model[26], we found that the expression of BDNF was reduced significantly after chronic IH treatment. Compelling evidence for critical role of BDNF was provided by showing that exogenous application or surgical replenishment of BDNF by intraventricular injection could rescue and prevent, respectively, IH-induced LTP deficits. Thus, BDNF could be a crucial factor contributing to the absence of normal hippocampal plasticity and therefore memory function in the IH model.

At present, the exact reason causing BDNF decrease in chronic IH is unknown. Being a neurotrophic factor, the level of BDNF has been shown to be increased under some pathological conditions of the brain[47, 48] and spinal cord[49]. This is usually regarded as a compensatory mechanism by the nervous system to help boost the survival of neurons. However, prolonged insult such as chronic IH may compromise the ability of neurons, and probably astrocytes as well, to express BDNF. The time-dependent decrease in BDNF level we found in our chronic IH model is in line with this notion. Interestingly, the level of another neurotrophic factor, NT4/5, was not decreased (unpublished data) indicating that the effect of IH on BDNF is specific, and also argues against the possibility that the decrease in BDNF level is simply due to neuronal loss. It is known that chronic IH affects gene transcription, including those driven by CREB[16]. While the total CREB production remains unchanged, the phosphorylated form of CREB was reduced, maximally at 3 d, after hypoxic treatment. Since BDNF is a CREB-dependent gene product, the impact of chronic IH at the gene level could provide an explanation of the observed decrease in BDNF expression. On the other hand, we found that the expression of plasmin, the extracellular enzyme that helps to cleave pro-BDNF to mature forms of BDNF is reduced in the chronic IH model (unpublished data). This result is consistent with our observation that the pro-BDNF level is not significantly affected by chronic IH treatment, and points to a role of proteolytic cleavage of proBDNF to mature BDNF rather than transcription of BDNF gene.

It should be pointed out that, in our study, although we did not specifically induce sleep fragmentation or deprivation on the subjects, the loss or interference in sleep could contribute to a certain extent the observed changes in BDNF as the sleep architecture may be affected[50, 51]. Furthermore, a recent study employing a chronic IH paradigm with a much longer cycle length resulted in an enhancement of BDNF expression in the hippocampus[52], and in another study, a less severe paradigm of daily intermittent hypoxia also augments BDNF expression in the spinal cord[53]. These results suggest that the number and frequency of hypoxia/re-oxygenation cycles could be a major factor in determining the effect on BDNF expression.

Relationship between BDNF, oxidative stress, and apoptosis

As described above, oxidative stress induced by repeated hypoxia/re-oxygenation challenge and ROS-induced apoptosis are two closely-related factors that are widely accepted to contribute to neuronal damage under chronic IH condition[27]. Given our discovery of the importance of BDNF in restoring hippocampal functions in IH animals, how can we reconcile our findings with these hypotheses? There is growing evidence that neurotrophic factors such as BDNF can significantly prevent neuronal damage caused by oxidative stress, as in neurodegenerative diseases (reviewed by NUMAKAWA *et al*[54]), or as shown in *in vitro* cultures against ROS generation and action directly[55]. Thus, it is possible that lack of BDNF in chronic IH not only contributes to impaired long-term synaptic plasticity but also fails to prevent neuronal injury, including apoptosis, induced by ROS. In other words, lack of BDNF is a key factor in the cascades of events leading to neurocognitive deficits in OSA, as depicted in Figure 1. In this model, chronic IH could lead directly to decrease in neuronal excit-

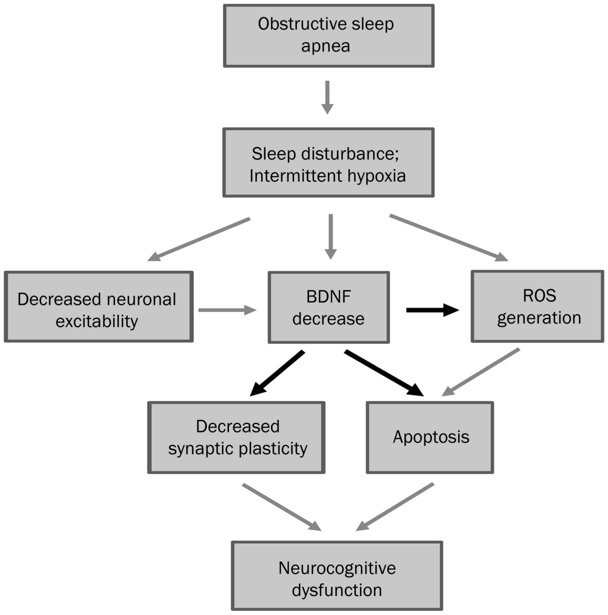

Figure 1. Proposed interactions between BDNF reduction and other pathological processes that lead to neuronal injury and decreased neuroplasticity in OSA. Chronic intermittent hypoxia and/or sleep fragmentation leads directly to decrease in neuronal excitability, decrease in BDNF expression and generation of ROS. These factors act together in a synergistic manner to increase apoptosis and also impairment in long-term synaptic plasticity underlying memory function. In this model, decreased expression of BDNF plays a pivotal role in ROS generation, apoptosis as well as impairment in synaptic plasticity.

ability, BDNF level and the generation of ROS. These factors act together in a synergistic manner to increase apoptosis and also impairment in long-term synaptic plasticity underlying memory function. Obviously, further experiments are needed to scrutinize this hypothesis.

Future directions

Here we would like to highlight a few issues that interest us and at the same time that we feel are important. First, the establishment of the chronic IH model in mimicking the hypoxia/re-oxygenation cycles in OSA has advanced our understanding of the pathophysiology of OSA. However, the differential effects of IH on short-term working memory and long-term memory are far from clear. In fact, it has been suggested that sleep fragmentation has a selective effect on working memory function[56]. Thus, the impact of chronic IH *vs* sleep disturbance on different types of memory, as well as the involvement of BDNF level in these processes, are key issues that need to be addressed.

IH definitely affects neuronal functions, but despite the obvious importance, the question of exactly what happens to neuronal activities in different brain regions during IH has never been addressed. Previous attempts only relied on *in vitro* brain slice preparations and recordings could be made only after the animals had been sacrificed[26, 57]. Long-term recording of the firing properties of neurons *in vivo* during or after the IH will give a direct answer to this question and will provide big insight into the cause of cognitive dysfunctions in OSA.

One of the main thrusts in investigating the mechanisms of synaptic plasticity impairment and neurocognitive deficits in OSA models is to provide a scientific basis for potential pharmacological treatment. We have shown that multiple intraventricular injections of BDNF is beneficial to IH-induced LTP impairment in the mice model[26]. Therefore, the level of BDNF may be a novel therapeutic target to improve OSA-associated neurocognitive impairments. There were reports indicating that endogenous BDNF level could be elevated by short-term administration of specific compounds, for example, the α-amino-3-hydroxy-5-methyl-4-isoxazolepropionic acid AMPA receptor modulator ampakine[58]. Ampakines are a group of small molecules that can delay deactivation and reduce desensitization of AMPA type glutamate receptors and thereby increase the size and duration of ligand-gated current flow, enhancing glutamate transmission[59, 60]. In addition, previous studies showed that regular ampakine administration would increase the expression of BDNF. Considering that ampakines can also cross the blood-brain barrier, are bioactive orally and improve cognitive function without obvious side effects, they are of great potential and in fact have been partially proved to be candidate for a range of neurological disability and disturbances, including Alzheimer's disease and Huntington's disease[58, 61–63]. We hypothesize that ampakines are beneficial to the neurocognitive problems found in OSA by its action in elevating endogenous BDNF level in the brain. If proven, adjunct pharmacological treatment for cognitive problems in OSA would become feasible.

Acknowledgements

The authors' work described in this article was supported by the Research Grants Council of Hong Kong, China (Project No 478308).

References

1 Caples SM, Gami AS, Somers VK. Obstructive sleep apnea. Ann Intern med 2005; 142: 187–97.
2 Mathieu A, Mazza S, De'cary A, Massicotte-Marquez J, Petit D, Gosselin N, *et al*. Effects of obstructive sleep apnea on cognitive function: A comparison between younger and older OSAS patient. Sleep Med 2007; 9: 112–20.
3 Deegan PC, McNicholas WT. Pathophysiology of obstructive sleep apnea. Eur Respir J 1995; 8: 1161–78.
4 Young T, Palta M, Dempsey J, Skatrud J, Weber S, Badr S. The occurrence of sleep-disordered breathing among middle-aged adults. N Eng J Med 1993; 328: 1230–5.
5 Lavie L. Oxidative stress — a unifying paradigm in obstructive sleep apnea and comorbidities. Prog Cardiovas Dis 2009; 4: 303–12.
6 Levy P, Bonsignore MR, Eckel J. Sleep, sleep-disordered breathing and metabolic consequences. Eur Respir J 2009; 34: 243–60.
7 Hoffman B, Wingenbach D, Kagey AN, Schaneman JL, Kasper D. The long-term health plan and disability cost benefit of obstructive sleep apnea treatment in a commercial motor vehicle driver population. J Occup Environ Med 2010; 52: 473–7.
8 Ali NJ, Pitson D, Stradling JR. Sleep disordered breathing: effects of adenotonsillectomy on behaviour and psychological functioning. Eur J Pediatr 1996; 155: 56–62.
9 Chervin RD, Dillon JE, Bassetti C, Ganoczy DA, Pituch KJ. Symptoms of sleep disorders, inattention, and hyperactivity in children. Sleep 1997; 20: 1185–92.
10 Gozal D. Sleep-disordered breathing and school performance in children. Pediatrics 1998; 102: 616–20.
11 Gozal D, Daniel JM, Dohanich GP. Behavioral and anatomical correlates of chronic episodic hypoxia during sleep in the rat. J Neurosci 2001; 21: 2442–50.
12 Gozal D. Effects of intermittent hypoxia on neurological function. In Brain Hypoxia and Ischemia 2009; (Eds Haddad GG, Yu SP). Humana Press.
13 Row BW, Kheirandish L, Neville JJ, Gozal D. Impaired spatial learning and hyperactivity in developing rats exposed to intermittent hypoxia. Pediatr Res 2002; 52: 449–53.
14 Tsai JC. Neurological and neurobehavioral sequelae of obstructive sleep apnea. NeuroRehabilitation 2010; 26: 85–94.
15 Jackson ML, Howard ME, Barnes M. Cognition and daytime functioning in sleep-related breathing disorders. Prog Brain Res 2011; 190: 53–68.
16 Goldbart A, Row BW, Kheirandish L, Schurr A, Gozal E, Guo SZ, *et al*. Intermittent hypoxic exposure during light phase induces changes in cAMP response element binding protein activity in the rat CA1 hippocampal region: Water maze performance correlates. Neuroscience 2003; 122: 583–90.
17 Goldbart A, Cheng ZJ, Brittia KR, Gozal D. Intermittent hypoxia induces time-dependent changes in the protein kinase B signaling pathway in the hippocampal CA1 region of the rat. Neurobiol Dis 2003; 14: 440–6.
18 Gozal D, Row BW, Gozal E, Kheirandish K, Neville JJ, Brittian KR, *et al*. Temporal aspects of spatial task performance during intermittent

hypoxia in the rat: evidence for neurogenesis. Eur J Neurosci 2003; 18: 2335–42.

19 Kheirandish K, Gozal D, Pequignot JM, Pequignot J, Row BW. Intermittent hypoxia during development induces long-term alteration in spatial working memory, monoamines, and dendritic branching in rat frontal cortex. Pediatr Res 2005; 58: 594–9.

20 Kheirandish K, Row BW, Li RC, Brittian KR, Gozal D. Apolipoprotein E-deficient mice exhibit increased vulnerability to intermittent hypoxia-induced spatial learning deficits. Sleep 2005; 28: 1412–7.

21 Tartar JL, Ward CP, McKenna JT, Thakkar M, Arrigoni E, McCarley RW, *et al*. Hippocampal synaptic plasticity and spatial learning are impaired in a rat model of sleep fragmentation. Eur J Neurosci 2006; 23: 2739–48.

22 Ward CP, McCoy JG, McKenna JT, Connolly NP, McCarley RW, Strecker RE. Spatial learning and memory deficits following exposure to 24 h of sleep fragmentation or intermittent hypoxia in a rat model of obstructive sleep apnea. Brain Res 2009; 1294: 128–37.

23 Payne RS, Goldbart A, Gozal D, Schurr A. Effect of intermittent hypoxia on long-term potentiation in rat hippocampal slices. Brain Res 2004; 1029: 195–9.

24 Gu XQ, Haddad GG. Maturation of neuronal excitability in hippocampal neurons of mice chronically exposed to cyclic hypoxia. Am J Physiol Cell Physiol 2003; 284: C1156–63.

25 Zhao P, Xue J, Gu XQ, Haddad GG, Xia Y. Intermittent hypoxia modulates Na^+ Channel expression in developing mouse brain. Int J Dev Neurosci 2005; 23: 327–33.

26 Xie H, Leung KL, Chen L, Chan YS, Cheung PK, Fok TF, *et al*. Brain-derived neurotrophic factor rescues and prevents chronic intermittent hypoxia-induced impairment of hippocampal long-term synaptic plasticity. Neurobiol Dis 2010; 40: 155–62.

27 Wang Y, Zhang SXL, Gozal D. Reactive oxygen species and the brain in sleep apnea. Respir Physio Neurobiol 2010; 174: 307–16.

28 Row BW, Liu R, Xu W, Kheirandish L, Gozal D. Intermittent hypoxia is associated with oxidative stress and spatial learning deficits in the rat. Am J Respir Crit Care Med 2003; 167: 1548–53.

29 Zhan G, Fenik P, Pratico D, Veasey SC. Inducible nitric oxide synthase in long-term intermittent hypoxia: hypersomnolence and bran injury. Am J Respir Crit Care Med 2005; 171: 1414–20.

30 Xu W, Chi L, Row BW, Xu R, Ke Y, Xu B, *et al*. Increased oxidative stress is associated with chronic intermittent hypoxia-mediated brain cortical neuronal cell apoptosis in a mouse model of sleep apnea. Neuroscience 2004; 126: 313–23.

31 Hui-guo L, Kui L, Yan-ning Z, Yong-jian X. Apocynin attenuate spatial learning eficits and oxidative responses to intermittent hypoxia. Sleep Med 2010; 11: 205–12.

32 Nair D, Dayyat EA, Zhang SX, Wang Y, Gozal D. Intermittent hypoxia-induced cognitive deficits are mediated by NADPH oxidase activity in a murine model of sleep apnea. PLoS One 2011; 6: e19847.

33 Fung SL, Xi MC, Zhang JH, Sampogna S, Yamuy J, Morales FR, *et al*. Apnea promotes glutamate-induced excitotoxicity in hippocampal neurons. Brain Res 2007; 1179: 42–50.

34 Li RC, Row BW, Kheirandish L, Brittian KR, Gozal E, Guo SZ, *et al*. Nitric oxide synthase and intermittent hypoxia-induced spatial learning deficits in the rat. Neurobiol Dis 2004; 17: 44–53.

35 Ryan S, McNicholas WT, Taylor C. A critical role for p38 map kinase in NF-kB signaling during intermittent hypoxia/reoxygenation. Biochem Biophys Res Com 2007; 355: 728–33.

36 Li RC, Row BW, Gozal E, Kheirandish L, Fan Q, Brittian KR, *et al*. Cyclooxygenase 2 and intermittent hypoxia-induced spatial deficits in the rat. Am J Respir Crit Care Med 2003; 15: 469–75.

37 Thoenen H. The changing scene of neurotrophic factors. Trends Neurosci 1991; 14: 165–70.

38 Lewin GR, Barde YA. Physiology of the neurotrophins. Ann Rev Neurosci 1996; 19: 289–317.

39 Bibel M, Barde YA. Neurotrophins: key regulators of cell fate and cell shape in the vertebrate nervous system. Genes Dev 2000; 14: 2919–37.

40 Poo MM. Neurotrophin as synaptic modulators Nat. Rev Neurosci 2001; 2: 24–32.

41 Lu B. Acute and long-term synaptic modulation by neurotrophins. Prog Brain Res 2004; 146: 137–50.

42 Rose CR, Blum R, Kafitz KW, Kovalchuk Y, Konnerth A. From modulator to mediator: rapid effects of BDNF on ion channels. Bioessays 2004; 26: 1185–94.

43 Lu Y, Christian K, Lu B. BDNF: a key regulator for protein synthesis-dependent LTP and long-term memory? Neurobiol Learn Mem 2008; 89: 312–23.

44 Pang P, Teng H, Zaitsev E, Woo NT, Sakata K, Zhen S, *et al*. Proteolytic conversion from pro- to mature BDNF by tPA/plasmin is essential for long-term hippocampal plasticity. Science 2004; 305: 487–91.

45 Egan M, Kojima M, Callicott JH, Goldberg TE, Kolachana BS, Bertolino A, *et al*. The BDNF val66met polymorphism affects activity-dependent secretion of BDNF and human memory and hippocampal function. Cell 2003; 112: 257–69.

46 Pezawas L, Verchinski BA, Mattay VS, Callicott JH, Kolachana BS, Straub RE, *et al*. The brain-derived neurotrophic factor val66met polymorphism and variation in human cortical morphology. J Neurosci 2004; 24: 10099–102.

47 Chiaretti A, Pastra M, Polidori G, Di Rocco C, Caresta E, Antonell A, *et al*. Correlation between neurotrophic factor expression and outcome of children with severe traumatic brain injury. Intensive Care Med 2003; 29: 1329–38.

48 Chiaretti A, Antonelli A, Piastra M, Genovese O, Polidori G, Aloe L. Expression of neurotrophic factors in cerebrospinal fluid and plasma of children with viral and bacterial meningoencephalitis. Acta Paediatr 2004; 93: 1178–84.

49 Dale-Nagle EA, Hoffman MS, MacFarlane PM, Satriotomo I, Lovett-Barr MR, Vinit S, *et al*. Spinal plasticity following intermittent hypoxia: implications for spinal injury. Ann N Y Acad Sci 2010; 1198: 252–9.

50 Veasey SC, Davis CW, Fenik P, Zhan G, Hsu YJ, Pratico D, *et al*. Long-term intermittent hypoxia in mice: protracted hypersomnolence with oxidative injury to sleep-wake brain region. Sleep 2004; 27: 194–201.

51 Polotsky VY, Rubin AE, Balbir A, Dean T, Smith PL, Schwartz AR, *et al*. Intermittent hypoxia causes REM sleep deficits and decreases EEG delta power in NREM sleep in the C57BL/6J mouse. Sleep Med 2006; 7: 7–16.

52 Zhu XH, Yan HC, Zhang J, Qu HD, Qiu XS, Chen L, *et al*. Intermittent hypoxia promotes hippocampal neurogenesis and produces antidepressant-like effects in adult rats. J Neurosci 2010; 30: 12653–63.

53 Wilkerson JE, Mitchell GS. Daily intermittent hypoxia augments spinal BDNF levels, ERK phosphorylation and respiratory long-term facilitation. Exp Neurol 2009; 217: 116–23.

54 Numakawa T, Matsumoto T, Numakawa Y, Ricahrds M, Yamawaki S, Kunugi H. Protective action of neurotrophic factors and estrogen against oxidative stress-mediated neurodegeneration. J Toxicol 2011; 2011: 405194.

55 Boutahar N, Reynaud E, Lassabliere F, Borg J. Brain-derived neurotrophic factor inhibits cell cycle reentry but not endoplasmic reticulum stress in cultured neurons following oxidative or excitotoxic stress. J Neurosci Res 2010; 8: 2263–71.

56 Thomas RJ, Rosen BR, Stern CE, Weiss W, Wong KK. Functional imaging of working memory in obstructive sleep-disordered nreathing. J Appl Physiol 2005; 98: 2226–34.

57 Tartar JL, McKenna JT, Ward CP, McCarley RW, Strecker RE, Brown RE. Sleep fragmentation reduces hippocampal CA1 pyramidal cell excitability and response to adenopsine. Neurosci Lett 2010; 469: 1–5.

58 Simmons DA, Rex CS, Palmer L, Pandyaranjan V, Fedulov V, Gall CM, *et al*. Up-regulating BDNF with an ampakine rescues synaptic plasticity and memory in Huntington's disease knockin mice. Proc Natl Acad Sci U S A 2009; 106: 4906–11.

59 Arai AC, Kessler M. Pharmacology of ampakine modulators: from AMPA receptors to synapses and behavior. Curr Drug Targets 2007; 8: 583–602.

60 Nagarajan N, Quast C, Boxall AR, Shahid M, Rosenmund C. Mechanism and impact of allosteric AMPA receptor modulation by the ampakine CX546. Neuropharmacology 2001; 41: 650–63.

61 Kramar EA, Chen LY, Lauterborn JC, Simmons DA, Gall CM, Lynch G. BDNF upregulation rescues synaptic plasticity in middle-aged ovariectomized rats. Neurobiol Aging 2010. doi:10.1016/j.neurobiolaging.2010.06.008

62 Lynch G. Memory enhancement: the search for mechanism-based drugs. Nat Neurosci 2002; 5: 1035–8.

63 Wezenberg E, Verkes RJ, Ruigt GS, Hulstjin W, Sabbe BG. Acute effects of ampakine farampator on memory and information processing in healthy elderly volunteers. Neuropsychopharmacol 2007; 32: 1272–83.

Acta Pharmacologica Sinica (2012) 33: 11–18
© 2012 CPS and SIMM All rights reserved 1671-4083/12 $32.00
www.nature.com/aps

Original Article

Glycyrrhizin attenuates rat ischemic spinal cord injury by suppressing inflammatory cytokines and HMGB1

Gu GONG, Li-bang YUAN, Ling HU, Wei WU, Liang YIN, Jing-li HOU, Ying-hai LIU, Le-shun ZHOU*

Department of Anesthesiology, General Hospital of the People's Liberation Army, Chengdu Military Region, Chengdu 610083, China

Aim: To investigate the neuroprotective effect of glycyrrhizin (Gly) against the ischemic injury of rat spinal cord and the possible role of the nuclear protein high-mobility group box 1 (HMGB1) in the process.
Methods: Male Sprague-Dawley rats were subjected to 45 min aortic occlusion to induce transient lumbar spinal cord ischemia. The motor functions of the animals were assessed according to the modified Tarlov scale. The animals were sacrificed 72 h after reperfusion and the lumbar spinal cord segment (L2–L4) was taken out for histopathological examination and Western blotting analysis. Serum inflammatory cytokine and HMGB1 levels were analyzed using ELISA.
Results: Gly (6 mg/kg) administered intravenously 30 min before inducing the transient lumbar spinal cord ischemia significantly improved the hind-limb motor function scores, and reduced the number of apoptotic neurons, which was accompanied by reduced levels of tumor necrosis factor-α (TNF-α), interleukin-1β (IL-1β) and interleukin-6 (IL-6) in the plasma and injured spinal cord. Moreover, the serum HMGB1 level correlated well with the serum TNF-α, IL-1β and IL-6 levels during the time period of reperfusion.
Conclusion: The results suggest that Gly can attenuate the transient spinal cord ischemic injury in rats via reducing inflammatory cytokines and inhibiting the release of HMGB1.

Keywords: glycyrrhizin; ischemic spinal cord injury; high-mobility group box 1; tumor necrosis factor-α; interleukin-1β; interleukin-6

Acta Pharmacologica Sinica (2012) 33: 11–18; doi: 10.1038/aps.2011.151; published online 12 Dec 2011

Introduction

Ischemic spinal cord injury (ISCI) is a serious complication that can result from thoracoabdominal aortic surgery and can cause paraplegia in 2% to 18% of patients[1, 2]. In a recent report, only 5% of 127 patients who underwent clamp/sew surgery developed paraplegia[3]; paraplegia caused by ISCI remains a problem that should be solved. Multiple studies have suggested that calcium overload, inflammatory processes, free radical production, platelet aggregation, neutrophil accumulation and adhesion following ischemia might contribute to the neuronal damage that was observed in patients with ISCI[4, 5]. However, the cellular and molecular mechanisms of ischemic spinal cord injury are not fully understood. Tumor necrosis factor-α (TNF-α), interleukin-1β (IL-1β) and interleukin-6 (IL-6) are key proinflammatory cytokines that play important functions in the central nervous system during inflammatory injury. Besides causing direct damage to cell membranes, free oxygen radicals activate the accumulation of neutrophils and stimulate various types of cells to produce TNF-α and IL-1β[6]. These cytokines further contribute to the production of other cytokines and to the expression of endothelial leukocyte adhesion factor-1, ultimately leading to endothelial cell damage and spinal cord ischemia[7, 8]. Recent studies have shown that the high-mobility group box 1 (HMGB1) protein, an abundant nuclear protein that acts as an architectural chromatin binding factor, can be passively released by necrotic or damaged cells and serves as a signaling molecule that is involved in acute and chronic inflammation[9, 10]. A wealth of evidence indicates that HMGB1 is massively released during the excitotoxicity-induced, acute damaging process in the post-ischemic brain, where it triggers inflammatory processes, and suggests that HMGB1 acts as a novel mediator that links excitotoxicity-induced acute damage and subsequent inflammatory processes in the post-ischemic brain[11–13].

Along these lines, we have recently recognized glycyrrhizin (Gly), a natural triterpene glycoconjugate that is derived from the root of licorice (*Glycyrrhiza glabra*), as an additional HMGB1 inhibitor. Gly binds directly to both HMG boxes in

---

* To whom correspondence should be addressed.
E-mail zhouleshun@126.com
Received 2011-07-07 Accepted 2011-10-12

HMGB1, thereby inhibiting its chemoattractant functions in fibroblasts and smooth muscle cells[14, 15]. Of note, Gly is a natural compound that is commonly used in Japan to treat patients with chronic hepatitis[16]; however, no study has been designed to examine its use in preventing ISCI.

The current study was designed to investigate the protective efficacy and dose-response relationship of Gly against the neurologic and histopathological outcomes of spinal cord ischemia and reperfusion injury that are related to aortic occlusion in rats, and to determine whether HMGB1 plays a pathogenetic role in ischemic spinal cord injury. First, we injected ischemic rats with either glycyrrhizin or a placebo. Second, we monitored the concentration of HMGB1, TNF-α, IL-1β, and IL-6 in the plasma of the rats. Third, we detected the expression of HMGB1 and cell death within the ischemic spinal cords of those rats.

Materials and methods

Animals and groups

Male Sprague-Dawley rats weighing 300–350 g were obtained from the Experimental Animal Center of Sichuan University (Chengdu, China) and were allowed free access to laboratory chow and tap water in day-night regulated quarters at 25 °C.

Rats were randomized into the following three experimental groups, each consisting of 15 animals: (i) ISCI rats that were pretreated with saline (NS group); (ii) ISCI rats that were pretreated with Gly (Minophagen Pharmaceutical Co, Tokyo, Japan) at a dose of 6 mg/kg (Gly group); and (iii) healthy, control, sham-operated rats (Sham group). In the pretreatment groups, glycyrrhizin or saline was administered intravenously via the tail vein 30 min before the induction of ischemia/reperfusion (I/R) ISCI.

Experimental I/R spinal cord injury

The detailed surgical method for transient lumbar spinal cord ischemia has been described previously[17]. Briefly, rats were initially anesthetized with intramuscular ketamine (50 mg/kg) and then by a half dose of ketamine, as required for the procedure. During the surgery, body temperature was monitored using a rectal probe and was maintained at 35.5–37.5 °C with a heat lamp. During the procedure, an intravenous catheter was placed into the tail vein, and 0.9% NaCl was infused. Cefazolin was injected intravenously at a single dose of 10 mg/kg immediately before the surgery to prevent infection. To monitor proximal and distal aortal blood pressures, catheters were surgically placed into the left common carotid artery and the left femoral artery, respectively. The abdominal aorta was accessed through a midline laparotomy, and animals in the sham group were subjected to laparotomy without aortic occlusion. For the other groups, animals were subjected to 45 min of cross clamping, where vascular clamps were placed under the left renal vein and above the bifurcation in the aorta. Each rat received 150 IU/kg of heparin before aortic occlusion, the aortic clamps were removed after 45 min, and the abdomen was closed appropriately. Animals were allowed to recover in a plastic box at 28 °C for 3 h and were subsequently placed in their cages with free access to food and water. The Crede maneuver was used twice daily to empty the urinary bladders of paraplegic animals. Animals that never recovered completely from the surgery and died within 24 h after reperfusion were excluded from the analyses.

Serum detection

Blood samples (0.4 mL) were collected from the femoral vein at 0 h, 0.5 h, 2 h, 6 h, 12 h, 24 h, 48 h, and 72 h after reperfusion. Serum was isolated from the blood after centrifugation at 1500 r/min for 15 min and was frozen at -80 °C until enzyme-linked immunosorbent assay (ELISA) analyses were performed. HMGB1 concentrations and the levels of inflammatory mediators (TNF-α, IL-1β, and IL-6) in the serum samples were quantified using specific ELISA kits for rats according to the manufacturers' instructions (Biosource International Inc, Camarillo, CA, USA).

Neurological assessment

The motor functions of the rats were assessed at 24 h, 48 h, and 72 h after the procedure using the following modified Tarlov scale[6, 17, 18]: 0, no voluntary movement (complete paraplegia); 1, perceptible movement at the joint; 2, good joint mobility but unable to stand; 3, ability to stand but unable to walk; 4, weak walking; 5, complete recovery.

Spinal cord HMGB1 contents

The lumbar enlargements of the spinal cords of rats that were killed at the completion of behavioral testing were removed. Five samples from every group were stored at -80 °C until Western blotting analyses were performed. Briefly, frozen samples were mechanically lysed in a homogenization buffer on ice. The lysates were centrifuged at 12000 r/min for 20 min at 4 °C, and the protein concentrations were estimated using a BCA protein assay kit (Jiancheng Bioengineering Institute, Nanjing, China). Each sample was adjusted to a final total protein concentration of 5 μg/μL in 4×sample buffer, heated at 95 °C for 10 min, and then stored at -20 °C. Protein samples (50 μg per lane) were loaded into a 12% SDS-PAGE gel and run at 100 V for 120 min in running buffer. Proteins were then transferred from the gel to a PVDF membrane at 250 mA for 90 min using transfer buffer. The membrane was blocked with 5% skimmed milk for 2 h at room temperature and incubated overnight at 4 °C with primary antibody directed against HMGB1 (Santa Cruz Biotechnology, Santa Cruz, CA, USA) at a dilution of 1:500. Glyceraldehyde-3-phosphate dehydrogenase (GAPDH) (diluted in 1:6000, Sigma-Aldrich Inc, St Louis, MO, USA) was used as a loading control. After 6×10 min rinses with PBS/Tween, the membrane was incubated in the appropriate HRP-conjugated secondary antibody (diluted 1:1000 in PBST) for 2 h. The blotted protein bands were visualized using enhanced chemiluminescence (ECL) Western blotting detection reagents (Millipore, Billerica, MA, USA), and the blots were exposed to X-ray film. Developed films were digitized using an Epson Perfection 2480 scanner (Seiko, Nagano, Japan), and optical densities were obtained using Glyko Bandscan software (Glyko, Novato, CA, USA). All experiments were repeated at least three times.

Histological examination

The remnant samples (n=10 for each group) were fixed in 10% formalin, embedded in paraffin and cut to a thickness of 6 μm, with a routine follow-up procedure. An observer who was uninformed of the experimental conditions of the animals recorded the data.

Coronal sections were stained with hematoxylin and eosin (HE) for light microscopic examination. Changes in rat motor neurons caused by ischemia were identified to be shrunken cellular bodies, a disappearance of Nissl granules, an intensely eosinophilic cytoplasm and triangular and pyknotic nuclei. The remaining normal neurons in the ischemic ventral spinal cord of each animal, as judged by their morphological appearance, were counted in three sections that were selected randomly from the rostral, middle, and caudal levels of the L4 segment and then averaged. The numbers of normal neurons per section of the anterior spinal cords of the rats (anterior to an imaginary line drawn through the central canal, which was perpendicular to the vertical axis) were compared between three groups.

TUNEL (terminal deoxynucleotidyl transferase dUTP nick-end labeling) reactions were applied to identify cells with fragmented DNA according to the instruction manual of a commercial TUNEL kit (Roche, Basel, Switzerland). Cell viability was assessed by visual inspection of damaged cells that had been stained with TUNEL, and data are presented as the number of TUNEL-positive cells from three sections of the same animal.

Statistical analysis

All data, except neurologic scoring, were presented as the mean±SEM (standard error of mean), which was calculated using SPSS (Statistical Package for the Social Sciences) 12.0 software (SPSS Inc, Chicago, IL, USA). The Mann-Whitney *U*-test was used to compare the behavior and activity score among groups, and the concentrations of serum HMGB1 and inflammatory mediators were analyzed using two-way repeated-measures (time and group) analysis of variance followed by the *post hoc* Student-Newman-Keuls test. Correlations between HMGB1 levels and concentrations of inflammatory mediators were analyzed using Spearman's rank correlation test, and the number of normal neurons and TUNEL-positive motor neurons in the anterior spinal cord were analyzed using the Kruskal-Wallis test followed by the Mann-Whitney *U*-test with the Bonferroni correction. The $P<0.05$ level of probability was used as the criteria for significance.

Results

Serum HMGB1 concentrations

As shown in Figure 1, the HMGB1 serum concentrations in the sham animals were unchanged during the period of the experimental procedure. However, the concentrations of HMGB1 in the serum of the NS and Gly groups significantly increased 2 h after reperfusion, when compared to pre-ischemia levels, and the concentrations remained at higher levels thereafter ($P<0.05$). Furthermore, HMGB1 serum concentrations in the animals that were treated with Gly were significantly lower than in those of the NS group from 2 h to 72 h after reperfusion ($P<0.05$).

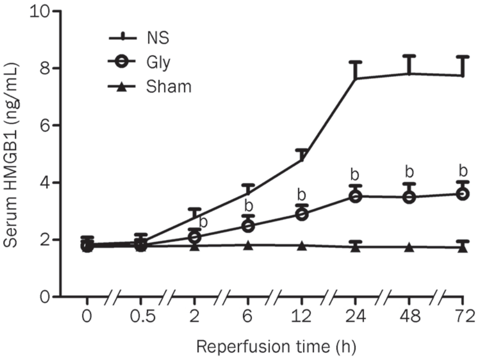

Figure 1. Time course of serum HMGB1 concentrations. The serum HMGB1 levels were significantly increased after spinal cord ischemia-reperfusion compared with that of preischemia ($P<0.05$), whereas they were significantly decreased in the animals treated by Gly compared with that of animals in NS group ($P<0.05$). Data are means±SEM. n=15 for each group. $^{b}P<0.05$ *vs* NS group.

Concentrations of inflammatory cytokines in the serum

The concentrations of TNF-α, IL-1β, and IL-6 were low in the serum of the rat sham group (Figure 2); however, serum levels of these inflammatory cytokines were greatly induced from 6 h to 72 h after reperfusion in the experimental groups ($P<0.05$). As shown in Figure 2, Gly administration before I/R resulted in significantly decreased IL-1β, TNF-α, and IL-6 concentrations compared to the NS group ($P<0.05$). Moreover, the serum HMGB1 contents correlated well with the levels of TNF-α (r=0.947), IL-1β (r=0.906), and IL-6 (r=0.935) at 2 h, 6 h, 12 h, 24 h, 48 h, and 72 h after reperfusion (Figure 3).

Neurologic outcomes

All animals survived until the final neurologic behavior assessments at 24 h, 48 h, and 72 h after reperfusion. The hind-limb motor function scores of the 3 groups at 24 h, 48 h, and 72 h after reperfusion are shown in Table 1. In the NS group, most of the animals developed complete paraplegia of the hind-limbs (grade 1) at 72 h after reperfusion. Importantly, the neurologic statuses of members of the Gly group were signifi-

Table 1. Tarlov scores in each group (mean). $^{b}P<0.05$ compared with sham group. $^{e}P<0.05$ compared with NS+SCI group.

Group	24 h	48 h	72 h
Sham	4.64^{e}	5^{e}	5^{e}
NS+SCI	2.18^{b}	1.27^{b}	1^{b}
Gly+SCI	3.25^{be}	2.33^{be}	2.17^{be}

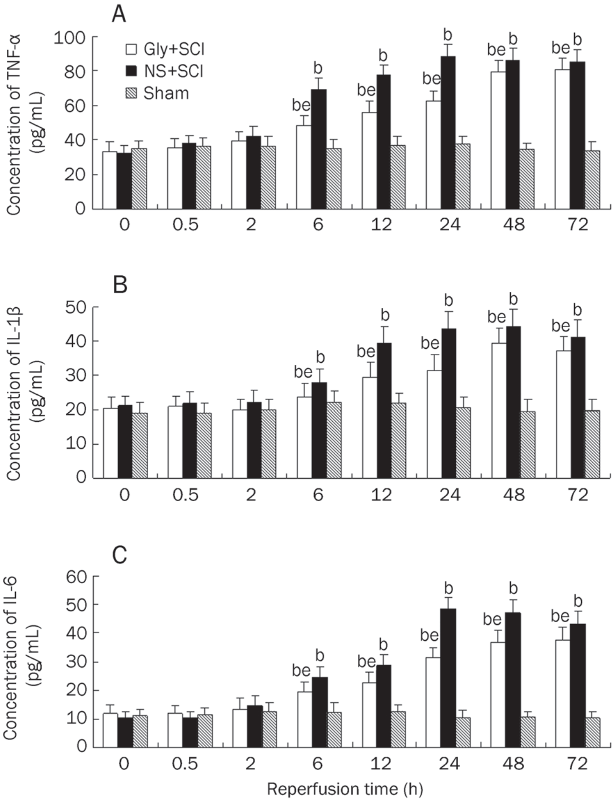

Figure 2. Serum concentrations of inflammatory cytokines. (A–C) respectively show the concentrations of TNF-α, IL-1β, and IL-6 at different time after I/R. Means±SEM. *n*=15. $^{b}P<0.05$ *vs* Sham group. $^{e}P<0.05$ *vs* NS group.

cantly improved, compared to those of the NS group, at 24 h, 48 h, and 72 h after reperfusion (*P*=0.029, 0.001, 0.004, respectively).

Western blotting

The protein levels of HMGB1 were detected by Western blot analysis (Figure 4). The protein was expressed at low levels in the spinal cords of the sham group members; however, the levels of HMGB1 significantly increased in the spinal cords of members of the experimental groups as compared with HMGB1 levels of the sham groups (*P*=0.006). Furthermore, the protein expression of HMGB1 in the spinal cords of members of the Gly group was significantly lower than that of the NS group (*P*=0.035).

Histological examination

The representative micrographs of HE staining of the ventral horn of the L4 spinal cord segment 72 h after reperfusion are shown in Figure 5A–5C. The number of normal cells in the Gly group was more than that in the NS group (Figure 5D, *P*=0.019), and TUNEL staining identified a few dead cells in the cord sections of the sham-operated animals (Figure 6A). In the spinal cords of members of the NS group, numerous cells were strongly positive for TUNEL staining (Figure 6B).

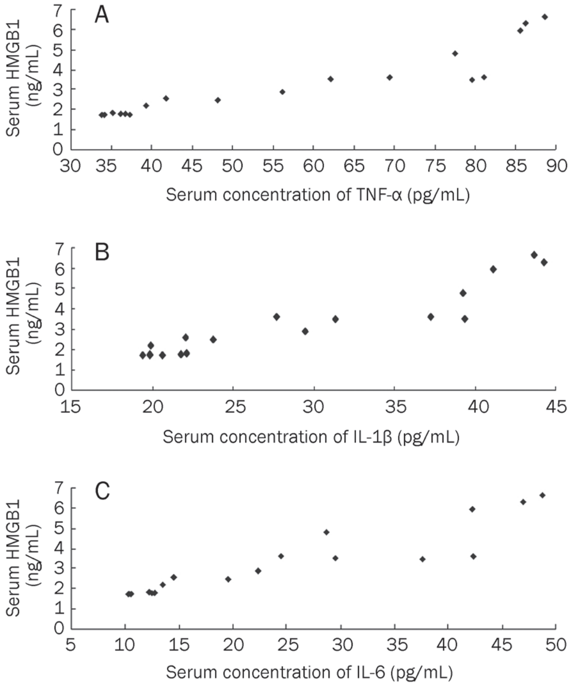

Figure 3. The serum HMGB1 contents correlated well with the levels of TNF-α (r=0.947, *P*=0.004), IL-1β (*r*=0.906, *P*=0.000), and IL-6 (*r*=0.935, *P*=0.000) at 2 h, 6 h, 12 h, 24 h, 48 h, and 72 h after reperfusion. *n*=17 pairs.

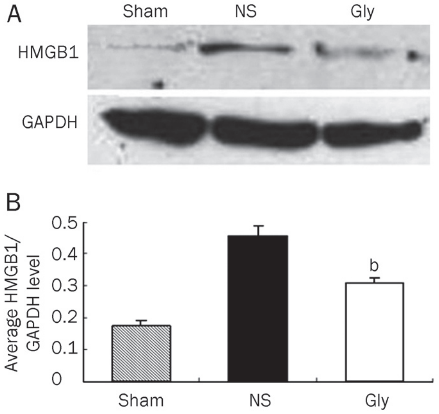

Figure 4. The spinal cord HMGB1 contents in sham, NS or Gly group animals at 72 h after I/R. (A) Result of Western blotting. (B) The bar graph showing the quantitative analysis of the protein levels of HMGB1 in the injured spinal cord in 3 groups. Means±SEM. *n*=5. $^{b}P<0.05$ *vs* NS group.

However, in samples from the Gly group, only a few cells were positive for TUNEL staining (Figure 6C). For quantitative measurement, the number of cells that were positive or negative for TUNEL was recorded for each specimen in a blind fashion. Administration of Gly 30 min before ischemia significantly reduced the total number of dead cells, compared to that of the NS group (Figure 6D, *P*=0.016). Moreover, the

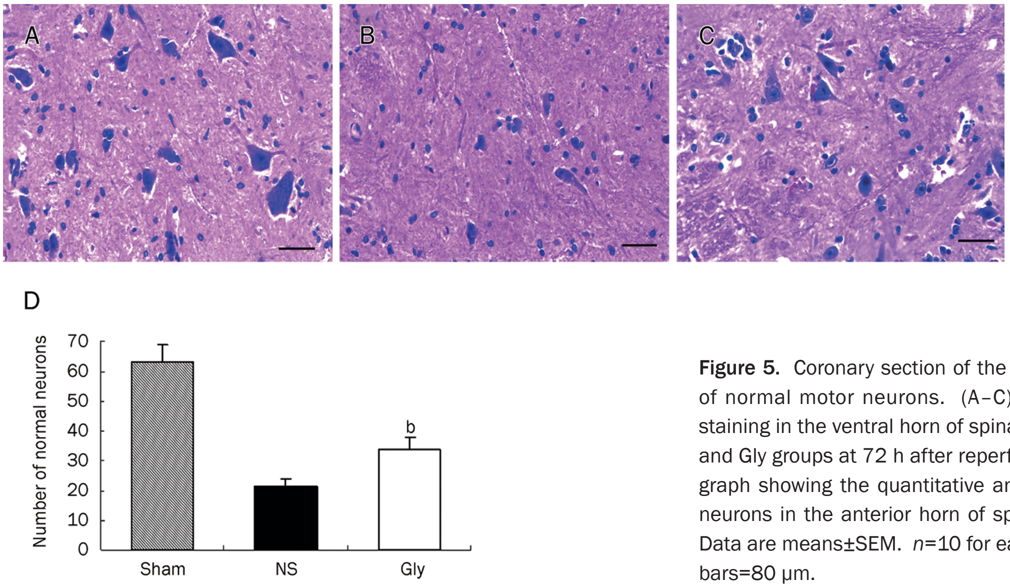

Figure 5. Coronary section of the lumbar spinal cords and quantification of normal motor neurons. (A–C) Representative micrographs of H&E staining in the ventral horn of spinal cord of L4 segments in the Sham, NS and Gly groups at 72 h after reperfusion, respectively (×200). (D) The bar graph showing the quantitative analysis of the number of normal motor neurons in the anterior horn of spinal cord of L4 segments in 3 groups. Data are means±SEM. n=10 for each group. $^{b}P<0.05$ *vs* NS group. Scale bars=80 μm.

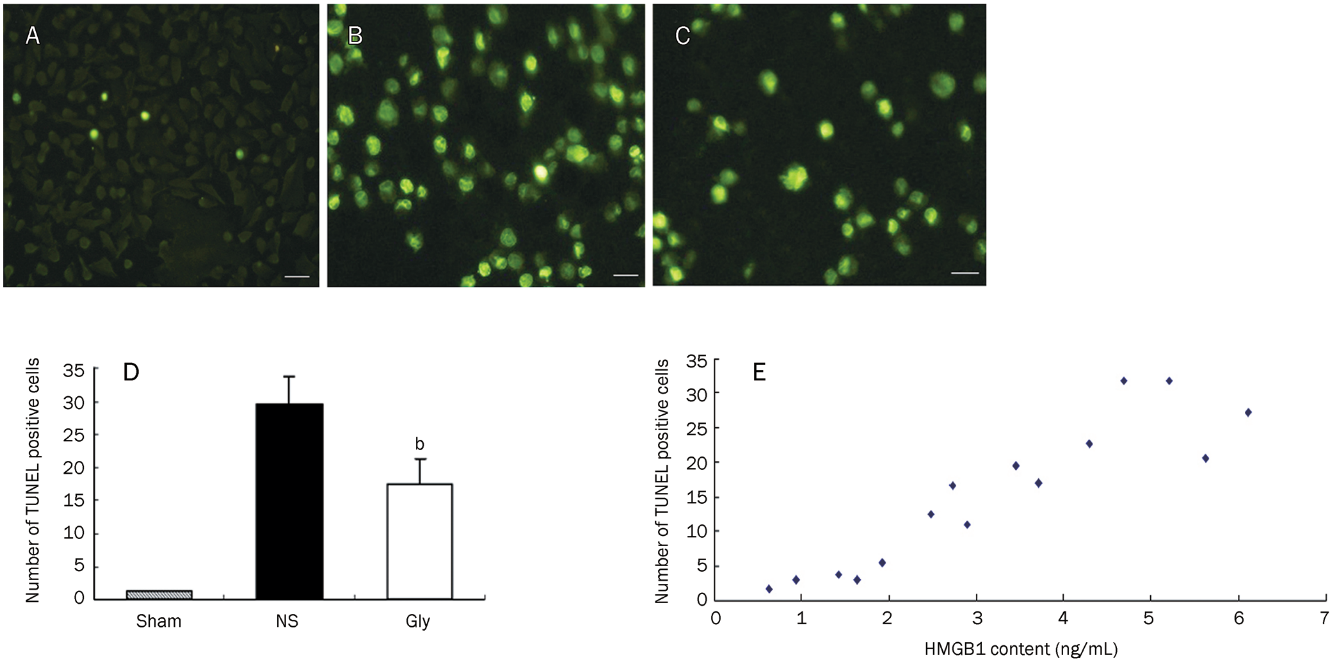

Figure 6. Representative fluorescence micrographs of TUNEL staining and quantification of apoptotic motor neurons. (A–C) Representative fluorescence micrographs of TUNEL staining in the ventral horn of spinal cord of L4 segments from animals in the sham, NS and Gly groups at 72 h after reperfusion, respectively (×200). (D) Quantitative analysis of the number of TUNEL-positive cells in the anterior horn of spinal cord of L4 segments in three groups. Data are means±SEM. n=10 for each group. $^{b}P<0.05$ *vs* NS group. Scale bars=80 μm. (E) The numbers of dead cells correlated well with the HMGB1 levels of spinal cord tissue in the spinal cord at 72 h after reperfusion. n=15 pairs, r=0.929, P=0.005.

number of dead cells correlated well with the HMGB1 levels in spinal cord tissue at 72 h after reperfusion (Figure 6E, n=15 pairs, r=0.929, P=0.005).

Discussion

There is a wealth of evidence to suggest that the systemic inflammatory response that is associated with I/R injury contributes to the morbidity and mortality that is associated with the repair of thoracoabdominal aortic aneurysms[19]. The principal mechanisms of pharmacological therapy, such as the administration of high doses of the glucocorticoid steroid methylprednisolone that are used in humans, are likely to inhibit posttraumatic lipid peroxidation and inflammatory responses. In this study, we show that Gly significantly attenuated spinal cord I/R injury when administered 30 min before ischemia, and this protection was accompanied by a reduction in serum inflammatory factors and the protein HMGB1.

HMGB1 is a non-histone, nuclear protein with dual functions. Inside cells, HMGB1 binds DNA and plays a role in transcriptional regulation. Outside cells, HMGB1 serves as a late cytokine-like mediator of systemic inflammation[20]. HMGB1 can activate inflammatory pathways when released from ischemic cells, and studies indicate that HMGB1 acts as an early mediator of inflammation and organ damage in hepatic I/R injury. HMGB1 levels were increased during liver I/R as early as 1 h after reperfusion and then further increased, in a time-dependent manner, up to 24 h. Inhibition of HMGB1 activity with a neutralizing antibody significantly decreased liver damage after I/R, whereas administration of recombinant HMGB1 worsened I/R injury[21, 22]. Moreover, HMGB1 is massively released extracellularly and plays a cytokine-like function in the postischemic brain[11, 12]. HMGB1, as a mediator of postischemic brain damage, plays a critical role in the development of brain infarction through the amplification of plural inflammatory responses in the ischemic region and could be an outstandingly suitable target for treatment for this damage[23]. Intravenous injection of a neutralizing, anti-HMGB1 monoclonal antibody provides a novel therapeutic strategy for ischemic stroke[24]. In addition, serum HMGB1 levels were significantly elevated in patients with myocardial ischemia and cerebral ischemia, suggesting that systemic HMGB1 levels are elevated in human ischemic disease[25]. In this study, serum HMGB1 concentrations and levels of IL-β, TNF-α, and IL-6 increased during spinal cord I/R as early as 2 h after reperfusion and in a time-dependent manner up to 72 h. These results indicate that HMGB1 is involved in the proinflammatory stress response to I/R injuries of the spinal cord in a time-dependent manner after spinal cord I/R in rats.

Obviously, inhibition of HMGB1 secretion or release represents a novel and promising strategy for the therapy of I/R injuries[23]. A growing amount of information implicates a possible responsibility of inflammatory mediators in the pathogenesis of spinal cord injury. In a rat model of traumatic SCI, the tissue level of TNF-α in the spinal cord significantly increased 24 h after injury[26]. Similarly, in a mouse model of traumatic SCI, TNF-α, and IL-1β were produced almost immediately following injury, and this production was followed by the expression of IL-6[27]. Clinical research has also revealed increased immunoreactivity of TNF-α, IL-1β, and IL-6 in neurons at both early and late phases of trauma in human spinal cord tissues after injury[28]. In the present study, we demonstrated that serum proinflammatory cytokine levels (TNF-α, IL-1β, and IL-6) significantly increased after spinal cord I/R in rats. These increases were accompanied by elevated HMGB1 concentrations, and by analyzing histopathological specimens, tissue damage to the spinal cord was evident. In the NS group, all three proinflammatory cytokine levels reached significantly higher levels when compared to the sham-operated group, and these elevated levels were relieved by treatment with Gly. Treatment with Gly attenuated serum HMGB1 levels after spinal cord I/R injury when the drug was administered 30 min before ischemia. Moreover, the HMGB1 contents of spinal cord tissue in animals that had been treated with Gly 72 h after reperfusion were found to be significantly lower than those of the controls. To the best of our knowledge, this is the first study to demonstrate a protective effect of Gly that is related to its inhibitory effect on HMGB1 release in spinal cord I/R injuries. We found that I/R upregulated the expression of HMGB1 in injured tissue and the levels of IL-β, TNF-α, and IL-6 in the peripheral blood, which was inhibited by Gly administration. These results suggest that I/R could activate HMGB1, which might play a central role in the inflammatory response that leads to secondary insults after ischemia. Therefore, the therapeutic benefit of pre-I/R Gly administration might be due to its salutary effect on modulating HMGB1.

However, apoptosis has been demonstrated to be an important mechanism of neuron death in the ischemic spinal cord, and to play an important role in delayed paraplegia in the animal model of aortic occlusion[29]. It is important to note that the TUNEL assay does not distinguish between cell death mechanisms (necrosis or apoptosis); however, this method is useful for detecting damaged cells using light or fluorescence microscopy[30]. Furthermore, histopathological examinations of the spinal cords in our study revealed that there was significant neuronal loss in both 72-h I/R groups, when compared to the sham-operated groups. In this study, dead cells were detected based on positive TUNEL staining because the fluorescent nucleus developed a granular pattern. We used this method because of its high sensitivity and specific means of identifying DNA fragmentation. As noted, numerous dead cells were observed in the spinal cords of the control animals, and the total number of TUNEL-positive cells was reduced significantly after Gly treatment. The results showed that Gly alleviated cell apoptosis that was induced by spinal cord I/R. In line with this, the animals that were treated with Gly had better neurologic outcomes than those of the NS group. Moreover, at 72 h after reperfusion, the HMGB1 levels in spinal cord tissue from animals that had been treated with Gly were significantly lower than those of the NS group, and these levels correlated well with the numbers of dead cells in the spinal cord 72 h after reperfusion. Together, these results indicate that inhibiting the release of HMGB1 with Gly results in less tissue damage and better functional recovery of neurons. In accordance with our experimental results, the relationship between apoptosis and HMGB1 release in macrophages and other cells was investigated in an *in vitro* study, and those results indicated that the release of HMGB1 from macrophages correlated with the occurrence of apoptosis, and suggested that these processes reflected common mechanisms and could occur concomitantly[31]. However, other studies have shown that HMGB1 production occurred downstream of apoptosis in the final common pathway to organ damage in severe sepsis[32]. Thus, the crosstalk between HMGB1 and apoptosis must be further explored.

Because there are two contradictory pathways for inflammation and apoptosis, it is interesting that Gly influences the two pathways simultaneously. Here, two mechanisms could be considered to cause this result. First, Gly could inhibit inflammation by suppressing HMGB1 expression. HMGB1 has been thought to take part in anti-inflammation because it activates inflammatory responses through multiple pathways, including activating the MAPK pathway and then NF-κB translocation, which triggers inflammatory responses[33]. These pathways lead to a cascade of inflammatory responses that can cause tissue damage and the release of inflammatory mediators. Secondly, the TUNEL assay is only useful for detecting dead cells, and this method does not distinguish between cell death mechanisms (necrosis or apoptosis)[30]. Because inflammatory responses can cause tissue damage and even death, Gly could reduce the number of TUNEL-positive cells by suppressing HMGB1 expression in this study. A limitation to our present study is that we did not assay the mechanism of Gly in attenuating cell damage.

In conclusion, our results confirmed that HMGB1 release plays an important role in spinal cord I/R damage[34], and we showed the Gly affords strong protection against transient spinal cord I/R injury by reducing inflammatory factors and cell apoptosis. Moreover, this protective effect by Gly is related to the inhibition of HMGB1 release that is induced by spinal cord I/R. These data suggest a new therapeutic possibility for treating ISCI with Gly. Future research should be directed toward developing a better understanding of the crosstalk between HMGB1 and apoptosis, as this ultimately might lead to therapeutic strategies for humans.

Author contribution

Prof Le-shun ZHOU designed the research and revised the manuscript; Gu GONG conducted the research, analyzed the data and wrote the paper; Li-bang YUAN, Ling HU, Wei WU, Liang YIN, and Jing-li HOU helped with portions of the research, and Ying-hai LIU helped write the manuscript.

References

1 Ronald AK, Marc ES, David MM. Anesthetic consideration for descending thoracic aortic aneurysm repair. Semin Cardiothorac Vasc Anesth 2007; 11: 205–23.
2 Tabayashi K. Spinal cord protection during thoracoabdominal aneurysm repair. Surg Today 2005; 35: 1–6.
3 Conrad MF, Ergul EA, Patel VI, Cambria MR, Lamuraglia GM, Simon M, *et al*. Evolution of operative strategies in open thoracoabdominal aneurysm repair. J Vasc Surg 2011; 53: 1195–201.
4 Danielisova V, Chavko M. Comparative effects of the N-methyl-D-aspartate antagonist MK-801 and the calcium channel blocker KB-2796 on neurologic and metabolic recovery after spinal cord ischemia. Exp Neurol 1998; 149: 203–8.
5 Agee JM, Flanagan T, Blackbourne LH, Kron IL, Tribble CG. Reducing postischemic paraplegia using conjugated superoxide dismutase. Ann Thorac Surg 1991; 51: 911–5.
6 Hirose K, Okajima K, Taoka Y, Uchiba M, Tagami H, Nakano K, *et al*. Activated protein C reduces the ischemia/reperfusion-induced spinal cord injury in rats by inhibiting neutrophil activation. Ann Surg 2000; 232: 272–80.
7 Klebanoff SJ, Vadas MA, Harlan JM, Sparks LH, Gamble JR, Agosti JM, *et al*. Stimulation of neutrophils by tumor necrosis factor. J Immunol 1986; 136: 4220–5.
8 Taoka Y, Okajima K, Murakami K, Johno M, Naruo M. Role of neutrophil elastase in compression-induced spinal cord injury in rats. Brain Res 1998; 799: 264–9.
9 Muller S, Ronfani L, Bianchi ME. Regulated expression and subcellular localization of HMGB1, a chromatin protein with a cytokine function. J Intern Med 2004; 255: 332–43.
10 Dumitriu IE, Baruah P, Manfredi AA, Bianchi ME, Rovere-Querini P. HMGB1: guiding immunity from within. Trends Immunol 2005; 26: 381–7.
11 Faraco G, Fossati S, Bianchi ME, Patrone M, Pedrazzi M, Sparatore B, *et al*. High mobility group box 1 protein is released by neural cells upon different stresses and worsens ischemic neurodegeneration *in vitro* and *in vivo*. J Neurochem 2007; 103: 590–603.
12 Kim JB, Lim CM, Yu YM, Lee JK. Induction and subcellular localization of high-mobility group box-1 (HMGB1) in the postischemic rat brain. J Neurosci Res 2008; 86: 1125–31.
13 Kim JB, Sig Choi J, Yu YM, Nam K, Piao CS, Kim SW, *et al*. HMGB1, a novel cytokine-like mediator linking acute neuronal death and delayed neuroinflammation in the postischemic brain. J Neurosci 2006; 26: 6413–21.
14 Arase Y, Ikeda K, Murashima N, Chayama K, Tsubota A, Koida I, *et al*. The long term efficacy of glycyrrhizin in chronic hepatitis C patients. Cancer 1997; 79: 1494–500.
15 Mollica L, De Marchis F, Spitaleri A, Dallacosta C, Pennacchini D, Zamai M, *et al*. Glycyrrhizin binds to high-mobility group box 1 protein and inhibits its cytokine activities. Chem Biol 2007; 14: 431–41.
16 van Rossum TG, Vulto AG, Hop WC, Schalm SW. Glycyrrhizin-induced reduction of ALT in European patients with chronic hepatitis C. Am J Gastroenterol 2001; 96: 2432–7.
17 Akgun S, Tekeli A, Kurtkaya O, Civelek A, Isbir SC, Ak K, *et al*. Neuroprotective effects of FK-506, *L*-carnitine and azathioprine on spinal cord ischemia-reperfusion injury. Eur J Cardiothorac Surg 2004; 25: 105–10.
18 Nakayama T, Harada N, Asano M, Nomura N, Saito T, Mishima A, *et al*. Atrial natriuretic peptide reduces ischemia/reperfusion-induced spinal cord injury in rats by enhancing sensory neuron activation. J Pharmacol Exp Ther 2007; 322: 582–90.
19 Fiane AE, Videm V, Lingaas PS, Heggelund L, Nielsen EW, Geiran OR, *et al*. Mechanism of complement activation and its role in the inflammatory response after thoracoabdominal aortic aneurysm repair. Circulation 2003; 108: 849–56.
20 Yamada S, Maruyama I. HMGB1, a novel inflammatory cytokine. Clin Chim Acta 2007; 375: 36–42.
21 Tsung A, Sahai R, Tanaka H, Nakao A, Fink MP, Lotze MT, *et al*. The nuclear factor HMGB1 mediates hepatic injury after murine liver ischemia-reperfusion. J Exp Med 2005; 201: 1135–43.
22 Watanabe T, Kubota S, Nagaya M, Ozaki S, Nagafuchi H, Akashi K, *et al*. The role of HMGB-1 on the development of necrosis during hepatic ischemia and hepatic ischemia/reperfusion injury in mice. J Surg Res 2005; 124: 59–66.
23 Wang H, Li W, Goldstein R, Tracey KJ, Sama AE. HMGB1 as a potential therapeutic target. Novartis Found Symp 2007; 280: 73–85.
24. Liu K, Mori S, Takahashi HK, Tomono Y, Wake H, Kanke T, *et al*. Anti-high mobility group box 1 monoclonal antibody ameliorates brain infarction induced by transient ischemia in rats. FASEB J 2007; 21: 3904–16.
25 Goldstein RS, Gallowitsch-Puerta M, Yang L, Rosas-Ballina M, Huston JM, Czura CJ, *et al*. Elevated high-mobility group box 1 levels in patients with cerebral and myocardial ischemia. Shock 2006; 25:

571–4.
26 Xu J, Beckman JS, Hogan EL, Hsu CY. Xanthine oxidase in experimental spinal cord injury. J Neurotrauma 1991; 8: 11–8.
27 Pineau I, Lacroix S. Proinflammatory cytokine synthesis in the injured mouse spinal cord: multiphasic expression pattern and identification of the cell types involved. J Comp Neurol 2007; 500: 267–85.
28 Yang L, Blumbergs PC, Jones NR, Manavis J, Sarvestani GT, Ghabriel MN. Early expression and cellular localization of proinflammatory cytokines interleukin-1beta, interleukin-6, and tumor necrosis factor-alpha in human traumatic spinal cord injury. Spine 2004; 29: 966–71.
29 Beattie MS, Farooqui AA, Bresnahan JC. Review of current evidence for apoptosis after spinal cord injury. J Neurotrauma 2000; 17: 915–25.
30 Ardeshiri A, Kelley MH, Korner IP, Hurn PD, Herson PS. Mechanism of progesterone neuroprotection of rat cerebellar Purkinje cells following oxygen-glucose deprivation. Eur J Neurosci 2006; 24: 2567–74.
31 Jiang W, Bell CW, Pisetsky DS. The relationship between apoptosis and high-mobility group protein 1 release from murine macrophages stimulated with lipopolysaccharide or polyinosinic-polycytidylic acid. J Immunol 2007; 178: 6495–503.
32 Qin S, Wang H, Yuan R, Li H, Ochani M, Ochani K, *et al*. Role of HMGB1 in apoptosis-mediated sepsis lethality. J Exp Med 2006; 203: 1637–42.
33 Sun NK, Chao CC. The cytokine activity of HMGB1 — extracellular escape of the nuclear protein. Chang Gung Med J 2005; 28: 673–82.
34 Wang Q, Ding Q, Zhou Y, Gou X, Hou L, Chen S, *et al*. Ethyl pyruvate attenuates spinal cord ischemic injury with a wide therapeutic window through inhibiting high-mobility group box 1 release in rabbits. Anesthesiology 2009; 110: 1279–86.

Acta Pharmacologica Sinica (2012) 33: 19–26
© 2012 CPS and SIMM All rights reserved 1671-4083/12 $32.00
www.nature.com/aps

npg

Original Article

Propofol increases the Ca^{2+} sensitivity of BK_{Ca} in the cerebral arterial smooth muscle cells of mice

Xue-ru LIU[1, #], Xiao-qiu TAN[2, #], Yan YANG[2], Xiao-rong ZENG[2], Xian-ling TANG[1, *]

[1]Anesthesiology Department of Affiliated Hospital of Luzhou Medical College, Luzhou 646000, China; [2]Key Lab of Medical Electrophysiology of Ministry of Education, Luzhou Medical College, Luzhou 646000, China

Aim: Propofol has the side effect of hypotension especially in the elderly and patients with hypertension. Previous studies suggest propofol-caused hypotension results from activation of large conductance Ca^{2+}-sensitive K channels (BKCa). In this study, the effects of propofol on the Ca^{2+} sensitivity of BKCa were investigated in mice cerebral arterial smooth muscle cells.
Methods: Single smooth muscle cells were prepared from the cerebral arteries of mice. Perforated whole-cell recoding was conducted to investigate the whole-cell BKCa current and spontaneous transient outward K^+ current (STOC). Inside-out patch configuration was used to record the single channel current and to study the Ca^{2+}- and voltage-dependence of BKCa.
Results: Propofol (56 and 112 μmol/L) increased the macroscopic BKCa and STOC currents in a concentration-dependent manner. It markedly increased the total open probability (NPo) of single BKCa channel with an EC_{50} value of 76 μmol/L. Furthermore, propofol significantly decreased the equilibrium dissociation constant (K_d) of Ca^{2+} for BKCa channel. The K_d value of Ca^{2+} was 0.881 μmol/L in control, and decreased to 0.694, 0.599, and 0.177 μmol/L, respectively, in the presence of propofol 28, 56, and 112 μmol/L. An analysis of the channel kinetics revealed that propofol (112 μmol/L) significantly increased the open dwell time and decreased the closed dwell time, which stabilized BKCa channel in the open state.
Conclusion: Propofol increases the Ca^{2+} sensitivity of BKCa channels, thus lowering the Ca^{2+} threshold of the channel activation in arterial smooth muscle cells, which causes greater vasodilating effects.

Keywords: propofol; BK_{Ca}; cerebral arterial vascular smooth muscle; hypotension; vasodilation

Acta Pharmacologica Sinica (2012) 33: 19–26; doi: 10.1038/aps.2011.134; published online 21 Nov 2011

Introduction

Propofol, an intravenous anesthetic, has been widely used for sedation in general anesthesia and in intensive care unit (ICU) because of its increasing agonist efficacy at the $GABA_A$ receptor[1, 2]. However, propofol has the potential side effect of hypotension, which especially affects elderly patients[3] and hypertensive rats[4, 5]. The wide variability of sensitivity to propofol may lead to circulatory instability among patients, the underlying mechanisms of which are complicated. The relaxation of vascular smooth muscle is the main mechanism of propofol-mediated vasodilation[6]. Some reports have shown that the modulation of ionic channels contributes to this effect through various modes of action, such as the inhibition of L-type voltage-dependent calcium channels (VDCCs) on vascular smooth muscle cells (SMCs), the activation of large conductance calcium- and voltage-activated potassium channels (BK_{Ca}), ATP-sensitive K^+ channels (K_{ATP}) and an increase in the calcium sensitivity of SMCs[7–9].

BK_{Ca} are expressed broadly on SMCs and play a critical role in the regulation of vascular tone, which is activated by both membrane depolarization and intracellular calcium[10–12]. The activation of BK_{Ca} leads to cell membrane hyperpolarization, which causes the closure of L-type VDCC, resulting in the block of the influx of extracellular Ca^{2+} [12–14]. The activation of BK_{Ca} may be one of the mechanisms affecting vasodilation and hypotension in many antihypertensive agents, such as the drug-mediated vasodilation of the endothelium-derived relaxing factors (EDRFs), which includes nitric oxide (NO)[15, 16]. Ketamine, an anesthetic associated with increases in arterial blood pressure, inhibits the activity of BK_{Ca}[17]. Structurally, BK_{Ca} are comprised of four pore-forming α subunits and four accessory β1 subunits in the arterial smooth muscle. The function of the β1 subunits is to enhance channel Ca^{2+} affinity and voltage sensitivity. Local $[Ca^{2+}]_{free}$ transients (Ca^{2+} sparks) have been widely studied in arterial smooth muscle cells[13, 18].

[#] These two authors contributed equally to this work.
[*] To whom correspondence should be addressed.
E-mail anesthesia2000@163.com
Received 2011-07-27 Accepted 2011-09-19

The Ca^{2+}-dependent relaxation of the SMCs, which is called Ca^{2+}-induced Ca^{2+} release (CICR), can be mediated by local Ca^{2+} releases through ryanodine receptor channels from the sarcoplasmic reticulum (SR). Higher local Ca^{2+} concentrations increase the activation of BK_{Ca} by more than 10^3 times and produce BK_{Ca} currents, which are called strong spontaneous transient outward K^+ currents (STOCs). Thus, STOCs have been noted as a singular type of BK_{Ca} current and represent the calcium sensitivity of BK_{Ca}[19, 20]. Studies have demonstrated the downregulated expression of the β1 subunit of BK_{Ca} and the abnormal coupling of Ca^{2+} spark/STOCs in spontaneously hypertensive rats (SHR)[21]. Studies have also noted abnormal coupling and downregulated Ca^{2+} sensitivity with hypertension in the β1-subunit knockout mouse[22, 23]. Ion channels, receptors, *etc* can be downregulated or upregulated, but the channel calcium sensitivity either increases or decreases.

Klockgether-Radke *et al* reported that the activation of BK_{Ca} may contribute to the propofol-mediated relaxation of porcine coronary artery rings[24]. Nagakawa *et al* showed that propofol-mediated hyperpolarization can be attributed to the activation of BK_{Ca} in the mesenteric vascular smooth muscle tissue of rats by measuring the membrane potential[25]. Stadnicka *et al* reported that the activation of BK_{Ca} was involved in the membrane hyperpolarization and in the propofol-mediated dilatation of mesenteric SMCs in rats, and that the effect of propofol on BK_{Ca} was significantly greater in Dahl salt-sensitive rats when using patch clamp techniques[26]. In elderly or hypertensive rats, the effect of propofol on hypotension was more serious[4, 27]. Vascular calcium overload occurred in the vascular SMCs during hypertension[28]. It has also been shown that the calcium sensitivity of BK_{Ca} is downregulated in patients with hypertension[29]. These reports suggest that the change in calcium sensitivity in BK_{Ca} may be linked to the differential effects of propofol among patients.

Previous research has demonstrated that BK_{Ca} are crucially involved in propofol-induced vasodilation, especially in the setting of hypertension. In our study, we hypothesized that the variable effect of propofol among patients was due in part to its effect on the calcium sensitivity of BK_{Ca}. To learn more about the mechanisms of these processes, we studied the interaction of propofol with the vascular smooth muscle BK_{Ca} by analyzing the macroscopic and single channel currents recorded on the cerebral arterial SMCs of mice.

Materials and methods

Single cell isolation

The Ethics Committee of Luzhou Medical College approved this study. The mice were obtained from the animal care center of Luzhou Medical College. The animals were deeply anesthetized with pentobarbital sodium (60 mg/kg ip). The brain was dissected out and placed in an ice-cold normal physiological saline solution (PSS). The cerebral arteries were carefully dissected out from the brain and then exposed to low Ca^{2+} PSS (0.1 mmol/L $CaCl_2$). The arteries were enzymatically dissociated for 9.5 min in a low Ca^{2+} PSS containing (in g/L) 0.3 papain and 0.2 dithioerythritol (DTE). The arteries were then treated for another 9.5 min in a low Ca^{2+} PSS containing (in g/L) 0.8 collagenase F, 1.0 collagenase II and 1.0 dithiothreitol (DTT) at 37 °C. The single cerebral arterial smooth muscle cells were obtained by gently triturating the digested tissues in culture dishes filled with PSS containing 1 g/L albumin. The cells were then stored at 4 °C until the subsequent electrophysiological experiments were performed.

All measurements were obtained at room temperature (23±2 °C).

Electrophysiological methods

Electrophysiological recordings were performed as previously described[16]. Macroscopic BK_{Ca} currents were recorded using stepwise 10-mV depolarizing pulses (400-ms duration, 1-s interval) from a constant holding potential of -60 mV in cells or a ramp pulse at 0.375 V/s from -80 to +70 mV. The bathing solution contained the following (in mmol/L): NaCl 137, KCl 5.9, $MgCl_2$ 1.2, $CaCl_2$ 1.8, glucose 10 and HEPES 10 (pH 7.4). The pipette solution contained the following (in mmol/L): KCl 128, NaCl 12, $MgCl_2$ 4, HEPES 10 and EGTA 0.05 (pH 7.2), with 0.2 g/L amphotericin B. STOCs were recorded at steady-state membrane potentials between -50 mV and 0 mV.

Single channel currents were recorded 20–30 min after a membrane patch formation and more than 5 min after each drug application. During the inside-out patch experiments, the pipette solution consisted of the following (in mmol/L): K-aspartate (K-Asp) 40, KCl 100, HEPES-K 10 (pH 7.2) and EGTA 2. The bath solution consisted of the following (in mmol/L) K-Asp 100, KCl 40, HEPES-K 10 (pH 7.4) and EGTA 1. The free Ca^{2+} concentration in the bath solution ($[Ca^{2+}]_{free}$) was calculated according to the following equation,

$$[Ca^{2+}]_{add} = (1+K'([EGTA]+[Ca^{2+}]_{free})\times[Ca^{2+}]_{free})/(1+[Ca^{2+}]_{free}\times K') \quad \text{(Eq 1)}$$

where $[Ca^{2+}]_{add}$ is the concentration of $CaCl_2$, $[Ca^{2+}]_{free}$ is the concentration of free calcium ion, [EGTA] is the concentration of EGTA, and K' is the association constant of calcium with EGTA, where $K'=10^{7.1}$ (pH=7.2, 22 °C). To prepare $[Ca^{2+}]_{free}$ of -0, 0.01, 0.1, 0.5, 1, or 10 μmol/L, the $CaCl_2$ concentration was changed to 0, 0.11, 0.55, 0.86, 0.92, or 1 mmol/L, respectively. The membrane potential (V_m) was expressed as the potential at the intracellular side minus the potential at the extracellular side.

Drug and chemicals

Propofol was purchased from AstraZeneca Co, England (production lot number: GF357). The drug was dissolved in DMSO to obtain a 100 mmol/L stock solution and was added to the bath solution to obtain the desired concentration. K-aspartate, HEPES, EGTA, and enzymes were obtained from Sigma (USA).

Statistical analysis

Whole-cell macroscopic currents were analyzed using pClamp software 10.0 (Axon, USA) and the STOCs were analyzed using MiniAnalysis program (Synaptosoft Software, Leonia, NJ). The total open probability (*N*Po), the amplitude and the kinetic characteristics of the channels were analyzed by pClamp software 10.0 and by QUB software (www.qub.buffalo.edu). Data are expressed as the mean±SEM. Student's *t*-test was used for paired data, and the independent test was used for statistical analysis. A value of $P<0.05$ was considered to be statistically significant, and "a" ($P>0.05$), "b" ($P<0.05$) and "c" ($P<0.01$) are indicated in the figures. The relationship between the drug concentration and the normalized *N*Po was integrated into the Hill equation,

$$y = x^b/(c^b+x^b) \qquad \text{(Eq 2)}$$

where x is the concentration of propofol or calcium, c is the half maximal effective concentration (EC_{50}) of propofol or equilibrium dissociation constant (K_d) of calcium and b is the slope factor (Hill coefficient, n_H).

Results

Properties of BK_{Ca} currents in cerebral arterial smooth muscle cells

We confirmed that BK_{Ca} in the cerebral arterial SMCs of mice possess the characteristic properties found in other tissues. A typical recording of whole-cell macroscopic BK_{Ca} currents is shown in Figure 1A. The STOCs are superimposed stochastically onto the whole-cell currents, and both currents were significantly suppressed by the external application of 200 nmol/L IbTX, a specific blocker of BK_{Ca}. The amplitude and frequency of the STOCs increased, as did the membrane depolarization. These effects can also be blocked with 200 nmol/L IbTX (Figure 1B). Figure 1C shows representative records of single BK_{Ca} currents under the inside-out configuration at different voltages with the symmetrical 140 mmol/L K^+ ($[Ca^{2+}]_{free}$=0.5 μmol/L). The activity of BK_{Ca} increased with membrane depolarization. The intracellular calcium also activated BK_{Ca} (Figure 1D). The single channel conductance of BK_{Ca}, measured with symmetrical K^+ concentration (140 mmol/L) on both sides of the membrane, was 205±44 pS (n=25). With the use of different salt compositions (substituting Na^+ for K^+ in the bath and pipette solution), the data indicated that the channels are K^+ selective (data not shown). The currents were blocked by 200 nmol/L IbTX applied to the bath through the outside-out patches (Figure 1E). These properties of BK_{Ca} are consistent with those previously reported[16, 30].

The effects of propofol on BK_{Ca} in the whole-cell configuration

Figure 2 shows the effects of propofol on the BK_{Ca} macroscopic currents using step depolarizations (A) or a ramp voltage (B). Propofol 56 and 112 μmol/L markedly increased the macroscopic current density. The external application of 200 nmol/L IbTX inhibited the STOCs completely and the macroscopic current partially (Figure 2B).

At +60 mV membrane potential, propofol 56 and 112 μmol/L increased the macroscopic current density 1.4-fold

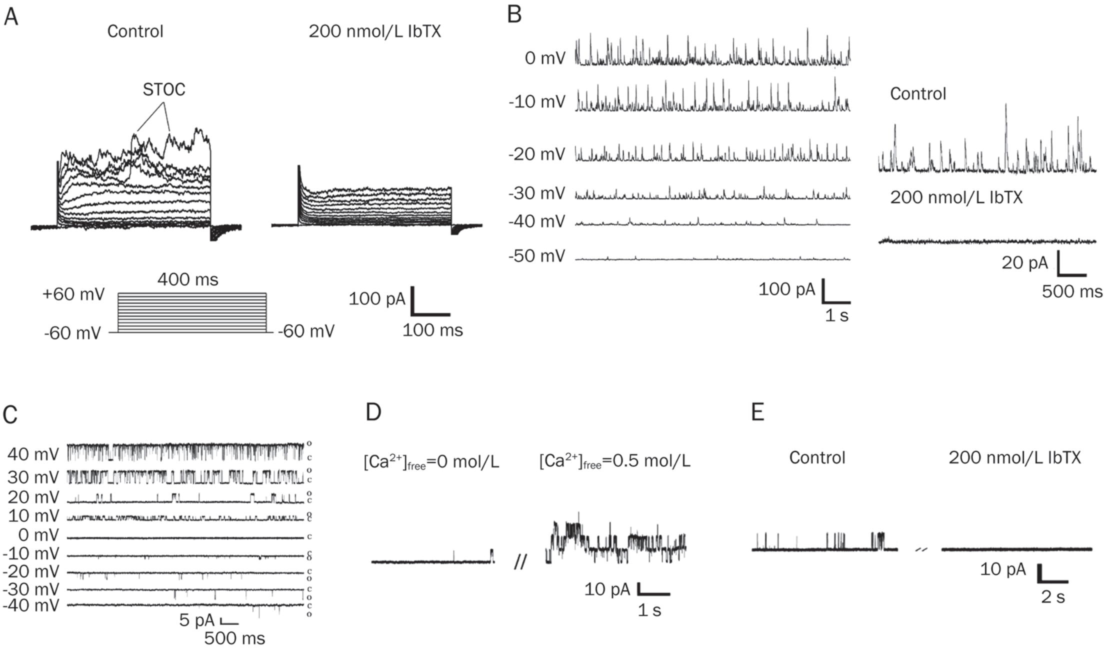

Figure 1. Properties of BK_{Ca} in mouse cerebral artery smooth muscle cells. (A) A typical recording of macroscopic currents of BK_{Ca}. STOCs superimposed stochastically onto whole-cell currents, and both currents were significantly suppressed by 200 nmol/L IbTX, a specific blocker of BK_{Ca}. (B) The properties of STOCs. The amplitude and frequency of STOCs increased as the membrane depolarization, which can also be blocked by 200 nmol/L IbTX. (C) A typical recording of single channel currents in an inside-out membrane patch configuration. The upward deflection indicates outward currents. (D) An example of testing Ca^{2+} dependence of BK_{Ca} (inside-out patch, at +40 mV membrane potential). (E) An example of testing IbTX blockage of BK_{Ca} (outside-out patch, at +40 mV membrane potential).

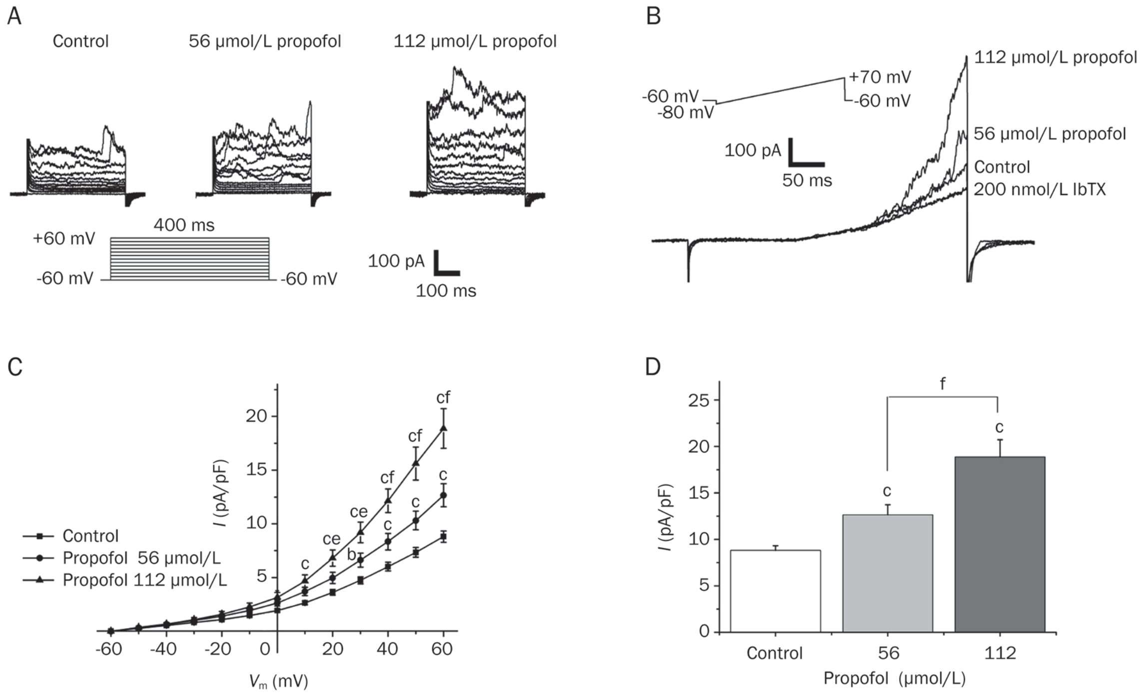

Figure 2. Effect of propofol on the macroscopic currents of BK_{Ca}. (A) The typical recording of the effect of 56 and 112 μmol/L propofol on BK_{Ca} by step pulse. (B) The typical recording of the effect of 56 and 112 propofol on BK_{Ca} by ramp pulse. The effect of propofol can be blocked by 200 nmol/L IbTX. (C) The *I–V* relation curve of the macro-currents. Propofol 56 and 112 μmol/L shifted the curve at various membrane voltages. (D) The histogram of the effect of 56 and 112 μmol/L propofol on the BK_{Ca} currents density at V_m=+60 mV. $^{b}P<0.05$, $^{c}P<0.01$ *vs* control group; $^{e}P<0.05$, $^{f}P<0.01$ *vs* 56 μmol/L propofol.

(12.7±1.1 pA/pF *vs* 8.8±0.5 pA/pF, $P<0.01$, n=15) and 2.4-fold (18.9±1.8 pA/pF *vs* 8.8±0.5 pA/pF, $P<0.01$, n=12), respectively (Figure 2D).

The STOCs were recorded at -30 mV membrane potential. As shown in Figure 3, propofol 56 and 112 μmol/L increased the amplitude of the STOCs 1.5-fold and 1.6-fold, respectively, from 18.5±0.8 pA to 28.0±1.1 pA ($P<0.01$, n=5) and to 30.1±5.7 pA ($P<0.01$, n=4), respectively. The frequency of the STOCs increased 1.7-fold and 2.7-fold from 3.6±1.4 Hz to 6.0±2.2 Hz ($P<0.05$, n=5) and to 9.5±3.4 Hz ($P<0.01$, n=4), respectively. Propofol 112 μmol/L increased the frequency of the STOCs more than the 56 μmol/L concentration ($P<0.05$). The results strongly suggest that the enhancement of the frequency and amplitude of the STOCs by propofol is one of the major causes

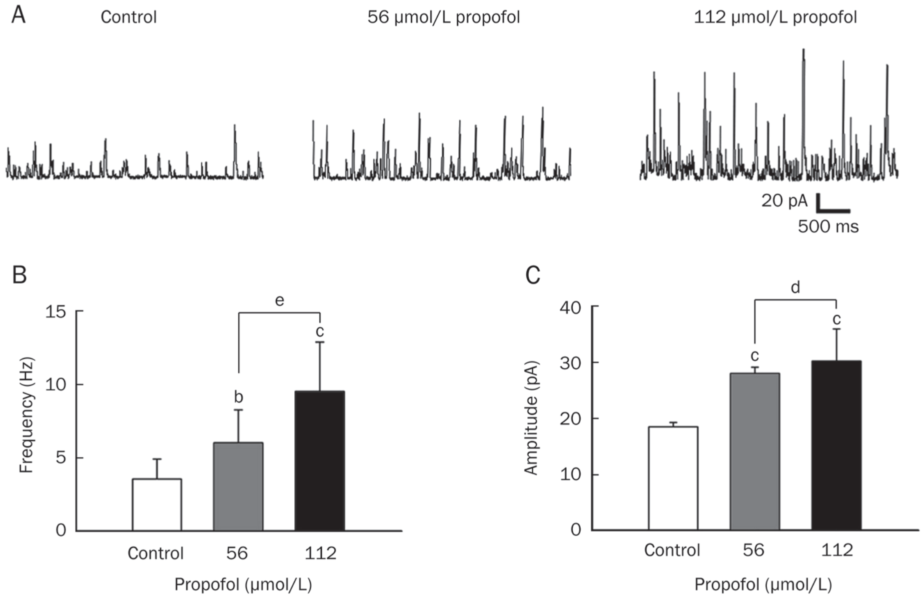

Figure 3. Effect of propofol on STOCs in mouse cerebral arterial SMCs. (A) A typical recording of STOCs. Propofol 56 and 112 μmol/L activates the STOCs. (B) The histogram shows that 56 and 112 μmol/L propofol increased frequency of STOCs. (C) The histogram shows the effect of 56 and 112 μmol/L propofol on the amplitude of STOCs. $^{b}P<0.05$, $^{c}P<0.01$ *vs* control group. $^{d}P>0.05$, $^{e}P<0.05$ *vs* 56 μmol/L propofol.

of propofol-induced vasodilation.

The effects of propofol on single BK_{Ca} channel activity

To investigate the mechanisms of propofol that increase the frequency and amplitude of the STOCs, we studied the effect of propofol on single channel activities. We examined the effect of propofol (0–224 μmol/L) on activity at $[Ca^{2+}]_{free}$=0.1 μmol/L when propofol was applied to the cytoplasmic side of a single BK_{Ca} using the inside-out patch configuration. Figure 4A shows examples of the records at V_m=+40 mV with different propofol concentrations. Propofol increased the activity of BK_{Ca} in a concentration-dependent manner. Propofol 56 and 112 μmol/L increased the *N*Po 52-fold and 193-fold, respectively, in comparison with the control group (0.23±0.09, 0.85±0.10 *vs* 0.004±0.001, *n*=5). The propofol dose-response curve is presented in Figure 4B. This figure shows that the values of *N*Po were normalized to the *N*Po value at a propofol concentration of 224 μmol/L. The data were integrated through the use of the Hill equation (Eq 2) with an EC_{50} of 76±8 μmol/L and an n_H of 3.62.

Propofol increases the calcium and voltage dependence of BK_{Ca}

We further investigated the effect of propofol on the calcium sensitivity of BK_{Ca} directly with the inside-out patches. The Ca^{2+} sensitivity of *N*Po increased when propofol was present in the bathing solution (Figure 5A). Figure 5B plots the relations of *N*Po when normalized to their maximum value against $[Ca^{2+}]_{free}$. These data were integrated into the Hill equation. When the propofol concentration was increased from 0 to 112 μmol/L, the K_d was shifted from 0.881 to 0.694, 0.599 to 0.177 μmol/L, respectively (Figure 5B). However, there was no significant difference in the value of n_H. As shown in Figure 5B, BK_{Ca} activity was very sensitive to propofol at the $[Ca^{2+}]_{free}$ range of 0.1 to 1 μmol/L. At 0.5 μmol/L $[Ca^{2+}]_{free}$, the values of normalized *N*Po at the propofol concentrations of 0, 28, 56, and 112 μmol/L were 0.06±0.01, 0.20±0.01, 0.34±0.03, and 0.94±0.06, respectively. The results were consistent with the effect of propofol on the STOCs. The augmentation of propofol on BK_{Ca} increased with higher levels of intracellular calcium.

We also studied the effects of propofol on the voltage dependence of BK_{Ca}. The NPo was normalized to the maximum open probability, and the data were integrated into the Boltzmann function (y=A2+ (A1–A2)/(1+exp((x–x0)/dx))). As shown in Figures 5E and 5F, the half activation voltage ($V_{1/2}$) was decreased by the 56 μmol/L propofol concentration from 78.1±1.2 mV (control) to 52.8±1.5 mV at 0.5 μmol/L $[Ca^{2+}]_{free}$ (P<0.05, n=5). These results suggest that propofol lowered the calcium and voltage thresholds for BK_{Ca} activation.

The effects of propofol on the kinetics of BK_{Ca}

We further investigated the effect of propofol on the kinetics of BK_{Ca} at 0.1 μmol/L $[Ca^{2+}]_{free}$. This investigation included an assessment of the open dwell time, the closed dwell time, the open time constant and the closed time constant (Figure 6). Figure 6A shows the typical current recording for a concentration of 112 μmol/L of propofol on BK_{Ca}. The right recording suggested that 112 μmol/L of propofol increased the open dwell time of BK_{Ca}. Propofol at a concentration of 112 μmol/L increased the open dwell time from 4.9±2.0 to 33.3±2.1 ms (P<0.01, n=5) and reduced the closed dwell time from 4511±604 to 114±47 ms (P<0.01, n=5) (Figure 6B). The histogram in Figure 6C shows the effect of propofol on the open and closed time constant. Propofol 112 μmol/L decreased the open time constant (0.90±0.24 *vs* 3.10±1.11 ms, P<0.05, n=5) and increased the closed time constant (1.48±0.15 *vs* 0.55±0.13 ms, P<0.01, n=5) of BK_{Ca}. A propofol 112 μmol/L sped up the transition from the closed to the open state and slowed down the transition from the open to the closed state. These findings indicate that propofol not only accelerates BK_{Ca} transition time from the closed to the open state, but also that propofol maintains the channel in the open state.

Discussion

Propofol, an intravenous general anesthetic, is widely used for the induction and maintenance of general anesthesia because of the rapid onset of the drug and the relatively few side effects. However, there is a marked variability in cardiovascular sensitivity to propofol among patients. This variability may induce the serious side effect of hypotension, especially in elderly and hypertensive patients[5]. There are several mechanisms that are known to cause the hypotensive effects

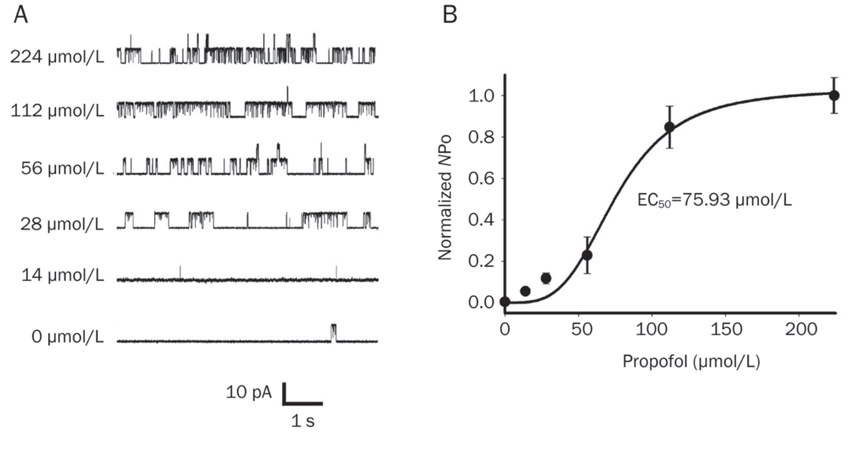

Figure 4. Effect of propofol on BK_{Ca} in inside-out configuration. (A) The typical recording shows that 14–224 μmol/L propofol activates BK_{Ca} in a concentration-dependent manner at V_m=+40 mV. (B) The dose-response curve of propofol at $[Ca^{2+}]_{free}$=0.1 μmol/L. The data were fitted by Hill equation (n_H=3.62, EC_{50}=76±8 μmol/L).

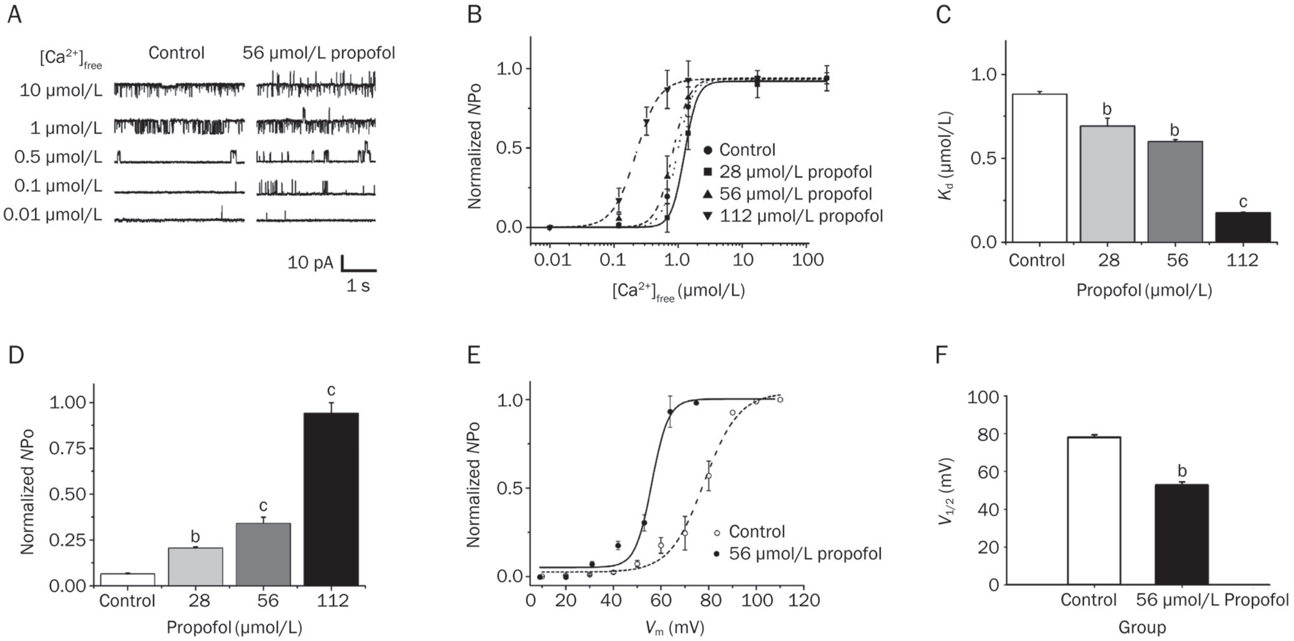

Figure 5. Effect of propofol on the calcium and voltage dependence of BK_{Ca}. (A) Examples of channel activity at different concentrations of Ca^{2+} recorded at V_m=+40 mV. (B) The dose-response curves of calcium on the BK_{Ca} with 0, 28, 56 and 112 μmol/L propofol. These data were fitted by Hill equation. (C) The K_d of Ca^{2+} with 0, 28, 56, and 112 μmol/L propofol was 0.881, 0.694, 0.599, and 0.177 μmol/L, respectively. (D) The normalized NP_o at $[Ca^{2+}]_{free}$=0.5 μmol/L from Fig 3B was 0.06±0.01, 0.20±0.01, 0.34±0.03, and 0.94±0.06 as the propofol was 0, 28, 56 and 112 μmol/L, respectively. (E) Propofol 56 μmol/L shifted the voltage dependence of BK_{Ca}. (F) Propofol 56 μmol/L shifted $V_{1/2}$ from 78.1±1.2 mV to 52.8±1.5 mV at $[Ca^{2+}]_{free}$=0.1 μmol/L. $^{a}P>0.05$, $^{b}P<0.05$, $^{c}P<0.01$ *vs* control group.

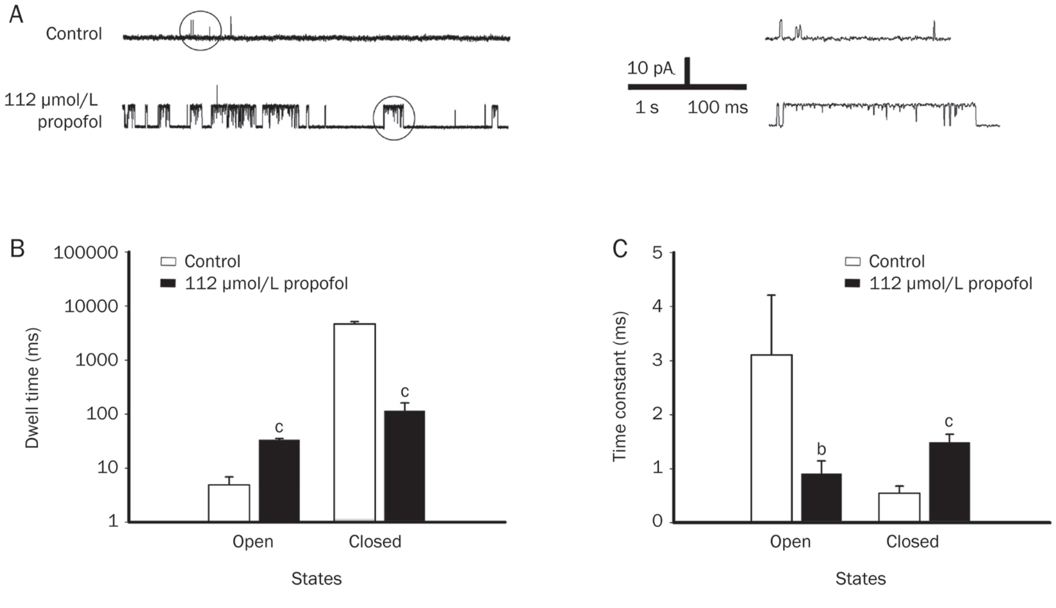

Figure 6. Effect of propofol on BK_{Ca} kinetics. (A) Typical recordings of 112 μmol/L propofol on BK_{Ca} ($[Ca^{2+}]_{free}$=0.1 μmol/L) at V_m=+40 mV. The right traces show that propofol increases the open dwell time. (B) The effect of 112 μmol/L propofol on the dwell time distributions (n=5). It increases the open dwell time (33.3±2.1 *vs* 4.9±2.0 ms, $P<0.01$) and reduces the closed dwell time (114±47 *vs* 4511±604 ms, $P<0.01$). (C) Effect of 112 μmol/L propofol on the time constant of BK_{Ca} (n=5). It decreased the open time constant (0.90±0.24 *vs* 3.10±1.11 ms, $P<0.05$) increased the close time constant (1.48±0.15 *vs* 0.55±0.13 ms, $P<0.01$). $^{b}P<0.05$, $^{c}P<0.01$ *vs* control group.

of propofol, such as inhibition of the renin-angiotensin system (RAS)[31, 32], blocking of the release of noradrenaline from the sympathetic nerve endings[33], reduction in cardiac contractility and cardiac output[34, 35], and direct relaxation of the peripheral vessels[36]. The major effect of propofol stems from the relaxation of the peripheral vessels. BK_{Ca} play a significant role in the regulation of vascular tone. We have confirmed the presence of propofol-activated BK_{Ca} in the mesenteric SMCs of humans in cell-attached and whole cell configurations[37]. In our study, propofol activated the macroscopic currents of BK_{Ca}, the STOCs and single channel currents in a concentration-dependent manner (Figures 2 and 4). These data indicate that BK_{Ca} may contribute to the vasodilating effects of propofol.

The variance in circulatory instability with propofol is marked among patients, especially those with hypertension. The characteristics of BK_{Ca} change in hypertension, including changes in calcium sensitivity. With the combination of factors that induce higher levels of intracellular calcium, how do BK_{Ca} participate in the variable effects of propofol among different patients?

In our study, 56 μmol/L and 112 μmol/L concentrations of propofol increased the amplitude and frequency of the STOCs, which suggests that an augmentation in calcium sensitivity is involved in the effects of propofol on BK_{Ca}. However, there was no significant difference between the effects of 56 μmol/L and 112 μmol/L of propofol on the amplitude of the STOCs ($P>0.05$), which may be due to the increasing frequency of many of the STOCs with lower amplitudes at 112 μmol/L of propofol. The effect of propofol on calcium sensitivity was also confirmed by the experiments in inside-out configuration. The data indicate that propofol increased the calcium sensitivity by decreasing the K_d from 0.881 to 0.177 μmol/L (Figure 5B). The effect of propofol on channel NPo was particularly evident at 0.1 to 1 μmol/L $[Ca^{2+}]_{free}$, the concentration that activates the contractile apparatus of the cells[38]. This indicates that under such conditions (0.1 to 1 μmol/L $[Ca^{2+}]_{free}$), propofol causes a significant hyperpolarization of the membrane potential. These results suggest that the augmentation effect of propofol on the calcium sensitivity of BK_{Ca} could be attributed to the hypotensive side effects of propofol, which are more extensive in the patients with hypertension. Propofol also shifted the voltage dependency of BK_{Ca} (Figure 5E, 5F) to more negative potentials. The effects of propofol on both calcium and voltage sensitivity indicate that the threshold of BK_{Ca} activation is lowered and that it may be easily activated in the presence of propofol, especially under higher intracellular levels of calcium.

The analysis of the kinetic properties of single channel currents revealed that propofol increased the open dwell time and decreased the closed dwell time. Propofol maintained and stabilized BK_{Ca} in the open state. This indicates that the molecular kinetics also participates in the augmenting action of propofol on BK_{Ca}.

In conclusion, this study has revealed the molecular mechanisms of propofol on BK_{Ca}. As one of the lipophilic anesthetics, propofol is absorbed by cell membrane lipids and directly alters BK_{Ca} properties. Propofol enhances calcium and voltage sensitivity, modulates channel kinetics and thus stabilizes BK_{Ca} in the open state. These effects may contribute to the greater vasodilator effects of BK_{Ca} activation under conditions that favor cellular Ca^{2+} overload, such as hypertension.

Acknowledgements

We thank Dr Isao INOUE, professor of Luzhou Medical College, for his assistance with language and with helpful comments during the preparation of this manuscript. This work was supported by the National Natural Science Foundation of China (N<u>o</u> 30370527 and 30670763).

Author contribution

Xian-ling TANG, Xiao-rong ZENG, and Xue-ru LIU designed the research; Xue-ru LIU, Xiao-qiu TAN, and Yan YANG performed the research; Xue-ru LIU and Xiao-qiu TAN analyzed the data; and Xue-ru LIU and Xiao-qiu TAN wrote the paper.

References

1 Smith I, White PF, Nathanson M, Gouldson R. Propofol. An update on its clinical use. Anesthesiology 1994; 81: 1005–43.
2 White PF. Propofol: its role in changing the practice of anesthesia. Anesthesiology 2008; 109: 1132–6.
3 Hug CC Jr, McLeskey CH, Nahrwold ML, Roizen MF, Stanley TH, Thisted RA, et al. Hemodynamic effects of propofol: data from over 25,000 patients. Anesth Analg 1993; 77: S21–9.
4 Boillot A, Laurant P, Berthelot A, Barale F. Effects of propofol on vascular reactivity in isolated aortae from normotensive and spontaneously hypertensive rats. Br J Anaesth 1999; 83: 622–9.
5 Gragasin FS, Davidge ST. The effects of propofol on vascular function in mesenteric arteries of the aging rat. Am J Physiol Heart Circ Physiol 2009; 297: H466–74.
6 Ririe DG, Lundell JC, Neville MJ. Direct effects of propofol on myocardial and vascular tissue from mature and immature rats. J Cardiothorac Vasc Anesth 2001; 15: 745–9.
7 Chang KS, Davis RF. Propofol produces endothelium-independent vasodilation and may act as a Ca^{2+} channel blocker. Anesth Analg 1993; 76: 24–32.
8 Kanaya N, Murray PA, Damron DS. Propofol increases myofilament Ca^{2+} sensitivity and intracellular pH via activation of Na^+–H^+ exchange in rat ventricular myocytes. Anesthesiology 2001; 94: 1096–104.
9 Kinoshita H, Ishida K, Ishikawa T. Thiopental and propofol impair relaxation produced by ATP-sensitive potassium channel openers in the rat aorta. Br J Anaesth 1998; 81: 766–70.
10 Ko EA, Han J, Jung ID, Park WS. Physiological roles of K^+ channels in vascular smooth muscle cells. J Smooth Muscle Res 2008; 44: 65–81.
11 Eichhorn B, Dobrev D. Vascular large conductance calcium-activated potassium channels: functional role and therapeutic potential. Naunyn Schmiedebergs Arch Pharmacol 2007; 376: 145–55.
12 Ledoux J, Werner ME, Brayden JE, Nelson MT. Calcium-activated potassium channels and the regulation of vascular tone. Physiology (Bethesda) 2006; 21: 69–78.
13 Jaggar JH, Porter VA, Lederer WJ, Nelson MT. Calcium sparks in smooth muscle. Am J Physiol Cell Physiol 2000; 278: C235–56.
14 Perez GJ, Bonev AD, Nelson MT. Micromolar Ca^{2+} from sparks activates Ca^{2+}-sensitive K^+ channels in rat cerebral artery smooth muscle. Am J Physiol Cell Physiol 2001; 281: C1769–75.
15 Waldron GJ, Cole WC. Activation of vascular smooth muscle K^+ channels by endothelium-derived relaxing factors. Clin Exp Pharmacol Physiol 1999; 26: 180–4.

16 Yang Y, Cai F, Li PY, Li ML, Chen J, Chen GL, *et al*. Activation of high conductance Ca^{2+}-activated K^+ channels by sodium tanshinone II-A sulfonate (DS-201) in porcine coronary artery smooth muscle cells. Eur J Pharmacol 2008; 598: 9–15.

17 Han J, Kim N, Joo H, Kim E. Ketamine blocks Ca^{2+}-activated K^+ channels in rabbit cerebral arterial smooth muscle cells. Am J Physiol Heart Circ Physiol 2003; 285: H1347–55.

18 Wellman GC, Nelson MT. Signaling between SR and plasmalemma in smooth muscle: sparks and the activation of Ca^{2+}-sensitive ion channels. Cell Calcium 2003; 34: 211–29.

19 Morimura K, Ohi Y, Yamamura H, Ohya S, Muraki K, Imaizumi Y. Two-step Ca^{2+} intracellular release underlies excitation-contraction coupling in mouse urinary bladder myocytes. Am J Physiol Cell Physiol 2006; 290: C388–403.

20 Wray S, Burdyga T, Noble K. Calcium signalling in smooth muscle. Cell Calcium 2005; 38: 397–407.

21 Chang T, Wu L, Wang R. Altered expression of BK channel beta1 subunit in vascular tissues from spontaneously hypertensive rats. Am J Hypertens 2006; 19: 678–85.

22 Brenner R, Perez GJ, Bonev AD, Eckman DM, Kosek JC, Wiler SW, *et al*. Vasoregulation by the beta1 subunit of the calcium-activated potassium channel. Nature 2000; 407: 870–6.

23 Pluger S, Faulhaber J, Furstenau M, Lohn M, Waldschutz R, Gollasch M, *et al*. Mice with disrupted BK channel beta1 subunit gene feature abnormal Ca^{2+} spark/STOC coupling and elevated blood pressure. Circ Res 2000; 87: E53–60.

24 Klockgether-Radke AP, Schulze H, Neumann P, Hellige G. Activation of the K^+ channel BK(Ca) is involved in the relaxing effect of propofol on coronary arteries. Eur J Anaesthesiol 2004; 21: 226–30.

25 Nagakawa T, Yamazaki M, Hatakeyama N, Stekiel TA. The mechanisms of propofol-mediated hyperpolarization of *in situ* rat mesenteric vascular smooth muscle. Anesth Analg 2003; 97: 1639–45.

26 Stadnicka A, Contney SJ, Moreno C, Weihrauch D, Bosnjak ZJ, Roman RJ, *et al*. Mechanism of differential cardiovascular response to propofol in Dahl salt-sensitive, Brown Norway, and chromosome 13-substituted consomic rat strains: role of large conductance Ca^{2+} and voltage-activated potassium channels. J Pharmacol Exp Ther 2009; 330: 727–35.

27 Bilotta F, Fiorani L, La Rosa I, Spinelli F, Rosa G. Cardiovascular effects of intravenous propofol administered at two infusion rates: a transthoracic echocardiographic study. Anaesthesia 2001; 56: 266–71.

28 Fleckenstein-Grun G, Frey M, Thimm F, Hofgartner W, Fleckenstein A. Calcium overload--an important cellular mechanism in hypertension and arteriosclerosis. Drugs 1992; 44: 23–30.

29 Wang Y, Zheng GQ, Wei ZD. Study on calcium-activated potassium channel of mesentery artery smooth muscle cells of hypertension patients study on calcium-activated potassium channel of mesentery artery smooth muscle cells of hypertension patients. Zhongguo Ying Yong Sheng Li Xue Za Zhi 2007; 23: 395–8.

30 Tan X, Yang Y, Cheng J, Li P, Inoue I, Zeng X. Unique action of sodium tanshinone II-A sulfonate (DS-201) on the Ca^{2+} dependent BK_{Ca} activation in mouse cerebral arterial smooth muscle cells. Eur J Pharmacol 2011; 656: 27–32.

31 Votta-Velis EG, Minshall RD, Visintine DJ, Castellon M, Balyasnikova IV. Propofol attenuates endotoxin-induced endothelial cell injury, angiotensin-converting enzyme shedding, and lung edema. Anesth Analg 2007; 105: 1363–70, table of contents.

32 Zou XJ, Yang L, Yao SL. Propofol depresses angiotensin II-induced cardiomyocyte hypertrophy *in vitro*. Exp Biol Med (Maywood) 2008; 233: 200–8.

33 Ebert TJ. Sympathetic and hemodynamic effects of moderate and deep sedation with propofol in humans. Anesthesiology 2005; 103: 20–4.

34 Gable BD, Shiga T, Murray PA, Damron DS. Propofol increases contractility during alpha1a-adrenoreceptor activation in adult rat cardiomyocytes. Anesthesiology 2005; 103: 335–43.

35 Larsen JR, Torp P, Norrild K, Sloth E. Propofol reduces tissue-Doppler markers of left ventricle function: a transthoracic echocardiographic study. Br J Anaesth 2007; 98: 183–8.

36 Chang YX, Yan DM, Chen LL, Ding XP, Qi J, Kang LY, *et al*. Potency fingerprint of herbal products Danshen injection for their quality evaluation. Chem Pharm Bull (Tokyo) 2009; 57: 586–90.

37 Du JG, Tang XL, WANG XB, Li ZW, Wang SD. Effect of propofol on large conductance calium-activated potassium channel in human mesentery smooth muscle cells. Chin J Anesthesiol 2006; 26: 87–8.

38 Karaki H, Ozaki H, Hori M, Mitsui-Saito M, Amano K, Harada K, *et al*. Calcium movements, distribution, and functions in smooth muscle. Pharmacol Rev 1997; 49: 157–230.

Acta Pharmacologica Sinica (2012) 33: 27–33
© 2012 CPS and SIMM All rights reserved 1671-4083/12 $32.00
www.nature.com/aps

Original Article

Lipid metabolism disturbances and AMPK activation in prolonged propofol-sedated rabbits under mechanical ventilation

Wei JIANG#, Zheng-bo YANG#, Quan-hong ZHOU, Xiang HUAN, Li WANG*

Department of Anesthesiology, Shanghai Sixth Municipal Hospital, Shanghai Jiaotong University, Shanghai 200233, China

Aim: To explore the mechanisms underlying the propofol infusion syndrome (PRIS), a potentially fatal complication during prolonged propofol infusion.
Methods: Male rabbits under mechanical ventilation through endotracheal intubation were divided into 3 groups (n=6 for each) that were sedated with 1% propofol (Group P), isoflurane (Group I) or isoflurane while receiving 10% intralipid (Group II), respectively. Blood biochemical parameters were collected at 0, 6, 12, 18, 24, and 30–36 h after the initiation of treatments. The hearts were removed out immediately after the experiments, and the level of tumor necrosis factor (TNF)-α in the hearts were studied using immunohistochemistry. AMP-activated protein kinase (AMPK) and phospho-AMPK in the hearts were assessed using Western blotting.
Results: The mortality rate was 50% in Group P, and 0% in Groups I and II. The serum lipids and liver function indices in Group P were significantly increased, but moderately increased in Group II. Significant decreases in these indices were found in Groups I. All the groups showed dramatically increased release of creatine kinase (CK). Intense positive staining of TNF-α was found in all the heart samples in Group P, but only weak and neglectful staining was found in the hearts from Group II and Group I, respectively. AMPK phosphorylation was significantly increased in the hearts of Group P.
Conclusion: Continuous infusion of large dose of propofol in rabbits undergoing prolonged mechanical ventilation causes hyperlipidemia, liver dysfunction, increased CK levels, AMPK activation and myocardial injury. The imbalance between energy demand and utilization may contribute to PRIS.

Keywords: propofol; propofol infusion syndrome (PRIS); sedation; isoflurane; intralipid; tumor necrosis factor alpha; AMPK

Acta Pharmacologica Sinica (2012) 33: 27–33; doi: 10.1038/aps.2011.155; published online 12 Dec 2011

Introduction

Propofol is the most commonly used intravenous anesthetic, and it has gained widespread popularity because of its rapid onset and short duration of recovery. However, a potentially fatal complication after prolonged propofol infusion has been described in an increasing number of reports[1–3]. This complication has been termed propofol infusion syndrome (PRIS)[4] and includes progressive myocardial failure, bradycardia, lactic acidosis, rhabdomyolysis, hyperkalemia, lipemia, acute renal failure, and death. Unfortunately, little data on the mechanisms of PRIS are available.

PRIS resembles mitochondrial cytopathies and acquired carnitine deficiency[5, 6]. Malonyl-carnitine, C5-acylcarnitine, creatine kinase, troponin T (TnT) and myoglobin levels are increased in pediatric PRIS, which is consistent with impaired fatty acid oxidation due to a reduction of the mitochondrial entry of long-chain acylcarnitine esters and the failure of the respiratory chain. High concentrations of propofol impair mitochondrial respiration in rat brain synaptosomes (Marion *et al* citation)[6]. An uncoupling of oxidative phosphorylation due to an increase in the proton permeability of the inner mitochondrial membrane has been observed in isolated rat liver mitochondria[7]. Propofol uncouples oxidative phosphorylation and inhibits the electron transport chain, which decreases mitochondrial energy production, in isolated perfused guinea pig hearts[8]. The mitochondrial damage that is associated with propofol infusion is characterized by an imbalance between energy demand and utilization, which is a key pathogenetic mechanism in PRIS. AMP-activated protein kinase (AMPK) is also a primary regulator of the cellular response to lowered ATP levels in eukaryotes[9, 10]. AMPK is

---

# These authors contributed equally to this work.
* To whom correspondence should be addressed.
E-mail liwang1118@hotmail.com
Received 2011-07-14 Accepted 2011-09-23

a serine/threonine protein kinase in the Snf1/AMPK protein kinase family[11]. AMPK activity requires the phosphorylation of the alpha subunit on Thr^{172} in its activation loop by one or more upstream kinases (AMPKKs)[11]. AMPK phosphorylation downregulates ATP-consuming processes, such as the synthesis of fatty acids, cholesterol, and protein, but it also upregulates ATP-producing catabolic pathways, such as fatty acid oxidation and glucose uptake[11, 12]. However, the role of AMPK in PRIS is not known.

This study examined the effects of a prolonged infusion of large doses of 1% propofol on the cardiac morphology and blood biochemical profiles in rabbits undergoing prolonged mechanical ventilation, and determined the role of AMPK signaling in PRIS. Our results demonstrated that the infusion of a large dose of propofol induced an emergent life-ending syndrome in rabbits that was consistent with PRIS and an increase in the phosphorylation of AMPK at Thr^{172}.

Materials and methods

Materials

Injections of 1% propofol (*w/v*) and 10% intralipid were purchased from AstraZeneca Pharmaceuticals (AstraZeneca, Cheshire, UK). Isoflurane was obtained from Baxter International, Inc (Deerfield, IL, USA). Antibodies against phospho-AMPK at Thr^{172} and α-AMPK were purchased from Cell Signaling Technology, Inc (China), and anti-TNF-α antibody was purchased from Santa Cruz Biotechnology, Inc (Santa Cruz, CA, USA). ECL reagent was purchased from Pierce Thermo Fisher Scientific, Inc (Rockford, IL, USA). Other chemical agents were purchased from Sigma (St Louis, MO, USA).

Animals

Healthy male New Zealand rabbits weighing 2.5–3.0 kg at 3 months of age were used in this study (n=18). The rabbits were exposed to a 12-h light/dark cycle and received food and water *ad libitum*.

The animals were premedicated with a mixture of xylazine (50 μg/kg, im) and atropine (50 μg/kg, im) after an overnight fast and anesthetized with ketamine hydrochloride (0.05 g/kg, im) for endotracheal intubation 20 min later. Artificial ventilation was initiated using a pressure ventilator (ALC-V8S, Alcott Biotech Co, Ltd, Shanghai, China). The initial settings (flow rate, 8 L/min; respiratory rate, 20–25 breath/min; peak inspiratory pressure, 12 cmH_2O; and inspiration triggering, -2 cmH_2O) provided a tidal volume of approximately 6–8 mL/kg, and these settings were adjusted to maintain an arterial P_{aCO2} between 30 and 40 mmHg if required. The initial 40% FIO_2 (fraction of inspired O_2) was adjusted to achieve a P_{aO2} over 90 mmHg or an SpO_2 >95%.

A 5-lead electrocardiogram invasive arterial blood pressure, heart rate, SpO_2, respiratory rate and body temperature were continuously monitored (Hewlett Packard M3046A/Viridia). The levels of electrolytes and glucose were assessed every 4 h (Hitachi 7600, Japan). An $NaHCO_3$ solution was administered iv if metabolic acidosis occurred (20 mL $NaHCO_3$ 5% was administered within 1 h if pH<7.25 and HCO_3^- <15 mEq/L). Electrolytes and glucose levels were corrected if necessary. A dose of 300 IU of heparin sodium per kilogram of bodyweight was used via subcutaneous injection every 12 h for thrombosis prophylaxis. A central ear artery and two marginal ear veins were catheterized (20-gauge polyethylene catheter) to provide intra-arterial and IV access, respectively. The animals were placed in a supine position on a heated operation table and covered with an isothermic blanket to maintain normothermia. The urinary bladder was catheterized using an 8 CH Foley catheter to facilitate urine collection. Animals received either Ringer's lactated saline solution iv for electrolyte and fluid support or dextrose 5% saline during the experiment when glucose levels decreased to <0.8 g/L (normal range 0.75–1.40 g/L). Animals (n=6/group) were randomly assigned to sedation with 1% propofol (Group P), isoflurane (Group I), or isoflurane while receiving 10% intralipid (Group II). The Shanghai Jiaotong University Animal Care and Use Committee approved all experimental procedures and protocols, and all studies were performed in accordance with the National Research Council (US) Institute Guidelines for Laboratory Animal Care.

Measurement of blood biochemical variables

Venous blood samples were collected in test tubes and centrifuged at 3000×*g* for 10 min to obtain serum. The following variables were measured (ILAB 600 Analyser, Lichtenfels, Germany): potassium, sodium, glucose, urea, creatinine, lactate dehydrogenase (LDH), total protein content, albumins, total bilirubin, direct bilirubin, glutamic oxaloacetic transaminase (GOT), glutamic pyruvic transaminase (GPT), cholesterol, triglycerides, and creatine kinase (CK).

Histological examination

Animals were exsanguinated after the termination of experiments, and the hearts were quickly excised and divided into two parts. One half was fixed in 10% neutral-buffered formaldehyde, embedded in paraffin wax, sectioned serially at 4 μm, and stained with hematoxylin-eosin (H&E). Immunohistochemical investigation of heart samples was performed utilizing an anti-TNF-α monoclonal antibody. Cardiac tissues slices were subjected to histological examination under an Olympus BX microscope by two independent researchers in a blinded manner.

The other half of the heart was rapidly frozen on dry ice. Frozen tissue was homogenized in ice-cold lysis buffer containing 10 mmol/L Tris, 100 mmol/L NaCl, 1 mmol/L EDTA, 1 mmol/L EGTA, 1 mmol/L NaF, 20 mmol/L $Na_4P_2O_7$, 2 mmol/L Na_3VO_4, 0.1% SDS, 0.5% sodium deoxycholate, 1% Triton X-100, 10% glycerol, 10 mg/L leupeptin, 60 mg/L aprotinin, and 1 mmol/L phenylmethanesulfonyl fluoride. Cell lysates were centrifuged at 16 000×*g* for 10 min, and the supernatants were collected.

Immunoblotting

Western blotting (WB) analysis was performed on total cell lysates. Protein concentrations were measured using the Bradford protein assay[13]. All samples were mixed with Laemmli sample buffer [sodium dodecyl sulfate (SDS)] and placed in a boiling water bath for 5 min. Proteins (50 μg) were resolved in 10% SDS-polyacrylamide gels, transferred to nitrocellulose, and incubated overnight with primary antibodies against phospho-AMPK at Thr^{172} and α-AMPK (1:2000). Immunoblots were developed using horseradish peroxidase-conjugated goat antimouse or goat antirabbit immunoglobulin G (1:3000). Protein bands were visualized using the ECL reagent (Pierce Thermo Fisher Scientific, Inc, Rockford, IL, USA), and density was quantified using the Scion Image software (Scion Corp, Frederick, MD, USA).

Experimental protocols

Protocol 1 (Group P): effect of prolonged 1% propofol sedation on rabbits under mechanical ventilation

Animals were sedated using a continuous propofol infusion (1% Diprivan, AstraZeneca, Cheshire, UK) for 36 h or until death. Propofol was administered at the first signs of awakening from general anesthesia (restoration of corneal reflex) and at an initial rate (IR) of 10 $mg·kg^{-1}·h^{-1}$ using an infusion pump (Baxter AS40A, 1800 Williamson Ct Louisville, KY, USA). The IR was adjusted in 5 $mg·kg^{-1}·h^{-1}$ steps to maintain the desired level of sedation when necessary. The level of sedation was assessed using a corneal reflex response every 30 min; earlier assessments were performed only when clinical signs of awakening were observed (25% increase in heart rate and/or arterial blood pressure from the previous measurement, any increase in respiratory rate from the ventilator setting). The criteria for the desired level of sedation are listed in Table 1. The IR was reduced if necessary in 5 $mg·kg^{-1}·h^{-1}$ steps every 15 min until the initial signs of awakening were observed to avoid propofol overdose. The IR was returned to the previously identified safe dose to maintain an adequate level of sedation.

Table 1. Criteria for reflex response evaluation indicating light level of sedation in mechanically ventilated rabbits.

Reflex	Response
Palpebral	–
Corneal	+
Swallowing	–

–, loss; +, preservation.

Protocol 2 (Group I): Effect of isoflurane sedation on rabbits undergoing prolonged mechanical ventilation

Animals were sedated using an alternative anesthetic, isoflurane (Baxter International, Inc, Deerfield, IL, USA), for 36 h with a conventional vaporizer at an initial rate of 1% to distinguish the effects of propofol sedation from the effects of prolonged mechanical ventilation. The doses were adjusted if necessary to maintain a light level of sedation (Table 1).

Protocol 3 (Group II): Effect of 10% intralipid on isoflurane-sedated rabbits undergoing prolonged mechanical ventilation

One group of animals was sedated using the inhaled anesthetic, isoflurane, during 10% intralipid administration for 36 h to distinguish the effect of a 1% propofol infusion from lipid vehicle (10% intralipid) in sedated rabbits under mechanical ventilation. The initial isoflurane concentration was 1%, and this concentration was adjusted if necessary to maintain a light level of sedation. Intralipid (10%) was infused continuously at a rate that was equal to the average hourly 1% propofol infusion rate in Group P.

Statistical analysis

Data from the blood biochemical analysis are presented as the mean±SD. These data were subjected to a repeated measures analysis of variance. The differences between the mean values within time points in the same group were tested using the Bonferroni test, and differences between groups for the same time point were compared using the Student's *t*-test. A probability of $P<0.05$ was considered statistically significant. The results shown in the blots are representative of ≥3 independent experiments and represent the mean±SD. Densitometry data were analyzed using a 1-way ANOVA with a significant level of $P<0.05$.

Results

Mortality rate, blood biochemistry, and blood pressure

The mortality rate in Group P was 50%; one animal survived for 30 h and the other animals survived for 34 h. No deaths were observed in Groups I and II. The deterioration of the clinical course in Group P was evident at 10±2.12 h following the onset of propofol infusion and included a significant increase in serum lipid, GOT, GPT, LDH, total protein, total bilirubin, direct bilirubin, and CK levels (Table 2). A rapid drop in arterial pressure without a corresponding increase in heart rate followed these increases (Table 3), which may mean that the heart rate is more sensitivity to the effects of these drugs.

A significant increase ($P<0.05$) in serum CK levels was observed, but total protein content, albumin and creatinine levels exhibited a significant decrease 12 h after the onset of isoflurane administration in Group I (Table 4). CK levels were significantly lower in Group I than in Group P ($P<0.05$). Arterial blood pressure demonstrated a significant decrease in Group I at the termination of the experiment, but these values remained much higher than the levels in Group P.

Total protein content, total bilirubin, direct bilirubin, triglycerides, cholesterol, and CK gradually increased beginning at 12 h of infusion in Group II, and GOT, GPT, and LDH levels increased 24 h after infusion. Serum albumin levels decreased 12 h after the onset of 10% intralipid administration in isoflurane-sedated rabbits (Table 5). Triglycerides, CK levels and total protein content were significantly lower in Group II compared with Group P ($P<0.05$). No deviations in vital signs were noted during the experiments, except for a decrease in systemic arterial pressure. However, systemic arterial pres-

Table 2. Blood biochemical measurements in propofol-sedated rabbits. Mean±SD. *n*=6. $^{b}P<0.05$ when compared with pretreatment (0 h) values.

Variable	Time (h) 0	12	24	30–36	Reference range
Creatinine (μmol/L)	72.0±5.6	61.1±6.2^{b}	77.8±16.7	86.8±22.2	70–120
GOT (U/L)	20.0±4.9	101.8±36.2^{b}	166.8±65.6^{b}	143.0±40.4^{b}	<30
GPT (U/L)	45.3±12.2	70.0±14.5^{b}	180.0±45.0^{b}	190.1±59.7^{b}	<5–47
LDH (U/L)	242.3±34.4	352.7±26.4^{b}	455.5±20.5^{b}	620.5±12.9^{b}	243±50
Total protein (g/L)	56.0±8.0	75.0±14.5	180.0±45.0^{b}	190.1±59.7^{b}	54–75
Albumins (g/L)	36±5.0	30±8.3	25±4.2^{b}	20±5.0^{b}	27–50
Total bilirubin (μmol/L)	11.1±5.5	144.4±8.6^{b}	250.0±8.3^{b}	227.8±12.1^{b}	<26
Direct bilirubin (μmol/L)	5.6±2.1	55.6±11.0^{b}	77.8±11.1^{b}	44.4±11.0^{b}	<7
Cholesterol (mmol/L)	3.98±2.4	11.4±1.2^{b}	19.3±2.8^{b}	18.3±3.1^{b}	<5.2
Triglycerides (mmol/L)	3.7±1.1	305.5±7.9^{b}	451.2±114.1^{b}	386.7±6.9^{b}	<2.0
CK (IU/L)	1059.3±383.0	5842.0±3428.6^{b}	8958.3±3645.1^{b}	11389.7±7462.6^{b}	50–1300

CK, creatine kinase; LDH, lactate dehydrogenase; GOT, glutamic oxaloacetic transaminase; GST, glutamic pyruvic transaminase.

Table 3. Hemodynamic data of mechanically ventilated rabbits sedated with propofol (Group P), isoflurane (Group I) and isoflurane while receiving intralipid (Group II). Mean±SD. *n*=6. $^{b}P<0.05$ when compared with pretreatment (0 h) values; $^{e}P<0.05$ when compared with the same time-point values in Group P.

Variable	Time (h) 0	6	12	18	24	30–36
Group P						
AP syst (mmHg)	90.5±13.5	98.3±15.6	81.6±12.3^{b}	79.5±10.1^{b}	71.4±10.6^{b}	33.2±4.4^{b}
AP diast (mmHg)	60±19.3	61.6±8.5	53.6±5.2	45.6±5.4	44.3±5.6	24.1±3.2^{b}
AP mean (mmHg)	69.5±10.5	73.1±11.3	62.8±7.8	56.3±7.3^{b}	53.4±7.1^{b}	26.8±3.8^{b}
HR	220±13.3	223.5±27.1	229.2±19.1	222±11.6	208.5±13.3	187±9^{b}
Group I						
AP syst (mmHg)	94.2±15.2	94.3±13.4	99.5±16.3	95±12.5	99.2±13.9	87.6±10.5
AP diast (mmHg)	70.8±9.2	65.1±8.2	72.4±8.6	70.1±7.6	73.3±8.1	55.3±4.7^{be}
AP mean (mmHg)	75±9.2	67.8±8.3	79.1±10.4	78.4±8.7	80.1±9.4	65.2±7.1
HR	230.6±20.3	232.8±16.1	227±19.9	228.6±18.9	219.4±18.4	216.2±14.5
Group II						
AP syst (mmHg)	105.1±15.4	100.3±18.9	87.9±10.1^{b}	86.5±8.9^{b}	80.6±7.6^{b}	70.3±7.5^{be}
AP diast (mmHg)	66.3±6.1	67.2±6.7	64.3±5.8	66.1±5.6	60.1±5.4	51.2±4.9^{be}
AP mean (mmHg)	79.1±8.9	77.6±7.1	71.2±6.7	73.1±6.7	66.5±6.2^{be}	57.5±5.6^{be}
HR	224.5±18.8	223.5±14.9	201.0±16.0	208.8±17.8	231.3±11.5	219.8±13.2

0 h=before intubation; AP, arterial blood pressure; HR, heart rate.

sure was significantly better than that in Group P.

Histological findings

The common characteristics of PRIS include cardiovascular collapse, cardiac arrhythmias, and metabolic acidosis[4, 14]. Therefore, the morphological features of heart specimens were investigated to determine whether these features were consistent with the features of PRIS. The histological examination revealed little infiltration of acute inflammatory cells in the myocardial fibers in all 3 groups (data not shown). However, TNF-α signals were intensely positive in all heart samples of Group P, but TNF-α staining intensity was weak in Group II and negligent in Group I (Figure 1).

Alterations in AMPK and phospho-AMPK expression in myocardial cells

This study revealed an increased phosphorylation of AMPK at Thr^{172} in the heart following large doses of propofol infusion; little AMPK phosphorylation was observed in cardiac tissues of the other two groups (Figure 2).

Discussion

This study demonstrated that prolonged propofol sedation at high doses contributes to the incidence of fatal complica-

Table 4. Blood biochemical measurements in isoflurane-sedated rabbits. Mean±SD. *n*=6. $^{b}P<0.05$ when compared with pretreatment (0 h) values. $^{e}P<0.05$ when compared with the same time-point values in Group P.

Variable	Time (h) 0	12	24	30–36	Reference range
Creatinine (μmol/L)	72.2±5.6	61.1±6.2^{b}	50.0±7.8^{be}	38.9±5.6^{be}	70–120
GOT (U/L)	5.5±2.0	25.0±3.3	35.5±3.0	31.5±6.0	<30
GPT (U/L)	41.2±4.8	45.0±3.2	42.2±1.1	46.0±9.1	<5–47
LDH (U/L)	236.5±90.5	241.1±76.6	253.3±152.2	201.1±92.1	243±50
Total protein (g/L)	59.1±6.1	40.1±18.2	31.1±9.0^{be}	41.0±4.1^{e}	54–75
Albumins (g/L)	40.0±2.0	26.1±10.1^{b}	23.1±11.2^{b}	25.2±2.0^{be}	27–50
Total bilirubin (μmol/L)	15.1±2.0	14.4±8.6	25.0±8.3	27.8±12.1	<26
Direct bilirubin (μmol/L)	5.1±0.5	4.2±0.8	5.9±1.1	6.2±1.2	<7
Cholesterol (mmol/L)	2.6±0.6	1.9±0.4	2.3±1.2	3.9±1.1	<5.2
Triglycerides (mmol/L)	2.6±0.5	3.1±0.6	2.8±1.1	1.8±1.0	<2.0
CK (IU/L)	1032.2±226	3468.1±7965^{b}	3548.2±1263^{be}	3108.3±3746^{be}	50–1300

CK, creatine kinase; LDH, lactate dehydrogenase; GOT, glutamic oxaloacetic transaminase; GST, glutamic pyruvic transaminase.

Table 5. Blood biochemical measurements in isoflurane-sedated rabbits receiving intralipid 10%. Mean±SD. *n*=6. $^{b}P<0.05$ *vs* pretreatment (0 h) values. $^{e}P<0.05$ *vs* the same time-point values in Group P.

Variable	Time (h) 0	12	24	30–36	Reference range
Creatinine (μmol/L)	77.7±5.6	55.6±11.2^{be}	44.5±5.6^{be}	46.6±5.2^{be}	70–120
GOT (U/L)	25.2±5.6	35.6±9.5	152.2±35.1^{b}	175.6±61.3^{b}	<30
GPT (U/L)	38.5±12.5	34.6±17.2	195.2±37.6b^{b}	252±62.1^{b}	<5–47
LDH (U/L)	250.5±12.5	215.4±32.6	385.1±89.6^{b}	575.1±124.2^{b}	243±50
Total protein (g/L)	58.1±4.1	75.1±1.2	82.2±3.2^{be}	133±4.1^{be}	54–75
Albumins (g/L)	37.2±2.0	29.2±2.1	22.1±4.2^{b}	24.2±1.0^{b}	27–50
Total bilirubin (μmol/L)	11.1±5.6	94.5±11.2^{be}	248.9±105.2^{b}	351.1±88.9^{be}	<26
Direct bilirubin (μmol/L)	5.6±0.2	55.6±16.7^{b}	100.1±22.3^{b}	102.2±25.6^{be}	<7
Cholesterol (mmol/L)	3.4±0.2	12.5±0.2^{b}	19.2±6.3^{b}	22.5±5.2^{b}	<5.2
Triglycerides (mmol/L)	6.17±2.7	31.6±1.2^{be}	33.4±1.6^{be}	35.2±2.2^{be}	<2.0
CK (IU/L)	1006.1±1226	3168.1±10965^{b}	3328.2±1562^{be}	3468.3±284.6^{be}	50–1300

CK, creatine kinase; LDH, lactate dehydrogenase; GOT, glutamic oxaloacetic transaminase; GST, glutamic pyruvic transaminase.

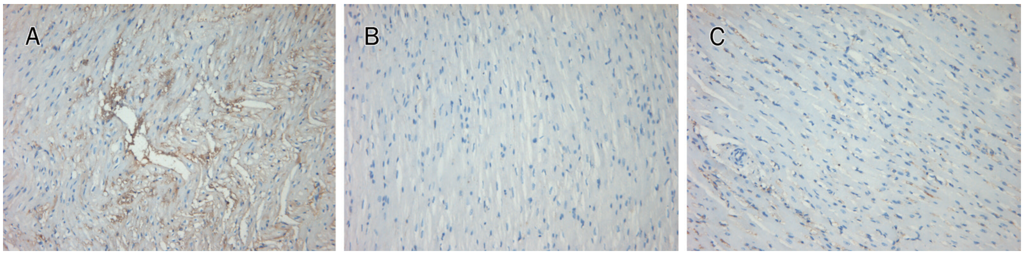

Figure 1. Immunohistochemical detection of tumor necrosis factor (TNF)-α in the heart. New Zealand rabbits under mechanically ventilation were subjected to sedation with 1% propofol (A), isoflurane (B) and isoflurane while receiving Intralipid 10% (C), respectively, for 30–36 h. Immunohistochemical detection of TNF-α with positive reaction in the propofol sedated heart (Brown reaction) (*n*=6). Original magnification ×100. Scale bar, 100 μm.

tions that resemble PRIS. This study also demonstrated that propofol produced an overexpression of TNF-α and AMPK activation, which has not been reported previously. The main features of PRIS include cardiovascular collapse, cardiac arrhythmias, and metabolic acidosis[4, 14]. Rhabdomyolysis, hyperlipemia, and hypertriglyceridemia are other commonly

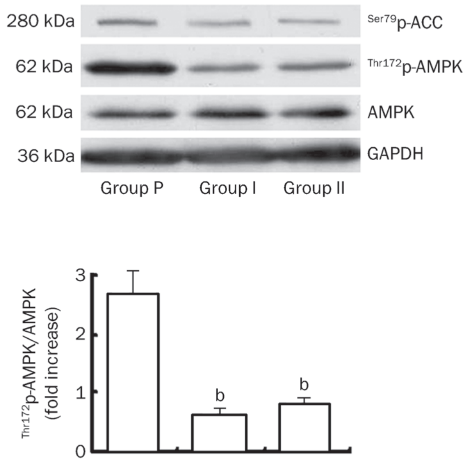

Figure 2. Immunoblot analysis of AMPK phosphorylation in the heart. New Zealand rabbits under mechanically ventilation were subjected to sedation with 1% propofol, isoflurane and isoflurane while receiving Intralipid 10%, respectively, for 30–36 h. AMPK phosphorylation at Thr 172 in myocardial tissues was observed by immunoblot analysis with phosphospecific antibody. The data shown are mean±SD. *n*=6. $^bP<0.05$ *vs* propofol sedation.

described features, but these features are not consistently observed in all case reports and animal studies[15, 16]. Cardiac failure, which is characterized by progressive bradycardia that leads to asystole, is the major cause of death in patients with PRIS[17]. Cardiac function in propofol-sedated animals in this study did not reveal any conduction defects or bradycardia during most of the experiment, except for a slight decrease in heart rate during the last 3–4 h of the experiment (220±13 and 187±9 beat/min, at 0 and 30–36 h, respectively). Histological examination did not demonstrate myofibril degeneration or rhabdomyolysis. Therefore, the negative signs of cardiac injury explicate the absence of terminal bradycardia, which is characteristic of PRIS in patients[3, 17]. The immunohistochemical results demonstrated a strong positive reaction for TNF-α in propofol-infused cardiac myocytes, which indicated a rise in cardioinhibitory cytokines. The increase in TNF-α may be an adaptive response of a jeopardized myocardium[18]. Low- and high-dose propofol (1 and 10 mg·kg^{-1}·h^{-1}, respectively) exert beneficial effects on septic shock in rats and reduce serum TNF-α and IL-10 production after sepsis[19]. The difference between the results obtained here and these previous reports may be due to the administration of a long-term high-dose propofol infusion in this study; the use of high doses of propofol for prolonged periods is generally linked to a decrease in performance[3, 15, 17]. Cardiac arrhythmias, multiorgan damage, metabolic acidosis, rhabdomyolysis, hyperlipemia, and hypertriglyceridemia have been observed in critically ill patients receiving propofol for sedation[1–5]. However, the present study examined the effects of large doses of continuously infused propofol on lipid metabolism imbalance. Therefore, the primary outcome measurements in this study were blood biochemical deteriorations. The increases in LDH, GOT, GPT, cholesterol, triglycerides and creatine kinase (CK) were greater in Group P compared to the intralipid group. More importantly, the increased concentrations of these parameters presented 12 h after propofol administration (Table 2). Therefore, clinicians in the ICU should be extremely suspicious of PRIS development when hyperlipidemia and abnormal indices of liver function are observed. Propofol should be discontinued immediately in these cases. The marked increase in triglyceride concentrations may be directly caused by an impaired β-oxidation of FFAs, which is induced by propofol, or by an altered mobilization of FFAs from triglycerides. An increase in sympathetic nervous system outflow and elevated cortisol and growth hormone concentrations, which are commonly observed in critically ill patients, may promote lipolysis and lipid oxidation, which further increase FFA concentrations[1]. Liver dysfunction due to circulatory failure or direct hepatotoxic effects of propofol may also adversely affect lipid kinetics. Lipemia alone impairs mitochondrial oxygen uptake, which contributes to the accelerated development and refractory nature of the PRIS. AMPK is activated during metabolic stress. AMPK activates a number of energy-producing metabolic pathways, but it also inhibits energy-consuming pathways[11]. AMPK has been termed a ‘fuel gauge’ for cellular energy levels because of this dual effect[9–12]. The role of AMPK as a fuel gauge is particularly relevant in the heart, which has a remarkably high demand for energy. In addition to its ‘fuel gauge’ role, AMPK influences apoptotic processes in eukaryotic cells, and the prolonged stimulation of AMPK induces apoptosis through c-Jun-N-terminal kinase activation[20]. The present study demonstrated that the continuous infusion of high-dose propofol induced AMPK activation. Whether the activation of AMPK is beneficial or harmful during PRIS is not known. Further studies to explore this potential are required.

Intralipid infusion in isoflurane-sedated rabbits under prolonged mechanical ventilation was performed to investigate the possible side effects of the lipid vehicle. No serious deviations in vital signs were observed, and all animals survived the 36-h study period. Histological examination revealed no inflammation of the heart, and immunohistochemistry revealed little TNF-α staining. These results demonstrated that the lipid solvent caused few catastrophic manifestations of PRIS, which is consistent with previous studies[16, 21].

Additionally, rabbits were mechanically ventilated under isoflurane sedation for the maximum survival period of the propofol-sedated rabbits. Therefore, prolonged mechanical ventilation did not contribute to the detrimental effects. Positive results have been observed when prolonged isoflurane sedation was used with an anesthetic-conserving device in critically ill patients[13].

The present study included the following limitations. A more objective and sensitive method for the evaluation of sedation depth, such as the Bispectral Index or the electroencephalogram, would offer more precise adjustments of the sedative infusion rate or concentration. Additionally, the replication of human anesthetic dosing in rabbits was difficult. The initial propofol infusion rate was 10 mg·kg^{-1}·h^{-1}, and this dose was increased up to 65 mg·kg^{-1}·h^{-1}, which is disproportionally higher than PRIS in humans (>4 mg·kg^{-1}·h^{-1})[4, 22]. However, this result may explain the early onset of PRIS development in this species.

In summary, the continuous infusion of 1% propofol at large doses for sedation in rabbits undergoing prolonged mechanical ventilation induced detrimental changes in blood biochemistry, including hyperlipemia, liver dysfunction and a profound increase in CK levels, which indicated extended myocytolysis. These biochemical changes resembled PRIS. TNF-α expression increased in cardiac tissue specimens, which indicated myocardial injury. This observation that prolonged large doses of propofol infusion induce AMPK activation is novel. These results may provide a potential strategy for the elucidation of the mechanism of the imbalance between energy demand and utilization, which is a key pathogenetic mechanism in PRIS. The role of the lipid vehicle in the development of PRIS was minor, and this result was confined to late hyperlipidemia and liver dysfunction. Finally, isoflurane was a viable alternative sedation choice for prolonged mechanical ventilation in this rabbit model.

Acknowledgements

This study was supported by a grant from Shanghai Sixth Hospital.

Author contribution

Li WANG designed research and wrote the paper; Wei JIANG performed research; Zheng-bo YANG contributed equally to this work with Wei JIANG; Quan-hong ZHOU analyzed data; Xiang HUAN assisted to perform research.

References

1 Parke TJ, Stevens JE, Rice AS, Greenaway CL, Bray RJ, Smith PJ, *et al*. Metabolic acidosis and fatal myocardial failure after propofol infusion in children: five case reports. BMJ 1992; 305: 613–6.

2 Machata AM, Gonano C, Birsan T, Zimpfer M, Spiss CK. Rare but dangerous adverse effects of propofol and thiopental in intensive care. J Trauma 2005; 58: 643–5.

3 Riezzo I, Centini F, Neri M, Rossi G, Spanoudaki E, Turillazzi E, *et al*. Brugada-like EKG pattern and myocardial effects in a chronic propofol abuser. Clin Toxicol 2009; 47: 358–63.

4 Otterspoor LC, Kalkman CJ, Cremer OL. Update on the propofol infusion syndrome in ICU management of patient with head injury. Curr Opin Anaesthesiol 2008; 21: 544–51.

5 Wolf A, Weir P, Segar P, Stone J, Shield J. Impaired fatty acid oxidation in propofol infusion syndrome. Lancet 2001; 357: 606–7.

6 Marian M, Parrino C, Leo AM, Vincenti E, Bindoli A, Scutari G. Effect of the intravenous anesthetic 2,6-diisopropylphenol on respiration and energy production by rat brain synaptosomes. Neurochem Res 1997; 22: 287–92.

7 Branca D, Roberti MS, Vincenti E, Scutari G. Uncoupling effect of the general anesthetic 2,6-diisopropylphenol in isolated rat liver mitochondria. Arch Biochem Biophys 1991; 290: 517–21.

8 Schenkman KA, Yan S. Propofol impairment of mitochondrial respiration in isolated perfused guinea pig hearts determined by reflectance spectroscopy. Crit Care Med 2000; 28: 172–7.

9 Dyck JR, Lopaschuk GD. AMPK alterations in cardiac physiology and pathology: enemy or ally? J Physiol 2006; 574: 95–112.

10 Tsou P, Zheng B, Hsu CH, Sasaki AT, Cantley LC. A fluorescent reporter of AMPK activity and cellular energy stress. Cell Metab 2011; 13: 476–86.

11 Shirwany NA, Zou MH. AMPK in cardiovascular health and disease. Acta Pharmacol Sin 2010; 31: 1075–84.

12 Oakhill JS, Steel R, Chen ZP, Scott JW, Ling N, Tam S. AMPK is s direct adenylate charge-regulated protein kinase. Science 2011; 332: 1433–5.

13 Bradform MM. A rapid and sensitive method for the quantitation of microgram quantities of proteins utilizing the principle of protein dye binding. Analytical Biochem 1976; 72: 248–54.

14 Diedrich DA, Brown DR. Propofol Infusion syndrome in the ICU. J Intens Care Med 2011; 26: 59–72.

15 Fudickar A, Bein B. Propofol infusion syndrome: update of clinical manifestation and pathophysiology. Minerva Anestesiol 2009; 75: 339–44.

16 Ypsilantis P, Politou M, Mikroulis D, Pitiakoudis M, Lambropoulou M, Tsigalou C, *et al*. Organ toxicity and mortality in propofol-sedated rabbits under prolonged mechanical ventilation. Anesth Analg 2007; 105: 155–66.

17 Bray RJ. Propofol infusion syndrome in children. Paediatr Anaesth 1998; 8: 491–9.

18 Neri M, Bello S, Bonsignore A, Centini F, Fiore C, Földes-Papp Z, *et al*. Myocardial expression of TNF-alpha, IL-1beta, IL-6, IL-8, IL-10, and MCP-1 after a single MDMA dose administered in a rat model. Curr Pharm Biotechnol 2010; 11: 413–20.

19 Taniguchi T, Kanakura H, Yamamoto K. Effects of post-treatment with propofol on mortality and cytokine responses to endotoxin-induced shock in rats. Crit Care Med 2002; 30: 904–7.

20 Shaw RJ, Kosmatka M, Bardeesy N, Hurley RL, Witters LA, DePinho RA, *et al*. The tumor suppressor LKB 1 kinase directly activates AMP-activated kinase and regulates apoptosis in response to energy stress. Proc Natl Acad Sci U S A 2004; 101: 3329–35.

21 Ypsilantis P, Mikroulis D, Politou M, Tsoukali H, Pitiakoudis M, Didilis V, *et al*. Tolerance to propofol's sedative effect in mechanically ventilated rabbits. Anesth Anal 2006; 103: 359–65.

22 Fodale V, La Monaca E. Propofol infusion syndrome: an overview of a perplexing disease. Drug Saf 2008; 31: 293–303.

npg

Acta Pharmacologica Sinica (2012) 33: 34–40

www.nature.com/aps

Original Article

Huperzine A derivative M3 protects PC12 cells against sodium nitroprusside-induced apoptosis

Na NING, Jin-feng HU, Yu-he YUAN, Xin-yuan ZHANG, Jun-gui DAI, Nai-hong CHEN*

State Key Laboratory of Bioactive Substances and Functions of Natural Medicines, Institute of Materia Medica, Chinese Academy of Medical Sciences and Peking Union Medical College, Beijing 100050, China

Aim: To investigate the effects of M3, a derivative of huperzine A, on the apoptosis induced by sodium nitroprusside (SNP) in PC12 cells.
Methods: Cell viability was detected using MTT method. Apoptosis was examined with annexin V/prodium iodide (PI) stain. The levels of reactive oxygen species (ROS) were measured using fluorophotometric quantitation. The amount of malonaldehyde (MDA) was determined with MDA detection kits. The expression of caspase-3 and Hsp70 were analyzed using Western blotting.
Results: Exposure of PC12 cells to SNP (200 μmol/L) for 24 h decreased the cell viability to 69.0% of that in the control group. Pretreatment with M3 (10 μmol/L) or huperzine A (10 μmol/L) significantly protected the cells against SNP-induced injury and apoptosis; the ratio of apoptotic bodies in PC12 cells was decreased from 27.3% to 15.0%. Pretreatment with M3 (10 μmol/L) significantly decreased ROS and MDA levels, and increased the expression of Hsp70 in the cells. Quercetin (10 μmol/L) blocked the protective effect of M3, while did not influence on that of huperzine A.
Conclusion: M3 protects PC12 cells against SNP-induced apoptosis, possible due to ROS scavenging and Hsp70 induction.

Keywords: huperzine A; M3; PC12 cell; sodium nitroprusside; apoptosis; ROS; Hsp70; quercetin

Acta Pharmacologica Sinica (2012) 33: 34–40; doi: 10.1038/aps.2011.147; published online 28 Nov 2011

Introduction

Alzheimer's disease (AD) and Parkinson's disease (PD) are multifaceted, progressive neurodegenerative disorders that occur mainly in older age groups; however, the incidence of these diseases has increased in younger populations in recent years. Although these two disorders are characterized by different clinical manifestations and pathological phenomena, they are both categorized by a selective loss of neurons. Free radical-induced oxidative stress, mitochondrial dysfunction, and excitotoxic processes have been suggested to play a key role in the loss of neurons[1, 2].

Hsp70, a member of the heat shock protein family, functions as an ATP-dependent molecular chaperone in protein folding, multi-protein complex assembly, transmembrane transport, and protein degradation[3]. This protein is also part of an inducible system that aids in cell survival by preventing and/or repairing stress-induced protein damage during and after detrimental environmental stresses, such as free-radical accumulation[4]. Pytlowany *et al* used PC12 cells to compare the protective effects of huperzine A (HupA) derivative M3 and HupA on sodium nitroprusside (SNP)-induced apoptosis[5]. PC12 cells are derived from a rat pheochromocytoma cell line and can acquire neuron-like properties, such as neurite extension, when exposed to nerve growth factor (NGF). These cells are often used to study PD because NGF-treated and untreated cells synthesize, store, secrete, and take up dopamine by processes that are similar to those of dopaminergic neurons[6]. PC12 cells are also used to study AD because they express β-amyloid (Aβ) precursor protein (APP), in keeping with the mRNA and protein levels found in cortical neurons[7].

HupA, which is isolated from the herb *Huperzia serrata*, has been shown to be a highly effective, selective, and reversible acetylcholinesterase (AChE) inhibitor. The use of HupA as a therapeutic treatment for early or mild stages of AD may be due to additional mechanisms other than the reversible inhibition of AChE in the central nervous system. For example, HupA may target oxidative stress, Aβ-associated neurotoxicity, APP processing, and NGF[8]. The capacity of AChE to hydrolyze acetylcholine is not involved in the aforementioned mechanisms[9]. Therefore, we sought to identify derivatives of HupA that retain a similar level of AChE inhibition but yield an increase in cell protection. Due to the rigid molecular

---

* To whom correspondence should be addressed.
E-mail chennh@imm.ac.cn
Received 2011-05-04 Accepted 2011-10-08

configuration of HupA, traditional chemical methods cannot be used to modify its structure. Instead, we chose to use microbial transformation to produce HupA derivatives. M3 is a product of the transformation of HupA by *Streptomyces griseus* CACC 200300 after a two-step procedure and various chromatographic techniques. The structure (Figure 1) was identified as huperzine A 8α,15α-epoxide using physical and chemical data collected through multiple analyses, such as HRMS, 1D NMR, 2D NMR, and IR. Although the IC_{50} value of M3 on AChE inhibition was established to be higher than that of HupA[10], the remarkable effect of protecting PC12 cells from oxidative stress was observed in our present screening.

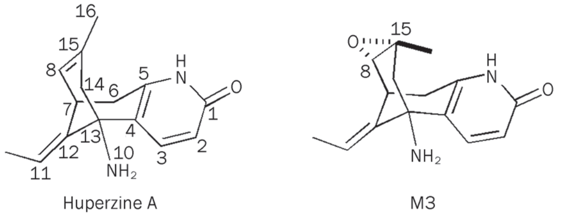

Figure 1. The structures of HupA and M3 by *Streptomyces griseus* CACC 200300.

Materials and methods

Materials and reagents

M3 was prepared as previously described[10]. HupA and SNP were bought from the National Institute of the Control of Pharmaceutical and Biological Products. Quercetin and Hoechst 33342 were purchased from Sigma. These compounds were dissolved in DMSO and diluted by PC12 medium. An annexin V/propidium iodide (PI) staining kit was bought from Beijing Biosea Biotechnology Company. Dichlorofluorescein diacetate (DCFH-DA) and MDA kits were bought from Beyotime Institute of Biotechnology. The anti-Hsp70 antibody and anti-mouse secondary antibody were bought from Santa Cruz Biotechnology. The anti-caspase-3 (17 kDa) antibody was bought from Cell Signaling Technology. The anti-β-actin antibody was bought from Sigma.

Cell culture and treatment

PC12 cells, purchased from the American Tissue Type Collection, were grown in 75-cm^2 tissue culture flasks in DMEM supplemented with 5% heat-inactivated fetal bovine serum (FBS), 10% equine serum (ES), penicillin (100 IU/mL), streptomycin (100 mg/L), and *L*-glutamine (2 mmol/L). Cultures were maintained at 37 °C in 95% air-5% CO_2 in a humidified incubator and passaged every 3 to 4 d. PC12 cells in logarithmic phase were seeded into 96-well or 6-well plates coated with 0.1 mg/mL poly-*L*-lysine (Sigma) and allowed to grow for at least 24 h. Different concentrations of M3 and HupA (0.1, 1, and 10 μmol/L) were added to the culture media for 1 h followed by addition of SNP (200 μmol/L) for 24 h. In some experiments, PC12 cells were pretreated with 10 μmol/L quercetin and 10 μmol/L M3 for 1 h and were exposed to 200 μmol/L SNP for the next 24 h.

MTT assay

PC12 cells were cultured at a density of 6000 cells per well in 96-well plates. MTT (5 mg/mL) was added to each well after the aforementioned treatments and the plates were incubated for 4 h. After centrifugation, the supernatant was removed from each well, and DMSO (100 μL) was added. After 30 min, the absorbance was recorded with a microplate reader (Bio-Rad model 550) at a wavelength of 570 nm. Each experiment was performed in triplicate.

Detection of apoptosis

PC12 cells were cultured at a density of 30000 cells per well in 6-well plates. Cells were harvested by being digested in 0.25% trypsin after treatment, stained with annexin V for 20 min, and PI for another 10 min at 37 °C before detection using flow cytometry (EPICS XL, Beckman Coulter, USA). To stain the DNA, cells were incubated with Hoechst 33342 (10 μg/mL) diluted in phosphate-buffered saline (PBS) for 10 min at room temperature. Cells were then observed by the IN Cell Analyzer 1000 (GE Healthcare, USA).

Measurement of reactive oxygen species (ROS)

Intracellular accumulation of ROS was measured using fluorophotometric quantitation. The cells were cultured with M3 or HupA (10 μmol/L) for 1 h before exposure to SNP (200 μmol/L) for 24 h. The harvested cells were subsequently stained with DCFH-DA for 30 min at 37 °C. The cell suspension was dispensed into 96-well black plates. DCFH-DA reacts with ROS and is converted to dichlorofluorescein (DCF). The fluorescence from the DCF was analyzed using a Spectra microplate fluorescence reader (Max Gemini XS, MD, USA) with the excitation wavelength set at 488 nm and the emission wavelength set at 525 nm.

Estimation of lipid peroxidation

MDA reacts with thiobarbituric acid (TBA) to produce a fluorescent product. Levels of MDA were measured in PC12 cell lysates with a microplate reader at a wavelength of 535 nm. PC12 cells were treated with M3 1 h prior to exposure to SNP and left to grow to more than 90% confluence in 75-cm^2 plates. Cells were harvested and washed with PBS after 24 h. The method described in the MDA detection kit was employed from Nanjing Jiancheng Bioengineering Institute, Nanjing, China.

Protein assay

After a 1-h treatment with M3 and 24 h exposure to SNP, cells were rapidly washed with PBS and lysed on ice in a lysis buffer (pH=8.0) containing 50 mmol/L Tris-HCl, 150 mmol/L NaCl, 1% NP-40, 1 mmol/L PMSF, 1 mmol/L EDTA, 50 mmol/L NaF, 1 mmol/L DTT, 1 mg/L aprotinin and 1% Triton X-100. Protein concentrations were measured with a BCA kit (Vigorous). The lysates were solubilized in an SDS sample buffer, separated with 15% SDS-PAGE, and transferred to PVDF membrane (Millipore). The membrane was blocked with 3% BSA and subsequently incubated with anti-Hsp70, anti-caspase-3 (17 kDa), or anti-β-actin antibodies followed by a horseradish peroxidase (HRP)-conjugated secondary antibody and detected with an ECL detection system (Molecular Device, Lmax). The density of each band was quantitated using image-analysis software (Science Lab 2005 Image Gauge; Fuji Film Co Ltd, Tokyo, Japan).

Statistical analysis

Data are expressed as the mean±standard deviation. An analysis of variance (ANOVA) followed by a Newman-Keuls *post-hoc* test was performed to assess the differences between groups. Values of $P<0.05$ were regarded as statistically significant.

Results

The neurotoxicity of SNP on PC12 cells

Before studying the protective effects of M3, we analyzed the toxicity of SNP on PC12 cells. PC12 cells treated with different concentrations of SNP for 24 h displayed a decrease in the production of formazan dye in a dose-dependent manner. Exposure to 200 μmol/L of SNP induced moderate injury to the cells when compared with the control group. This concentration of SNP was used to compare the neuroprotective effects of M3 and HupA (Figure 2).

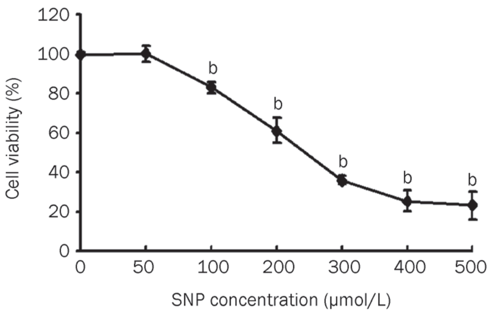

Figure 2. Effect of SNP on the cell viability in PC12 cells. Cells were exposed to SNP for 24 h. The cell viability was evaluated by measuring the quantity of formazan generated by activated mitochondria. The values were expressed as percentage of control, which is set to 100%. The percentage of cell viability was presented as mean±SD for six replicates. $^{b}P<0.05$ *vs* control group.

Pre-incubation with M3 and HupA protected PC12 cells from SNP-induced injury

Exposure to 200 μmol/L of SNP for 24 h decreased the viability of PC12 cells to 69.0%±4.8% compared with the control group. Pre-incubation with M3 or HupA for 1 h attenuated the injury induced by SNP in a dose-dependent manner. This effect was statistically significant at a concentration of 10 μmol/L ($P<0.05$). The cell viability after pre-incubation with M3 was 84.1%±2.7% of the control, while the cell viability after pre-incubation with HupA was 77.1%±3.5% of the control ($P<0.05$, Figure 3). There was no significant difference in cell viability between the M3 and HupA pre-treated groups ($P>0.05$).

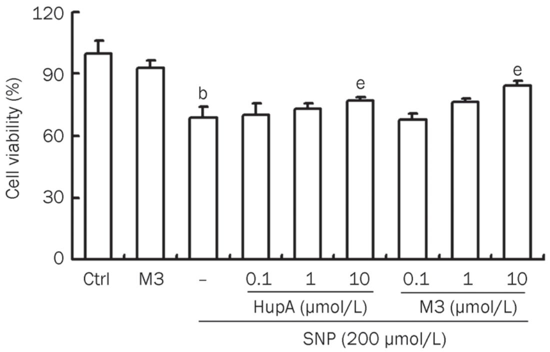

Figure 3. Effect of HupA and M3 on the cell viability in PC12 cells induced by SNP. PC12 cells were pre-treated with HupA and M3 at different concertrations for 1 h before 200 μmol/L SNP was added. The percentage of cell viability was presented as mean±SD for six replicates. $^{b}P<0.05$ *vs* control group. $^{e}P<0.05$ *vs* SNP group.

M3 and HupA attenuated the SNP-induced apoptosis of PC12 cells

Analysis of an annexin V/PI stain using flow cytometry and Hoechst 33342 stain with a fluorescence microscope revealed that pretreatment with HupA or M3 significantly decreased the apoptosis of PC12 cells induced by SNP. M3 pretreatment alone showed no effect on apoptotic bodies or the nuclear morphology of PC12 cells. Pre-treatment with HupA and M3 (10 μmol/L) attenuated nuclear fragmentation and chromatin condensation, and inhibited apoptosis at the early and intermediate stages of SNP exposure. There was no statistically significant difference in the percentage of apoptotic bodies between the M3 and HupA groups (Figure 4).

M3 inhibited the production of SNP-induced ROS in PC12 cells

DCFH-DA is hydrolyzed to DCFH by intracellular esterases, which is subsequently oxidized by ROS to DCF, which is a fluorescent compound. The fluorescence intensity is directly proportional to the amount of ROS generated from SNP exposure. Using an excitation wavelength of 488 nm and an emission wavelength of 525 nm, the mean fluorescence intensity increased to 183.5%±18.3% in the SNP-treated group compared with the control group. Pre-incubation with 10 μmol/L of M3 or 10 μmol/L of HupA resulted in a decrease in the mean fluorescence intensity to 142.3%±20.2% or 132.0%±6.5%, respectively, compared with the SNP-treated group (Figure 5). There was no statistically significant difference in the levels of ROS between the M3 and HupA groups ($P>0.05$).

Treatment with M3 decreased SNP-induced MDA accumulation in PC12 cells

MDA, formed by degradation of polyunsaturated lipids by

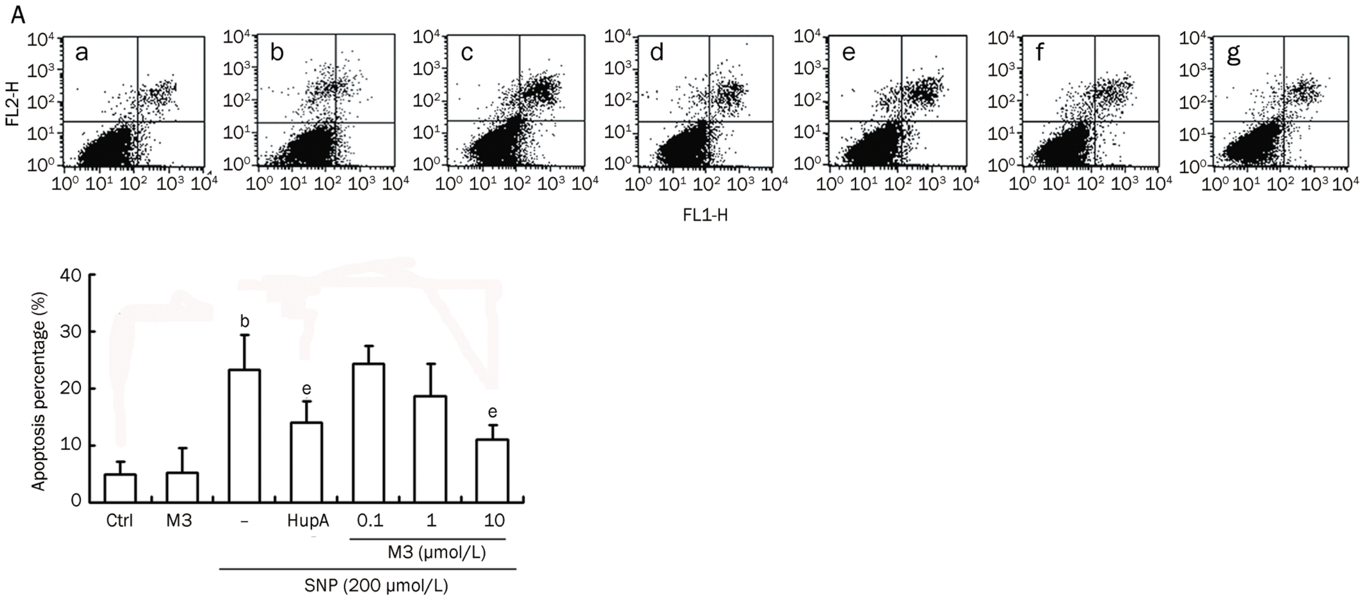

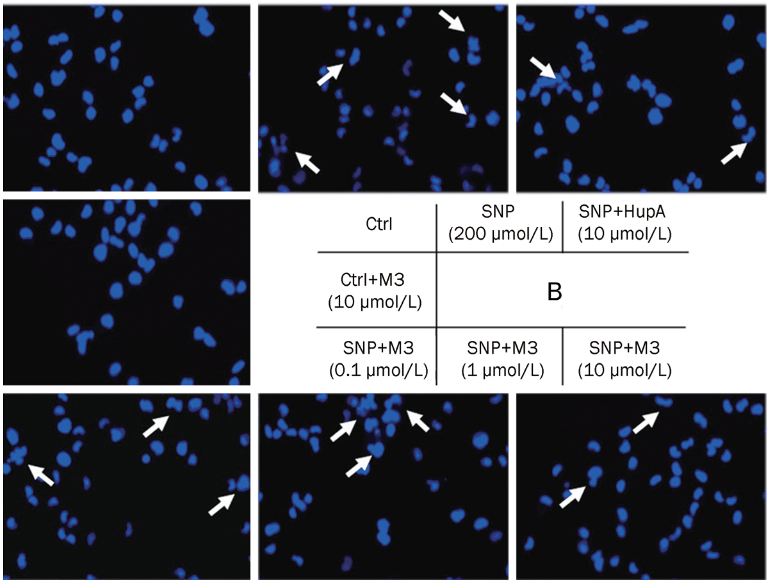

Figure 4. M3 protected PC12 cells from apoptosis induced by SNP. PC12 cells were pre-treated with different doses of M3 for 1 h before 200 μmol/L SNP was added. (A) Cells were stained by annexin V and PI, and detected by flow cytometry. (a) control group; (b) 10 μmol/L M3 group; (c) 200 μmol/L SNP group; (d) 200 μmol/L SNP+10 μmol/L HupA group; (e) 200 μmol/L SNP+0.1 μmol/L M3 group; (f) 200 μmol/L SNP+1 μmol/L M3 group; (g) 200 μmol/L SNP+10 μmol/L M3 group. The percentage of apoptotic body was presented as mean±SD for three individual experiments. $^{b}P<0.05$ *vs* control group. $^{e}P<0.05$ *vs* SNP group. (B) Cells were stained by Hoechst 33342. The arrow indicates nuclear fragmentation or chromatin condensation.

ROS, is used as a marker to measure the level of oxidative stress in an organism. In our previous study, SNP increased MDA levels to 382.4%±57.2% compared with the control group. However, pre-incubation with 10 μmol/L of M3 or 10 μmol/L of HupA for 1 h caused a decrease in the levels of MDA to 288.7%±21.6% in the HupA pretreated group and 246.9%±44.2% in the M3 pretreated group (Figure 5). There was no statistically significant difference between the level of MDA in the M3 and HupA groups ($P>0.05$).

Treatment with M3 increased the expression of Hsp70 in PC12 cells

It was reported that an increase in the expression of Hsp70 confers an improvement in the survival ability of cells against SNP toxicity. The effect of M3 on the expression of Hsp70 in PC12 cells was analyzed in this study. The expression of Hsp70 increased in a time-dependent manner after M3 exposure, peaking after 0.5 h. No change was observed in Hsp70 expression after pre-incubation with HupA. After 1 h of exposure to SNP, the expression of Hsp70 increased. Pretreatment with M3 increased the Hsp70 level compared with cells exposed to SNP (Figure 6).

Quercetin blocked the protective effect of M3 treatment on SNP-induced apoptosis in PC12 cells

Quercetin, a HSP biosynthesis inhibitor, was used to confirm if Hsp70 was involved in the protective effect of M3. As shown in Figure 7A, quercetin attenuated the protection conferred from M3 pretreatment on SNP-induced apoptosis while showing almost no effect on HupA-treated cells. As displayed in

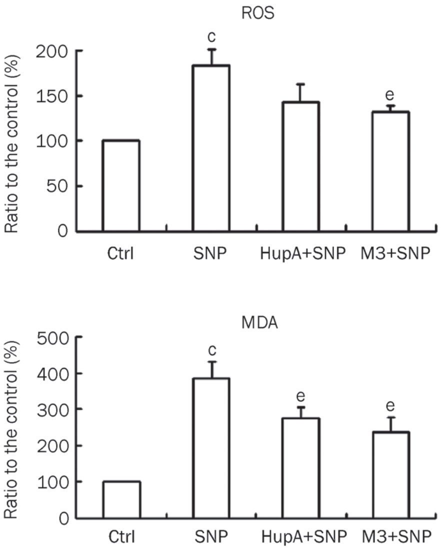

Figure 5. Effect of 10 μmol/L M3 on accumulation of ROS and MDA in PC12 cells induced by SNP. PC12 cells were pre-treated with 10 μmol/L M3 for 1 h before 200 μmol/L SNP was added. Cells were stained by DCFH-DA and detected by fluorometric analysis, or followed by the MDA detection kit. The percentage of ROS and MDA were presented as mean±standard deviation for at least three individual experiments. ^{c}P<0.01 *vs* control group. ^{e}P<0.05 *vs* SNP group.

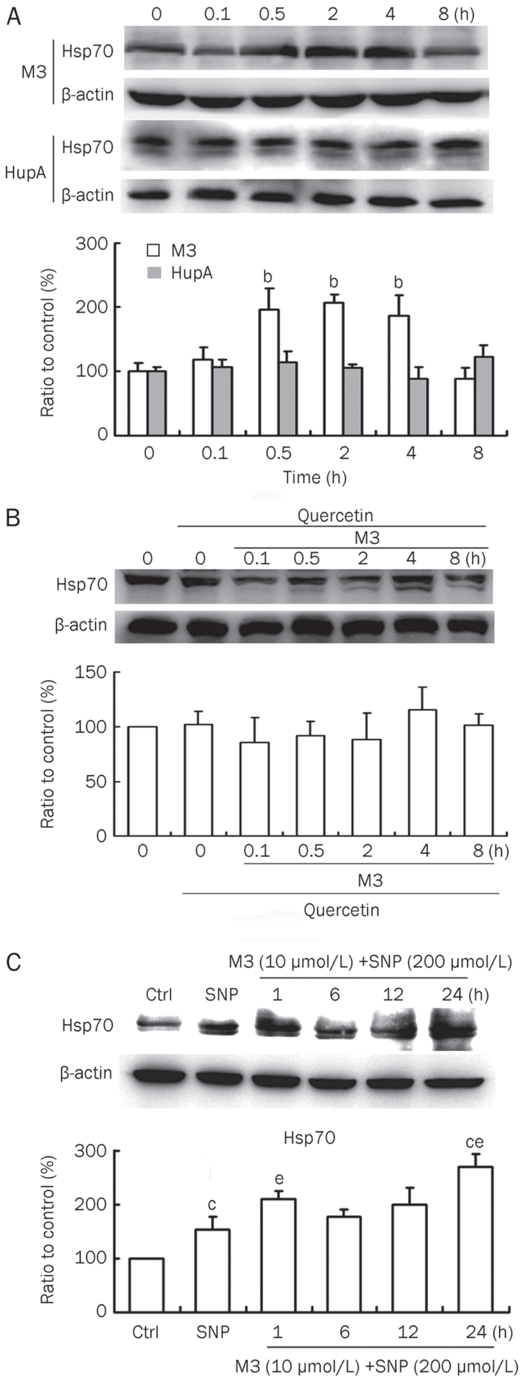

Figure 6. Effect of M3 on the expression of Hsp70 at different time. (A) Analysis of Hsp70 protein expression in PC12 cells by Western blotting at different time after exposure to M3 or HupA and the quantification of protein levels compare to the 0 h treating group by density scanning. ^{b}P<0.05 *vs* 0 h treating group. (B) Analysis of Hsp70 protein expression in PC12 cells by Western blotting after quercetin alone or with M3 co-application at different time and the quantification of protein levels compare to the 0 h treating group by density scanning. (C) Analysis of Hsp70 protein expression in PC12 cells with pretreatment of M3 at different time after exposure to SNP and the quantification of protein levels compare to the control group by density scanning. The percentage of density was presented as mean±standard deviation for at least three individual experiments. ^{c}P<0.01 *vs* control group. ^{e}P<0.05 *vs* SNP group.

Figure 7B, treatment with HupA failed to significantly change the expression of Hsp70 compared with the expression of the SNP-exposed group. In M3 pretreated cells, the expression of Hsp70 increased to 212.5%±26.7% compared with control group. Caspase-3 expression remarkably increased in PC12 cells after exposure to SNP for 24 h, and pre-incubation with HupA and M3 for 1 h reversed this effect. Quercetin had no effect on the activation of caspase-3 in the control or HupA pretreated group, but it significantly increased the expression of caspase-3 in the M3 pretreated group (*P*<0.05).

Discussion

Oxidative stress is recognized as an important mechanism in several neurodegenerative diseases. It has been proven that the activity of inducible nitric oxide synthases (iNOS) was increased in the brains of AD patients[11]. Free-radical production and nitration of endogenous biomolecules are the two main reasons that accumulation of nitric oxide (NO) induces cell loss[12]. In this study, SNP was used to induce the apoptosis of PC12 cells in order to evaluate potential neuroprotective compounds. Exposure to SNP *in vitro* could partially mimic the oxidative stress observed in the brains of neurodegenerative patients[5]. We found that, similar to the effect of HupA, pretreatment with M3 attenuated the apoptosis induced by SNP in PC12 cells. Although M3 and HupA showed a similar level of ROS scavenging, it seems that this was not the only mechanism involved in the protective effects of M3. Indeed, treatment with M3 induced the expression of Hsp70 in a time-dependent manner, unlike HupA. Hsp70, a member of the

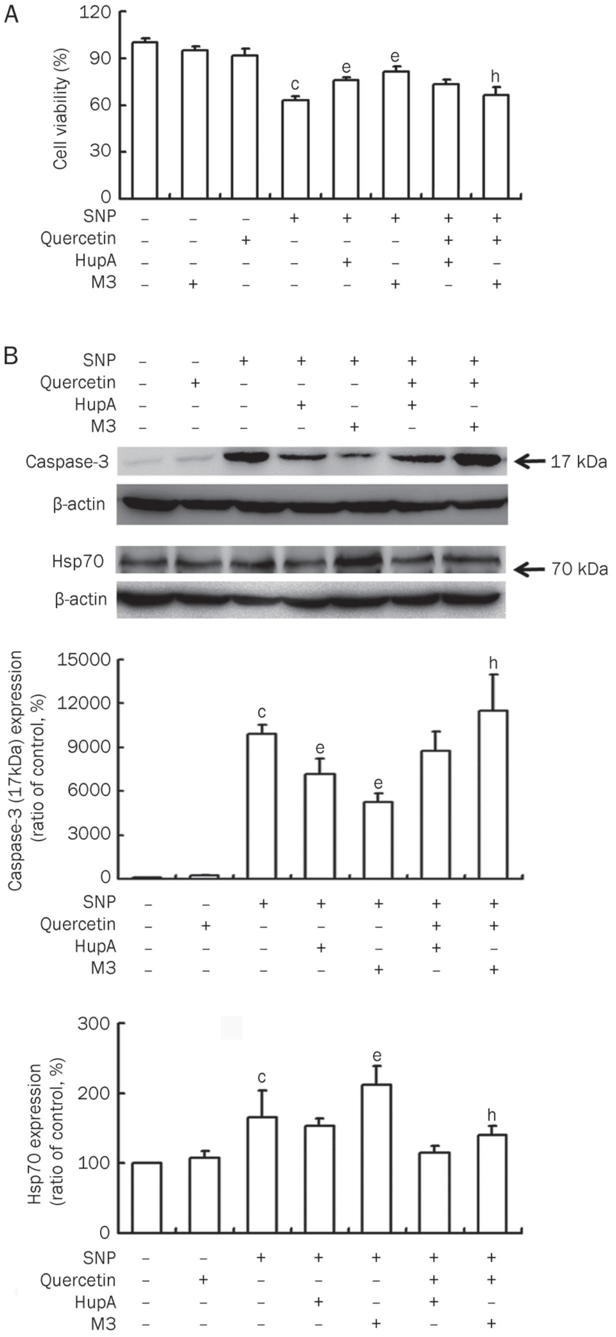

Figure 7. Quercetin inhibited the protective effect of M3 against SNP-induced apoptosis in PC12 cells. PC12 cells were pre-treated with 10 μmol/L HupA, M3, or 10 μmol/L quercetin for 1 h then exposed to 200 μmol/L SNP for the next 24 h. (A) Effect of quercetin on the cell viability in PC12 cells by MTT method. The percentage of cell viability was presented as mean±standard deviation for six replicates. (B) Effect of quercetin on the ratio of Caspase-3 and Hsp70 in PC12 cells. The percentage of density was presented as mean±standard deviation for three individual experiments. $^{c}P<0.01$ *vs* control group. $^{e}P<0.05$ *vs* SNP group. $^{h}P<0.05$ *vs* M3 pretreated group.

heat shock protein family, functions as a chaperone in protein folding, which can reduce abnormal protein aggregation[13, 14]. Overproduction of Hsp70 was shown to strongly protect brain cells from ischemia/reperfusion injuries both *in vitro* and *in vivo*[15]. Some of the anti-apoptotic activity of Hsp70 could be attributed to its ability to suppress the activity of JUN-kinase or Bid proteins[16, 17]. Thus, the decreased activation of caspase-3 in the M3 treated group might be due to the inhibition of the JNK/Bim pathway by the induction of Hsp70.

NO exposure has been established to induce Hsp70 expression in order to protect cells from tumor necrosis factor-induced apoptosis[18]. In our study, expression of Hsp70 could not save the PC12 cells from SNP-induced apoptosis. However, the M3 pretreatment remarkably increased the Hsp70 response without causing detrimental effects.

To confirm whether the induction of Hsp70 by M3 was responsible for its protective effects, quercetin, which is an HSP biosynthesis inhibitor, was used. Our results showed that pretreatment with quercetin attenuated the protective effect of M3 against SNP-induced apoptosis. This finding suggests that the protective effect of M3 was mediated, at least partly, by increasing the expression of Hsp70. However, quercetin failed to attenuate the protection of HupA on SNP-induced apoptosis, suggesting that the protective mechanism of HupA might have little interaction with Hsp70. Therefore, it appears that the protective mechanisms for these two compounds are different.

Taken together, M3 was similar to HupA with respect to free-radical scavenging. However, M3 treatment was able to elevate the expression of Hsp70 and decrease the expression of active caspase-3. M3 may activate the stress response without causing detrimental effects, thereby allowing the cells to survive under lethal conditions. Pretreatment with HupA also displayed ROS scavenging in PC12 cells exposed to SNP, but the presence of other protective mechanisms is not clear. Our research suggests that the distinctive chemical structure of HupA and its derivatives may be related to its anti-apoptotic properties. Further studies will concentrate on optimizing and analyzing these chemical structures in order to facilitate the design of novel anti-neurodegenerative drugs.

Acknowledgements

This research was supported by the National Natural Sciences Foundation of China (No 81072541 and 30973887), and the Joint Funds of NSFC-Guangdong of China (No U0832008).

Author contribution

Na NING, Jin-feng HU, Yu-he YUAN, and Nai-hong CHEN developed the research plan; Na NING performed the experiments; Xin-yuan ZHANG and Jun-gui DAI contributed reagents or analytical tools; Na NING and Nai-hong CHEN analyzed the data; and Na NING prepared the manuscript.

References

1 Abdulwahid AI, Ahmad KH. Environmental toxins and Parkinson's disease: putative roles of impaired electron transport chain and oxidative stress. Toxicol Ind Health 2010; 26: 121–8.
2 Bonda DJ, Wang X, Perry G, Smith MA, Zhu X. Mitochondrial dynamics

in Alzheimer's disease: opportunities for future treatment strategies. Drugs Aging 2010; 27: 181–92.

3 Thirumalai D, Lorimer GH. Chaperonin mediated protein folding. Annu Rev Biophys Biomol Struct 2001; 30: 245–69.

4 Hartl FU. Molecular chaperones in cellular protein folding. Nature 1996; 381: 571–9.

5 Pytlowany M, Strosznajder JB, Jeśko H, Cakała M, Strosznajder RP. Molecular mechanism of PC12 cell death evoked by sodium nitroprusside, a nitric oxide donor. Acta Biochim Pol 2008; 55: 339–47.

6 Yoko Hirata. Manganese-induced apoptosis in PC12 cells. Neurotoxicol Teratol 2002; 24: 639–53.

7 Lahiri DK, Ge YW. Role of the APP promoter in Alzheimer's disease: cell type-specific expression of the β-amyloid precursor protein. Ann N Y Acad Sci 2004; 1030: 310–6.

8 Zhang HY, Tang XC. Neuroprotective effects of huperzine A: new therapeutic targets for neurodegenerative disease. Trends Pharmacol Sci 2006; 27: 619–25.

9 Zhang HY, Brimijoin S, Tang XC. Apoptosis induced by beta-amyloid25–35 in acetylcholinesterase-overexpressing neuroblastoma cells. Acta Pharmacol Sin 2003; 24: 853–8.

10 Zhang XY, Zou JH, Dai JG. Microbial transformation of (–)-huperzine A. Tetrahedron Lett 2010; 51: 3840–2.

11 Malinski T. Nitric oxide and nitroxidative stress in Alzheimer's disease. J Alzheimers Dis 2007; 11: 207–18.

12 Imam SZ, el-Yazal J, Newport GD, Itzhak Y, Cadet JL, Slikker W Jr, *et al*. Methamphetamine-induced dopaminergic neurotoxicity: role of peroxynitrite and neuroprotective role of antioxidants and peroxynitrite decomposition catalysts. Ann N Y Acad Sci 2001; 939: 366–80.

13 Hishiya A, Takayama S. Molecular chaperones as regulators of cell death. Oncogene 2008; 27: 6489–506.

14 Tutar L, Tutar Y. Heat shock proteins, an overview. Curr Pharm Biotechnol 2010; 11: 216–22.

15 Kabakov AE, Gabai VL. Heat-shock proteins maintain the viability of ATP-deprived cells: what is the mechanism? Trends Cell Biol 1994; 4: 193–6.

16 Gabai VL, Meriin AB, Yaglom JA, Volloch VZ, Sherman MY. Role of Hsp70 in regulation of stress-kinase JNK: implications in apoptosis and aging. FEBS Lett 1998; 438: 1–4.

17 Kumar Y, Tatu U. Stress protein flux during recovery from simulated ischemia: induced heat shock protein 70 confers cytoprotection by suppressing JNK activation and inhibiting apoptotic cell death. Proteomics 2003; 3: 513–26.

18 Kim YM, de Vera ME, Watkins SS, Billiar TR. Nitric oxide protects cultured rat hepatocytes from tumor necrosis factor induced apoptosis by inducing heat shock protein 70 expression. J Biol Chem 1997; 272: 1402–11.

Acta Pharmacologica Sinica (2012) 33: 41–48
© 2012 CPS and SIMM All rights reserved 1671-4083/12 $32.00
www.nature.com/aps

Original Article

Salvianolic acid A inhibits angiotensin II-induced proliferation of human umbilical vein endothelial cells by attenuating the production of ROS

Luan-luan YANG[1], Dong-ye LI[1, *], Yan-bin ZHANG[2, *], Man-yi ZHU[1], Dan CHEN[1], Tong-da XU[2]

[1]Institute of Cardiovascular Disease, Xuzhou Medical College, Xuzhou 221002, China; [2]Department of Cardiology, Affiliated Hospital of Xuzhou Medical College, Xuzhou 221002, China

---

Aim: To investigate the action of salvianolic acid A (SalA) on angiotensin II (Ang II)-induced proliferation of human umbilical vein endothelial cells (HUVECs) and the possible signaling pathways mediating this action.
Methods: Cell proliferation was examined with MTT assay. The expression levels of Src phosphorylation (phospho-Src), Akt phosphorylation (phospho-Akt), and NADPH oxidase 4 (Nox4) in HUVECs were determined by Western blot. The production of reactive oxygen species (ROS) was estimated using fluorescence-activated cell sorting (FACS).
Results: SalA (6.25–50 μmol/L) did not affect the viability of HUVECs. Treatment of HUVECs with Ang II (1 μmol/L) markedly increased the cell viability; pretreatment of HUVECs with SalA (12.5, 25, and 50 μmol/L) prevented Ang II-induced increase of the cell viability in a concentration-dependent manner. Treatment of HUVECs with Ang II (1 μmol/L) markedly up-regulated the protein expression levels of phospho-Src, phospho-Akt (473) and Nox4; pretreatment of HUVECs with SalA (12.5, 25, and 50 μmol/L) blocked all the effects in a concentration-dependent manner. Treatment of HUVECs with Ang II (1 μmol/L) dramatically increased ROS production in HUVECs; pretreatment of HUVECs with SalA (12.5, 25, and 50 μmol/L) blocked the ROS production in a concentration-dependent manner.
Conclusion: SalA inhibits Ang II-induced proliferation of HUVECs via reducing the expression levels of phospho-Src and phospho-Akt (473), thereby attenuating the production of ROS.

Keywords: salvianolic acid A; human umbilical vein endothelial cells; angiotensin II; phospho-Src; phospho-Akt (473); NADPH oxidase 4; reactive oxygen species (ROS)

Acta Pharmacologica Sinica (2012) 33: 41–48; doi: 10.1038/aps.2011.133; published online 21 Nov 2011

Introduction

Endothelial cell proliferation plays an important role in angiogenesis, as well as atherogenesis, postangioplasty restenosis and other inflammatory vascular diseases such as rheumatoid arthritis and proliferative diabetic retinopathy[1–3]. In atherosclerosis, the proliferation of endothelial cells triggers platelet aggregation, leukocyte adhesion and transmigration, and vascular smooth muscle cell proliferation[1].

Angiotensin II (Ang II), one of the key components of the renin-angiotensin system, regulates a variety of physiological and pathological processes, including fluid homeostasis, aldosterone production, and renal function. It has recently been suggested that Ang II is not simply an autacoid with hemodynamic and renal actions but rather a biologically active mediator that acts directly on endothelial cells. Evidence is rapidly accumulating to support the theory that Ang II stimulates NADPH oxidase-dependent superoxide production in endothelial cells and that this is the main source of reactive oxygen species (ROS) in these cells[4–6]. NADPH oxidases (Noxs) are a family of multicomponent transmembrane enzymes that transport electrons across biological membranes to generate super-oxide, $O_2(-)$, by the reduction of oxygen[7]. A growing body of evidence has demonstrated that ROS production plays an important role in a variety of signal transduction pathways. ROS have been implicated in growth factor receptor signaling, as well as in the regulation of various transcription factors involved in cell proliferation, differentiation, and apoptosis[8–10].

Src is a cytoplasmic protein tyrosine kinase, and the activation and recruitment of this protein to perimembranous signaling complexes has important implications for a cell's fate[11]. At present, there are at least 14 confirmed varieties of Src kinase. The 60 kDa c-Src isoform is the most widely expressed

---

* To whom correspondence should be addressed.
E-mail dongyeli@medmail.com.cn (Dong-ye LI);
zhangyanbin99@sina.com (Yan-bin ZHANG)
Received 2011-07-10 Accepted 2011-09-15

version in vascular endothelial cells[12], and c-Src is the main modulator of NADPH oxidase-mediated superoxide anion production, which induces the vascular redox reaction[13]. Indeed, activation of the Src family kinases has been known to play an important role in cellular proliferation and migration, angiogenesis, and chemokine induction. Phosphoinositide 3-kinase (PI3K) and its downstream serine/threonine kinase Akt, also termed protein kinase B (PKB), play a central role in promoting the survival of a wide range of cell types. Akt is believed to play a crucial role in apoptosis, cell cycle regulation, angiogenesis, and tumor progression[14, 15]. Furthermore, Windham *et al*[16] reported that Src activation contributes to the resistance of cancer cells to cell death through the PI3K/Akt pathway because increased Src kinase activity leads to increased Akt phosphorylation.

The dried root of *Salvia miltiorrhiza* Bunge (Danshen) is a popular traditional Chinese medicine that has been widely used in both Asian and Western countries for the treatment of various diseases, including cerebrovascular diseases, coronary artery disease, myocardial infarction, hepatitis, hemorrhage, diabetes mellitus, and menstrual abnormalities, for thousands of years. Salvianolic acids include salvianolic acid A (SalA), salvianolic acid B (SalB), rosmarinic acid, and other polyphenolic acids. SalA ((2*R*)-3-(3,4-dihydroxyphenyl)-2-[(E)-3-[2-[(E)-2-(3,4-dihydroxyphenyl) ethenyl]-3,4-dihydroxyphenyl] prop-2-enoyl]oxypropanoic acid, see Figure 1) is the main active constituent of *S miltiorrhiza*[17]. This water-soluble compound has been reported to possess a wide range of pharmacological effects, including anti-inflammatory, anticarcinogenic, antioxidant, estrogenic, antiplatelet, and antifibrotic activities[18–21]. Investigative results from our laboratory showed that SalA also exhibited cardioprotective effects[22].

To date, little is known about the effects of SalA on vascular endothelial cells. The aims of this study, therefore, were to examine the inhibitory effect of SalA on the Ang II-induced proliferation of HUVECs and to further investigate the compound's effects on interrelated signaling pathways .

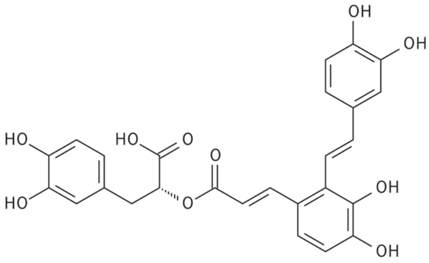

Figure 1. The chemical structure of salvianolic acid A (SalA).

Materials and methods

Chemicals

SalA lyophilized powder (product number 20091201, purity>98%), was supplied by Qing Feng Pharmaceutical Products (Jiangxi, China). Ang II, DMSO, and MTT were obtained from Sigma Chemical Co (St Louis, MO, USA). SalA and Ang II were dissolved in distilled water to reach a concentration of 0.1 mmol/L and were stored at 4 °C, for use as soon as possible. F12K was supplied by Hyclone (Logan, Utah, USA). Endothelial cell growth factor (ECGF) was obtained from Sciencell (San Diego, USA). Fetal bovine serum (FBS) and 0.25% trypsin were purchased from Gibco (Grand Island, NY). DCFH-DA (2′,7′-dichlorofluorescin diacetate) and heparin were from Beyotime Institute of Biotechnology (Jiangsu, China). Antibodies for phospho-Akt (Ser-473) and phospho-Src were obtained from Cell Signaling Technology Inc (Danvers, MA, USA). Antibody for Nox4 was obtained from Proteintech Group (Chicago, IL, USA).

Cell culture

HUVECs were obtained from American Type Culture Collection (ATCC). The HUVECs were cultured in a medium containing F12K, 10% fetal bovine serum, 0.1 mg/mL heparin, and 0.03–0.05 mg/mL ECGS, at 37 °C and 5% humidified atmospheric CO_2. The medium was refreshed every 2–3 d.

Cellular proliferation assay

Cellular proliferation was determined by MTT chromatometry, as originally described by Mosmann[23]. In brief, HUVECs were seeded in 96-well plates at a density of 5000 cells/well. First, the cells were treated with 0, 6.25, 12.5, 25, 50, 100, or 200 μmol/L SalA for 24 h and then, after treatment with either 12.5, 25, or 50 μmol/L SalA for 12 h, we treated the cells with 1 μmol/L Ang II for 24 h. Twenty microliters of MTT solution (5 mg/mL in PBS) were added to each well, and the plates were incubated for an additional 4 h at 37 °C. Then, the medium was removed, and wells were rinsed twice with PBS. To each well, 150 μL of DMSO was added at room temperature for 5 min to dissolve the formazan crystals, and then the optical density at 570 nm was determined with a Microplate Reader (Bio-Rad 550, Hercules, CA, USA). Each assay was performed in triplicate. Cellular proliferation is expressed as an index of percent viability (% viability), compared to the control cells.

Western blotting analysis for phospho-Akt, phospho-Src, and Nox4 expression

To investigate the mechanisms underlying the effects of SalA on the HUVEC proliferation induced by Ang II, the expression levels of Akt, Src, phospho-Akt, phospho-Src, and Nox4 in SalA-treated HUVECs were evaluated by Western blotting. The expression of β-actin was measured as an internal standard. After designated treatment, the HUVECs were lysed and centrifuged. The protein concentrations were quantitatively determined through the use of a modified Bradford assay (Bio-Rad, CA, USA). Equivalent amounts (40 μg) of protein samples were loaded and separated by 8% to 12% SDS-polyacrylamide gel electrophoresis and the proteins were then transferred to a polyvinylidene difluoride (PVDF) membrane. After blocking with 5% non-fat dry milk in Tris-buffered saline containing 0.1% Tween 20 (TBST), the membranes were incubated with rabbit polyclonal primary antibody or mouse monoclonal antibody, at a dilution of 1:1000 overnight at 4 °C, against each of the following proteins: Akt, Src, phospho-Akt, phospho-Src, and Nox4. After washing, the membranes were incubated with the requisite secondary antibody at room temperature for 120 min. The protein bands were visualized with nitro blue tetrazolium and 5-bromo-4-chloro-3-indolyl-phosphate. The membranes were scanned, and the relative intensity of the bands was analyzed using Image J 3.0. Prestained markers were used for molecular mass determinations and were photographed after color development. The levels of proteins were determined using densitometry (Image J software), which allowed direct comparisons to be made between experimental sets. The optical density of the control group was 1 arbitrary densitometric unit.

Measurement of ROS production

To investigate the generation of ROS in HUVECs, DCFH-DA was used to determine the amount of intracellular ROS production. DCFH-DA can readily penetrate the cell membrane, where it can be rapidly de-esterified by membrane-bound esterases to yield free DCFH. On reaction with ROS, DCFH is oxidized to yield the fluorescent dichlorofluorescein (DCF). Thus, the intensity of the cellular fluorescence correlates with the amount of ROS formed *in situ*. For this assay, HUVECs were pre-incubated in 6-well plates for 24 h at 37 °C in culture medium. After pretreatment for 12 h with varying concentrations of SalA and for an additional 12 h with 1 μmol/L Ang II, the HUVECs were incubated with 10 μmol/L DCFH-DA for 30 min at 37 °C. After washing with PBS, the cells were collected in 500 μL PBS. The cell fluorescence intensity was measured at 490 nm excitation and 530 nm emission using a fluorescence-activated cell sorting (FACS) flow cytometer (Becton Dickinson, San Jose, CA, USA), as previously described[24].

Statistical analyses

For each experiment, data are presented as mean±SEM. Statistical analysis was performed using GraphPad Prism 4.0. Statistical significance ($P<0.05$) for each variable was estimated by 1-way or 2-way analysis of variance, followed by Bonferroni *post-hoc* tests.

Results

Effects of SalA on Ang II-induced HUVEC proliferation

To examine the toxicity of SalA, cell viability was assessed using the MTT metabolism assay. Within the tested concentrations (6.25–200 μmol/L), cell viability was not significantly influenced by SalA at concentrations of 6.25–50 μmol/L. However, cell viability was significantly attenuated with both 100 μmol/L ($P<0.05$) and 200 μmol/L ($P<0.01$) doses of SalA in a concentration-dependent manner, as shown in Figure 2A. For our study, we chose to use SalA concentrations of 6.25, 12.5, 25, and 50 μmol/L. The MTT assay was also used to assess cellular proliferation. Ang II (1 μmol/L) significantly increased cell proliferation compared with the control group ($P<0.01$). However, compared with Ang II, pretreatment with 25 or 50 μmol/L SalA significantly inhibited cellular proliferation ($P<0.01$) (Figure 2B).

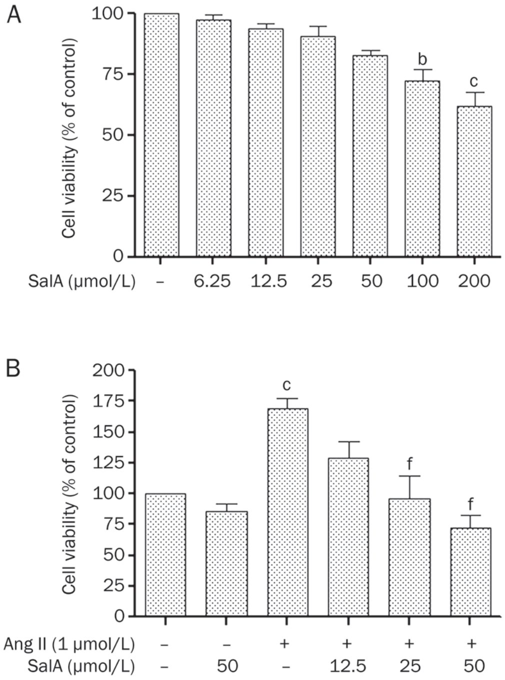

Figure 2. Effects of SalA on proliferation of Ang II-induced HUVECs. (A) The toxicity of SalA (6.25–200 μmol/L) in HUVECs was measured using MTT metabolism assay after 24-h incubation. (B) Cells were pretreated with different concentrations of SalA (12.5, 25, and 50 μmol/L) for 12 h prior to incubation with of Ang II (1 μmol/L) for 24 h. Data represent means±SEM. *n*=3. $^{b}P<0.05$, $^{c}P<0.01$ *vs* control. $^{f}P<0.01$ *vs* Ang II.

Effects of SalA on the expression levels of total and phosphorylated-Src

We incubated serum-deprived HUVECs with 1 μmol/L Ang II for 0, 2.5, 5, 10, 15, and 30 min. Ang II caused an increase in phospho-Src levels, starting 2.5 min after stimulation, with a maximal 2.91±0.23-fold increase relative to basal levels at 5 min ($P<0.01$). Thereafter, phospho-Src decreased rapidly (Figure 3A). When we pretreated serum-deprived HUVECs with 50 μmol/L SalA for 12 h, the levels of phospho-Src significantly decreased, compared with the group treated by Ang II alone ($P<0.01$) (Figure 3A).

As shown in Figure 3B, Ang II significantly increased the phosphorylation of Src, whereas SalA (12.5, 25, or 50 μmol/L) downregulated phospho-Src in a dose-dependent manner. Figure 3C shows that, in serum-deprived HUVECs pretreated with 50 μmol/L SalA for varying lengths of time (3, 6, 12, or 24 h), the level of phospho-Src significantly decreased ($P<0.01$), whereas it increased in the Ang II-treated group compared to the control ($P<0.01$).

Effects of SalA on the expression levels of total Akt and phosphorylated Akt

To examine whether SalA inhibits the proliferation of HUVECs, the expression of phospho-Akt was assessed by Western blot analysis (Figure 4). We incubated serum-

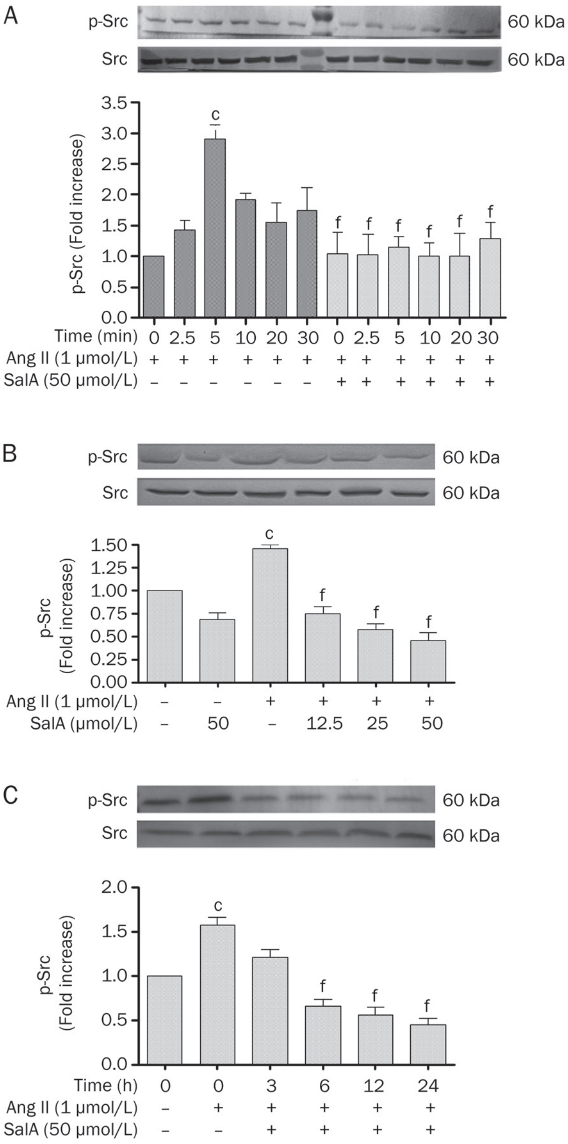

Figure 3. The effects of SalA on the expression levels of both total and phosphorylated src. (A) The time dependent effects of Ang II on src phosphorylation in HUVECs. Ang II (1 µmol/L) caused a time-dependent increase in phospho-src level, starting at 2.5 min after stimulation, with a maximal 2.91±0.23 fold basal after 5 min. Thereafter, phospho-src signaling decreased rapidly. (B) The effect of pretreatment with different doses SalA for 12 h on p-Src. Ang II increased the level of p-Src, whereas SalA down-regulated p-Src in a dose-dependent manner. (C) The effect of SalA on phosphor-src, petreated with 50 µmol/L SalA for 3, 6, 12, and 24 h downregulated phosphorylation of src in a time-dependent manner. Data represent mean±SEM. *n*=3. $^{c}P<0.01$ *vs* control. $^{f}P<0.01$ *vs* Ang II.

deprived HUVECs with 1 µmol/L Ang II for 0, 5, 15, 30, 45, or 60 min and found that Ang II caused an increase in phospho-Akt levels, starting at 5 min post-stimulation, with a maximal 1.96±0.09 fold-increase over basal levels after 15 min ($P<0.01$). Thereafter, phospho-Akt signaling decreased rapidly (Figure 4A). When we pretreated serum-deprived HUVECs with 50 µmol/L SalA for 12 h, the levels of phospho-Akt were significantly reduced, when compared with the Ang II group ($P<0.01$) (Figure 4A).

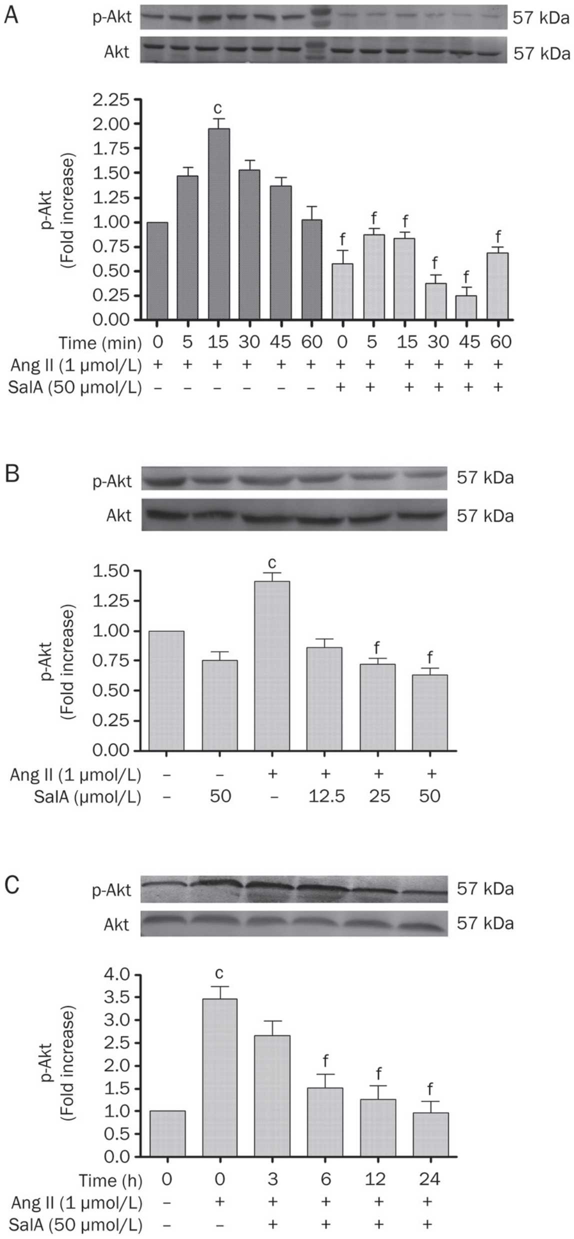

Figure 4. The effects of SalA on the expression levels of both total and phosphorylated Akt. (A) The time dependent effects of Ang II on Akt phosphorylation in HUVECs. Ang II (1 µmol/L) caused a time-dependent increase in phospho-Akt level, starting at 5 min post stimulation, with a maximal 1.96±0.09 fold basal after 15 min. Thereafter, phospho-Akt signaling decreased rapidly. (B) The effect of different doses SalA on phosphor-Akt. Ang II increased the level of phosphorylation of Akt, whereas pretreatment with SalA for 12 h downregulated phosphorylation of Akt in a dose-dependent manner. (C) The effect of different times SalA on phosphor-Akt. Ang II increased the level of phosphorylation of Akt, whereas SalA (3, 6, 12, and 24 h) down-regulated phosphorylation of Akt ~~with~~ in a time-dependent manner. Data represent means ±SEM. *n*=3. $^{c}P<0.01$ *vs* Control. $^{f}P<0.01$ *vs* Ang II.

As shown in Figure 4B, Ang II significantly increased the phosphorylation of Akt, whereas SalA (12.5, 25, or 50 μmol/L) downregulated Akt phosphorylation in a dose-dependent manner. Figure 4C showed that, in serum-deprived HUVECs pretreated with SalA (50 μmol/L) for different lengths of time (3, 6, 12, or 24 h), the level of phospho-Akt was significantly reduced ($P<0.01$), whereas the phosphorylation of Akt increased in the Ang II group, compared with the control ($P<0.01$).

Effects of SalA on the level of Nox4 expression

HUVECs were pretreated with SalA at different concentrations before exposure to Ang II (1 μmol/L) for 24 h. As shown in Figure 5A, Ang II significantly increased the expression level of Nox4, compared with the control ($P<0.01$). However, the level of Nox4 decreased after pretreatment with SalA (25 and 50 μmol/L) for 12 h, compared with Ang II treatment alone ($P<0.01$). Pretreatment with SalA (50 μmol/L) for 3, 6, 12, or 24 h led to time-dependent decreases in Nox4 levels. In contrast, Nox4 expression was significantly increased in the Ang II group ($P<0.01$) (Figure 5B).

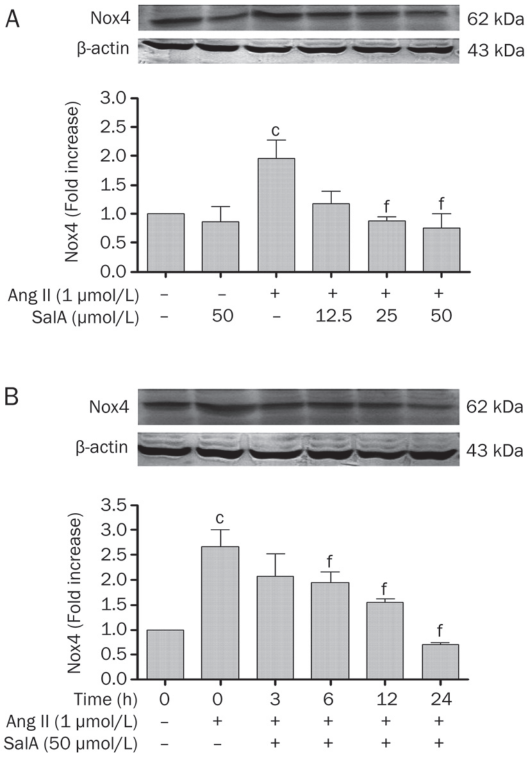

Figure 5. SalA decreased the level of Nox4 induced by Ang II in HUVECs. Pretreated with SalA at different doses for 12 h, HUVECs were incubated with 1 μmol/L Ang II for 24 h. The level of Nox4 was determined by Western blot analysis. SalA (12.5, 25, and 50 μmol/L) downregulated the level of Nox4 in a dose-dependent manner (A). Pretreated with SalA (50 μmol/L) for 3, 6, 12, or 24 h, the level of Nox4 were decreased whereas increased in the Ang II group (B). Data represent means±SEM. *n*=3. ${}^{c}P<0.01$ *vs* Control. ${}^{f}P<0.01$ *vs* Ang II.

Effects of SalA on ROS production

The DCFH-DA fluorescence method was used to measure ROS production in the HUVECs (Figure 6A). As shown in Figure 6B, the fluorescence intensity of the Ang II-treated group was significantly increased, compared with the control group ($P<0.01$). However, when the cells were pretreated with SalA (12.5, 25 and 50 μmol/L), the fluorescence intensity significantly decreased ($P<0.01$), relative to the cells treated with Ang II alone.

Discussion

Because endothelial cell proliferation is an important variable in the initiation and progression of atherosclerosis, it is of great importance to understand the mechanisms underlying the cardioprotective effects of several drugs. In China, Danshen has been widely used to treat cardiovascular diseases for hundreds of years. Salvianolic acids are the most abundant water-soluble compounds extracted from Danshen. Salvianolic acids, especially SalA and SalB, have been found to have potent anti-inflammatory, antioxidant, antiplatelet, and antifibrotic properties. Previous studies have demonstrated that SalA and SalB are the most abundant components in Danshen and that they share a similar structure. However, SalA produces stronger effects on the above-mentioned functions than SalB does. Some studies have reported that Ang II is an endogenous modulator of endothelium proliferation[25]. The rate of stent restenosis is high following percutaneous coronary intervention (PCI), mainly due to excessive proliferation of endothelial cells. In the present study, we found that SalA exerted a strong protective effect against the proliferation of HUVECs induced by Ang II, providing evidence for an important potential clinical application of SalA.

To examine whether SalA affects Ang II-induced proliferation of HUVECs, we used the MTT assay to measure cellular proliferation. Treating HUVECs with different concentrations of SalA (6.25–200 μmol/L) for 24 h resulted in no change in cell viability at concentrations of 6.25–50 μmol/L (Figure 2A). Ang II (1 μmol/L) significantly increased cellular proliferation, compared with the control group. Pretreatment with 25 or 50 μmol/L of SalA, compared to treatment with Ang II alone, significantly inhibited cellular proliferation (Figure 2B). This result demonstrated that, in the range of 6.25–50 μmol/L, SalA had no influence on HUVEC viability and that SalA could inhibit the Ang II-induced proliferation of HUVECs in a concentration-dependent manner.

All of the effects ascribed to Ang II coalesce on the high-affinity G-protein coupled receptors localized on the surface of target cells, regulating their physiological and pathophysiological processes. There are two main Ang II receptor subtypes that have been identified thus far, the Ang II type 1 (AT_1) and Ang II type 2 (AT_2) receptors. In the development and progression of Ang II-mediated high blood pressure, atherosclerosis, and other cardiovascular disease, endothelial cells are some of Ang II's target cells. Ang II, acting through AT_1R[26], can promote the proliferation of endothelial cells and cause endothelial cell basement membrane egradation, as well

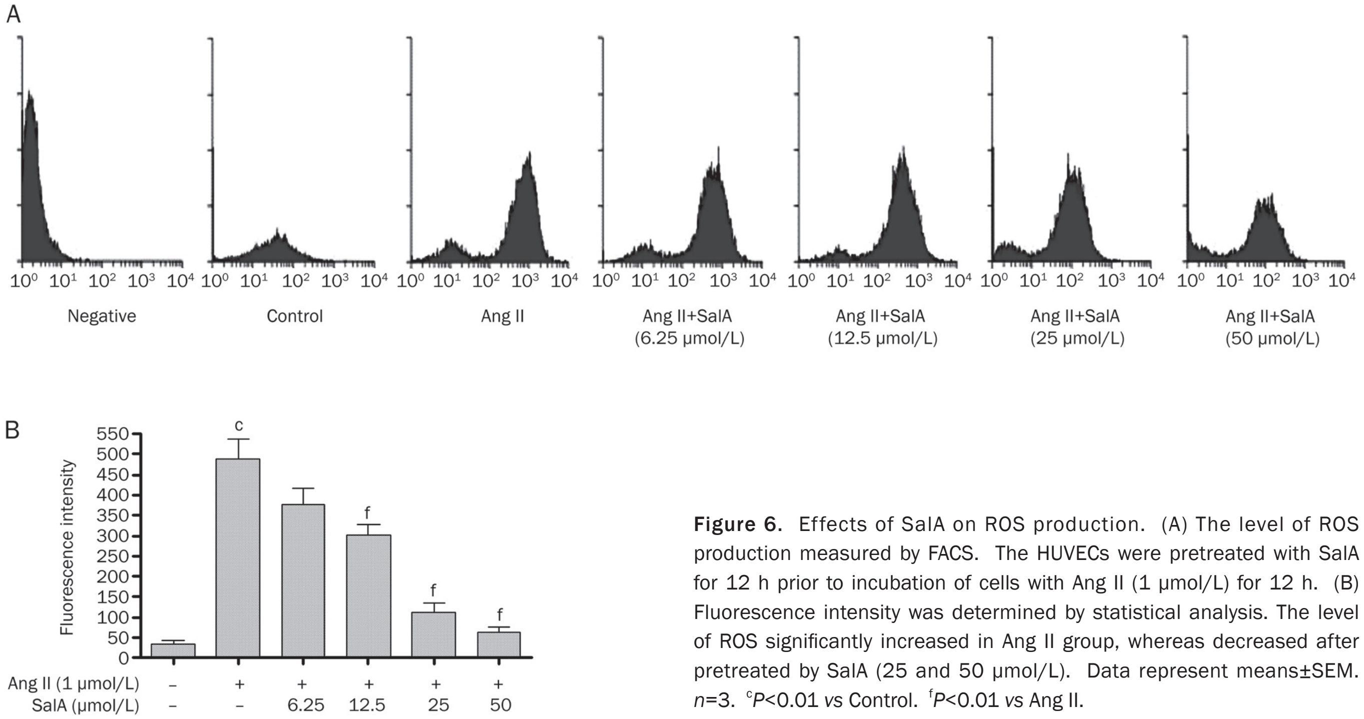

Figure 6. Effects of SalA on ROS production. (A) The level of ROS production measured by FACS. The HUVECs were pretreated with SalA for 12 h prior to incubation of cells with Ang II (1 μmol/L) for 12 h. (B) Fluorescence intensity was determined by statistical analysis. The level of ROS significantly increased in Ang II group, whereas decreased after pretreated by SalA (25 and 50 μmol/L). Data represent means±SEM. *n*=3. $^{c}P<0.01$ *vs* Control. $^{f}P<0.01$ *vs* Ang II.

as reconstruction migration.

Thomas and Brugge investigated the involvement of Src in cellular proliferation and migration, including the important role this kinase plays in signaling[27]. They reported that the activation of Src kinase in response to cellular signaling promoted proliferation and survival. The serine/threonine kinase Akt/PKB regulates multiple biological processes, including cell survival, proliferation, and growth. Akt is a member of the protein kinase B group and is a downstream kinase of PI3K. Ser-473 is phosphorylated by S473K thereby activating Akt[28]. Signaling molecules such as Src and Akt play important roles in many pathophysiological processes, including cell cycle regulation, cell survival, cell growth, glycogen metabolism, and cell migration. Thus, efforts to reduce the proliferation of endothelial cells have recently focused on inhibiting Src and Akt activity. We studied the phosphorylation levels of both Src and Akt to examine the inhibitory effects of SalA on HUVEC proliferation. Ang II has recently been found to cause rapid phosphorylation of Akt, mediated by the PI3K pathway[29]. As shown in Figure 3A, Ang II increased the level of phospho-Src which reached a peak at 5 min, while simultaneously increasing the level of phospho-Akt (peak at 15 min), as depicted in Figure 4A. However, after pretreatment with 50 μmol/L SalA for 12 h, the phosphorylation levels of both proteins decreased. This result demonstrated that Ang II can activate both Src and Akt phosphorylation, whereas SalA downregulates this modification in a concentration and time-dependent manner.

NADPH oxidase was originally identified and characterized in phagocytes, where it contributes to host defense. All of the components of the NADPH complex have been identified in endothelial cells[30–33]. Vascular NADPH oxidase, which plays an important role in both physiology and pathophysiology, is the primary source of ROS in endothelial cells. NADPH oxidase activity varies between vascular cells and between different sites of the vasculature. For example, vascular smooth muscle cells express high levels of Nox1 and Nox4, whereas endothelial cells express high levels of gp91phox/Nox2 and Nox4[34–36]. ROS have long been implicated in the pathogenesis of cardiovascular diseases, including atherosclerosis, hypertension, and diabetes. There is a growing appreciation for the role of ROS in physiological signaling in many cell types, including vascular endothelial cells. ROS, as a secondary messenger, activates a series of cell protein kinases, including c-Src and Akt/PKB, and this activation plays a decisive role in the process of atherosclerosis. Some evidence indicates that Ang II has a stimulatory effect on ROS production in the endothelium by activating and up-regulating NADPH oxidase[37]. We sought to clarify whether the inhibitory effect of SalA on the proliferation of HUVECs might be mediated through its antioxidative activity. HUVECs were pretreated with increasing concentrations of SalA for different times prior to incubation with 1 μmol/L Ang II. The results indicated that Ang II treatment increased the level of Nox4 expression, whereas SalA inhibited the Ang II-induced changes in Nox4 expression in a time- and concentration-dependent manner (Figure 5). In addition, the production of ROS was significantly decreased with SalA (25 and 50 μmol/L) treatment compared with treatment with Ang II alone (Figure 6). This result demonstrated that SalA inhibited the induction of Nox4 by Ang II and reduced ROS production accordingly.

Ang II has been proposed to participate in the production of ROS. ROS can activate Src, which can then promote further ROS production[38, 39]. Increased Src kinase activity was shown to increase Akt phosphorylation. Akt is an important kinase for promoting cellular proliferation and migration. Our data have shown that SalA decreased the level of phosphor-Src and phospho-Akt in a time- and concentration-dependent manner and that SalA also inhibited increases in Nox4 protein expression, ultimately resulting in a significant decrease in ROS production. All of these events contribute in part to the inhibitory effect of SalA on the proliferation of HUVECs.

In summary, we have identified a novel function for SalA by demonstrating the significant role it plays in inhibiting the Ang II-induced proliferation of HUVECs. Further studies are needed to determine the exact mechanism by which SalA acts to protect vascular endothelial cells against Ang II-mediated injury.

Acknowledgements

We gratefully acknowledge the excellent technical assistance of Yang LIU.

Author contribution

Dong-ye LI and Yan-bin ZHANG designed research; Luan-luan YANG and Man-yi ZHU performed research; Dan CHEN contributed new analytical tools and reagents; Tong-da XU analyzed data; Luan-luan YANG and Dong-ye LI wrote the paper.

References

1 Ross R. Atherosclerosis–an inflammatory disease. N Engl J Med 1999; 340: 115–26.
2 Hunt BJ. The endothelium in atherogenesis. Lupus 2000; 9: 189–93.
3 Brasen JH, Kivela A, Roser K, Rissanen TT, Niemi M, Luft FC, *et al*. Angiogenesis, vascular endothelial growth factor and platelet-derived growth factor-BB expression, iron deposition, and oxidation-specific epitopes in stented human coronary arteries. Arterioscler Thromb Vasc Biol 2001; 21: 1720–6.
4 Alvarez E, Rodino-Janeiro BK, Ucieda-Somoza R, Gonzalez-Juanatey JR. Pravastatin counteracts angiotensin II-induced upregulation and activation of NADPH oxidase at plasma membrane of human endothelial cells. J Cardiovasc Pharmacol 2010; 55: 203–12.
5 Shuvaev VV, Christofidou-Solomidou M, Bhora F, Laude K, Cai H, Dikalov S, *et al*. Targeted detoxification of selected reactive oxygen species in the vascular endothelium. J Pharmacol Exp Ther 2009; 331: 404–11.
6 Ushio-Fukai M. Redox signaling in angiogenesis: role of NADPH oxidase. Cardiovasc Res 2006; 71: 226–35.
7 Bedard K, Krause KH. The NOX family of ROS-generating NADPH oxidases: physiology and pathophysiology. Physiol Rev 2007; 87: 245–313.
8 Chen K, Thomas SR, Keaney JF Jr. Beyond LDL oxidation: ROS in vascular signal transduction. Free Radic Biol Med 2003; 35: 117–32.
9 Sauer H, Wartenberg M, Hescheler J. Reactive oxygen species as intracellular messengers during cell growth and differentiation. Cell Physiol Biochem 2001; 11: 173–86.
10 Na AR, Chung YM, Lee SB, Park SH, Lee MS, Yoo YD. A critical role for Romo1-derived ROS in cell proliferation. Biochem Biophys Res Commun 2008; 369: 672–8.
11 Ali N, Yoshizumi M, Yano S, Sone S, Ohnishi H, Ishizawa K, *et al*. The novel Src kinase inhibitor M475271 inhibits VEGF-induced vascular endothelial-cadherin and β-catenin phosphorylation but increases their association. J Pharmacol Sci 2006; 102: 112–20.
12 Oda Y, Renaux B, Bjorge J, Saifeddine M, Fujita DJ, Hollenberg MD. c-Src is a major cytosolic tyrosine kinase in vascular tissue. Can J Physiol Pharmacol 1999; 77: 606–17.
13 Touyz RM, Yao G, Schiffrin EL. c-Src induces phosphorylation and translocation of p47phox: role in superoxide generation by angiotensin II in human vascular smooth muscle cells. Arterioscler Thromb Vasc Biol 2003; 23: 981–7.
14 Brazil DP, Yang ZZ, Hemmings BA. Advances in protein kinase B signalling: AKTion on multiple fronts. Trends Biochem Sci 2004; 29: 233–42.
15 Manning BD, Cantley LC. AKT/PKB signaling: navigating downstream. Cell 2007; 129: 1261–74.
16 Windham TC, Parikh NU, Siwak DR, Summy JM, McConkey DJ, Kraker AJ, *et al*. Src activation regulates anoikis in human colon tumor cell lines. Oncogene 2002; 21: 7797–807.
17 Wang SB, Tian S, Yang F, Yang HG, Yang XY, Du GH. Cardioprotective effect of salvianolic acid A on isoproterenol-induced myocardial infarction in rats. Eur J Pharmacol 2009; 615: 125–32.
18 Li HY, Li Y, Yan CH, Li LN, Chen XG. Inhibition of tumor growth by S-3-1, a synthetic intermediate of salvianolic acid A. J Asian Nat Prod Res 2002; 4: 271–80.
19 Lin TJ, Zhang KJ, Liu GT. Effects of salvianolic acid A on oxygen radicals released by rat neutrophils and on neutrophil function. Biochem Pharmacol 1996; 51: 1237–41.
20 Liu CH, Hu YY, Wang XL, Liu P, Xu LM. Effects of salvianolic acid-A on NIH/3T3 fibroblast proliferation, collagen synthesis and gene expression. World J Gastroenterol 2000; 6: 361–4.
21 Tang MK, Ren DC, Zhang JT, Du GH. Effect of salvianolic acids from Radix Salviae miltiorrhizae on regional cerebral blood flow and platelet aggregation in rats. Phytomedicine 2002; 9: 405–9.
22 Pan HJ, Li DY, Fang F, Chen D, Qi L, Xu TD, et al. Salvianolic acid A demonstrates cardioprotective effects in rat hearts and cardiomyocytes following ischemia/reperfusion injury. J Cardiovasc Pharmacol 2011; 58: 535–42.
23 Mosmann T. Rapid colorimetric assay for cellular growth and survival: application to proliferation and cytotoxicity assays. J Immunol Methods 1983; 65: 55–63.
24 Holmes KL, Otten G, Yokoyama WM. Flow cytometry analysis using the bectondickinson facs calibur. Curr Proto Immunol 2002; Chapter 5: Unit 5.4.
25 Herr D, Rodewald M, Fraser HM, Hack G, Konrad R, Kreienberg R, *et al*. Regulation of endothelial proliferation by the rennin-angiotensin system in human umbilicai vein endothelial cells. Reproduction 2008; 136 : 125–30.
26 Mc Ewan PE, Vinson GP, Kenyon CJ. Control of adrenal cell proliferation by AT1 receptors in response to angiotensin II and low-sodium diet. Am J Physiol 1999; 276: E303–309.
27 Thomas SM, Brugge JS. Cellular functions regulated by Src family kinases. Annu Rev Cell Dev Biol 1997; 13: 513–609.
28 Huang J, Kontos CD. Inhibition of vascular smooth muscle cell proliferation, migration, and survival by the tumor suppressor protein PTEN. Arterioscler Thromb Vasc Biol 2002; 22: 745–51.
29 Das DK, Maulik N, Engelman RM. Redox regulation of angiotensin II signalling in the heart. J Cell Mol Med 2004; 8: 144–52.
30 Gorlach A, Brandes RP, Nguyen K, Amidi M, Dehghani F, Busse R. A gp91phox containing NADPH oxidase selectively expressed in

endothelial cells is a major source of oxygen radical generation in the arterial wall. Circ Res 2000; 87: 26–32.

31 Abid MR, Spokes KC, Shih SC, Aird WC. NADPH oxidase activity selectively modulates vascular endothelial growth factor signaling pathways. J Biol Chem 2007; 282: 35373–85.

32 Haurani MJ, Cifuentes ME, Shepard AD, Pagano PJ. Nox4 oxidase overexpression specifically decreases endogenous Nox4 mRNA and inhibits angiotensin II induced adventitial myofibroblast migration. Hypertension 2008; 52: 143–9.

33 Abid MR, Kachra Z, Spokes KC, Aird WC. NADPH oxidase activity is required for endothelial cell proliferation and migration. FEBS Lett 2000; 486: 252–6.

34 Ago T, Kitazono T, Ooboshi H, Iyama T, Han YH, Takada J, *et al*. Nox4 as the major catalytic component of an endothelial NAD(P)H oxidase. Circulation 2004; 109: 227–33.

35 Van Buul JD, Fernandez-Borja M, Anthony EC, Hordijk PL. Expression and localization of NOX2 and NOX4 in primary human endothelial cells. Antioxid Redox Signal 2005; 7: 308–17.

36 Li JM, Shah AM. Endothelial cell superoxide generation: regulation and relevance for cardiovascular pathophysiology. Am J Physiol 2004; 287: R1014–R1030.

37 Zhang H, Schmeisser A, Garlichs CD, Plotze K, Damme U, Mugge A, *et al*. Angiotensin II-induced superoxide anion generation in human vascular endothelial cells: role of membrane-bound NADH-/NADPH-oxidases. Cardiovasc Res 1999; 44: 215–22.

38 Vasant C, Rajaram R, Ramasami T. Apoptosis of lymphocytes induced by chromium (VI/V) is through ROS-mediated activation of Src-family kinases and caspase-3. Free Radic Biol Med 2003; 35: 1082–100.

39 Gianni D, Taulet N, DerMardirossian C, Bokoch GM. c-Src-mediated phosphorylation of Nox1 and Tks4 induces the reactive oxygen species (ROS)-dependent formation of functional invadopodia in human colon cancer cells. Mol Biol Cell 2010; 21: 4287–98.

Acta Pharmacologica Sinica (2012) 33: 49–56

www.nature.com/aps

npg

Original Article

Thrombin induced connective tissue growth factor expression in rat vascular smooth muscle cells via the PAR-1/JNK/AP-1 pathway

Wen-chin KO[1, 2], Bing-chang CHEN[3], Ming-jen HSU[4], Chia-ti TSAI[5], Chuang-ye HONG[1, 6, *], Chien-huang LIN[6, 7, *]

[1]Graduate Institute of Clinical Medicine, College of Medicine, Taipei Medical University, Taipei, Taiwan, China; [2]Division of Cardiology, Department of Internal Medicine, Cathay General Hospital, Taipei, Taiwan, China; [3]School of Respiratory Therapy, College of Medicine, Taipei Medical University, Taipei, Taiwan, China; [4]Department of Pharmacology, School of Medicine, College of Medicine, Taipei Medical University, Taipei, Taiwan, China; [5]Division of Cardiology, Department of Internal Medicine, National Taiwan University Hospital, Taipei, Taiwan, China; [6]Department of Internal Medicine, Wan Fang Hospital, Taipei Medical University, Taipei, Taiwan, China; [7]Graduate Institute of Medical Sciences, College of Medicine, Taipei Medical UniversityTaipei, Taiwan, China

---

Aim: To investigate the signaling pathways involved in thrombin-induced connective tissue growth factor (CTGF) expression in rat vascular smooth muscle cells (VSMCs).
Methods: Experiments were preformed on primary rat aortic smooth muscle cells (RASMCs) and a rat VSMC line (A10). CTGF protein levels were measured using Western blotting. Luciferase reporter genes and dominant negative mutants (DNs) were used to investigate the signaling pathways mediating the induction of CTGF expression by thrombin.
Results: Thrombin (0.3–3.0 U/mL) caused a concentration- and time-dependent increase in CTGF expression in both RASMCs and A10 cells. Pretreating A10 cells with the protease-activated receptor 1 (PAR-1) antagonist SCH79797 (0.1 μmol/L) significantly blocked thrombin-induced CTGF expression, while the PAR-4 antagonist tcY-NH_2 (30 μmol/L) had no effect. The PAR-1 agonist SFLLRN-NH_2 (300 μmol/L) induced CTGF expression, while the PAR-4 agonist GYPGQV-NH_2 (300 μmol/L) had no effect. Thrombin (1 U/mL) caused time-dependent phosphorylation of c-Jun N-terminal kinase (JNK). Pretreating with the JNK inhibitor SP600125 (3–30 μmol/L) or transfection with DNs of JNK1/2 significantly attenuated thrombin-induced CTGF expression. Thrombin (0.3–3.0 U/mL) increased activator protein-1 (AP-1)-luciferase activity, which was inhibited by the JNK inhibitor SP600125. The AP-1 inhibitor curcumin (1–10 μmol/L) concentration-dependently attenuated thrombin-induced CTGF expression.
Conclusion: Thrombin acts on PAR-1 to activate the JNK signaling pathway, which in turn initiates AP-1 activation and ultimately induces CTGF expression in VSMCs.

Keywords: thrombin; protease-activated receptor; activator protein-1 (AP-1); connective tissue growth factor; mitogen-activated protein kinase (MAPK); c-Jun N-terminal kinase (JNK); vascular smooth muscle cell

---

Acta Pharmacologica Sinica (2012) 33: 49–56; doi: 10.1038/aps.2011.178

Introduction

Thrombin, a serine protease, has been studied for its pleiotropic actions beyond hemostasis[1]. The biological actions of thrombin in tissues and cells are mostly transduced by the protease-activated receptors (PARs), a family of G protein-coupled receptors. At present, 4 different PARs (PAR1–4) have been cloned. PAR-1, PAR-3, and PAR-4 are activated by thrombin, whereas PAR-2 is activated by tryptase[2]. Thrombin is implicated in the process of vascular remodelling in atherosclerosis and restenosis[3]. Thrombin can stimulate the formation of collagen in a PAR-1-dependent mechanism in vascular smooth muscle cells (VSMCs)[4]. Connective tissue growth factor (CTGF) is a recently identified profibrotic agent. It is an immediate-early gene and belongs to the CCN family [Cyr61 (CCN1), CTGF (CCN2), Nov (CCN3), Wisp-1/elm1 (CCN4), Wisp-2/rCop1 (CCN5), and Wisp-3 (CCN6)] of growth factors[5]. The CTGF protein is a 38-kDa cysteine-rich, heparin-binding, secreted protein initially identified in the conditioned medium of cultured endothelial cells[6]. It is expressed by many human organs and is involved in various biological functions, including embryonic development,

---

* To whom correspondence should be addressed.
E-mail chlin@tmu.edu.tw (Chien-huang LIN);
hongprof@tmu.edu.tw (Chuang-ye HONG)
Received 2011-10-07 Accepted 2011-11-24

wound repair, and angiogenesis[7]. CTGF has been implicated in a variety of cardiovascular pathophysiological conditions. CTGF is overexpressed in human atherosclerotic lesions[8]. It has been proved to be a mediator of angiotensin II-induced fibrosis in VSMCs[9]. Transforming growth factor-β, endothelin-1, and homocysteine can regulate CTGF expression in VSMCs[10–12]. However, the role of thrombin in the induction of CTGF expression in VSMCs has not been reported. The promoter region of the human CTGF gene contains binding sites for multiple transcription factors. These transcription factors include activator protein-1 (AP-1), STAT, SMAD, basal control element (BCE) 1, NF-κB, specificity protein 1 (Sp1), and Elk-1[13, 14]. Therefore, we hypothesized that thrombin can induce CTGF expression in VSMCs and its signaling pathways involve PAR-1, mitogen-activated protein kinases (MAPKs), and AP-1. In the present study, we demonstrated that thrombin acts on PAR-1 to activate the JNK signaling pathway, which in turn initiates AP-1 activation and ultimately induces CTGF expression in VSMCs.

Materials and methods

Materials

Thrombin (from bovine plasma), SCH79797, curcumin, actinomycin D (ActD), and cycloheximide (CHX) were purchased from Sigma-Aldrich (St Louis, MO, USA). SFLLRN-NH_2 and GYPGQV-NH_2 were purchased from Bachem Americas (Torrance, CA, USA). The human CTGF promoter (-747/+214) luciferase construct (pGL3-CTGF-Luc) was provided by Dr ML KUO (National Taiwan University, Taipei, Taiwan, China). JNK1 dominant-negative mutant (DN), JNK2DN[15], and pcDNA were provided by Dr MC CHEN (Taipei Medical University, Taipei, Taiwan, China). pBK-CMV-*LacZ* (*LacZ*) was provided by Dr WW LIN (National Taiwan University, Taipei, Taiwan, China). Dulbecco's modified Eagle's medium (DMEM), fetal calf serum (FCS), penicillin/streptomycin, sodium pyruvate, *L*-glutamine, nonessential amino acids (NEAAs), and Lipofectamine Plus reagent were purchased from Invitrogen (Carlsbad, CA, USA). An antibody (Ab) specific for α-tubulin was purchased from Novus Biologicals (Littleton, CO, USA). Abs specific for CTGF, phospho-c-Jun N-terminal kinase (JNK), and anti-mouse, anti-rabbit, and anti-goat IgG-conjugated horseradish peroxidase were purchased from Santa Cruz Biotechnology (Santa Cruz, CA, USA). SP600125 and tcY-NH_2 were purchased from Tocris Bioscience (Ellisville, MO, USA). The AP-1-luciferase plasmid was purchased from Stratagene (La Jolla, CA, USA). All materials for SDS-PAGE were purchased from Bio-Rad (Hercules, CA, USA). All other chemicals were obtained from Sigma-Aldrich.

Cell culture

Primary rat aortic smooth muscle cells (RASMCs) were obtained from Cell Applications, Inc (San Diego, CA, USA) and maintained in growth media at 37 °C in a humidified atmosphere containing 95% air and 5% CO_2. Cells were used from passage 2 through passage 5. A VSMC line (A10) from the embryonic rat thoracic aorta was obtained from the American Type Culture Collection (Manassas, VA, USA). The cells were grown in DMEM nutrient mixture containing 10% FCS, 2 mmol/L *L*-glutamine, 0.1 mmol/L NEAA, 1 mmol/L sodium pyruvate, 50 U/mL penicillin G, and 100 μg/mL streptomycin in a humidified 37 °C incubator with 5% CO_2. Cells were used between passages 18 and 30 for all experiments. After reaching confluence, cells were seeded onto 6-cm dishes for cell transfection and immunoblotting and onto 12-well plates for cell transfection and luciferase assays.

Western blot analysis

Western blot analyses were performed as described previously[16]. In brief, A10 cells were cultured in 6-cm dishes. After reaching confluence, cells were treated with the vehicle and thrombin or pretreated with specific inhibitors as indicated followed by thrombin. Whole-cell lysates (50 μg) were subjected to SDS-PAGE and transferred onto a polyvinylidene difluoride membrane that was then incubated in TBST buffer (150 mmol/L NaCl, 20 mmol/L Tris-HCl, and 0.02% Tween 20; pH 7.4) containing 5% BSA. Proteins were visualized using specific primary Abs and then incubated with HRP-conjugated secondary Abs. The immunoreactivity was detected using the enhanced chemiluminescence (ECL) system according to the manufacturer's instructions. Quantitative data were obtained using a computing densitometer with scientific imaging systems (Kodak, Rochester, NY, USA).

Transfection and CTGF-luciferase assays

A10 cells (5×10^4 cells/well) were seeded onto 12-well plates, and were transfected the following day using Lipofectamine Plus with 0.5 μg of CTGF-luciferase plasmid, 0.8 μg of AP-1-luciferase plasmid, 1 μg of JNK1DN, or 1 μg of JNK2DN. Cells were also cotransfected with 0.2 μg of *LacZ*. After 6 h, the medium was aspirated and replaced with basal medium devoid of FCS overnight, and cells were stimulated with thrombin for another 16 h before being harvested. To assess the effects of the indicated inhibitors, drugs were added to cells 30 min before thrombin addition. Luciferase activity was determined and normalized on the basis of *LacZ* expression. The level of induction of luciferase activity was computed as the ratio of cells with and without stimulation.

Statistical analysis

Continuous variables are presented as the mean±SEM. Intergroup differences were analyzed by 1-way ANOVA for comparisons among 3 or more groups and the independent Student's *t*-test for comparisons between 2 groups. A probability value < 0.05 was regarded as significant.

Results

Thrombin induces CTGF expression

Incubation of the RASMC with thrombin (0.3–3 U/mL) for 4 h induced CTGF protein expression in a concentration-dependent manner, with maximum effects after 1 U/mL thrombin treatment (Figure 1A). The thrombin (1 U/mL)-induced increases in CTGF expression were time-dependent

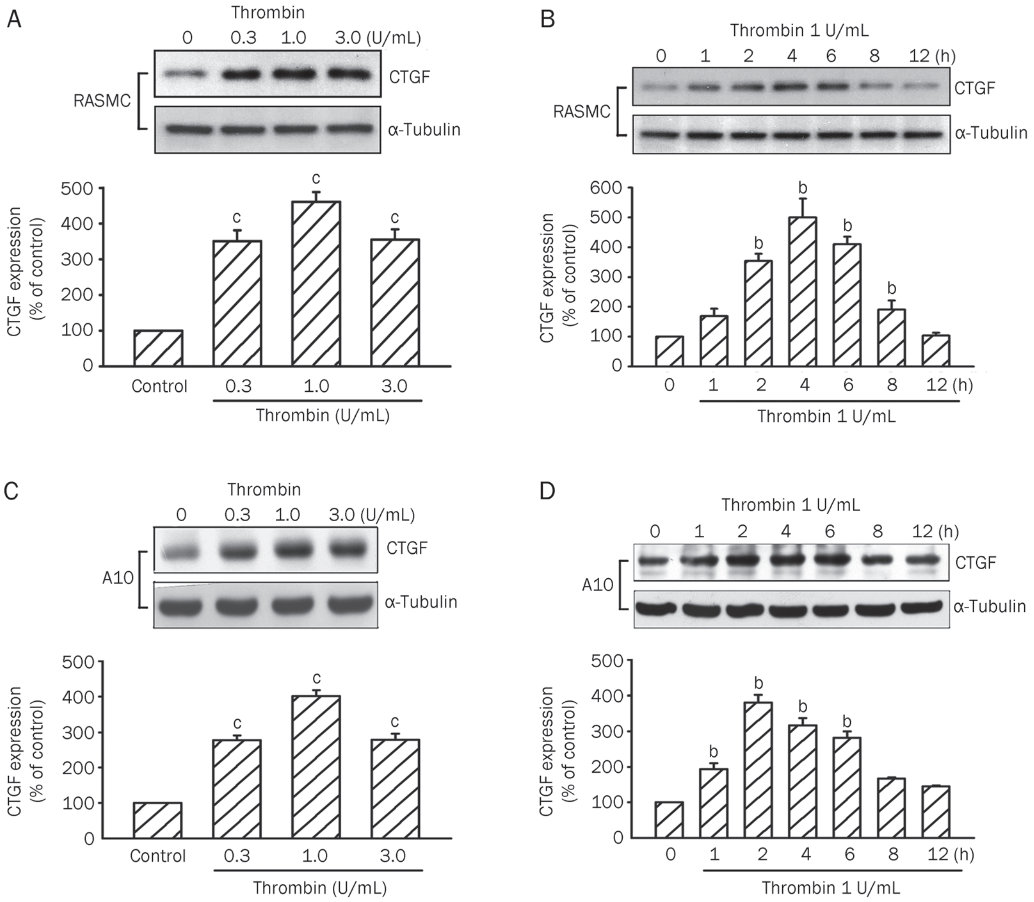

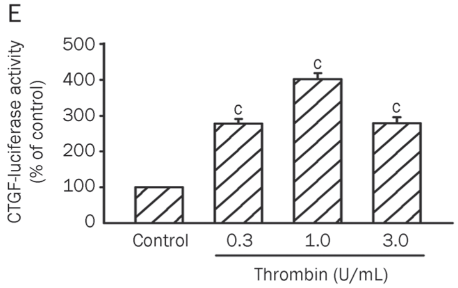

Figure 1. Thrombin-induced increases in CTGF expression and CTGF-luciferase activity in primary RASMCs and A10 cells. RASMCs were incubated with various concentrations of thrombin for 4 h (A) or with 1 U/mL thrombin for the indicated time intervals (B). A10 cells were incubated with various concentrations of thrombin for 2 h (C) or with 1 U/mL thrombin for the indicated time intervals (D). Cells were lysed and then immunoblotted with Abs specific for CTGF or α-tubulin. Data are presented as mean±SEM. *n*=3. [b]*P*<0.05, [c]*P*<0.01 *vs* basal level. (E) A10 cells were transiently transfected with 0.5 μg of CTGF-luciferase plasmid and 0.2 μg of *LacZ* for 6 h and then stimulated with 0.3–3 U/mL thrombin for 16 h. Cells were harvested for the luciferase activity assay. Data are presented as mean±SEM. *n*=3. [c]*P*<0.01 *vs* untreated cells.

with a maximal effect at 4 h (Figure 1B). Incubation of the A10 cell line, a rat VSMC cell line, with thrombin (0.3–3 U/mL) for 2 h also induced CTGF protein expression in a concentration-dependent manner, with maximum effects after 1 U/mL thrombin treatment (Figure 1C). The thrombin (1 U/mL)-induced increases in CTGF expression were time-dependent (Figure 1D). The induction of CTGF protein began by 1 h after treatment, reached a maximum at 2 h, and then gradually diminished to 8 h after thrombin treatment (Figure 1D). Thrombin-induced CTGF expression obtained from A10 cells was similar to that of the primary RASMC response. Therefore, we used A10 cells in further studies. A10 cells were transiently transfected with a CTGF-luciferase plasmid. As shown in Figure 1E, A10 cells treated with thrombin (0.3–3 U/mL) for 16 h exhibited a 302%±19% (*n*=3) increase in CTGF-luciferase activity. In the following experiments, A10 cells were treated with 1 U/mL thrombin for 2 h. A10 cells were pretreated with either ActD (a transcriptional inhibitor) or CHX (a translational inhibitor) and then treated with 1 U/mL thrombin. As a result, thrombin-induced elevation of CTGF expression was almost completely inhibited by ActD (1, 3, and 10 μmol/L) and CHX (1, 3, and 10 μmol/L) (*n*=3 in each group) (Figures 2A and 2B). These results suggest that the increase in CTGF protein level in A10 cells responsive to thrombin was dependent on *de novo* transcription and translation.

Involvement of PAR-1 in thrombin-induced CTGF expression

To identify the PARs involved in thrombin-induced CTGF expression, the PAR-1 antagonist SCH79797 and PAR-4 antagonist tcY-NH_2 were tested. As shown in Figure 3A, pretreating A10 cells with SCH79797 (0.1 μmol/L) inhibited thrombin-induced CTGF expression by 83%±22%, while tcY-NH_2 (30

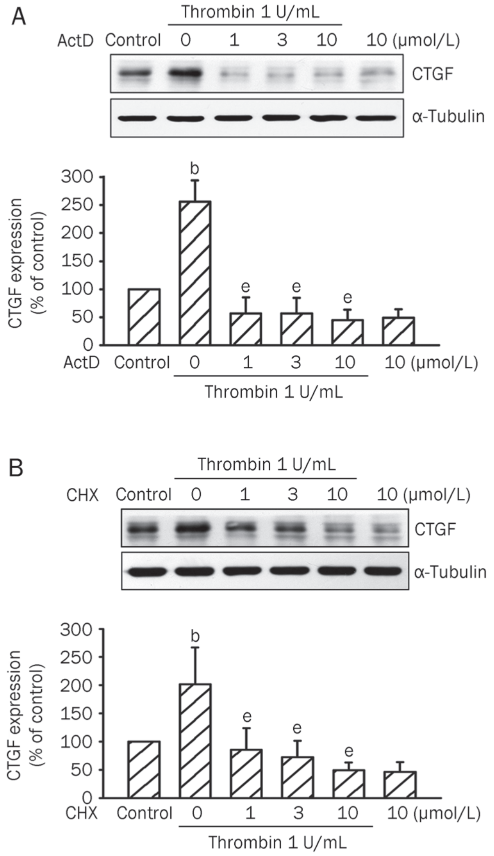

Figure 2. Effects of ActD and CHX on CTGF expression induced by thrombin. A10 cells were pretreated for 30 min with ActD (1–10 μmol/L) (A) or CHX (1–10 μmol/L) (B) and then stimulated with 1 U/mL thrombin for another 2 h. Cell lysates were prepared and then immunoblotted with Abs specific for CTGF or α-tubulin. Data are presented as mean±SEM. *n*=3. $^{b}P<0.05$ *vs* control. $^{e}P<0.05$ *vs* the thrombin treatment group.

μmol/L) had no effect (*n*=3; Figure 3B). Moreover, treatment of A10 cells with the PAR-1 agonist peptide SFLLRN-NH_2 (300 μmol/L) also resulted in a 391%±117% (*n*=3) increase in CTGF expression, whereas the PAR-4 agonist peptide GYPGQV-NH_2 (300 μmol/L) had no effect (*n*=3; Figure 3C). These results suggest that thrombin-mediated CTGF expression in A10 cells may occur via activation of PAR-1, but not PAR-4, signaling.

JNK is involved in thrombin-induced CTGF expression

We next attempted to determine whether JNK signaling events are involved in thrombin-induced CTGF expression by using SP600125, a specific inhibitor of JNK[17]. As shown in Figure 4A, thrombin-induced CTGF expression was concentration-dependently attenuated by pretreating A10 cells with SP600125 (3–30 μmol/L). Pretreating A10 cells with 30 μmol/L SP600125 completely inhibited thrombin-induced CTGF expression (*n*=3). We then examined whether thrombin could activate JNK. Treating A10 cells with 1 U/mL thrombin resulted in a time-dependent phosphorylation of JNK. The phosphorylation of JNK was maximal at 3–5 min and returned to basal level after 30 min of thrombin treatment (Figure 4B).

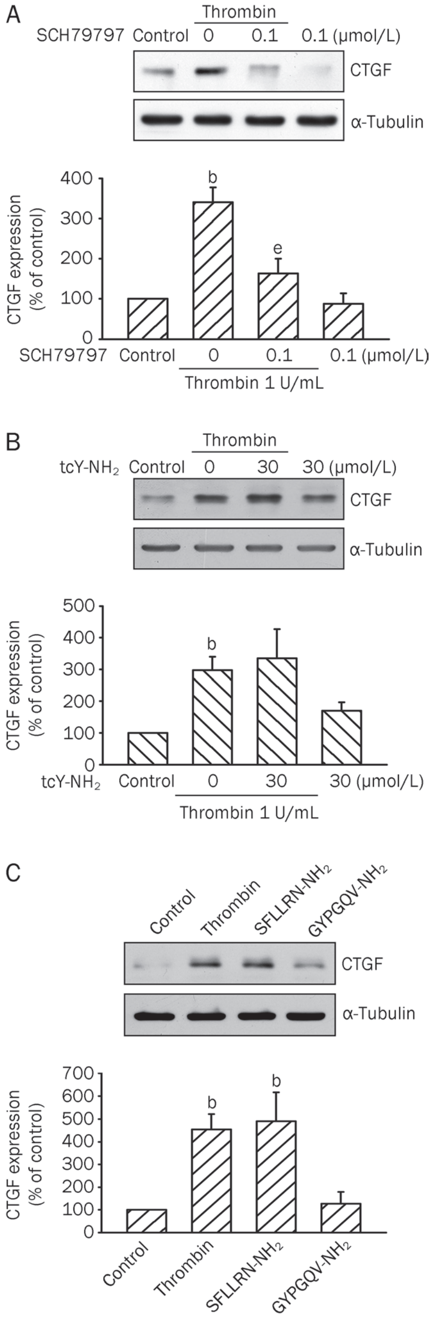

Figure 3. Involvement of PAR-1 in thrombin-induced CTGF expression in A10 cells. Cells were pretreated with 0.1 μmol/L SCH79797 (A) or 30 μmol/L tcY-NH_2 (B) for 30 min and then stimulated with 1 U/mL thrombin for another 2 h. Cell lysates were prepared and then immunoblotted with Abs specific for CTGF or α-tubulin. Data are presented as mean±SEM. *n*=3. $^{b}P<0.05$ *vs* control; $^{e}P<0.05$ *vs* the thrombin treatment group. (C) Cells were incubated with 1 U/mL thrombin, 300 μmol/L SFLLRN-NH_2 (a PAR-1 agonist), or 300 μmol/L GYPGQV-NH_2 (a PAR-4 agonist) for 2 h. Cells were lysed and then immunoblotted with Abs specific for CTGF or α-tubulin. Data are presented as mean±SEM. *n*=3. $^{b}P<0.05$ *vs* control.

To further confirm that JNK mediates thrombin-induced CTGF expression JNK1DN and JNK2DN were used. As shown in Figure 4C, transfection of A10 cells with 1 μg of JNK1DN and

JNK2DN, respectively, inhibited thrombin-induced CTGF expression by 86%±21% and 90%±25% (*n*=3).

AP-1 mediates thrombin-induced CTGF expression

Next, we explored the role of AP-1 in thrombin-induced CTGF expression by using the AP-1 inhibitor curcumin[18]. As shown in Figure 5A, thrombin-induced CTGF expression was mark-

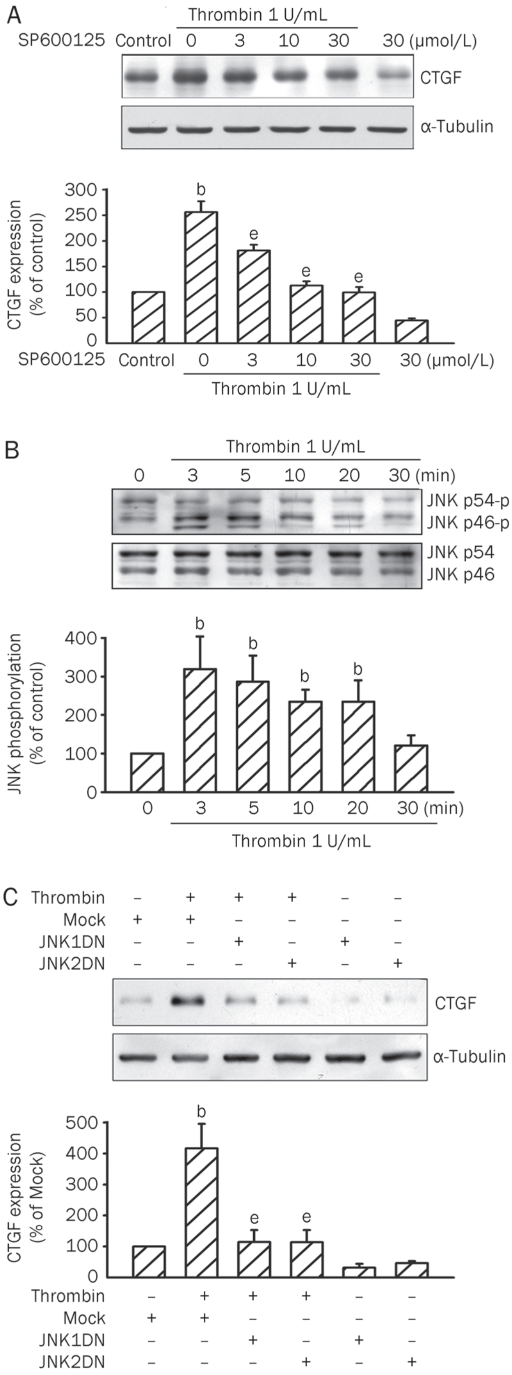

Figure 4. JNK is involved in thrombin-induced CTGF expression in A10 cells. (A) Cells were pretreated with various concentrations (3–30 μmol/L) of SP600125 for 30 min and then stimulated with 1 U/mL thrombin for another 2 h. Cells were lysed and then immunoblotted with Abs specific for CTGF or α-tubulin. Data are presented as mean±SEM. *n*=3. $^{b}P<0.05$ *vs* control. $^{e}P<0.05$ *vs* the thrombin treatment group. (B) Cells were treated with 1 U/mL thrombin for different time intervals. Cell lysates were prepared and then immunoblotted with Abs specific for phospho-JNK or JNK. Data are presented as mean±SEM. *n*=3. $^{b}P<0.05$ *vs* basal level. (C) Cells were transiently transfected with 1 μg of JNK1DN or JNK2DN for 6 h and then stimulated with 1 U/mL thrombin for another 2 h. Cells were lysed and then immunoblotted with Abs specific for CTGF or α-tubulin. Data are presented as mean±SEM. *n*=3. $^{b}P<0.05$ *vs* the mock group; $^{e}P<0.05$ *vs* the thrombin treatment group.

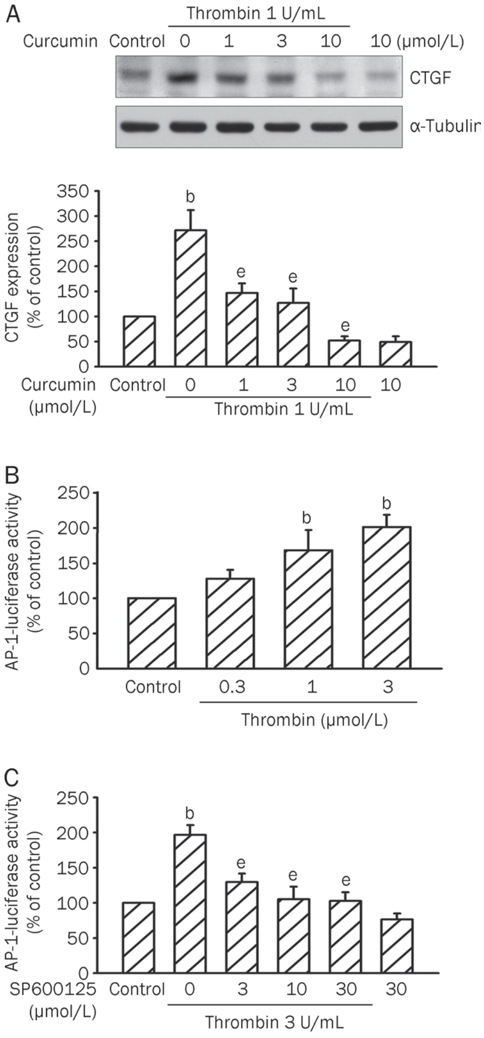

Figure 5. Involvement of AP-1 in thrombin-induced CTGF expression in A10 cells. (A) Cells were pretreated with various concentrations (1–10 μmol/L) of curcumin for 30 min and then stimulated with 1 U/mL thrombin for another 2 h. Cells were lysed and then immunoblotted with Abs specific for CTGF or α-tubulin. Data are presented as mean±SEM. *n*=3. $^{b}P<0.05$ *vs* control; $^{e}P<0.05$ *vs* the thrombin treatment group. (B) Cells were transiently transfected with 0.8 μg of AP-1-luciferase plasmid and 0.2 μg of *LacZ* for 4 h and then stimulated with 0.3–3 U/mL thrombin for 16 h. Cells were harvested for the luciferase activity assay. Data are presented as mean±SEM. *n*=3. $^{b}P<0.05$ *vs* control. (C) Cells were transiently transfected with 0.8 μg of AP-1-luciferase plasmid and 0.2 μg of *LacZ* for 4 h and then were pretreated with various concentrations (3–30 μmol/L) of SP600125 for 30 min. The cells were then stimulated with 3 U/mL thrombin for 16 h. Cells were harvested for the luciferase activity assay. Data are presented as mean±SEM. *n*=3. $^{b}P<0.05$ *vs* control. $^{e}P<0.05$ *vs* the thrombin treatment group.

edly attenuated by pretreating A10 cells with curcumin (1–10 μmol/L) in a concentration-dependent manner. Curcumin at 10 μmol/L completely suppressed thrombin-induced CTGF expression (*n*=3). To further confirm that AP-1 is involved in thrombin-induced CTGF expression, transient transfection was performed using the AP-1-luciferase reporter plasmids. Exposure to thrombin (0.3–3 U/mL) led to a concentration-dependent increase in AP-1-luciferase activity in A10 cells. There was a 101%±23% increase in AP-1-luciferase activity after treatment with 3 U/mL thrombin for 16 h (Figure 5B). To further confirm that thrombin-induced AP-1-luciferase activity occurs via JNK pathways, we used the JNK inhibitor. As shown in Figure 5C, pretreating A10 cells with SP600125 (3–30 μmol/L) exhibited decreases in thrombin-induced AP-1-luciferase activity (*n*=3 in each group).

Discussion

In this study, we found for the first time that in VSMCs thrombin acts on PAR-1 to activate the JNK signaling pathway, which in turn initiates AP-1 activation and ultimately induces CTGF expression. Thrombin is a serine protease that is generated by cleavage of its inactive precursor prothrombin. Thrombin converts the monomer fibrinogen to insoluble fibrin, in addition to activating other clotting factors V, VIII, and XIII, thus facilitating thrombus formation[19]. However, more than 95% of thrombus-associated thrombin is formed after clotting is complete and is continuously released by mural thrombi[20]. Endothelial injury allows thrombin to have direct contact with the subendothelial VSMCs. Tissue factor presented by VSMCs can further trigger the formation of thrombin[21]. Therefore, subendothelial VSMCs may be exposed to high levels of thrombin continuously. Subsequently, activation of PAR-1 in VSMCs by thrombin causes the activation of several pathways, including calcium signaling, proliferation, cytoskeletal rearrangement, contraction, and extracellular matrix synthesis[4, 22].

CTGF gene is highly conserved among species[7]. The CTGF primary translational product is more than 90% conserved in mammals[23]. The expression patterns of CTGF in RASMC and A10 cells were similar to that in human lung fibroblasts in our previous study[15]. The similar expression pattern of CTGF was also found in human umbilical vein smooth muscle cells[12] and in human aortic smooth muscle cells[24]. Because the expression pattern was similar in rat and human VSMCs, we used A10 cells in this study that focused on the signaling pathways involving CTGF expression. CTGF has been suggested to play an important role in the development and progression of atherosclerosis through its paracrine effects[25]. CTGF is a mitogenic and chemotactic factor for VSMCs and stimulates extracellular matrix production[26]. CTGF also stimulates the expression of matrix metalloproteinase (MMP)-2[27]. It is possible that CTGF overexpressed in advanced atherosclerotic plaques may contribute to plaque destabilization[25]. Atherosclerotic plaques are composed of a lipid-rich core, a cap of fibrous tissue, VSMCs, connective tissue extracellular matrix, and inflammatory cells. Plaque disruption may result in mural thrombi. Such thrombi may be the main contributor of progression of atherosclerosis[28]. In our present study, we found that thrombin could induce CTGF expression in VSMCs. This suggested that CTGF might play a role in the pathogenesis of atherothrombosis.

PARs play crucial roles in coagulation and vascular homeostasis[29]. Overexpression of PAR-1 has been found in the VSMCs from thickening intimas of human atherosclerotic arteries[30]. Although subtypes of thrombin-responsive PARs, PAR-1, PAR-3, and PAR-4, are present and functionally active in VSMCs, PAR-1 has the highest affinity for thrombin[31]. PAR-1 is the prototypic thrombin receptor and the main isoform involved in VSMC neointimal formation and restenosis *in vivo*[32], whereas PAR-3 appears to function as a cofactor for PAR-4[33]. In this study, we found that a PAR-1 antagonist (SCH79797) significantly inhibited thrombin-induced CTGF expression, while a PAR-4 antagonist (tcY-NH_2) had no effect. We also demonstrated that a PAR-1 agonist (SFLLRN-NH_2) induced CTGF expression, while a PAR-4 agonist (GYPGQV-NH_2) had no effect. These results suggest that PAR-1, but not PAR-4, is responsible for thrombin-induced CTGF expression in A10 cells.

MAPKs, composed of ERK, JNK, and p38 MAPK, are serine/threonine kinases that play a critical role in cell differentiation, growth, apoptosis, and the regulation of various transcription factors and gene expression[34]. MAPKs are significantly activated in vascular tissues by hypertension, angiotensin II, or balloon injury[35]. MAPK also participate in platelet-derived growth factor-induced vascular proliferation, migration, and gene expression[36]. The JNK cascade plays an important role in a variety of physiological and pathological processes such as cell apoptosis, the inflammatory response, and cytokine production[37]. Activation of JNK family activity is suggested to be involved in atherosclerosis. JNK activation was shown using atherosclerosis prone ApoE knockout mice and a high cholesterol diet[38]. JNK2 knockout mice were protected from the development of abdominal aortic aneurysm through a reduction in tissue breakdown and enhanced tissue repair[39]. In this study, we found that thrombin-induced CTGF expression was concentration-dependently attenuated by a JNK inhibitor (SP600125). Furthermore, thrombin caused a time-dependent phosphorylation of JNK. These results suggest that JNK is involved in thrombin-induced CTGF expression in VSMCs. This was further confirmed by transfection of A10 cells with JNK1DN and JNK2DN, which inhibited thrombin-induced CTGF expression. In addition, specific knockdown of JNK expression by using RNA interference would be also an appropriate method to study JNK signaling. A limitation of this study was that we did not perform RNA interference studies.

The promoter region of the human CTGF gene contains multiple transcription factor-binding sites, including those for AP-1, STAT, SMAD, BCE-1, NF-κB, Sp1, and Elk-1[13]. AP-1 is one of the main transcription factors activated by MAPK, and it plays a central role in a variety of cellular responses[40]. In our previous report, we found that thrombin-induced CTGF expression required the JNK and AP-1 pathway in human lung fibroblasts[15]. In the present study, we demonstrated that AP-1 is involved in thrombin-induced CTGF expression in VSMCs by using an AP-1 inhibitor and the luciferase activity. We also demonstrated that thrombin-induced increase in AP-1-luciferase activity was inhibited by a JNK inhibitor. These results suggest that thrombin-induced AP-1 activation occurs via the JNK pathway. Nevertheless, one of the limitations of our study was that we did not directly assess the binding of AP-1 to CTGF promoter by using chromatin immunoprecipitation or electrophoretic mobility shift assay. In addition to this important JNK/AP-1 pathway, thrombin may act upon VSMCs through several other signaling pathways. Thrombin enhanced VSMC proliferation through epidermal growth factor receptor, ERK, and AP-1 pathways[41]. Thrombin also stimulated VSMC migration through an ROS-sensitive p38 MAPK pathway[42].

Much evidence suggests that thrombin acts as a powerful modulator in the progression of atherosclerosis[43]. Overexpression of CTGF has been found in atherosclerotic carotid arteries and in the aortic wall from patient with thoracic aortic dissection[8, 44]. Based on the result of this study, together with evidence from clinical specimens, it might suggest that CTGF is one of the mediators in the progression of atherosclerosis[44]. There are many new and emerging antithrombotic agents including PAR-1 antagonists, thrombin inhibitors, *etc*[45, 46]. The direct thrombin inhibitor, dabigatran, could prevent thrombin-induced cleavage of the extracellular N-terminal domain of PAR-1[47]. It may have clinical significance to study further the effects of the new antithrombotic agents on CTGF expression and atherosclerosis.

In conclusion, our results demonstrate for the first time that thrombin acts on PAR-1 to activate the JNK signaling pathway, which in turn initiates AP-1 activation and ultimately induces CTGF expression in VSMC. Our results provide a mechanism linking thrombin and the profibrotic protein CTGF and may provide an insight into the pathogenesis of atherothrombosis.

Acknowledgements

This study was supported by a grant (96CGH-TMU-03) from the Cathay General Hospital, Taipei, Taiwan, China.

Author contribution

Wen-chin KO, Chien-huang LIN, and Bing-chang CHEN designed the research; Wen-chin KO and Bing-chang CHEN performed the experiments; Ming-jen HSU and Chia-ti TSAI performed some of the experiments; Wen-chin KO analyzed the data and wrote the article; and Chuang-ye HONG and Chien-huang LIN revised the article.

References

1 Schrör K, Bretschneider E, Fischer K, Fischer JW, Pape R, Rauch BH, *et al.* Thrombin receptors in vascular smooth muscle cells — function and regulation by vasodilatory prostaglandins. Thromb Haemost 2010; 103: 884–90.
2 Steinhoff M, Buddenkotte J, Shpacovitch V, Rattenholl A, Moormann C, Vergnolle N, *et al.* Proteinase-activated receptors: transducers of proteinase-mediated signaling in inflammation and immune response. Endocr Rev 2005; 26: 1–43.
3 Martorell L, Martinez-Gonzalez J, Rodriguez C, Gentile M, Calvayrac O, Badimon L. Thrombin and protease-activated receptors (PARs) in atherothrombosis. Thromb Haemost 2008; 99: 305–15.
4 Dabbagh K, Laurent GJ, McAnulty RJ, Chambers RC. Thrombin stimulates smooth muscle cell procollagen synthesis and mRNA levels via a PAR-1 mediated mechanism. Thromb Haemost 1998; 79: 405–9.
5 Perbal B. CCN proteins: multifunctional signalling regulators. Lancet 2004; 363: 62–4.
6 Bradham DM, Igarashi A, Potter RL, Grotendorst GR. Connective tissue growth factor: a cysteine-rich mitogen secreted by human vascular endothelial cells is related to the SRC-induced immediate early gene product CEF-10. J Cell Biol 1991; 114: 1285–94.
7 Blom IE, Goldschmeding R, Leask A. Gene regulation of connective tissue growth factor: new targets for antifibrotic therapy? Matrix Biol 2002; 21: 473–82.
8 Cicha I, Yilmaz A, Klein M, Raithel D, Brigstock DR, Daniel WG, *et al.* Connective tissue growth factor is overexpressed in complicated atherosclerotic plaques and induces mononuclear cell chemotaxis *in vitro*. Arterioscler Thromb Vasc Biol 2005; 25: 1008–13.
9 Ruperez M, Lorenzo O, Blanco-Colio LM, Esteban V, Egido J, Ruiz-Ortega M. Connective tissue growth factor is a mediator of angiotensin II-induced fibrosis. Circulation 2003; 108: 1499–505.
10 Ruiz-Ortega M, Rodríguez-Vita J, Sanchez-Lopez E, Carvajal G, Egido J. TGF-β signaling in vascular fibrosis. Cardiovasc Res 2007; 74: 196–206.
11 Rodriguez-Vita J, Ruiz-Ortega M, Ruperez M, Esteban V, Sanchez-Lopez E, Plaza J, *et al.* Endothelin-1, via ETA receptor and independently of transforming growth factor-beta, increases the connective tissue growth factor in vascular smooth muscle cells. Circ Res 2005; 97: 125–34.
12 Liu X, Luo F, Li J, Wu W, Li L, Chen H. Homocysteine induces connective tissue growth factor expression in vascular smooth muscle cells. J Thromb Haemost 2008; 6: 184–92.
13 Blom IE, van Dijk AJ, de Weger RA, Tilanus MGJ, Goldschmeding R. Identification of human ccn2 (connective tissue growth factor) promoter polymorphisms. Mol Pathol 2001; 54: 192–6.
14 Grotendorst G, Okochi H, Hayashi N. A novel transforming growth factor beta response element controls the expression of the connective tissue growth factor gene. Cell Growth Differ 1996; 7: 469–80.
15 Yu CC, Hsu MJ, Kuo ML, Chen RF, Chen MC, Bai KJ, *et al.* Thrombin-induced connective tissue growth factor expression in human lung fibroblasts requires the ASK1/JNK/AP-1 pathway. J Immunol 2009; 182: 7916–27.
16 Chen BC, Chang YS, Kang JC, Hsu MJ, Sheu JR, Chen TL, *et al.* Peptidoglycan induces nuclear factor-κB activation and cyclooxygenase-2 expression via Ras, Raf-1, and ERK in RAW 264.7 macrophages. J Biol Chem 2004; 279: 20889–97.
17 Bennett BL, Sasaki DT, Murray BW, O'Leary EC, Sakata ST, Xu W, *et al.* SP600125, an anthrapyrazolone inhibitor of Jun N-terminal kinase. Proc Natl Acad Sci U S A 2001; 98: 13681–6.
18 Temkin V, Kantor B, Weg V, Hartman M-L, Levi-Schaffer F. Tryptase activates the mitogen-activated protein kinase/activator protein-1 pathway in human peripheral blood eosinophils, causing cytokine production and release. J Immunol 2002; 169: 2662–9.
19 Coughlin SR. Thrombin signalling and protease-activated receptors. Nature 2000; 407: 258–64.
20 Brummel KE, Paradis SG, Butenas S, Mann KG. Thrombin functions

during tissue factor-induced blood coagulation. Blood 2002; 100: 148–52.

21 Bretschneider E, Braun M, Fischer A, Wittpoth M, Glusa E, Schror K. Factor Xa acts as a PDGF-independent mitogen in human vascular smooth muscle cells. Thromb Haemost 2000; 84: 499–505.

22 Damiano BP, Derian CK, Maryanoff BE, Zhang HC, Gordon PA. RWJ-58259: a selective antagonist of protease activated receptor-1. Cardiovasc Drug Rev 2003; 21: 313–26.

23 Brigstock DR. The connective tissue growth factor/cysteine-rich 61/nephroblastoma overexpressed (CCN) family. Endocr Rev 1999; 20: 189–206.

24 Kang SW, Kim JL, Kwon GT, Lee YJ, Park JH, Lim SS*, et al.* Sensitive fern (*Onoclea sensibilis*) extract suppresses proliferation and migration of vascular smooth muscle cells inflamed by neighboring macrophages. Biol Pharm Bull 2011; 34: 1717–23.

25 Game BA, He L, Jarido V, Nareika A, Jaffa AA, Lopes-Virella MF*, et al.* Pioglitazone inhibits connective tissue growth factor expression in advanced atherosclerotic plaques in low-density lipoprotein receptor-deficient mice. Atherosclerosis 2007; 192: 85–91.

26 Moussad EE-DA, Brigstock DR. Connective tissue growth factor: what's in a name? Mol Genet Metab 2000; 71: 276–92.

27 Fan WH, Karnovsky MJ. Increased MMP-2 expression in connective tissue growth factor over-expression vascular smooth muscle cells. J Biol Chem 2002; 277: 9800–5.

28 Corti R, Hutter R, Badimon JJ, Fuster V. Evolving concepts in the triad of atherosclerosis, inflammation and thrombosis. J Thromb Thrombolysis 2004; 17: 35–44.

29 Leger AJ, Covic L, Kuliopulos A. Protease-activated receptors in cardiovascular diseases. Circulation 2006; 114: 1070–7.

30 Ku DD, Dai J. Expression of thrombin receptors in human atherosclerotic coronary arteries leads to an exaggerated vasoconstrictory response *in vitro*. J Cardiovasc Pharmacol 1997; 30: 649–57.

31 Steinberg SF. The cardiovascular actions of protease–activated receptors. Mol Pharmacol 2005; 67: 2–11.

32 Andrade-Gordon P, Derian CK, Maryanoff BE, Zhang H-C, Addo MF, Cheung W-m*, et al.* Administration of a potent antagonist of protease-activated receptor-1 (PAR-1) attenuates vascular restenosis following balloon angioplasty in rats. J Pharmacol Exp Ther 2001; 298: 34–42.

33 Nakanishi-Matsui M, Zheng YW, Sulciner DJ, Weiss EJ, Ludeman MJ, Coughlin SR. PAR3 is a cofactor for PAR4 activation by thrombin. Nature 2000; 404: 609–13.

34 Kyriakis JM, Avruch J. Mammalian mitogen-activated protein kinase signal transduction pathways activated by stress and inflammation. Physiol Rev 2001; 81: 807–69.

35 Kim S, Iwao H. Stress and vascular responses: mitogen-activated protein kinases and activator protein-1 as promising therapeutic targets of vascular remodeling. J Pharmacol Sci 2003; 91: 177–81.

36 Zhan Y, Kim S, Izumi Y, Izumiya Y, Nakao T, Miyazaki H*, et al.* Role of JNK, p38, and ERK in platelet–derived growth factor-induced vascular proliferation, migration, and gene expression. Arterioscler Thromb Vasc Biol 2003; 23: 795–801.

37 Ip YT, Davis RJ. Signal transduction by the c-Jun N-terminal kinase (JNK) from inflammation to development. Curr Opin Cell Biol 1998; 10: 205–19.

38 Ricci R, Sumara G, Sumara I, Rozenberg I, Kurrer M, Akhmedov A*, et al.* Requirement of JNK2 for scavenger receptor A-mediated foam cell formation in atherogenesis. Science 2004; 306: 1558–61.

39 Yoshimura K, Aoki H, Ikeda Y, Fujii K, Akiyama N, Furutani A*, et al.* Regression of abdominal aortic aneurysm by inhibition of c-Jun N-terminal kinase. Nat Med 2005; 11: 1330–8.

40 Shaulian E, Karin M. AP–1 in cell proliferation and survival. Oncogene 2001; 20: 2390–400.

41 Hsieh HL, Tung WH, Wu CY, Wang HH, Lin CC, Wang TS*, et al.* Thrombin induces EGF receptor expression and cell proliferation via a PKC(δ)/c-Src-dependent pathway in vascular smooth muscle cells. Arterioscler Thromb Vasc Biol 2009; 29: 1594–601.

42 Wang Z, Castresana MR, Newman WH. Reactive oxygen species-sensitive p38 MAPK controls thrombin-induced migration of vascular smooth muscle cells. J Mol Cell Cardiol 2004; 36: 49–56.

43 Borissoff JI, Spronk HMH, Heeneman S, ten Cate H. Is thrombin a key player in the 'coagulation-atherogenesis' maze? Cardiovasc Res 2009; 82: 392–403.

44 Wang X, LeMaire SA, Chen L, Shen YH, Gan Y, Bartsch H*, et al.* Increased collagen deposition and elevated expression of connective tissue growth factor in human thoracic aortic dissection. Circulation 2006; 114: I200–5.

45 Meyer Michel S. The mechanism of action of rivaroxaban — an oral, direct Factor Xa inhibitor — compared with other anticoagulants. Thromb Res 2011; 127: 497–504.

46 Leonardi S, Tricoci P, Becker RC. Thrombin receptor antagonists for the treatment of atherothrombosis: therapeutic potential of vorapaxar and E-5555. Drugs 2010; 70: 1771–83.

47 Bogatkevich GS, Ludwicka-Bradley A, Silver RM. Dabigatran, a direct thrombin inhibitor, demonstrates antifibrotic effects on lung fibroblasts. Arthritis Rheum 2009; 60: 3455–64.

Acta Pharmacologica Sinica (2012) 33: 57–65
© 2012 CPS and SIMM All rights reserved 1671-4083/12 $32.00
www.nature.com/aps

Original Article

Human vascular endothelial cells reduce sphingosylphosphorylcholine-induced smooth muscle cell contraction in co-culture system through integrin β4 and Fyn

Di GE[1], Ning MENG[1], Le SU[1, 2], Yun ZHANG[2], Shang-li ZHANG[1, 2], Jun-ying MIAO[1, 2], Jing ZHAO[1, 2, *]

[1]Institute of Developmental Biology, School of Life Science, Shandong University, Ji-nan 250100, China; [2]Key Laboratory of Cardiovascular Remodeling and Function Research, Chinese Ministry of Education and Chinese Ministry of Health, Shandong University Qilu Hospital, Ji-nan 250100, China

Aim: In vascular strips, the adjacent endothelial cells modulate the contraction of vascular smooth muscle cells (VSMCs) induced by sphingosylphosphorylcholine (SPC) through nitric oxide (NO). The aim of this study was to elucidate the mechanisms by which vascular endothelial cells (VECs) reduce the SPC-induced contraction of VSMCs in a co-culture system.
Methods: Human umbilical VECs and VSMCs were co-cultured. The VECs were transfected with integrin β4- or Fyn-specific siRNA. The areas of VSMCs that are involved in cell contractility were quantified using the Leica confocal software and collagen contractility assay. The production of NO in VECs was measured in the cell supernatants using NO Detection Kit. The levels of integrin β4 and Fyn in VECs and the levels of Rho kinase (ROCK) in VSMC were detected using immunofluorescence assays or Western blots.
Results: Co-culture with VECs reduced the contraction of VSMCs induced by SPC (30 μmol/L). The down-regulation of integrin β4 or Fyn in VECs by the specific siRNA (20 nmol/L) was able to counteract the effects of VECs on the SPC-induced VSMC contractions. Furthermore, the integrin β4-specific siRNA (20 and 40 nmol/L) significantly reduced the level of Fyn protein and the production of NO in VECs, while increased the level of ROCK in VSMCs that had been stimulated by SPC.
Conclusion: The VECs reduced the SPC-induced contraction of VSMCs in the co-culture system through integrin β4 and Fyn proteins. In this process, NO may be the factor downstream of integrin β4 in VECs, while ROCK may be the key protein regulating the contraction of VSMCs.

Keywords: human umbilical vein; vascular endothelial cells; vascular smooth muscle cells; integrin β4; Fyn; contraction; sphingosylphosphorylcholine

Acta Pharmacologica Sinica (2012) 33: 57–65; doi: 10.1038/aps.2011.142;

Introduction

Vasoconstriction that is caused by the tonic contraction of vascular smooth muscle cells in large arteries may invoke vasospasms, which are not only peculiar occurrences that are limited to arcane forms of angina, acute myocardial infarction and sudden cardiac death but also acute events that promote thrombosis, atherosclerotic plaque ruptures and mural plaque hemorrhages[1–4]. It has been reported that the Ca^{2+} sensitization of contractile proteins is the principal event that induces vasospasms[5]. Therefore, research on the Ca^{2+} sensitization-induced contraction of vascular smooth muscle cells (VSMCs) could greatly contribute to understanding the mechanism underlying vasospasms.

The lysosphingolipid sphingosylphosphorylcholine (SPC) is an important cardiovascular mediator that is derived from sphingomyelin. It mainly associates with high-density lipoproteins (HDLs) in plasma and has atheroprotective effects via its actions on endothelial cells *in vivo*. However, when endothelial cells are damaged, SPC may target VSMCs and contribute to cardiovascular disease[6]. Recently, high concentrations of SPC (30 μmol/L) have been reported to be novel messengers for the Rho kinase-mediated Ca^{2+} sensitization of VSMC contraction *in vitro*, and thus SPC has been used as a tool to research Ca^{2+} sensitization-induced vasospasms[7]. It is now clear that SPC may increase nitric oxide production in VECs and subsequently reduce the contraction of smooth

---

* To whom correspondence should be addressed.
E-mail jingzhao@sdu.edu.cn
Received 2011-02-28 Accepted 2011-09-19

muscle cells in the intact vascular strips[8], which may be the main mechanism for the cardiovascular protection that is provided by SPC via its actions on endothelial cells *in vivo*. However, the identities of the upstream mediators of the known pathway that are involved in the reduction of SPC-induced vasospasms by endothelial cells have only been speculated.

Integrin β4, which possesses an exceptionally large cytoplasmic domain, plays a crucial role in hemidesmosome assembly by binding to extracellular matrix (ECM) proteins in the basement membrane zones of epithelial tissues[9]. Our recent research has shown that this membrane protein plays an important role in the regulation of vascular endothelial cell functions, such as apoptosis, differentiation and senescence[10–12]. Furthermore, in our previous research, integrin β4 was associated with NO production[12]. Therefore, in this study, we attempted to elucidate whether and how the integrin β4 in VECs is involved in the VEC-modulated VSMC contraction induced by SPC.

Fyn is a member of the Src family of protein tyrosine kinases that is widely expressed in various types of cells and has greater functional redundancy compared to most of the other SrcPTK members[13, 14]. Recent reports have indicated that the co-culturing of endothelial and smooth muscle cells affects the gene expression of angiogenic factors in VECs[15], suggesting the important roles of angiogenic factors in endothelial/smooth muscle interactions. In addition, Fyn is an important factor in endothelial cell capillary morphogenesis[16]. However, the possible involvement of the VEC-derived Fyn in the contraction of VSMCs is not yet clear.

Here, we report that VECs reduce the SPC-induced contraction of VSMCs in the co-culture system of VECs and VSMCs. The VECs perform this function through the integrin β4 and Fyn proteins. Moreover, NO and Fyn may be the factors downstream of integrin β4 in the reduction of SPC-induced VSMC contraction that is caused by the VECs, and ROCK in the VSMCs may be the key protein that regulates VSMC contraction.

Materials and methods

Materials

M199 medium and fetal bovine serum (FBS) were purchased from Hyclone Lab Inc, USA. Fibroblast growth factor (FGF) was purchased from EssexBio Group, China. SPC was obtained from Sigma Co, USA and was dissolved in ethanol, and a concentration of 30 μmol/L was applied to the cells. This concentration was previously used for the promotion of the contraction of arteries and rat VSMCs *in vitro*[7, 17, 18]. The primary antibodies (mouse anti-human integrin β4 or Fyn and rabbit anti-human ROCK), secondary antibodies (goat anti-mouse TR antibody and goat anti-rabbit FITC antibody) and the specific small interfering RNA (siRNA) oligonucleotides of human integrin β4 (SC-35678) were all purchased from the Santa Cruz Co, USA. The human Fyn siRNA was synthesized by Qiagen, USA. The following primers were used: human Fyn sense RNAi, 5′-GAGUAUAUGAACAAAGGAA-3′ and human Fyn antisense RNAi, 5′-UUCCUUUGUUCAUAUACUC-3′. The RNAiFect™ Transfection Reagent, β-actin siRNA and rhodamine-labeled siRNA were all purchased from Qiagen, USA. All other reagents were ultrapure grade products from China.

Culturing of VSMCs

This investigation conformed to the Declaration of Helsinki. The VSMCs were cultured as previously described[19]. In brief, human umbilical veins were excised; the endothelium was stripped away; the media of the veins were cut into small pieces and placed into 35 mm culture plates that had been coated with lumens; and these pieces were grown in M199 medium with 10% fetal calf serum and 2 ng/mL FGF-2 at 37 °C in 5% CO_2 and 95% air. Every 72 h thereafter, the medium was replaced with fresh, complete M199. Cells appeared from explants within 2 weeks and grew to confluence in approximately 4 weeks. The identities of the cultured cells as smooth muscle cells were confirmed by the "hill and valley" patterns of cell growth and by positive staining for smooth muscle α-actin (α-SMA). The experiments were performed on cells that had undergone 5–8 passages.

Culturing of HUVECs

Human umbilical vein endothelial cells (HUVECs) were obtained as previously described[20]. Cells were grown in M199 medium with 10% fetal calf serum and 2 ng/mL of FGF-2. The experiments were performed on cells that had undergone 10–20 passages.

Co-culturing of VECs and VSMCs

In the direct co-culture system, VECs were grown to confluence on the bottom of a 24-well plate, and then the VSMC suspension was adjusted to 1.7×10^4 cells/mL, 1 mL of which was placed on the confluent monolayer of endothelial cells. After the VECs and VSMCs were co-cultured for 24 h, the medium was replaced with basal M199 medium (without FBS or FGF-2). Then, the separate co-cultures were treated as follows: (a) cultured in M199 medium with FBS and FGF-2 (normal); (b) cultured in M199 medium with ethanol at 0.3% (*v*/*v*) (control) and no serum or FGF-2; and (c) cultured in basal M199 medium with SPC (30 μmol/L). The contractile changes of the cells were quantified using the Leica software, which analyzed the images at 1 h.

To observe the changes in VSMC morphology clearly, an additional micropore membrane co-culture system was also used[21]. Briefly, the VECs and VSMCs were seeded onto the upside of microporous filtering membranes in 48-well plates at a density of 8.5×10^3 cells/mL. Each membrane consisted of a mixed cellulose ester with a 0.45 μm micropore that was precoated with matrigel. After allowing 48 h for attachment, the membrane was placed with the VEC side down into a 48-well plate containing VSMCs. After the VECs and VSMCs were co-cultured for 24 h, the medium was replaced with basal M199 medium (without FBS or FGF-2). Then, the separate co-cultures were treated as follows: culturing in M199 medium with ethanol at 0.3% (*v*/*v*) (control) and culturing in basal M199 medium with SPC (30 μmol/L). The cell morphologies were observed using a phase contrast microscope (Nikon, Japan).

Immunofluorescence assay

The VSMCs were co-cultured with VECs in the micropore membrane insert well system for 24 h, and then an immunofluorescence assay was performed on the sub-confluent VECs and VSMCs to examine the expression of integrin β4 and Fyn in the VECs and ROCK in the VSMCs as previously described[10]. After the addition of the primary antibodies (mouse anti-human integrin β4, Fyn or α-SMA IgG and rabbit anti-human ROCK IgG) and appropriate secondary antibodies (goat anti-mouse-TR or goat anti-rabbit-FITC), the samples were evaluated by laser scanning confocal microscopy (LSCM) (Leica, Germany). We randomly selected the region of interest and then zoomed in on the same frames. The relative fluorescent intensity per cell was calculated as the total value of the sample in the zoom scan divided by the total number of cells (at least 200 cells) in the same scan. The mean areas of α-SMA-positive cells (smooth muscle cells) that showed contractility were quantified (at least 200 cells). The percent reduction in cell area (%)=(mean area of treated cells/mean area of normal cells)×100%.

RNA interference

RNA interference (RNAi) was performed as described previously[12]. Briefly, cells that were at approximately 60% confluence were transfected with scramble RNA (negative control) or siRNA against integrin β4 (10–40 nmol/L) or Fyn (60 nmol/L) using the RNAiFect Transfection Reagent according to the manufacturer's instructions. After 24 h, the medium was replaced with M199 medium supplemented with serum and FGF-2. Cells were cultured for another 24 h for the desired assays. Western blot analyses were conducted to estimate the effects of gene silencing.

Western blotting

The Western blots were performed as previously described[10]. Briefly, equal amounts of total proteins were loaded onto 7.5% SDS-polyacrylamide gels and electrophoretically transferred to nitrocellulose transfer membranes. After blocking with 5% skim milk in PBS and 0.5% (*v/v*) Tween 20 for 1 h, the membranes were incubated with monoclonal Fyn or the integrin β4 protein antibody (mouse anti-human) overnight at 4 °C and then incubated with HRP-linked secondary antibodies (goat anti-mouse) for 1 h at room temperature (RT), followed by color development with 0.06% DAB (diaminobenzidine) and 0.03% H_2O_2 in PBS for 3–5 min at RT. Distilled water was used to stop the reaction. The monoclonal anti-β-actin antibody (mouse anti-human) was used to ascertain that equal protein amounts were loaded. The relative quantities of the proteins were analyzed using the ImageTool software.

Cell contraction analysis

Collagen gels were prepared from rat tail type 1 collagen and seeded in 24-well culture dishes. Each well contained 400 μL collagen (final collagen concentration of 1.5 mg/mL), 100 μL neutralization solution and 1×10^5 VSMCs based on the technique that was described previously[22–24]. The VSMCs in the collagen gels were allowed to equilibrate overnight in M199 medium. The VECs grew to confluence on the bottom of the 24-well plates, and the collagen gel in which the VSMCs were embedded was placed on the confluent monolayer of endothelial cells. After the VECs and VSMCs were co-cultured for 24 h, they were used for the SPC treatment. Gel images were captured at 2 h using a camera, and the areas (cm^2) of the gels were measured using the Image J software (http://rsb.info.nih.gov/ij/). The original area of a collagen gel was represented by the area (2 cm^2) of a well from a 24-well plate. A decrease in the gel area correlates with an increase in contractility. Changes in contractility that resulted from the experimental treatments were expressed as the percent of the gel area that was observed relative to that of the untreated control. Three fields were analyzed for each experiment that was performed.

NO level assay

After the VECs were treated with the siRNA for 48 h and stimulated with SPC for 0, 3, 15, and 30 min, the supernatant was used for a NO level assay using the NO Detection Kit (Nanjing Jiancheng, China) according to the manufacturer's instructions. The optical density was measured at 550 nm (wavelength). The level of NO was expressed as μmol/L.

Cell viability assay

HUVECs were plated in 96-well cell culture plates. Cells that were at approximately 60% confluence were transfected with scramble RNA (negative control) or integrin β4 siRNA (40 nmol/L). After 24 h, the medium was replaced with M199 medium for another 24 h. Then, the cells were treated with basal M199 medium to which 0.3% ethanol (*v/v*) or SPC was added for 1 h, and the cell viability was assayed by the MTT assay as previously described[10]. The viability (%)=(*OD* of treated group/*OD* of control group)×100%.

Statistic analysis

Data were expressed as mean±SEM and accompanied by the number of experiments that were performed independently. A statistical analysis was conducted using a one-way ANOVA, and differences of $P<0.05$ were considered to be statistically significant.

Results

VECs reduced SPC-induced VSMC contraction in co-culture systems

The VECs and VSMCs were co-cultured in the micropore membrane insert well co-culture system for 24 h. Then, the VSMCs were treated with SPC for 30, 45, or 60 min, and the cell contraction morphologies were observed under a microscope. The images show that the single-culture SPC treatment decreased the area of each individualVSMC significantly at 60 min compared with cocultured ones, but the same treatment failed to decrease the areas of the VSMCs in the co-cultures (Figure 1A).

After the VSMCs were treated with SPC for 1 h, the cell contraction morphologies were observed using an immunofluorescence assay. The results showed that SPC caused the α-SMA-positive VSMC layer to shrink in the single-cultures, but this phenomenon was not observed in the co-cultures. As shown in the column (Figure 1B), the average length of the VSMCs in the co-cultured systems was significantly longer than that in the single-cultured ones ($P<0.01$ and $P<0.01$). These results indicate that VECs inhibit SPC-induced VSMC contraction.

In addition, we examined the VSMCs using a collagen contractility assay, and the images show that the SPC treatment of the single-cultures decreased the collagen-containing areas, but the same treatment failed to decrease these areas in the co-cultures ($P<0.01$ and $P<0.01$) (Figure 1C). Thus, the VECs reduced VSMC contraction in co-cultures that had been stimulated with SPC.

Integrin β4-knockdown VECs failed to show reduced SPC-induced VSMC contraction

To identify integrin β4 in VECs that had been co-cultured with VSMCs, we measured integrin β4 protein levels in single-cultured and co-cultured VECs. As shown in Figure 2A, the level of integrin β4 was higher in the co-cultured VECs than that in the single-cultured ones ($P<0.05$), indicating a possible role for integrin β4 in the interaction between VECs and VSMCs.

To further elucidate the role of integrin β4 in the effects of VECs on SPC-induced VSMC contraction, RNAi was used. As shown in Figure 2B, integrin β4 siRNA administered at 20 nmol/L clearly downregulated integrin β4 expression at 48 h ($P<0.01$). After the VECs were transfected with integrin β4 siRNA or scramble siRNA for 24 h, the medium was changed, and the VECs were co-cultured with VSMCs as described above. As shown in Figure 2C and 2D, after the VSMCs were treated with SPC for 1 h, the areas of the VSMCs and collagens that had been co-cultured with the integrin β4-knockdown VECs were significantly smaller than those of the VSMCs that

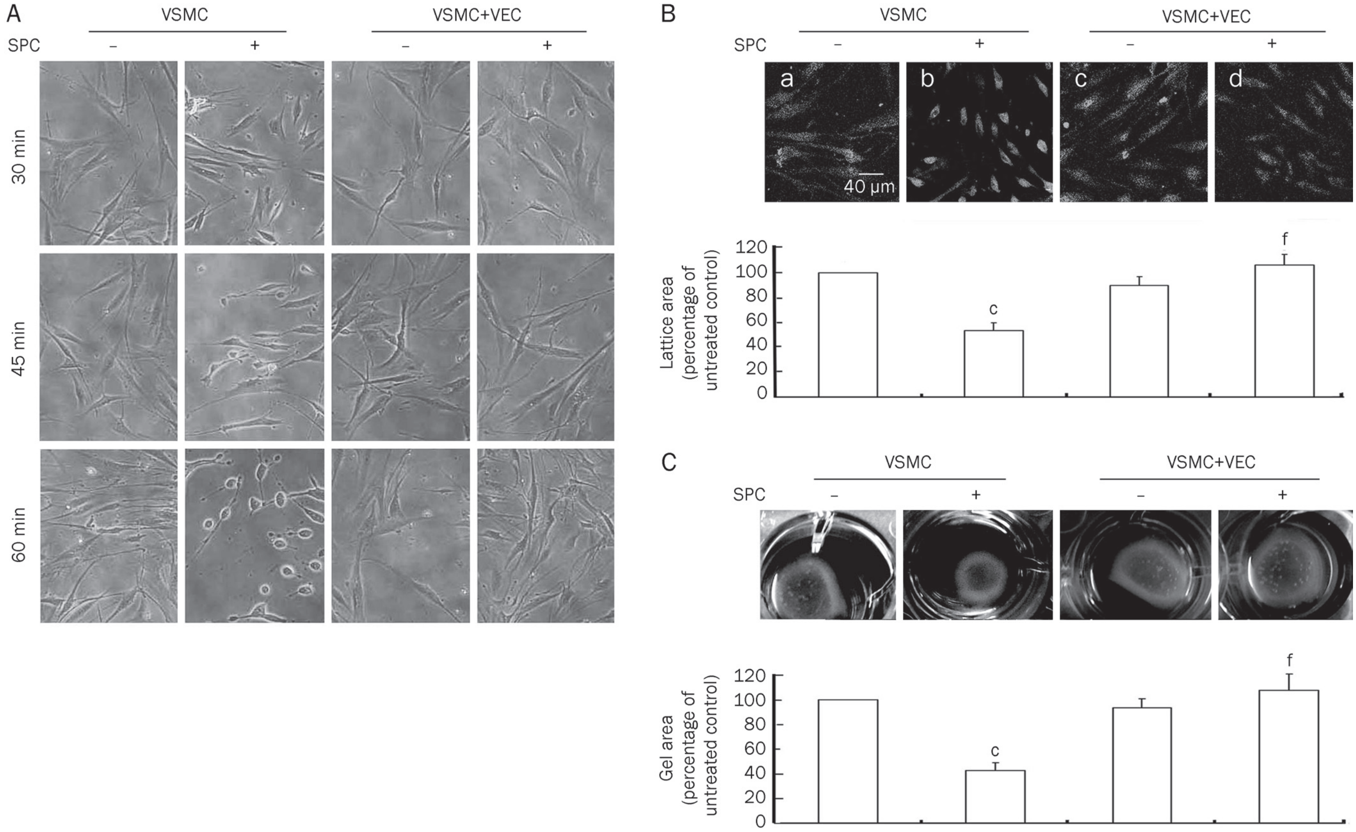

Figure 1. VECs inhibited the SPC-induced contraction of VSMCs. Cells were preincubated for 30, 45, or 60 min at 37 °C in basal M199 medium with 30 μmol/L SPC, and the morphology of the VSMCs in the micropore membrane insert well system was observed under a phase contrast microscope (×200) (A). In the direct co-cultured systems that had been preincubated for 60 min with SPC, after staining with α-SMA, the areas of α-SMA-positive cells were also analyzed using the laser confocal software (B). The bar graph shows the relative contractilities following the SPC treatment, which are represented as the ratios of the average SMC area to that of the untreated control ($^{c}P<0.01$ *vs* SPC-non-stimulated VSMCs; $^{f}P<0.01$ *vs* SPC-stimulated VSMCs, $n=3$). (C) VSMCs in collagen gels were co-cultured with VECs and preincubated with SPC as mentioned above, and then the gel images were captured at 2 h, and the areas (cm^2) of the gels were measured. The bar graph shows the relative contractility following SPC treatment, which is represented as the ratio of the gel area to that of the untreated control ($^{c}P<0.01$ *vs* SPC non-stimulated VSMCs; $^{f}P<0.01$ *vs* SPC stimulated VSMCs, $n=3$).

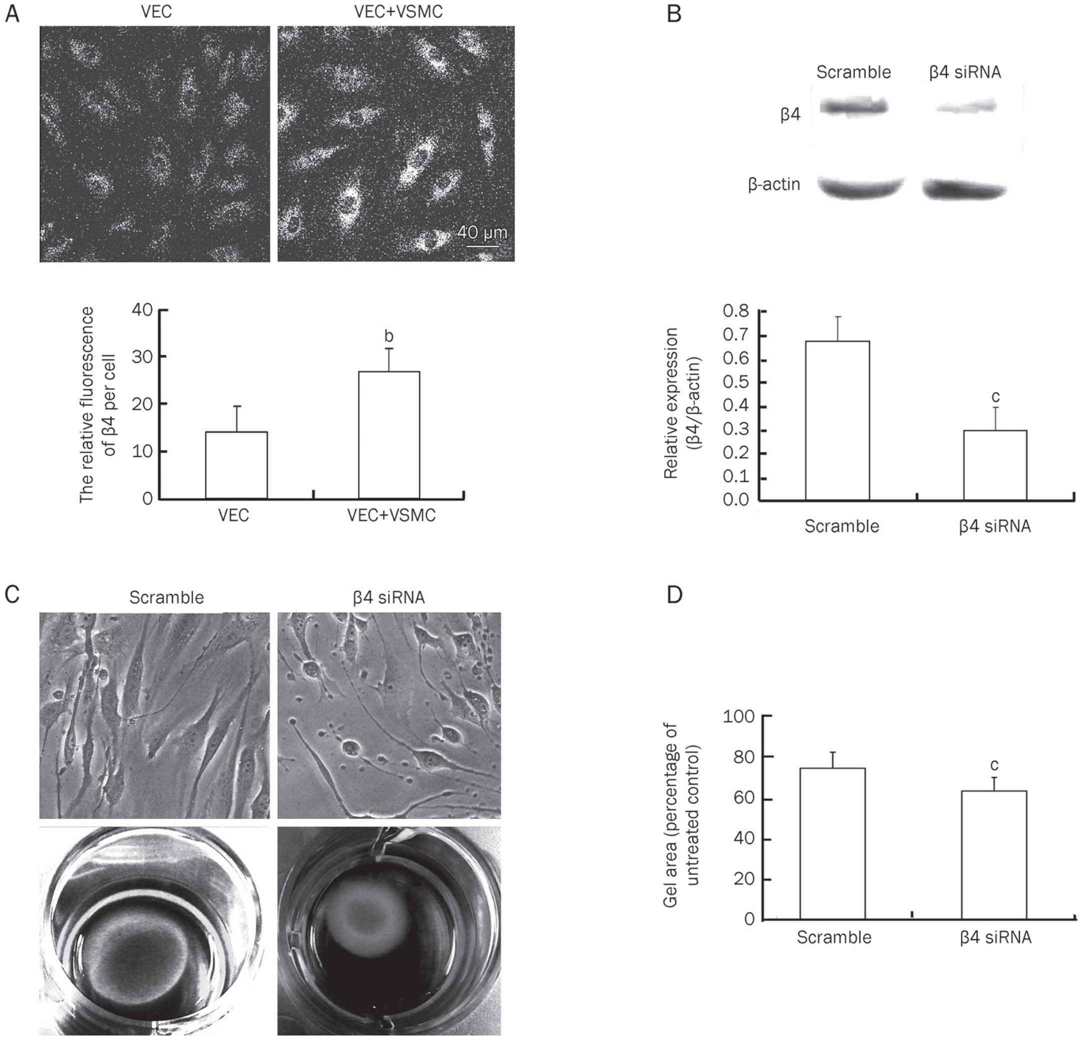

Figure 2. Effects of integrin β4 knockdown in VECs on VSMC contraction. (A) VECs and VSMCs were co-cultured in the micropore membrane insert well co-culture system for 24 h. Then, the levels of integrin β4 in the VECs were examined using the immunofluorescence assay. The bar graph shows the relative intensity of integrin β4 in the single-cultured and co-cultured VECs ($^{b}P<0.05$ *vs* single-cultured VECs, $n=3$). (B) SiRNA-mediated down-regulation of integrin β4 in VECs. The levels of integrin β4 were determined by Western blotting 48 h after the start of the siRNA treatment. In the scramble control group (scramble ctrl), cells were transfected with scramble control siRNA ($^{c}P<0.01$ *vs* scramble ctrl, $n=3$). (C) VECs were treated with 20 nmol/L integrin β4-specific siRNA or with scramble siRNA for 48 h. After the addition of SPC, the effects of the integrin β4 knockdown on the contraction of the VSMCs in the micropore membrane insert well system were observed under a phase contrast microscope (×200) and analyzed by the collagen contractility assay. (D) The bar graph shows the relative contractility following SPC treatment, which is represented as the ratio of the gel area to that of the untreated control ($^{c}P<0.01$ *vs* SPC-stimulated scramble ctrl, $n=3$).

had been co-cultured with the VECs that were transfected with the scramble siRNA ($P<0.01$). Thus, the siRNA-mediated down-regulation of integrin β4 in VECs could block the SPC-induced contraction of the VSMCs.

Fyn-knockdown VECs failed to show reduced SPC-induced VSMC contraction

To analyze the possible actions of Fyn in VECs that had been co-cultured with VSMCs, we measured the levels of this protein in single-cultured and co-cultured VECs. As shown in Figure 3A, the Fyn levels were higher in the co-cultured VECs than in the single-cultured VECs ($P<0.05$), which is indicative of a possible key role of Fyn in the interaction between VECs and VSMCs.

As shown in Figure 3B, the expression levels of Fyn in the VECs that were transfected with Fyn siRNA at 60 nmol/L for 48 h were down-regulated compared with those in the untransfected VECs ($P<0.01$). After the VECs were transfected with Fyn siRNA for 24 h, the medium was changed, and the VECs were co-cultured with VSMCs as described above. As shown in Figure 3C and 3D, after the VSMCs were treated with SPC for 1 h, the areas of the VSMCs and collagens that had been co-cultured with the Fyn-knockdown VECs were significantly smaller compared than those of the VSMCs that had been co-cultured with the scramble-siRNA-transfected VECs ($P<0.01$). These results show that the siRNA-mediated down-

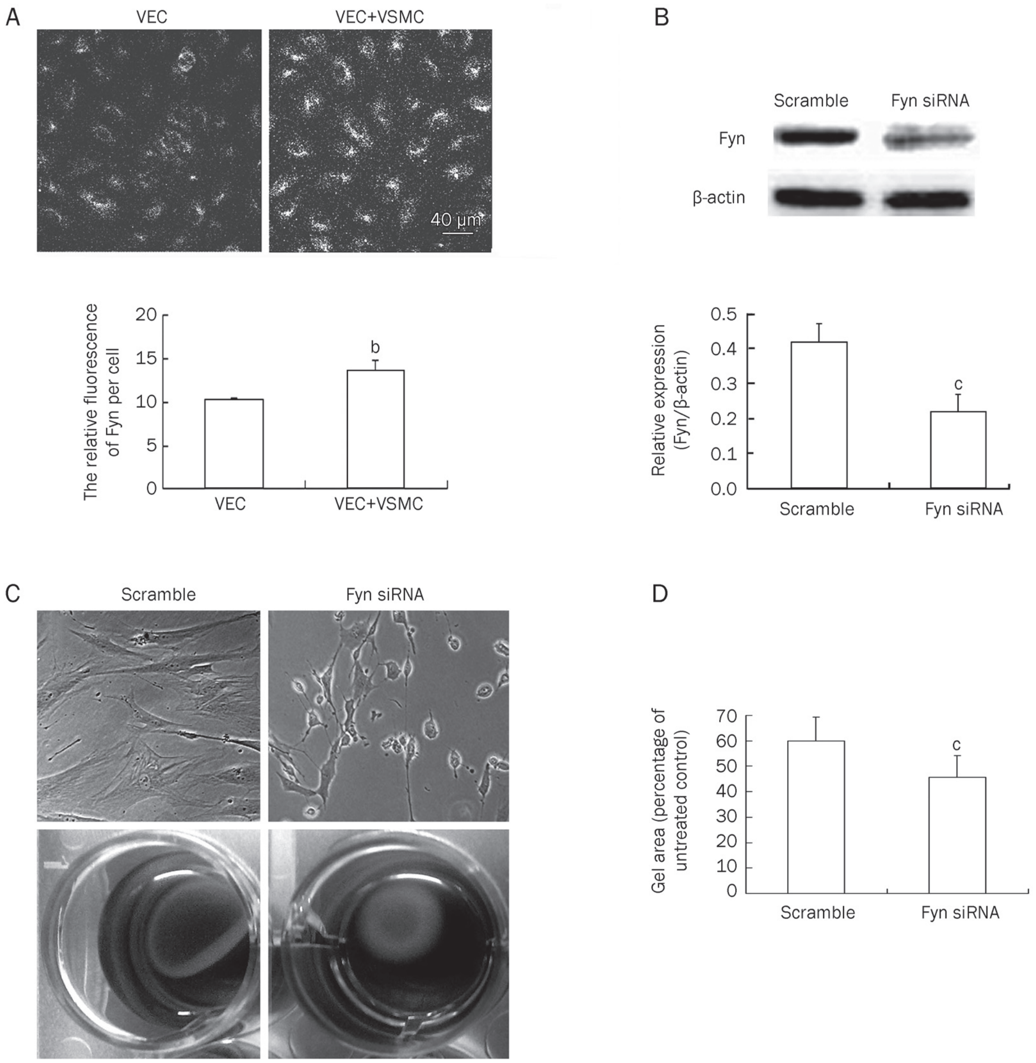

Figure 3. Effects of Fyn knockdown in VECs on VSMC contraction. (A) VECs and VSMCs were co-cultured in the micropore membrane insert well co-culture system for 24 h. Then, the levels of Fyn in the VECs were examined using the immunofluorescence assay. The bar shows the relative intensity of Fyn in single-cultured and co-cultured VECs ($^bP<0.05$ *vs* single-cultured VECs, $n=3$). (B) SiRNA-mediated down-regulation of Fyn in VECs. The value of Fyn was determined by Western blotting 48 h after the start of the siRNA treatment. In the scramble control group (scramble ctrl), the cells were transfected with scramble control siRNA ($^cP<0.01$ *vs* scramble ctrl, $n=3$). (C) VECs were treated with 20 nmol/L Fyn-specific siRNA or with scramble siRNA for 48 h. After the SPC was added, the effects of the Fyn knockdown on the contraction of the VSMCs in the micropore membrane insert well system were observed under a phase contrast microscope (×200) and analyzed using the collagen contractility assay. (D) The bar graph shows the relative contractility following SPC treatment, which is represented as a ratio of the gel area to that of the untreated control ($^cP<0.01$ *vs* SPC-stimulated scramble ctrl, $n=3$).

regulation of Fyn in VECs could also counteract the inhibitory effects of the VECs on SPC-induced VSMC contraction.

Knockdown of integrin β4 inhibited Fyn expression in VECs

An integrin β4 knockdown strategy was used to elucidate the possible relationship between integrin β4 and Fyn in the VECs. The results show that the knockdown of integrin β4 inhibits the expression of Fyn ($P<0.05$ and $P<0.01$) (Figure 4).

Knockdown of integrin β4 inhibited NO production in VECs

To understand the underlying mechanism by which integrin β4 participates in the effects of VECs on SPC-induced VSMC contraction, we analyzed the relationship between integrin β4 and NO, the latter of which was the key factor in the VEC-reduced VSMC contraction stimulated by SPC. The results show that SPC promotes the production of NO at 3 and 15 min in VECs, whereas the knockdown of integrin β4 inhibits SPC-induced NO production ($P<0.05$) (Figure 5A).

Knockdown of integrin β4 did not change viability of VECs

To clarify whether the knockdown of integrin β4 abolishes VEC function as related to SPC-induced VSMC contraction by decreasing cell numbers, we assessed the viabilities of the VECs before and after the integrin β4 siRNA treatment.

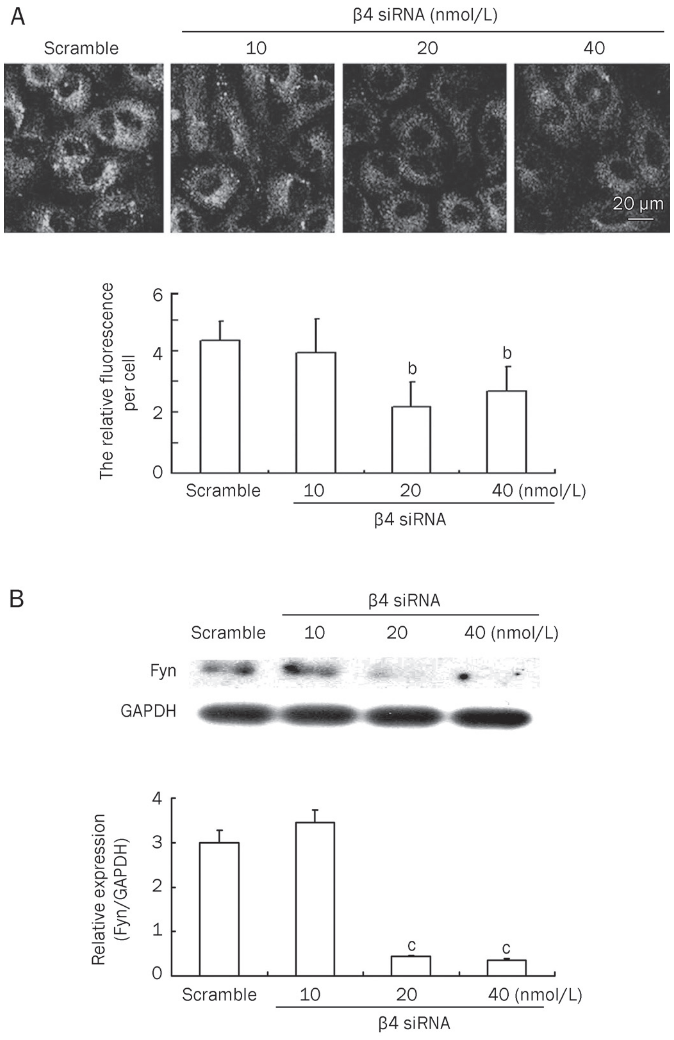

Figure 4. Effects of integrin β4 knockdown on the changes in Fyn levels in VECs. (A) VECs were treated with 10–40 nmol/L integrin β4 siRNA or scramble siRNA for 48 h. The levels of integrin β4 in the VECs were determined by the immunofluorescence assay, and the bar graph shows the relative fluorescent intensity of integrin β4 per cell as determined by laser scanning confocal microscopy ($^bP<0.05$ *vs* scramble ctrl, *n*=3). (B) After 10–40 nmol/L integrin β4 siRNA or scramble siRNA were treated for 48 h, the Fyn levels in the VECs were assessed using Western blotting ($^cP<0.01$ *vs* scramble ctrl, *n*=3).

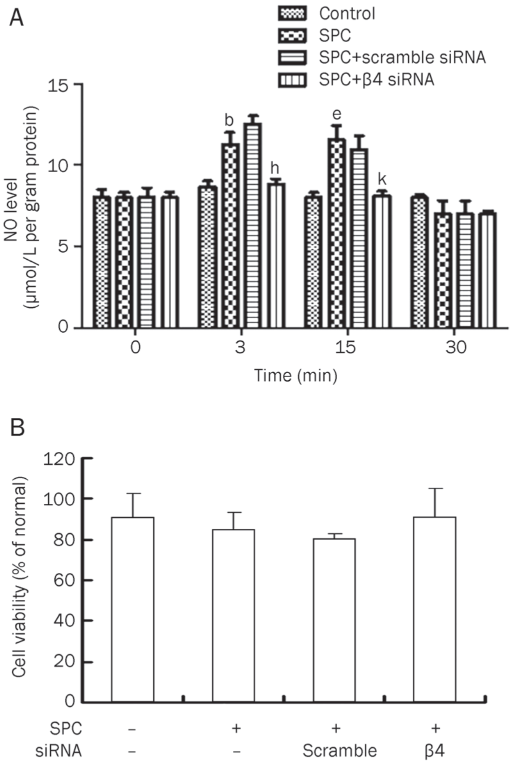

Figure 5. Effects of integrin β4 knockdown on NO production in VECs. (A) VECs were cultured under normal conditions or with siRNA for 48 h and stimulated with SPC for 0, 3, 15, or 30 min, and the supernatant was used for the NO level assay using the NO Detection Kit. In the control group (ctrl), the cells were cultured in M199 medium with 0.3% (*v/v*) ethanol instead of SPC. In the scramble control group (scramble ctrl), cells were transfected with scramble control siRNA in the presence of SPC. The bar graph shows the changes in NO levels in VECs that had been treated with SPC ($^bP<0.05$ *vs* ctrl at 3 min, $^eP<0.05$ *vs* ctrl at 15 min, *n*=5) or with siRNA in the presence of SPC ($^hP<0.05$ *vs* scramble ctrl at 3 min, $^kP<0.05$ *vs* scramble ctrl at 15 min, *n*=5). (B) The viabilities of VECs were measured by MTT, and no significant changes were observed (*n*=3).

The results show that the knockdown of integrin β4 does not change the viabilities of the VECs (Figure 5B).

ROCK levels in VSMCs that were treated with SPC and co-cultured with integrin β4-knockdown VECs were increased by SPC

Because the translocation of Rho kinase (ROCK) has been shown to participate in SPC-induced VSMC contraction[18], we further analyzed the changes in ROCK levels in relation to VSMC contraction. As shown in Figure 6, when VSMCs were treated with SPC and when SPC-treated VSMCs were co-cultured with integrin β4-knockdown VECs, contraction occurred, and the levels of ROCK in the VSMCs significantly increased compared to the corresponding controls ($P<0.05$).

Discussion

Recently, SPC has been regarded as a novel messenger for the Rho kinase–mediated Ca^{2+} sensitization of VSMC contraction[7], but its effects on VSMCs depend on the presence of VECs. In this study, to obtain further information regarding the mechanism by which VECs inhibit SPC-induced VSMC contraction, we utilized a co-culture system containing VECs and VSMCs. The results show that VECs inhibit SPC-induced VSMC contraction in co-culture systems. Therefore, *in vitro* co-culture systems could be used to study the underlying mechanisms by which VECs inhibit SPC-induced VSMC contraction.

We have previously reported that integrin β4 is a very important membrane protein in VEC apoptosis, senescence and differentiation[10–12]. The data from the present study suggest that integrin β4 is also a key factor in the VEC-mediated

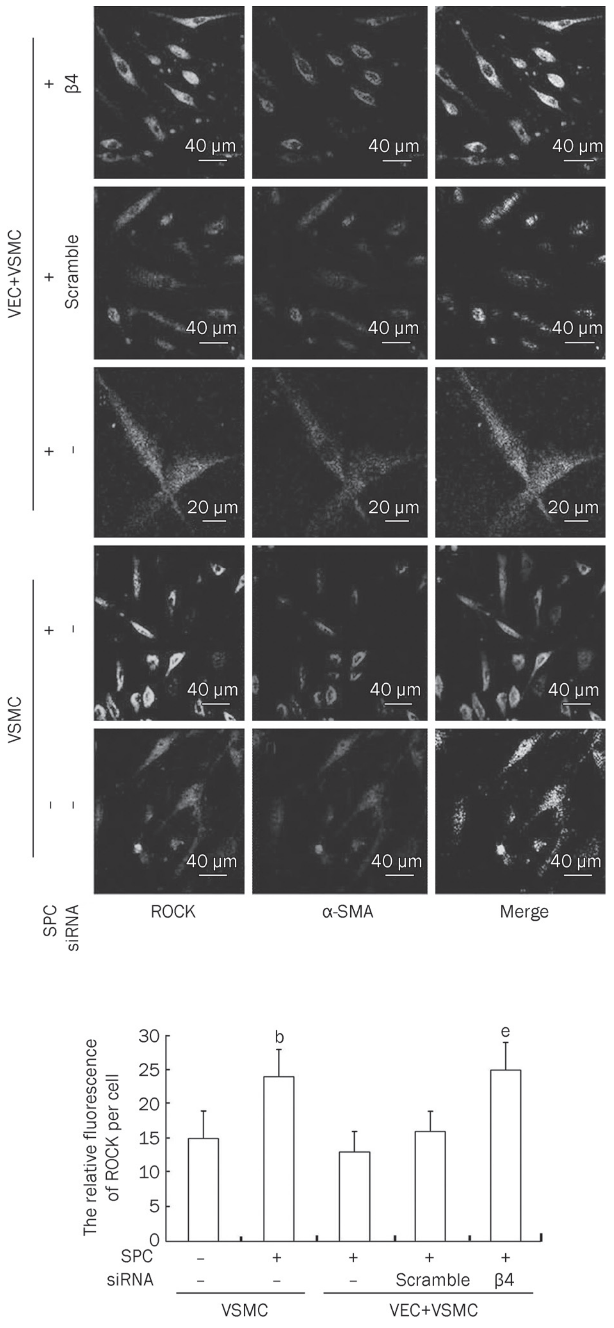

Figure 6. Effects of integrin β4 knockdown in VECs on changes in ROCK levels in co-cultured VSMCs. VSMCs that had been co-cultured with VECs that were treated with or without integrin β4-specific siRNA (β4) or scramble control siRNA in the presence of SPC were immunostained for ROCK, α-SMA, or both. The bar graph shows the relative fluorescence intensity of ROCK per VSMC as determined by laser scanning confocal microscopy ($^bP<0.05$ *vs* SPC-non-stimulated VSMCs; $^eP<0.05$ *vs* SPC-stimulated scramble ctrl in co-cultured system, $n=4$).

regulation of SPC-induced VSMC contraction. It is clear that NO is an important factor for the modulation of VSMC contraction by SPC-stimulated VECs[8]. Our current results show that SPC promotes the production of NO in VECs, and the knockdown of integrin β4 rescues the levels of NO in VECs that have been stimulated with SPC. Thus, integrin β4 may regulate VSMC contraction through the action of NO. We will use NO inhibitors in future studies to verify the role of NO generation in endothelial cells in the reduction of SPC-stimulated VSMC contraction.

It has been reported that Fyn may act as an regulator in coronary artery contraction[25]. However, research into the role of Fyn in VECs is limited to endothelial cell migration and capillary morphogenesis[16, 26]. To date, the possible role of VEC-derived Fyn in SPC-induced VSMC contraction is not known. In the present study, the siRNA-mediated down-regulation of Fyn in the VECs counteracted the SPC-induced contraction of the VSMCs, suggesting that Fyn is another important factor in the SPC-induced regulation of VSMC contraction by VECs.

The association between integrin β4 and Fyn has been analyzed previously. It has been reported that α6β4 integrin selectively activates the Src family member Fyn in response to receptor engagement during tumor progression and promotes this tumor progression[27]. However, Wang *et al* discovered that Fyn phosphorylates the β4 cytoplasmic domain and causes the disassembly of hemidesmosomes, which is a prerequisite for normal keratinocyte migration and squamous carcinoma invasion[28]. Therefore, the relationship between integrin β4 and Fyn remains to be elucidated. Our data show that Fyn levels are regulated by integrin β4, but changes in the protein levels that are observed in integrin β4-silenced cells in this study may reflect solely the effects of integrin β4 silencing on the transcription of the Fyn gene or the degradation of the Fyn protein. The kinase assay and the detection of changes in phosphorylation statuses and post-activation translocation are the generally accepted methods for verifying kinase activation in a signaling cascade. Therefore, the mechanism by which Fyn regulates contraction, in addition to its relationship with integrin β4, requires further study.

In the present study, the contraction of the collagen gel when the VSMCs were co-cultured with the scramble-siRNA-transfected VECs amounted to 60%–75% of that of the control (Figure 2D and Figure 3D), and Figure 1C shows that co-culturing with untransfected VECs completely blocks VSMC contraction. Therefore, the effects of the RNAiFect transfection reagent or the inactive siRNA sequence must be acknowledged as was previously described by Kriegel *et al*[29]. However, the use of integrin β4 and Fyn siRNA resulted in the statistically significant promotion of collagen gel contraction. Therefore, integrin β4 and Fyn in the VECs indeed played important roles in the reduction of VSMC contraction.

In rat aortic smooth muscle cells, the translocation of ROCK from the cytosol to the cell membrane may play a role in SPC-induced contraction[30]. In this study, we further observed that the levels of ROCK were associated with the contraction of VSMCs, which may be a marker for indicating VSMC contraction. However, the elucidation of the exact function of ROCK requires further analyses involving kinase activation.

In summary, our results showed that VECs inhibited SPC-induced VSMC contraction in co-culture systems. VECs performed this function using the integrin β4 and Fyn proteins.

NO may be downstream of integrin β4 in VECs and assist in performing this function. Furthermore, the levels of ROCK in the VSMCs may be novel markers for the detection of VSMC contraction. The present data provided novel clues for understanding the mechanism by which VECs control the SPC-induced contraction of VSMCs.

Acknowledgements

This work was supported by the National Natural Science Foundation of China (No 30570749, 31070999, and 30800398) and National 973 Research Project (No 2006CB503803). We thank Dr Sei KOBAYASHIC (Yamaguchi University School of Medicine) for his beneficial advice on VSMC contraction research. We also thank Dr Bao-xiang ZHAO (Shandong University) for his critical reading of the manuscript.

Author contribution

Jun-ying MIAO, Jing ZHAO, and Yun ZHANG designed the research; Di GE, Ning MENG, Le SU, Shang-li ZHANG, and Jing ZHAO performed the research; Shang-li ZHANG analyzed the data; and Jing ZHAO, Di GE, and Ning MENG wrote the paper.

References

1 Kalsner S. Coronary artery spasm. Multiple causes and multiple roles in heart disease. Biochem Pharmacol 1995; 49: 859–71.
2 Hellstrom HR. Evidence in favor of the vasospastic cause of coronary artery thrombosis. Am Heart J 1979; 97: 449–52.
3 Factor SM, Cho S. Smooth muscle contraction bands in the media of coronary arteries: A postmortem marker of antemortem coronary spasm. J Am Co11 Cardiol 1985; 6: 1329–37.
4 Lin CS, Penha PD, Zak FG, Lin JC. Morphodynamic interpretation of acute coronary thrombosis, with special reference to volcano-like eruption of atheromatous plaque caused by coronary artery spasm. Angiology 1988; 39: 535–47.
5 Hirano K. Current topics in the regulatory mechanism underlying the Ca^{2+} sensitization of the contractile apparatus in vascular smooth muscle. J Pharmacol Sci 2007; 104: 109–15.
6 Nixon GF, Mathieson FA, Hunter I. The multi-functional role of sphingosylphosphorylcholine. Prog Lipid Res 2008; 47: 62–75.
7 Shirao S, Kashiwagi S, Sato M, Miwa S, Nakao F, Kurokawa T, *et al*. Sphingosylphosphorylcholine is a novel messenger for Rho-kinase-mediated Ca^{2+} sensitization in the bovine cerebral artery: unimportant role for protein kinase C. Circ Res 2002; 91: 112–9.
8 Mogami K, Mizukami Y, Todoroki-Ikeda N, Ohmura M, Yoshida K, Miwa S, *et al*. Sphingosylphosphorylcholine induces cytosolic Ca^{2+} elevation in endothelial cells *in situ* and causes endothelium-dependent relaxation through nitric oxide production in bovine coronary artery. FEBS Lett 1999; 457: 375–80.
9 Tarone G, Hirsch E, Brancaccio M, De Acetis M, Barberis L, Balzac F, *et al*. Integrin function and regulation in development. Int J Dev Biol 2000; 44: 725–31.
10 Su L, Zhao J, Zhao BX, Miao JY, Yin DL, Zhang SL. Safrole oxide induced human umbilical vein vascular endothelial cell differentiation into neuron-like cells by depressing the reactive oxygen species level at the low concentration. Biochim Biophys Acta 2006; 1763: 247–53.
11 Miao JY, Araki S, Kaji K, Hayashi H. Integrin beta4 is involved in apoptotic signal transduction in endothelial cells. Biochem Biophys Res Commun 1997; 233: 182–6.
12 Sun C, Liu X, Qi L, Xu J, Zhao J, Zhang Y, *et al*. Modulation of vascular endothelial cell senescence by integrin β4. J Cell Physiol 2010; 225: 673–81.
13 Thomas SM, Soriano P, Iwamoto A. Specific and redundant roles of Src and Fyn in organizing the cytoskeleton. Nature 1995; 376: 267–71.
14 Cobb BS, Schaller MD, Leu TH, Parsons JT. Stable association of pp60src and pp59fyn with the focal adhesion-associated protein tyrosine kinase, pp125FAK. Mol Cell Biol 1994; 14: 147–55.
15 Heydarkhan-Hagvall S, Helenius G, Johansson BR, Li JY, Mattsson E, Risberg B. Co-culture of endothelial cells and smooth muscle cells affects gene expression of angiogenic factors. J Cell Biochem 2003; 89: 1250–9.
16 Kanda S, Mochizuki Y, Nakamura T, Miyata Y, Matsuyama T, Kanetake H. Pigment epithelium-derived factor inhibits fibroblast-growth-factor-2-induced capillary morphogenesis of endothelial cells through Fyn. J Cell Sci 2005; 118: 961–70.
17 Morikage N, Kishi H, Sato M, Guo F, Shirao S, Yano T, *et al*. Cholesterol primes vascular smooth muscle to induce Ca^{2+} sensitization mediated by a sphingosylphosphorylcholine-Rho-kinase pathway: possible role for membrane raft. Circ Res 2006; 99: 299–306.
18 Nakao F, Kobayashi S, Mogami K, Mizukami Y, Shirao S, Miwa S, *et al*. Involvement of Src family protein tyrosine kinases in Ca^{2+} sensitization of coronary artery contraction mediated by a sphingosylphosphorylcholine-Rho-kinase pathway. Circ Res 2002; 91: 953–60.
19 Leik CE, Willey A, Graham MF, Walsh SW. Isolation and culture of arterial smooth muscle cells from human placenta. Hypertension 2004; 43: 837–40.
20 Jaffe EA, Nachman RL, Becker CG, Minick RC. Culture of human endothelial cells derived from umbilical veins. J Clin Invest 1973; 52: 2745–56.
21 Wang HQ, Bai L, Shen BR, Yan ZQ, Jiang ZL. Coculture with endothelial cells enhances vascular smooth muscle cell adhesion and spreading via activation of beta1-integrin and phosphatidylinositol 3-kinase/Akt. Eur J Cell Biol 2007; 86: 51–62.
22 Bell E, Ivarsson B, Merrill C. Production of a tissue-like structure by contraction of collagen lattices by human fibroblasts of different proliferative potential *in vitro*. Proc Natl Acad Sci U S A 1979; 76: 1274–8.
23 Fitzgibbon J, Morrison JJ, Smith TJ, O'Brien M. Modulation of human uterine smooth muscle cell collagen contractility by thrombin, Y-27632, TNF alpha and indomethacin. Reprod Biol Endocrinol 2009; 7: 2.
24 Vi L, Feng L, Zhu RD, Wu Y, Satish L, Gan BS, *et al*. Periostin differentially induces proliferation, contraction and apoptosis of primary Dupuytren's disease and adjacent palmar fascia cells. Exp Cell Res 2009; 315: 3574–86.
25 Nakao F, Kobayashi S, Mogami K, Mizukami Y, Shirao S, Miwa S, *et al*. Involvement of Src family protein tyrosine kinases in Ca^{2+} sensitization of coronary artery contraction mediated by a sphingosylphosphorylcholine-Rho-kinase pathway. Circ Res 2002; 91: 953–60.
26 Lamalice L, Houle F, Huot J. Phosphorylation of Tyr1214 within VEGFR-2 triggers the recruitment of Nck and activation of Fyn leading to SAPK2/p38 activation and endothelial cell migration in response to VEGF. J Biol Chem 2006; 281: 34009–20.
27 Yang X, Dutta U, Shaw LM. SHP2 mediates the localized activation of Fyn downstream of the α6β4 integrin to promote carcinoma invasion. Mol Cell Biol 2010; 30: 5306–17.
28 Wang H, Leavitt L, Ramaswamy R, Rapraeger AC. Interaction of syndecan and alpha6beta4 integrin cytoplasmic domains: regulation of ErbB2-mediated integrin activation. J Biol Chem 2010; 285: 13569–79.
29 Kriegel C, Amiji M. Oral TNF-α gene silencing using a polymeric microsphere-based delivery system for the treatment of inflammatory bowel disease. J Control Release 2011; 150: 77–86.
30 Davis JR, Giardina JB, Green GM, Alexander BT, Granger JP, Khalil RA. Reduced endothelial NO-cGMP vascular relaxation pathway during TNF — induced hypertension in pregnant rats. Am J Physiol Regul Integr Comp Physiol 2002; 282: R390–9.

npg
Acta Pharmacologica Sinica (2012) 33: 66–74
© 2012 CPS and SIMM All rights reserved 1671-4083/12 $32.00
www.nature.com/aps

Original Article

Dose-dependent effects of genistein on bone homeostasis in rats' mandibular subchondral bone

Yong-qi LI[1, #], Xiang-hui XING[2, #], Hui WANG[2], Xi-li WENG[2], Shi-bin YU[2, *], Guang-ying DONG[2, *]

[1]Xijing Hospital, Fourth Military Medical University, Xi'an 710032, China; [2]School of Stomatology, Fourth Military Medical University, Xi'an 710032, China

Aim: To investigate the effect of genistein on bone homeostasis in mandibular subchondral bone of rats.
Methods: Female SD rats were administered with genistein (10 and 50 mg/kg) or placebo by oral gavage for 6 weeks. Then the animals were sacrificed, and histomorphology and micro-structure of mandibular condyle were examined using HE staining and micro-CT analysis, respectively. The expression levels of alkaline phosphatase (ALP), osteocalcin (OC), osteoprotegerin (OPG), the receptor activator of nuclear factor κB ligand (RANKL) and estrogen receptors (ERs) in mandibular condyle were detected using real-time PCR. Cultured osteoblasts were prepared from rat mandibular condyle for in *in vitro* study. The cells were treated with genistein (10^{-7} or 10^{-4} mol/L) for 48 h. The expression of the bone homeostasis-associated factors and estrogen receptors (ERs) was detected using real-time PCR, and ER silencing was performed.
Results: At both the low- and high-doses, genistein significantly increased the bone mineral density (BMD) and bone volume, and resulted in thicker subchondral trabecular bone *in vivo*. In both *in vivo* and *in vitro* study, the low-dose genistein significantly increased the expression of ALP, OC and OPG, but decreased the expression of RANKL and the RANKL/OPG ratio. The high-dose genistein decreased the expression of all these bone homeostasis-associated factors. Both the low and high doses of genistein significantly increased the expression of ERβ, while ERα expression was increased by the low dose genistein and decreased by the high dose genistein. ERβ silencing abrogated most of the effects of genistein treatment.
Conclusion: In rat mandibular condylar subchondral bone, low-dose genistein increases bone formation and inhibit bone resorption, while excess genistein inhibits both bone formation and resorption. The effects of genistein were predominantly mediated through ERβ.

Keywords: genistein; estrogen receptor; mandibular subchondral bone; osteoblast; alkaline phosphatase; osteocalcin; osteoprotegerin; the receptor activator of nuclear factor κB ligand (RANKL)

Acta Pharmacologica Sinica (2012) 33: 66–74; doi: 10.1038/aps.2011.136; published online 28 Nov 2011

Introduction

Osteoporosis is a systemic disease characterized by reduced bone mass and structural deterioration of bone tissue. Osteoporosis has become a public health issue threatening a large portion of the population over 50 years of age[1, 2]. Estrogen replacement therapy (ERT) is effective in reducing or reversing postmenopausal bone loss[3]. In addition to its use for the treatment of postmenopausal symptoms, potential benefits of ERT include a reduction in the risk of osteoarthritis[4–6] and prevention of cardiovascular disease and dementia[7]. However, recent studies have shown that ERT is associated with a higher risk for breast, endometrial and ovarian cancer as well as cardiovascular disease and stroke[8, 9]. Due to the side-effects of long-term ERT use, the number of ERT users has fallen dramatically.

Observational studies suggest that Asian women who consume traditional diets high in isoflavones from soybean have a lower rate of postmenopausal fractures than Caucasian women[10, 11]. Phytoestrogen, especially genistein, which structurally resembles 17β-estradiol, is abundant in soybean products. Previous animal studies have shown that genistein treatment increased bone mineral density (BMD) and improved bone biomechanical performance in ovariectomized (OVX) rodents[12, 13]. Clinical studies have also demonstrated that phytoestrogen can effectively increase the BMD of vertebrae and hip bones in postmenopausal women without side effects, which suggested that genistein plays an important role in the regulation of bone formation and bone resorption[14–17]. phos-

---

[#] These authors contributed equally to this work.
[*] To whom correspondence should be addressed.
E-mail yushibin@fmmu.edu.cn (Shi-bin YU);
donggy@fmmu.edu.cn (Guang-ying DONG)
Received 2011-07-23 Accepted 2011-09-15

phatase (ALP) and osteocalcin (OC) are widely used markers for bone formation. Genistein treatment (45 mg/kg by oral gavage) was observed to significantly increase the serum ALP and OC levels in OVX rats[18]. In the process of bone resorption, osteoprotegerin (OPG) and the receptor activator of nuclear factor κB ligand (RANKL) constitute a complex mediator system. The RANKL to OPG ratio is the key regulatory determinant of bone resorption[19]. It is suggested that genistein (10 mg/kg, subcutaneous administration) significantly increased serum OPG level as well as decreased serum RANKL level and the RANKL/OPG ratio in OVX rats[20]. Additionally, the most abundant protein in bone is type I collagen. Type I collagen carboxy terminal telopeptide (CTX) is formed during bone collagen breakdown and is liberated into the circulation. Serum concentration of CTX reflects the degree of bone resorption[21].

In the literature, the effects of genistein on bone were almost exclusively focused on changes in long bones or lumbar spines in OVX animals or postmenopausal women with estrogen deficiency. It has been suggested that patients with a history of osteoporotic fractures tend to have increased mandibular bone loss and relevant trabecular micro-structural changes[22]. Additionally, a dense trabecular pattern in the mandibular alveolar process has been proven to be a reliable sign of normal BMD in dentate middle-aged subjects whereas a sparse trabecular pattern indicates osteopenia[23]. In developed countries, a large proportion of the population visits dentists annually, and dental radiographs are performed routinely. Thus, researchers worldwide have recently tried to develop methods for using the jawbones, especially the mandible, to predict skeletal BMD[23]. The mandibular condyle, one important section of the mandible, is one of the most common sites of OA[24]. Furthermore, the articular surfaces of the mandibular condyle are composed of fibrocartilage that is distinct from the hyaline cartilage of the appendicular skeleton[25]. Unlike appendicular joints whose cartilage and subchondral bone are separated by tidemark and calcified cartilage, mandibular condylar cartilage and its subchondral bone are not obviously separated by an osteochondral interface[26]. However, in the literature few reports focused on the effect of phytoestrogens on mandibular bone, particularly in intact animals with normal estrogen levels. How genistein affects bone homeostasis in mandibular subchondral bone and whether different doses of genistein play different roles in this process remain unclear. The aim of the present study was to investigate the effect of different doses of genistein on bone homeostasis in the mandibular condylar subchondral bone in intact female rats.

Materials and methods

Genistein treatment *in vivo*

All experimental procedures administered to the animals were approved by the Animal Research Committee of the Fourth Military Medical University. Thirty female 7-week-old SD rats, weighing 180–190 g, were provided by the animal center of the Fourth Military Medical University. All animals were housed under conditions of 22 °C and 30%–60% relative humidity with a normal day-night rhythm, consisting of a 12 h:12 h light-dark cycle. Animals were randomly assigned into the control, low- or high-dose genistein-treated groups, 10 animals in each group. Rats had free access to tap water and a phytoestrogen-free diet where corn oil replaced soybean oil. Based on a series of safety studies with genistein, it is estimated that the no observed adverse effect level (NOAEL) of genistein is 50 $mg \cdot kg^{-1} \cdot d^{-1}$ for rats, and the no observed effect level (NOEL) is 10 $mg \cdot kg^{-1} \cdot d^{-1}$ [27]. Thus, in the present study, 50 $mg \cdot kg^{-1} \cdot d^{-1}$ genistein was chosen as the high dose, and 10 $mg \cdot kg^{-1} \cdot d^{-1}$ as the low dose. The animals were treated once daily with genistein (10 or 50 mg/kg body weight, 99.5% pure, Winherb Med Sci Co Ltd, China) or placebo by oral gavage. Genistein was dissolved in a placebo solution (0.9% NaCl, 2% Tween 80, and 0.5% methyl cellulose in water). Application volume was 5 mL/kg body weight. Changes in body weight during the experimental period were taken into account in calculating the genistein dosage. All animals were sacrificed following 6 weeks of genistein administration.

Histological analysis

Under deep anesthesia, 12 rats (4 in each group) were sacrificed for histological analysis. The right temporomandibular joints (TMJs), including the mandibular ramus, were dissected and fixed in 4% paraformaldehyde (pH 7.4) overnight at 4 °C and then decalcified for 1 week in Kristensen's fluid (sodium formate 52.2 g, formic acid 174.2 mL, 1000 mL distilled water). Samples were then dehydrated and embedded in paraffin, followed by cutting into 5 μm middle-sagittal sections. HE staining was carried out for histological analysis. As we previously reported[26], two square areas (0.5 mm×0.5 mm) were selected under the interface of the cartilage and subchondral bone. They were located in the center of the middle and posterior third sections of the condylar cartilage that appeared consistent among animals. Using a computer-assisted image analyzing system (Leica Qwin Plus, Leica Microsystem Imaging Solutions Ltd, Cambridge, United Kingdom), the 2D measurements within the selected squares were performed by directed measurement of the trabecular bone area (B.Ar in mm^2) and perimeter (B.Pm in mm). Then, the histomorphometric parameters of the subchondral trabecular bone were calculated according to Parfitt's formula as follows: bone volume fraction (BV/TV)=B.Ar/T.Ar; trabecular thickness (Tb.Th)=B.Ar/B.Pm; trabecular number (Tb.N)=B.Pm/T.Ar; trabecular separation (Tb.Sp)=(T.Ar–B.Ar)/B.Pm. The means of the data from two squares were used for statistical analysis.

Micro-computed tomography (micro-CT) analysis

As reported previously[26], the left mandibular condyles from animals for histological analysis were scanned in a micro-CT system (GE eXplore Locus SP, London, UK) at an isotropic spatial resolution of 8 μm and a peak voltage of 80 kV. Twelve condyles, 4 in each group, were inserted in parallel into a home-made, round synthetic foam and mounted in the cylindrical specimen holders. Four projections were performed for each scan angle in each slice. These projections had an exposure time of 3000 ms each and were averaged in order to improve the signal-to-noise ratio. The time of each scanning was over 270 min. General Electric Health Care MicroView ABA 2.1.2 Software was used to analyze reconstructive images of condyles and to calculate the parameters of architecture and mineralization. Similar to histomorphometric analysis, the interface of the cartilage and subchondral bone was divided into anterior, middle and posterior regions. As shown in Figure 1, two cubic regions of interest (ROI) (0.5 mm×0.5 mm×0.5 mm) were selected in the center of the middle and posterior regions of the condyle for the model-independent, three-dimensional morphometric analysis (Figure 1). The following micro-structural parameters were obtained: 1) BMD; 2) BMC; 3) trabecular bone volume fraction (BV/TV); 4) bone surface-to-volume ratio (BS/BV); 5) mean trabecular thickness (Tb.Th); 6) trabecular number (Tb.N), 7) mean trabecular separation (Tb.Sp), and 8) bone volume (BV). The means of the data from two ROIs were used for statistical analysis.

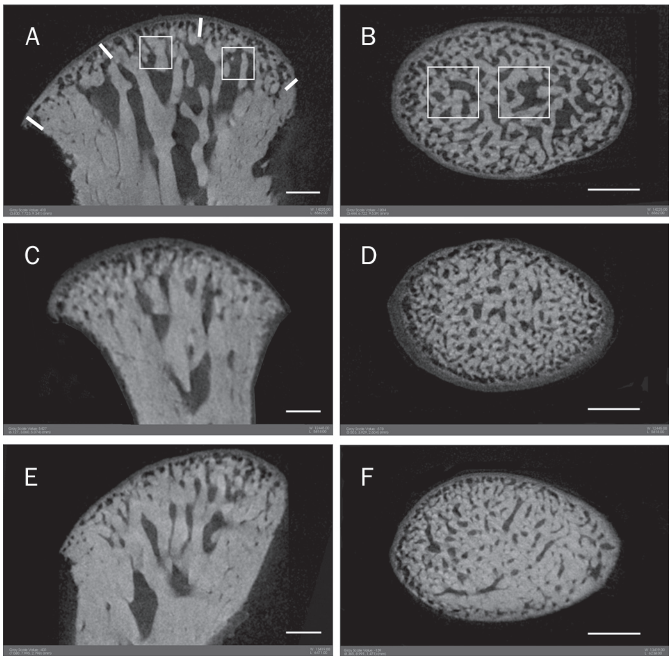

Figure 1. Sagittal central and coronal section of mandibular condyle scanned by micro-CT. A and B from control group, C and D from low dose genistein-treatment group, and E and F from high dose genistein-treatment group. The area of trabecular bone in both genistein-treatment groups was obviously higher than that in control group. White cubes in A and B represented the selected regions of interest for three-dimensional morphometric analysis. Scale bar is 500 μm.

Quantitative real-time PCR *in vivo*

Under deep anesthesia, the remaining 18 rats (6 in each group) were sacrificed for real-time PCR. Twelve mandibular condyles in each group were randomly assigned into 3 samples. Mandibular condylar subchondral bone samples were pulverized in liquid nitrogen. The total RNA was isolated using a standard TRIzol® protocol (Invitrogen, Carlsbad, CA, USA), followed by first-strand cDNA synthesis with the RevertAid^{TM} First Strand cDNA Synthesis Kit (Fermentas). Real-time PCR was performed in an ABI 7500 Fast thermal cycler. The protocol comprised 40 cycles of 94 °C for 5 s, 62 °C for 34 s, and 72 °C for 1 min each. The detected cytokines were ALP, OC, OPG, RANKL, ERα, and ERβ. Table 1 shows the sequences of the primers used in this study. Expression levels of all detected cytokines were normalized according to ribosomal protein 18S RNA levels to account for differences arising from reverse transcription efficiency and quality of the total RNA[28].

Table 1. Primer sequences for ALP, OC, OPG, RANKL, ERα, ERβ, and S18.

Gene	Sequence	Fragment length (bp)	Accession number
ALP	F: 5′-CGAGCAGGAACAGAAGTTTGC-3′ R: 5′-TGGCCAAAAGGCAGTGAATAG-3′	105 bp	NM_013059
OC	F: 5′-ATGCCACTGCGTATTGGTTGA-3′ R: 5′-TCCGCTAGCTCGTCACAATTG-3′	122 bp	M25490
OPG	F: 5′-AGCTGGCACACGAGTGATGAA-3′ R: 5′-CACATTCGCACACTCGGTTGT-3′	106 bp	U94330
RANKL	F: 5′-GGAGGATTTTTCAAGCTCCGG-3′ R: 5′-TGAAAGCCCCAAAGTACGTCG-3′	103 bp	NM_057149
ERα	F: 5′-TGCGCAAGTGTTACGAAGTGG-3′ R: 5′-TTCGGCCTTCCAAGTCATCTC-3′	108 bp	NM_012689
ERβ	F: 5′-AAAAACTCACCGTCGAGCCTT-3′ R: 5′-GCTGAATACTCATGGCGGTTG-3′	124 bp	NM_012754
S18	F: 5′-CGGCTACCACATCCAAGGAA-3′ R: 5′-GCTGGAATTACCGCGGCT-3′	187 bp	M11188

ALP, alkaline phosphatase; OC, osteocalcin; OPG, osteoprotegerin; RANKL, receptor activator of nuclear factor κB ligand; ERα, estrogen receptor α; ERβ, estrogen receptor β; S18, ribosomal protein S18, a housekeeping gene.

Serum chemistry

Before animals were sacrificed, blood was taken from the abdominal aorta by puncture exsanguination. Serum was collected by centrifugation and stored at -80 °C for further biochemical analysis. Serum bone-ALP, OC, OPG, RANKL, and CTX levels were measured by enzyme-linked immunosorbent assay (ELISA) using commercial kits (CSB-E11865r, CSB-E05129r, CSB-E07404r, and CSB-E05126r from Cusabio Biotech Co, Ltd, and QRCT-301330013301EIA\UTL from Adlitteram Diagnostic Laboratories) according to the manufacturer's instructions. The absorbance was read on an Elx800^{TM} microplate spectrometer (Bio-tec).

Culture of primary osteoblasts and genistein treatment *in vitro*

Primary osteoblasts were obtained from the mandibular subchondral bone of 8-week-old SD rats. In brief, the mandibular condyles were dissected with aseptic technique. The soft tissues and cartilage were removed to obtain mandibular subchondral bone, which was reduced to small fragments and gently digested at 37 °C with 0.125% trypsin for 8 min. The digestion process was repeated 6 times. Fractionated cells were collected from the final four digestions and combined together as the primary osteoblasts. Cells were plated at a density of 1×10^{4}/cm^{2} into appropriate dishes and then cultured under 37 °C and 5% CO_2 conditions. Culture medium was DMEM containing 10% FBS, 100 U/mL penicillin and 100 U/mL streptomycin. The cell medium was changed every three days.

For experiments, osteoblasts from the second generation were seeded in 12-well plates at a concentration of 3×10^{4}/cm^{2}. It has previously been identified that genistein increases OPG levels with a maximum effect at 10^{-7} mol/L[29]. Thus, in the present study, 10^{-7} mol/L genistein was regarded as physiological or low dose, and 10^{-4} mol/L as the high dose *in vitro*. At confluence, cells were treated with 0.1% DMSO (Sigma D-2650) or genistein (10^{-7} and 10^{-4} mol/L, Sigma G6649) for an additional 48 h. Cells were collected for total RNA isolation. The mRNA expression levels of ALP, OC, OPG, RANKL, ERα, and ERβ were evaluated by real-time PCR.

RNAi of ERs and genistein treatment

Small interfering RNA (siRNA) duplexes targeted against rat ERα and ERβ genes were designed and synthesized by Gene-Pharma (Shanghai, China). The siRNA sequences for ERα (GeneBank Accession No NM 012689) were as follows: sense, 5′-GGGAGCUGGUUCAUAUGAUTT-3′ and anti-sense, 5′-AUCAUAUGAACCAGCUCCCTT-3′. The siRNA sequences for ERβ (GenBank Accession No NM 012754) were as follows: sense, 5′-GAGCACACCUUACCUGUAATT-3′ and anti-sense, 5′-UUACAGGUAAGGUGUGCUCTT-3′. The nonsense siRNA sequences were as follows: sense, 5′-UUCUCCGAACGUGUCACGUTT-3′ and anti-sense, 5′-ACGUGACACGUUCGGAGAATT-3′. Briefly, cells were grown in 6-well plates for 36 h and transfected at 70%–80% confluency. ERα and ERβ siRNAs were transfected with Lipofectamine 2000 (Invitrogen), respectively. Transfection medium was replaced after 6 h. At confluence, cells were treated with 0.1% DMSO (Sigma D-2650), 10^{-7} mol/L or 10^{-4} mol/L genistein for another 48 h. Cells were collected for total RNA isolation. The mRNA expression levels of ALP, OC, OPG, and RANKL mRNA were evaluated by real-time PCR.

Statistical analysis

SPSS 13.0 (SPSS Inc, Chicago, IL, USA) was used to analyze and describe the data. Single-factor analysis of variance was adopted. When significant main effects were found, specific comparisons between groups were made by Student's *t* test. *P*-values were considered to be statistically significant when less than 0.05.

Results

Morphology and micro-architectural properties of mandibular condylar subchondral bone

In the mandibular condyles of control, low-, and high-dose genistein-treated groups, condylar cartilage covering subchondral bone was arranged regularly with good continuity in each layer (Figure 2). As identified by histomorphological analysis, the mandibular subchondral trabecular bone became larger and thicker after both high- and low-dose genistein treatment (Table 2), which was also identified by micro-CT (Figure 1). As shown in Table 3, genistein induced significant increase in BMD, BMC, and bone volume in both the low-dose ($P<0.05$, $P<0.05$, $P<0.01$, respectively) and high-dose genistein-treated groups (all $P<0.01$). The BMD in the high-dose genistein-treated group was higher than that in the low-dose group ($P<0.05$). With respect to the micro-architecture of subchondral bone, the BV/TV and Tb.Th increased in both low-dose ($P<0.05$, $P<0.01$) and high-dose genistein-treated groups (both $P<0.01$), as well as obvious decrease in BS/BV, Tb.N and Tb.Sp in both genistein-treated groups ($P<0.05$, $P<0.01$). The BV/TV

Table 2. Values of the histomorphological parameters after genistein treatment. Mean±SEM. $^{b}P<0.05$, $^{c}P<0.01$ *vs* control group. $^{e}P<0.05$, $^{f}P<0.01$ *vs* low dose (10 mg/kg) genistein-treatment groups.

Parameters	Control group	Genistein (10 mg/kg)	Genistein (50 mg/kg)
BV/TV (%)	57.76±2.35	63.15±2.92^{b}	72.4±3.37^{cf}
Tb.Th (μm)	58.02±4.66	75.45±5.02^{c}	83.18±3.45^{ce}
Tb.N (#/mm^{3})	114.73±2.31	9.34±0.88^{c}	9.03±0.81^{c}
Tb.Sp (μm)	45.64±4.35	29.52±2.88^{c}	26.48±3.35^{c}

BV/TV, trabecular bone volume fraction; Tb.Th, mean trabecular thickness; Tb.N, mean trabecular number; Tb.Sp, mean trabecular separation.

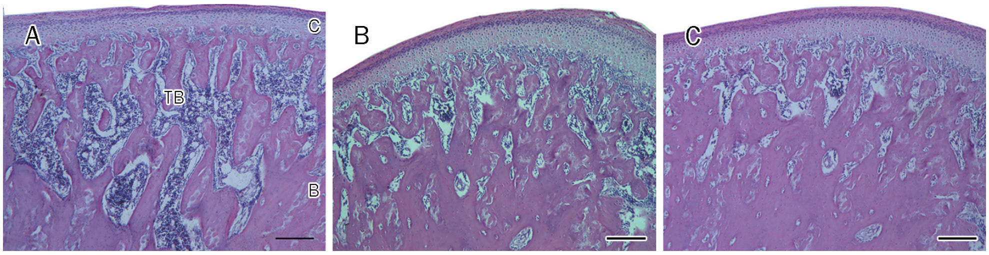

Figure 2. The histological morphology of mandibular condyle. (A–C) showed the morphology of middle-posterior region of mandibular condyle from control, low dose and high dose genistein-treatment groups. The area of trabecular bone in genistein-treatment group was obviously higher than that in control group. The space between trabecular bones in genistein-treatment group was obviously less than that in control group. C, cartilage; B, subchondral bone; TB, trabecular bone. Scale bar is 200 μm.

Table 3. Values of BMD and microstructural parameters after genistein treatment. Means±SEM. $^{b}P<0.05$, $^{c}P<0.01$ *vs* control group. $^{e}P<0.05$, $^{f}P<0.01$ *vs* low dose (10 mg/kg) genistein-treatment groups.

Parameters	Control group	Genistein (10 mg/kg)	Genistein (50 mg/kg)
BMD (mg/mm^3)	761.273±38.076	887.893±31.714^{b}	993.276±47.386^{ce}
BMC (mg)	0.097±0.004	0.111±0.007^{b}	0.124±0.008^{c}
Bone volume (mm^3)	0.079±0.002	0.089±0.005^{c}	0.093±0.004^{c}
BV/TV (%)	61.297±1.903	67.228±2.578^{b}	73.568±1.782^{cf}
Tb.Th (μm)	61.748±1.444	72.794±1.999^{c}	77.593±7.111^{c}
BS/BV (%)	31.993±1.184	27.806±1.325^{c}	25.923±2.112^{c}
Tb.N (#/mm^3)	10.170±0.296	9.182±0.611^{b}	9.088±0.525^{b}
Tb.Sp (μm)	0.102±3.654	31.204±1.504^{c}	28.176±1.850^{ce}

BMD, bone mineral density; BMC, bone mineral content; BV/TV, trabecular bone volume fraction; BS/BV, bone surface-to-volume ratio; Tb.Th, mean trabecular thickness; Tb.N, trabecular number; Tb.Sp, mean trabecular separation; BV, bone volume.

in the high-dose genistein-treated group was higher than that in low-dose group ($P<0.01$), while the Tb.Sp was lower in the high-dose group than that in the low-dose group ($P<0.05$).

Effect of genistein-treatment on the mRNA expression of ALP, OC, OPG, RANKL, ERα, and ERβ *in vivo*

As shown in Figure 3, gene expression of ALP, OC, OPG, ERα, and ERβ increased in the low-dose genistein-treated group (all $P<0.01$) compared with the control group, but that of RANKL decreased ($P<0.01$). In the high-dose genistein-treated group, however, the gene expression of ALP, OC, OPG, RANKL, and ERα decreased significantly (all $P<0.01$), but that of ERβ still increased compared with the control group ($P<0.01$). Gene expression of ALP, OC, OPG, and ERα in the low-dose genistein-treated group was higher than that in the high-dose group (all $P<0.01$). Additionally, the RANKL/OPG ratio decreased in both genistein-treated groups.

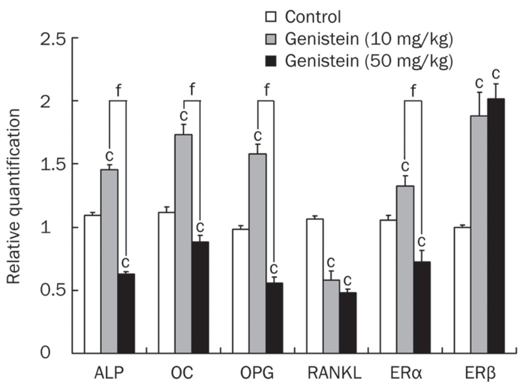

Figure 3. Effect of genistein treatment on the mRNA expression of ALP, OC, OPG, RANKL, ERα, and ERβ. Values were normalized to the expression of S18. Data shown are mean±SD (n=3). $^{c}P<0.01$ indicates significant difference between genistein-treatment and control groups. $^{f}P<0.01$ indicates significant difference between high and low dose genistein-treatment groups.

Effect of genistein-treatment on serum levels of bone-ALP, OC, OPG, RANKL, and CTX

Compared with the control group, the serum b-ALP, OC, and OPG levels increased significantly (all $P<0.01$), but the sRANKL level decreased ($P<0.01$) in the low-dose genistein-treated group (Table 3). No significant difference was found in the CTX level between control and low-dose genistein-treated groups. However, compared with the control group, not only the serum sRANKL and CTX (both $P<0.01$), but also b-ALP, OC, and OPG levels decreased ($P<0.05$, $P<0.05$, and $P<0.01$, respectively) in the high-dose genistein-treated group. The serum b-ALP, OC, OPG, and CTX levels in the low-dose genistein-treated group were higher than those in the high-dose group ($P<0.01$, $P<0.01$, $P<0.01$, and $P<0.05$, respectively). The RANKL/OPG ratio decreased in both genistein-treated groups (Table 4).

Table 4. Values of serum bone markers after genistein treatment. Mean±SEM. $^{b}P<0.05$, $^{c}P<0.01$ *vs* control group. $^{e}P<0.05$, $^{f}P<0.01$ *vs* low dose (10 mg/kg) genistein-treatment groups.

Parameters	Control group	Genistein (10 mg/kg)	Genistein (50 mg/kg)
b-ALP (U/L)	118.00±9.90	151.33±9.01^{c}	98.93±13.02^{bf}
OC (ng/mL)	9.95±1.27	13.93±2.55^{c}	7.76±1.73^{bf}
OPG (pg/mL)	335.24±18.50	403.67±19.36^{c}	255.64±23.14^{cf}
sRANKL (pg/mL)	22.53±3.18	13.15±2.17^{c}	11.64±2.56^{c}
CTX (ng/mL)	53.93±7.49	49.40±8.07	38.46±6.62^{ce}

b-ALP, bone alkaline phosphatase; sRANKL, soluble receptor activator of nuclear factor κB ligand.

Effect of genistein-treatment on the mRNA expression of ALP, OC, OPG, RANKL, ERα, and ERβ *in vitro*

As shown in Figure 4, genistein affected osteoblasts from mandibular condylar subchondral bone in a concentration-dependent manner. The presence of 10^{-7} mol/L genistein in

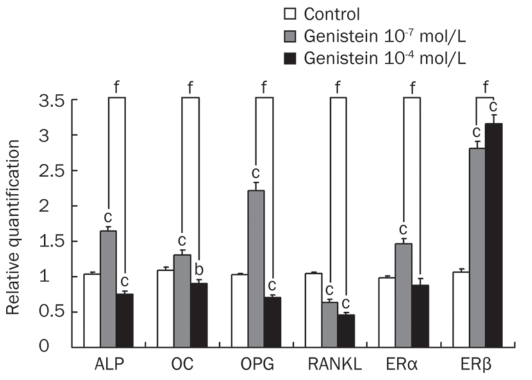

Figure 4. Effect of genistein treatment on the mRNA expression of ALP, OC, OPG, RANKL in osteoblasts. Values were normalized to the expression of 18S. Data shown are mean±SD (*n*=3). $^{b}P<0.05$, $^{c}P<0.01$ indicate significant difference between genistein treatment and control group. $^{f}P<0.01$ indicates significant difference between high and low dose genistein-treatment groups.

the culture medium induced a significant decrease in the gene expression of RANKL ($P<0.01$), as well as increase in ALP, OC, OPG, ERα, and ERβ (all $P<0.01$). However, the presence of 10^{-4} mol/L genistein reduced the expression of ALP, OC, OPG, RANKL ($P<0.01$, $P<0.05$, $P<0.01$, and $P<0.01$, respectively), as well as increase in ERβ expression ($P<0.01$). The expression of ALP, OC, OPG, RANKL and ERα in the 10^{-7} mol/L genistein-treated group were higher than those in the 10^{-4} mol/L group (all $P<0.01$). Alternatively, expression of ERβ was lower in the low-dose group than in the high-dose group (both $P<0.01$). The RANKL/OPG ratio was decreased by both 10^{-4} and 10^{-7} mol/L genistein treatment, respectively.

Effect of ER silencing on the effect of genistein treatment

In order to explore the function of ERα and ERβ, we performed gene silencing experiments in osteoblasts. The mRNA levels of ERα and ERβ were decreased in cells as detected by real-time PCR (Figure 5). ERα and ERβ siRNA were able to knockdown 72% and 80% of ER expression, respectively. As shown in Figure 6 and Figure 7, ERβ silencing reversed the effect of both 10^{-7} and 10^{-4} mol/L genistein treatment in the expression of ALP, OC, OPG, and RANKL. ERα silencing only reversed the expression of ALP and OPG (both $P<0.01$) in 10^{-7} mol/L genistein-treatment group, and that of OPG in the 10^{-4} mol/L genistein-treated group ($P<0.05$). Importantly, the effect of ERβ silencing was greater than that of ERα silencing in nearly all of the groups with the exception of OC expression in the 10^{-4} mol/L genistein-treated group (all $P<0.01$).

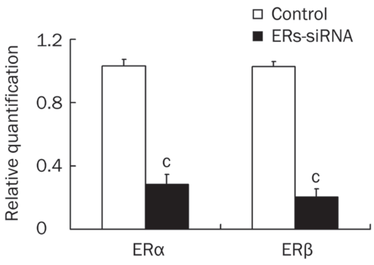

Figure 5. Effect of ERα and ERβ siRNA on the mRNA expression of ERα and ERβ in osteoblasts. Values were normalized to the expression of 18S. Data shown are mean±SD (*n*=3). $^{c}P<0.01$ *vs* control.

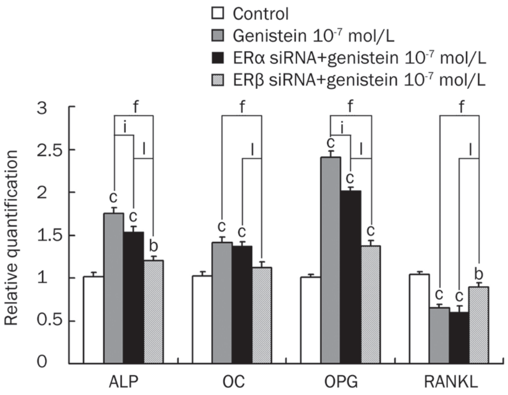

Figure 6. Effect of ERα and ERβ silencing on the expression of ALP, OC, OPG, RANKL in osteoblasts treated by 10^{-7} mol/L genistein. Values were normalized to the expression of 18S. Data shown are mean±SD (*n*=3). $^{b}P<0.05$, $^{c}P<0.01$ indicate significant difference between genistein treatment and control group. $^{f}P<0.01$ indicates significant difference between 10^{-7} mol/L genistein-treatment group and ERα siRNA+10^{-7} mol/L genistein-treatment group. $^{i}P<0.01$ indicates significant difference between 10^{-7} mol/L genistein-treatment group and ERβ siRNA+10^{-7} mol/L genistein-treatment group. $^{l}P<0.01$ indicates significant difference between ERα siRNA+10^{-7} mol/L genistein-treatment group and ERβ siRNA+10^{-7} mol/L genistein-treatment group.

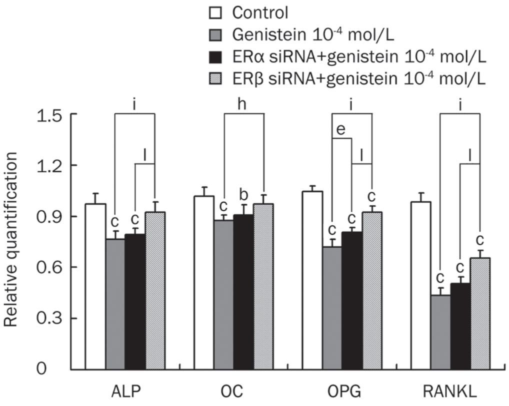

Figure 7. Effect of ERα and ERβ silencing on the expression of ALP, OC, OPG, RANKL in osteoblasts treated by 10^{-4} mol/L genistein. Values were normalized to the expression of 18S. Data shown are mean±SD (*n*=3). $^{b}P<0.05$, $^{c}P<0.01$ indicate significant difference between genistein treatment and control group. $^{e}P<0.05$ indicates significant difference between 10^{-4} mol/L genistein-treatment group and ERα siRNA+10^{-4} mol/L genistein-treatment group. $^{h}P<0.05$, $^{i}P<0.01$ indicate significant difference between 10^{-4} mol/L genistein-treatment group and ERβ siRNA+10^{-4} mol/L genistein-treatment group. $^{l}P<0.01$ indicates significant difference between ERα siRNA+10^{-4} mol/L genistein-treatment group and ERβ siRNA+10^{-4} mol/L genistein-treatment group.

Discussion

In the literature, the protective effects of genistein in OVX rats and mice preventing OVX-induced bone loss have been reported in appendicular bone or vertebrae for various treatment periods (2–15 weeks), application routes (oral gavage, intraperitoneal administration, subcutaneous administration) and doses of genistein (3–50 $mg \cdot kg^{-1} \cdot d^{-1}$)[18, 20, 30–36]. Similarly, oral administration of genistein (54 $mg \cdot kg^{-1} \cdot d^{-1}$) increased BMD of the spine and hip in osteopenic postmenopausal Caucasian women with an observation period of 24 months[17]. In the present study on female rats with normal estrogen levels, both low and high doses of genistein treatment were observed to induce significant increase in BMD, BMC and bone volume, as well as inducing thicker and larger trabecular bone in the mandibular subchondral bone. These results were consistent with the above-mentioned studies on appendicular bone or vertebrae[17, 18, 20, 30–36], indicating that the effect of genistein on mandibular subchondral bone is similar to that on appendicular bone or vertebrae.

Similar to the biphasic effects of estrogen depending on dosage[37], genistein was also observed to have a biphasic cell proliferative response, stimulation at low concentrations and inhibition at high concentrations[38–40]. In the present study low dose genistein treatment increased the expression of ALP, OC, and OPG at the serum level and mRNA level both *in vivo* and *in vitro*. Low-dose genistein treatment also decreased the expression of RANKL and the RANKL/OPG ratio in agreement with previous studies[20, 41–44]. These data suggest that normal doses of genistein improve bone formation and inhibit bone resorption. However, high-dose genistein treatment decreased not only the expression of RANKL and the RANKL/OPG ratio, but also that of ALP, OC, and OPG. It indicates that excess genistein inhibits both bone resorption and bone formation in rat mandibular subchondral bone. This phenomenon is consistent with the fact that the number of both active osteoclasts and active osteoblasts is increased in postmenopausal osteoporosis induced by estrogen deficiency[45]. Although bone formation was also inhibited by excess genistein, the RANKL/OPG ratio was still lower in the high-dose genistein-treated group than in the control group, which is in line with the increased BMD and bone volume in the high-dose genistein-treated group. Interestingly, though bone formation was inhibited by excess genistein to some extent, high doses of genistein induced more mandibular subchondral trabecular bone compared to low-dose genistein. This discrepancy might be due to the sampling time-point, or the asynchronism between microstructural parameters and the expression of bone homeostasis-associated factors. Allowing for these considerations, further studies with additional time-points are needed.

A mechanism has been proposed in which genistein affects bone homeostasis directly via ER activation in bone[34]. The two subtypes of ER, ERα, and ERβ, are distinct proteins encoded by separate genes located on different chromosomes. Genistein is almost exclusively ERβ selective and binds with a 7- to 30-fold greater affinity to ERβ than to ERα[40]. Furthermore, genistein activates transcriptional activation of ERβ at a 10-fold lower concentration than for ERα[40]. In the present study, the expression of ERβ was increased significantly by both low and high doses of genistein, while the expression of ERα was increased by low dose of genistein, but decreased by high dose of genistein. Furthermore, ERβ silencing reversed the effect of genistein treatment on the expression of ALP, OC, OPG, and RANKL. The effect of ERβ silencing was greater than that of ERα silencing. It seems that the effect of genistein on rat mandibular subchondral bone was preferentially mediated via ERβ activation, which is in keeping with the previous report that the effect of genistein on skeletal muscle myosin heavy chain expression was predominantly mediated through ERβ[46].

In the literature, a few studies support ERα's involvement in the adaptive response of osteoblasts to mechanical strain[47–50]. ERα–/– mice produced three times less new cortical bone in response to the same mechanical stimulus as their ERα+/+ littermates[47, 48]. Similarly, osteoblasts derived from ERα–/– mice failed to increase in number in response to mechanical stimulation, which can be rescued by transfection with fully functional ERα[49, 50]. The decreased expression of ERα in the high-dose genistein-treated group may imply a decreased adaptive capacity of mandibular subchondral bone to mechanical loads. Considering the difference and fluctuation of estrogen levels in individual people, the proper dose of genistein should be studied in more depth prior to wide application of genistein in the treatment of osteoporosis or OA.

In summary, low-dose genistein can increase bone formation and inhibit bone resorption, while excess genistein can inhibit both bone resorption and bone formation in rat mandibular condylar subchondral bone, which was predominantly mediated through ERβ.

Acknowledgements

The authors thank Mr Jun WANG (Xijing Hospital, Fourth Military Medical University) for technical assistance in micro-CT. This work was financially supported by the National Natural Science Foundation of China (N<u>o</u> 30901699 and N<u>o</u> 30928028).

Author contribution

Shi-bin YU and Guang-ying DONG designed the present study and wrote the manuscript. Yong-qi LI performed the animal treatments, sample preparation and micro-CT analysis. Xiang-hui XING performed the ELISA assay, PCR and revised the manuscript. Hui WANG performed the osteoblast culture, ER silencing and PCR *in vivo*. Xi-li WENG performed the HE staining, data analysis and revised the manuscript.

References

1 Hohenhaus MH, McGarry KA, Col NF. Hormone therapy for the prevention of bone loss in menopausal women with osteopenia: is it a viable option? Drugs 2007; 67: 2311–21.

2 Levine JP. Effective strategies to identify postmenopausal women at risk for osteoporosis. Geriatrics 2007; 62: 22–30.

3 Fitzpatrick LA. Estrogen therapy for postmenopausal osteoporosis. Arq Bras Endocrinol Metabol 2006; 50: 705–19.
4 Nevitt MC, Cummings SR, Lane NE, Hochberg MC, Scott JC, Pressman AR, *et al*. Association of estrogen replacement therapy with the risk of osteoarthritis of the hip in elderly white women. Study of Osteoporotic Fractures Research Group. Arch Intern Med 1996; 156: 2073–80.
5 Zhang Y, McAlindon TE, Hannan MT, Chaisson CE, Klein R, Wilson PW, *et al*. Estrogen replacement therapy and worsening of radiographic knee osteoarthritis: the Framingham Study. Arthritis Rheum 1998; 41: 1867–73.
6 Spector TD, Nandra D, Hart DJ, Doyle DV. Is hormone replacement therapy protective for hand and knee osteoarthritis in women? The Chingford Study. Ann Rheum Dis 1997; 56: 432–4.
7 Stevenson JC. Hormone replacement therapy: review, update, and remaining questions after the Women's Health Initiative Study. Curr Osteoporos Rep 2004; 2: 12–6.
8 Collaborative Group on Hormonal Factors in Breast Cancer. Breast cancer and hormone replacement therapy: collaborative reanalysis of data from 51 epidemiological studies of 52,705 women with breast cancer and 108,411 women without breast cancer. Lancet 1997; 350: 1047–59.
9 Million Women Study Collaborators. Breast cancer and hormone-replacement therapy in the Million Women Study. Lancet 2003; 362: 419–27.
10 Setchell KD, Lydeking-Olsen E. Dietary phytoestrogens and their effect on bone: evidence from *in vitro* and *in vivo*, human observational, and dietary intervention studies. Am J Clin Nutr 2003; 78: 593S–609S.
11 Messina M, Ho S, Alekel DL. Skeletal benefits of soy isoflavones: a review of the clinical trial and epidemiologic data. Curr Opin Clin Nutr Metab Care 2004; 7: 649–58.
12 Chanawirat A, Khemapech S, Patumraj S, Siriviriyakul P. Genistein replacement therapy on endothelial dysfunction and bone loss in bilateral ovariectomized rats. Clin Hemorheol Microcirc 2006; 34: 309–14.
13 Erlandsson MC, Islander U, Moverare S, Ohlsson C, Carlsten H. Estrogenic agonism and antagonism of the soy isoflavone genistein in uterus, bone and lymphopoiesis in mice. APMIS 2005; 113: 317–23.
14 Chen YM, Ho SC, Lam SS, Ho SS, Woo JL. Beneficial effect of soy isoflavones on bone mineral content was modified by years since menopause, body weight, and calcium intake: a double-blind, randomized, controlled trial. Menopause 2004; 11: 246–54.
15 Wu J, Oka J, Higuchi M, Tabata I, Toda T, Fujioka M, *et al*. Cooperative effects of isoflavones and exercise on bone and lipid metabolism in postmenopausal Japanese women: a randomized placebo-controlled trial. Metabolism 2006; 55: 423–33.
16 Morabito N, Crisafulli A, Vergara C, Gaudio A, Lasco A, Frisina N, *et al*. Effects of genistein and hormone-replacement therapy on bone loss in early postmenopausal women: a randomized double-blind placebo-controlled study. J Bone Miner Res 2002; 17: 1904–12.
17 Marini H, Minutoli L, Polito F, Bitto A, Altavilla D, Atteritano M, *et al*. Effects of the phytoestrogen genistein on bone metabolism in osteopenic postmenopausal women: a randomized trial. Ann Intern Med 2007; 146: 839–47.
18 Li B, Yu S. Genistein prevents bone resorption diseases by inhibiting bone resorption and stimulating bone formation. Biol Pharm Bull 2003; 26: 780–6.
19 Sliwiński L, Folwarczna J, Nowińska B, Cegieła U, Pytlik M, Kaczmarczyk-Sedlak I, *et al*. A comparative study of the effects of genistein, estradiol and raloxifene on the murine skeletal system. Acta Biochim Pol 2009; 56: 261–70.
20 Bitto A, Burnett BP, Polito F, Marini H, Levy RM, Armbruster MA, *et al*. Effects of genistein aglycone in osteoporotic, ovariectomized rats: a comparison with alendronate, raloxifene and oestradiol. Br J Pharmacol 2008; 155: 896–905.
21 Tähtelä R, Thölix E. Serum concentrations of type I collagen carboxy-terminal telopeptide (ICTP) and type I procollagen carboxy-and amino-terminal propeptides (PICP, PINP) as markers of metastatic bone disease in breast cancer. Anticancer Res 1996; 16: 2289–93.
22 Shoji K, Elsubeihi ES, Heersche JN. Effects of ovariectomy on turnover of alveolar bone in the healed extraction socket in rat edentulous mandible. Arch Oral Biol 2011; 56: 114–20.
23 Jonasson G, Alstad T, Vahedi F, Bosaeus I, Lissner L, Hakeberg M. Trabecular pattern in the mandible as bone fracture predictor. Oral Surg Oral Med Oral Pathol Oral Radiol Endod 2009; 108: e42–51.
24 Griffin CJ, Powers R, Kruszynski R. The incidence of osteoarthritis of the temporomandibular joint in various cultures. Aust Dent J 1979; 24: 94–106.
25 Milam SB. Pathophysiology and epidemiology of TMJ. J Musculoskelet Neuronal Interact 2003; 3: 382–90.
26 Jiao K, Dai J, Wang MQ, Niu LN, Yu SB, Liu XD. Age- and sex-related changes of mandibular condylar cartilage and subchondral bone: a histomorphometric and micro-CT study in rats. Arch Oral Biol 2010; 55: 155–63.
27 Michael MR, Wolz E, Davidovich A, Pfannkuch F, Edwards JA, Bausch J. Acute, subchronic and chronic safety studies with genistein in rats. Food Chem Toxicol 2006; 44: 56–80.
28 Seibel J, Molzberger AF, Hertrampf T, Laudenbach-Leschowski U, Diel P. Oral treatment with genistein reduces the expression of molecular and biochemical markers of inflammation in a rat model of chronic TNBS-induced colitis. Eur J Nutr 2009; 48: 213–20.
29 Viereck V, Gründker C, Blaschke S, Siggelkow H, Emons G, Hofbauer LC. Phytoestrogen genistein stimulates the production of osteoprotegerin by human trabecular osteoblasts. J Cell Biochem 2002; 84: 725–35.
30 Ishida H, Uesugi T, Hirai K, Toda T, Nukaya H, Yokotsuka K, *et al*. Preventive effects of the plant isoflavones, daidzin and genistin, on bone loss in ovariectomized rats fed a calcium-deficient diet. Biol Pharm Bull 1998; 21: 62–6.
31 Nakajima D, Kim CS, Oh TW, Yang CY, Naka T, Igawa S, *et al*. Suppressive effects of genistein dosage and resistance exercise on bone loss in ovariectomized rats. J Physiol Anthropol Appl Human Sci 2001; 20: 285–91.
32 Ye SF, Saga I, Ichimura K, Nagai T, Shinoda M, Matsuzaki S. Coumestrol as well as isoflavones in soybean extract prevent bone resorption in ovariectomized rats. Endocr Regul 2003; 37: 145–52.
33 Pie JE, Park JH, Park YH, Ryu YM, Kim KN, Suh SW, *et al*. Effect of genistein on the expression of bone metabolism genes in ovariectomized mice using a cDNA microarray. J Nutr Biochem 2006; 17: 157–64.
34 Hertrampf T, Gruca MJ, Seibel J, Laudenbach U, Fritzemeier KH, Diel P. The bone-protective effect of the phytoestrogen Genistein is mediated via ERα-dependent mechanisms and strongly enhanced by physical activity. Bone 2007; 40: 1529–35.
35 Hertrampf T, Schleipen B, Offermanns C, Velders M, Laudenbach U, Diel P. Comparison of the bone protective effects of an isoflavone-rich diet with dietary and subcutaneous administrations of genistein in ovariectomized rats. Toxicol Lett 2009; 184: 198–203.
36 Dai R, Ma Y, Sheng Z, Jin Y, Zhang Y, Fang L, *et al*. Effects of genistein on vertebral trabecular bone microstructure, bone mineral density, microcracks, osteocyte density, and bone strength in ovariectomized rats. J Bone Miner Metab 2008; 26: 342–9.
37 Cheng P, Ma X, Xue Y, Li S, Zhang Z. Effects of estradiol on proliferation and metabolism of rabbit mandibular condylar cartilage cells *in*

vitro. Chin Med J (Engl) 2003; 116: 1413–7.

38 Maggiolini M, Bonofiglio D, Marsico S, Panno ML, Cenni B, Picard D, Ando S. Estrogen receptor α mediates the proliferative but not the cytotoxic dose-dependent effects of two major phytoestrogens on human breast cancer cells. Mol Pharmacol 2001; 60: 595–602.

39 Power KA, Thompson LU. Ligand-induced regulation of ERα and ERβ is indicative of human breast cancer cell proliferation. Breast Cancer Res Treat 2003; 82: 209–21.

40 Rajah TT, Du N, Drews N, Cohn R. Genistein in the presence of 17beta-estradiol inhibits proliferation of ERbeta breast cancer cells. Pharmacology 2009; 84: 68–73.

41 Marini H, Minutoli L, Polito F, Bitto A, Altavilla D, Atteritano M, *et al*. OPG and sRANKL serum concentrations in osteopenic, postmenopausal women after 2-year genistein administration. J Bone Miner Res 2008; 23: 715–20.

42 Crisafulli A, Altavilla D, Squadrito G, Romeo A, Adamo EB, Marini R, *et al*. Effects of the phytoestrogen genistein on the circulating soluble receptor activator of nuclear factor kappaB ligand-osteoprotegerin system in early postmenopausal women. J Clin Endocrinol Metab 2004; 89: 188–92.

43 Zhang Y, Li Q, Wan HY, Helferich WG, Wong MS. Genistein and a soy extract differentially affect three-dimensional bone parameters and bone-specific gene expression in ovariectomized mice. J Nutr 2009; 139: 2230–6.

44 Ha H, Lee HY, Lee JH, Jung D, Choi J, Song KY, *et al*. Formononetin prevents ovariectomy-induced bone loss in rats. Arch Pharm Res 2010; 33: 625–32.

45 Lerner UH. Bone remodeling in post-menopausal osteoporosis. J Dent Res 2006; 85: 584–95.

46 Velders M, Solzbacher M, Schleipen B, Laudenbach U, Fritzemeier KH, Diel P. Estradiol and genistein antagonize the ovariectomy effects on skeletal muscle myosin heavy chain expression via ER-beta mediated pathways. J Steroid Biochem Mol Biol 2010; 120:53–9.

47 Lee K, Jessop H, Suswillo R, Zaman G, Lanyon L. Endocrinology: bone adaptation requires oestrogen receptor-alpha. Nature 2003; 424: 389.

48 Lee KC, Jessop H, Suswillo R, Zaman G, Lanyon LE. The adaptive response of bone to mechanical loading in female transgenic mice is deficient in the absence of oestrogen receptor-alpha and -beta. J Endocrinol 2004; 182: 193–201.

49 Jessop HL, Suswillo RF, Rawlinson SC, Zaman G, Lee K, Das-Gupta V, *et al*. Osteoblast-like cells from estrogen receptor alpha knockout mice have deficient responses to mechanical strain. J Bone Miner Res 2004; 19: 938–46.

50 Zaman G, Cheng MZ, Jessop HL, White R, Lanyon LE. Mechanical strain activates estrogen response elements in bone cells. Bone 2000; 27: 233–9.

Acta Pharmacologica Sinica (2012) 33: 75–81
© 2012 CPS and SIMM All rights reserved 1671-4083/12 $32.00
www.nature.com/aps

Original Article

Glucagon-like peptide-1 activates endothelial nitric oxide synthase in human umbilical vein endothelial cells

Li DING, Jin ZHANG*

Department of Endocrinology, First Affiliated Hospital of China Medical University, Shenyang 110001, China

Aim: To investigate the effects of glucagon-like peptide-1 (GLP-1) on endothelial NO synthase (eNOS) in human umbilical vein endothelial cells (HUVECs), and elucidate whether GLP-1 receptor (GLP-1R) and GLP-1(9–36) are involved in these effects.
Methods: HUVECs were used. The activity of eNOS was measured with NOS assay kit. Phosphorylated and total eNOS proteins were detected using Western blot analysis. The level of eNOS mRNA was quantified with real-time RT-PCR.
Results: Incubation of HUVECs with GLP-1 (50–5000 pmol/L) for 30 min significantly increased the activity of eNOS. Incubation of HUVECs with GLP-1 (500–5000 pmol/L) for 5 or 10 min increased eNOS phosphorylated at ser-1177. Incubation with GLP-1 (5000 pmol/L) for 48 h elevated the level of eNOS protein, did not affect the level of eNOS mRNA. GLP-1R agonists exenatide and GLP-1(9–36) at the concentration of 5000 pmol/L increased the activity, phosphorylation and protein level of eNOS. GLP-1R antagonist exendin(9–39) or DPP-4 inhibitor sitagliptin, which abolished GLP-1(9–36) formation, at the concentration of 5000 pmol/L partially blocked the effects of GLP-1 on eNOS.
Conclusion: GLP-1 upregulated the activity and protein expression of eNOS in HUVECs through the GLP-1R-dependent and GLP-1(9–36)-related pathways. GLP-1 may prevent or delay the formation of atherosclerosis in diabetes mellitus by improving the function of eNOS.

Keywords: glucagon-like peptide-1; human umbilical vein endothelial cell; endothelial NO synthase; atherosclerosis; diabetes mellitus

Acta Pharmacologica Sinica (2012) 33: 75–81; doi: 10.1038/aps.2011.149; published online 28 Nov 2011

Introduction

Endothelial nitric oxide synthase (eNOS), which synthesizes nitric oxide (NO) from the substrate *L*-arginine in endothelial cells (ECs), plays an important role in regulating a broad spectrum of functions in the cardiovascular system, including vasorelaxation, the inhibition of leukocyte-endothelial adhesion, vascular smooth muscle cell (SMC) migration and proliferation, and platelet aggregation[1]. NO is the most important endothelium-derived vasodilator and has a potent anti-atherosclerotic effect because of its anti-oxidative, anti-inflammatory and anti-coagulatory properties[2, 3]. Pathological changes such as insulin resistance and the metabolic alterations in type 2 diabetes mellitus (T2DM) can lead to eNOS dysfunction and relatively low NO production, which are now considered the major mechanisms of macrovascular complications in T2DM.

Glucagon-like peptide-1 (GLP-1) is a gut hormone that is released into the bloodstream after feeding. Potentiating the insulinotropic action of glucose, GLP-1 is effective in controlling glucose by stimulating insulin secretion. The impaired secretion of GLP-1 in patients with T2DM has been considered to be one of the mechanisms underlying their abnormal glucose metabolism[4–7]. Thus, its analogues have been used clinically to treat T2DM[8]. Recently, many researchers have turned their attention to the cardiovascular effects of GLP-1 and have found that GLP-1 can induce endothelium-dependent vasorelaxation[9–11] and improve the response of vessels to other vasodilators[12–14]. Furthermore, GLP-1 can elevate the NO levels in coronary effluent from mouse hearts, and its vasorelaxing effect can be blocked by an eNOS inhibitor[11], suggesting that GLP-1 upregulates eNOS. Taken together, we reason that GLP-1 may be an endogenous vascular-protective hormone and an extremely effective drug target for pharmacological intervention in T2DM patients.

GLP-1 exerts its actions through GLP-1 receptor (GLP-1R), which is also expressed in the endothelium[11, 13, 15]. Native GLP-1, existing mainly as an intact, biologically active form

---

* To whom correspondence should be addressed.
E-mail zhangjininsy@gmail.com
Received 2011-05-20 Accepted 2011-09-30

(GLP-1 [7–36 amide]), is rapidly degraded after secretion by depeptidyl peptidase-4 (DPP-4) to its inactive form, N-terminally truncated GLP-1(9–36). GLP-1(9–36) has a weak affinity to GLP-1R and was previously considered to have no biological function. However, some research has suggested that GLP-1(9–36), which offers significant cardioprotection against ischemia-reperfusion injury and induces vasodilation[10, 11, 16], may affect GLP-1 function, at least in the cardiovascular system.

In the present study, to improve our understanding of the mechanism by which GLP-1 may exert cardiovascular-protective effects, we investigated the effect of GLP-1 on the activation and expression of eNOS in human umbilical vein endothelial cells (HUVECs). In addition, we investigated whether the GLP-1R-dependent or GLP-1(9–36)-related pathways are involved in these effects.

Materials and methods

Cell culture

Primary human umbilical vein endothelial cells (HUVECs) derived from normal human placenta umbilical cord tissues were purchased from Pricells Company (Wuhan, China). They were verified with vWF, FactorVIII and CD31 (P-CAM), and frozen in liquid nitrogen at the end of primary culture. After the purchase, they were recovered and sub-cultured in endothelial cell medium containing 5% fetal bovine serum (FBS) and 1% endothelial cell growth supplement (ScienCell, San Diego, CA, USA) in a humidified atmosphere of 95% air and 5% CO_2 at 37 °C. The cells from the 3rd–6th passages were used in all of the experiments. When grown to 70%–90% confluence, the cells were incubated in the presence or absence of GLP-1 (ProSpec, Rehovot, Israel), exenatide (a GLP-1R agonist) (Lilly, Indianapolis, IN, USA), GLP-1(9–36) (Chinese Peptide, Hangzhou, China), exendin(9–39) (a GLP-1R antagonist) (Sigma, St Louis, MO, USA) or sitagliptin (an inhibitor of DPP-4) (HKBY, Beijing, China) for various times and then collected for further analysis.

Measurement of eNOS activity

The activities of eNOS were assayed with an NOS assay kit (Beyotime, Haimen, China) according to the manufacturer's instructions. The cells were grown to 90% confluence in 96-well microplates and incubated with or without 5-5000 pmol/L GLP-1, GLP-1(9–36) or exenatide in a 200 µL system containing sufficient substrates of NOS (*eg*, NADPH and *L*-Arginine) and 3-Amino, 4-aminomethyl-2′,7′-difluorescein, diacetate (DAF-FM DA), a cell-permeable fluorescent substance. After incubation at 37 °C for 30 min, the fluorescence intensity (FI) was detected using a microplate reader (Infinite®200 Pro, Tecan, Switzerland) with an excitation wavelength of 495 nm and an emission wavelength of 515 nm. Each plate also included at least 2 negative control wells to which no cells were added. The relative activities (RA) of eNOS were calculated as follows:

$$RA=(FI_{\text{sample}}\text{-}FI_{\text{negative}})/(FI_{\text{control}}\text{-}FI_{\text{negtive}})$$

Western blot analysis

Western blot analysis was used to quantify the total and phosphorylated (ser-1177) levels of eNOS proteins and to detect the expression of GLP-1R and DPP-4 in HUVECs. Cells were washed 3 times with ice-cold PBS and then lysed with ice-cold RIPA lysis buffer (Beyotime) supplemented with 1 mmol/L phenylmethanesulfonyl fluoride (Beyotime) and phosphatase inhibitors (YuanPingHao Bio, Beijing, China). The cell lysates were centrifuged (12 000×*g*, 12 min, 4 °C), and the supernatants were collected. Protein concentrations were determined using a BCA kit (Beyotime). Equal amounts of samples (50 µg) were denatured and subjected to 10% SDS-PAGE. The separated proteins were then electro-transferred onto a PVDF membrane blocked with 5% (*w/v*) fat-free milk powder in Tris-buffered saline with Tween (TBST) for 2 h. The membranes were incubated overnight at 4 °C with primary antibodies as follows: anti-eNOS (1:400), anti-phospho-eNOS (ser-1177) (1:200), anti-GLP-1R (1:400), anti-DPP-4 (1:400) and anti-β-actin (1:500) (Santa Cruz Biotechnology, Santa Cruz, CA, USA). The membranes were then washed and incubated with horseradish peroxidase-conjugated goat anti-rabbit IgG (1:5000) in TBST for 2 h at room temperature. The immunostained proteins were visualized by enhanced chemiluminescence (ECL; Santa Cruz Biotechnology). The intensities of the bands were quantified using a Gel Doc™ XR imaging system (Bio-Rad Laboratories, Hercules, CA, USA) and Quantity One software.

Real-time RT-PCR

HUVECs were lysed on ice with TRIzol (1 mL/well) (GBCBIO, Guangzhou, China), and total RNA was extracted with chloroform and isopropanol according to the manufacturer's protocol. The extracted RNA was quantified using NaNoDrop (NaNoDrop Technologies, Wilmington, DE, USA). cDNA was synthesized from 1 µg of total RNA using the PrimeScript® RT Reagent Kit (Takara, Dalian, China). The levels of eNOS transcripts were quantified with real-time RT-PCR using SYBR® Premix Ex Taq™ (Takara Bio) according to the manufacturer's instructions. The primer pairs used in the real-time PCR for human eNOS were 5′-TCCACGATGGTGACTTTGGCTA-3′ (sense) and 5′-GCTGTCTGCATGGACCTGGA-3′ (antisense), and the primer pairs used for the human housekeeping gene β-actin were 5′-TGGCACCCAGCACAATGAA-3′ (sense) and 5′-CATAGTCATAGTCCGCCTAGAAGCA-3′ (antisense). The PCR reactions were carried out in a Rotor–Gene 6000 system (Corbett Life Science, Australia) under the following conditions: 95 °C for 30 s, 45 cycles at 95 °C for 5 s and 55 °C for 30 s. The expression level of eNOS relative to β-actin (the internal reference gene) was calculated and adjusted against the expression levels of untreated samples, which were deemed to be 1.0. The calculation formula is as follows: eNOS relative gene expression=(eNOS gene concentration in treatment group/β-actin gene concentration of the same sample)/(eNOS gene concentration in control group/β-actin gene concentration of the same sample).

Statistical analysis

A statistical analysis was performed with SPSS version 13.0 (SPSS Inc, Chicago, IL, USA). Data are presented as the mean±SD. Multiple comparisons were evaluated by a one-way ANOVA followed by the S-N-K test. $P<0.05$ was considered statistically significant.

Results

GLP-1 promotes eNOS activities in HUVECs

The incubation of HUVECs with GLP-1 for 30 min increased eNOS activity (Figure 1A). GLP-1 increased eNOS activity at 5 pmol/L, but the difference was not significant. Higher concentrations of GLP-1 (50–5000 pmol/L) significantly enhanced eNOS activity. As indicated in Figure 1B, GLP-1-induced NO production was blocked by N^G-nitro-*L*-arginine methyl ester (*L*-NAME) (1 mmol/L), suggesting that eNOS activation mediated the effect of GLP-1 on NO release in HUVECs.

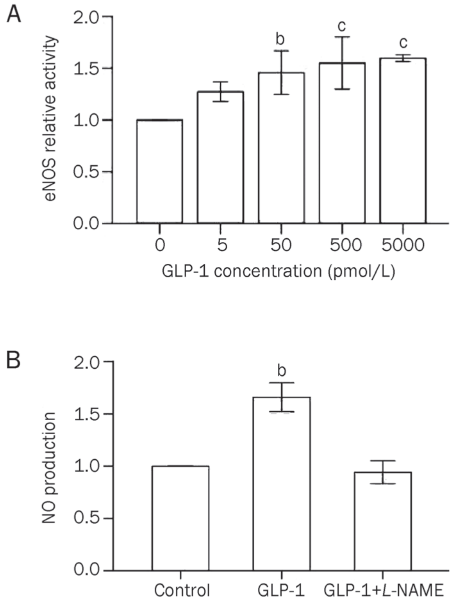

Figure 1. GLP-1 promotes endothelial nitric oxide synthase (eNOS) activity in human umbilical vein endothelial cells (HUVECs). HUVECs were incubated for 30 min in the absence or presence of GLP-1 (5–5000 pmol/L). Nitric oxide production was assayed using the fluorescent probe DAF-FM in the presence or absence of *L*-NAME (1 mmol/L). The experiment was repeated 3 times, and the values are means±SD. $^bP<0.05$, $^cP<0.01$ compared with control.

GLP-1 stimulates the phosphorylation of eNOS in HUVECs

The activity of eNOS is regulated by phosphorylation at multiple sites. The most thoroughly studied site is the activation site ser-1177[17]. Several protein kinases, including Akt/PKB, PKA, and AMPK, activate eNOS by phosphorylating ser-1177 in response to various stimuli, such as insulin and fluid shear stress[18, 19]. We thus investigated whether GLP-1 increases ser-1177 phosphorylation. The incubation of HUVECs with GLP-1 (5000 pmol/L) for 5, 10, and 30 min increased the phosphorylation of eNOS (ser-1177), with the most significant effect being obtained at 5 min (Figure 2A). For the dose course study, 500–5000 but not 50 pmol/L GLP-1 significantly enhanced the phosphorylation of eNOS at ser-1177 (Figure 2B).

The effects of GLP-1 on eNOS mRNA and protein levels in HUVECs

Cells were incubated with 5000 pmol/L GLP-1 for 6, 12, 24, and 48 h. Real-time RT-PCR revealed no significant difference in eNOS mRNA expression between these groups (Figure 2C). Western blot analysis indicated that GLP-1 could upregulate eNOS protein expression after a 48-h incubation (Figure 2D).

The GLP-1R and GLP-1(9–36)-related pathways are involved in the effect of GLP-1 on eNOS

Exenatide is a synthesized GLP-1 receptor agonist, and it may mimic GLP-1R-mediated effects, such as GLP-1-stimulated insulin release. To determine whether a GLP-1R-dependent or GLP-1(9–36)-related pathway (*ie*, GLP-1R independent) is responsible for the effects of GLP-1 on eNOS, we investigated the influence of exenatide and GLP-1(9–36) on eNOS in HUVECs. We also confirmed the expression of GLP-1R and DPP-4 proteins in HUVECs[15, 20] by Western blot analysis (Figure 3A). Like GLP-1, exenatide or GLP-1(9–36) treatment (5000 pmol/L) effectively promoted eNOS activity (Figure 3B), the phosphorylation of eNOS at ser-1177 (Figure 3C) and eNOS protein levels (Figure 3D) in HUVECs. Exenatide and GLP-1 had no effect on eNOS mRNA expression, but GLP-1(9–36) increased the mRNA levels approximately twofold after an incubation period of 48 h (Figure 3E). To further confirm the involvement of the GLP-1R-dependent and GLP-1(9–36)-related pathways in the effects of GLP-1 on eNOS, we investigated the influence of GLP-1R blockage and DPP-4 inhibition on the effects of GLP-1. The synthesized GLP-1R antagonist exendin(9–39) and the DPP-4 inhibitor sitagliptin, which can abolish GLP-1(9–36) formation, were employed in this study. The incubation of 5000 pmol/L exendin(9–39) or sitagliptin (Figure 3F–3H) partially blocked the GLP-1-induced enhancement of eNOS activity, phosphorylation and total eNOS protein levels. Unexpectedly, cotreatment with exendin(9–39) and sitagliptin, compared with each single treatment, further attenuated but could not completely abolish the aforementioned upregulatory effects of GLP-1 on eNOS (Figure 3F–3H).

Discussion

Because GLP-1 induces endothelium-dependent vasodilation in human and rat arteries, we speculate that it may activate eNOS and increase NO production. eNOS plays an important role in maintaining normal endothelial function, and its dysfunction may be significantly associated with the cardiovascular complications in T2DM. Here, we investigated the effects of GLP-1 on the activation and expression of eNOS in HUVECs and whether GLP-1R and GLP-1(9–36) mediate these effects. Administration of 500–5000 pmol/L of GLP-1 promoted eNOS activity and phosphorylation at ser-1177 after 5

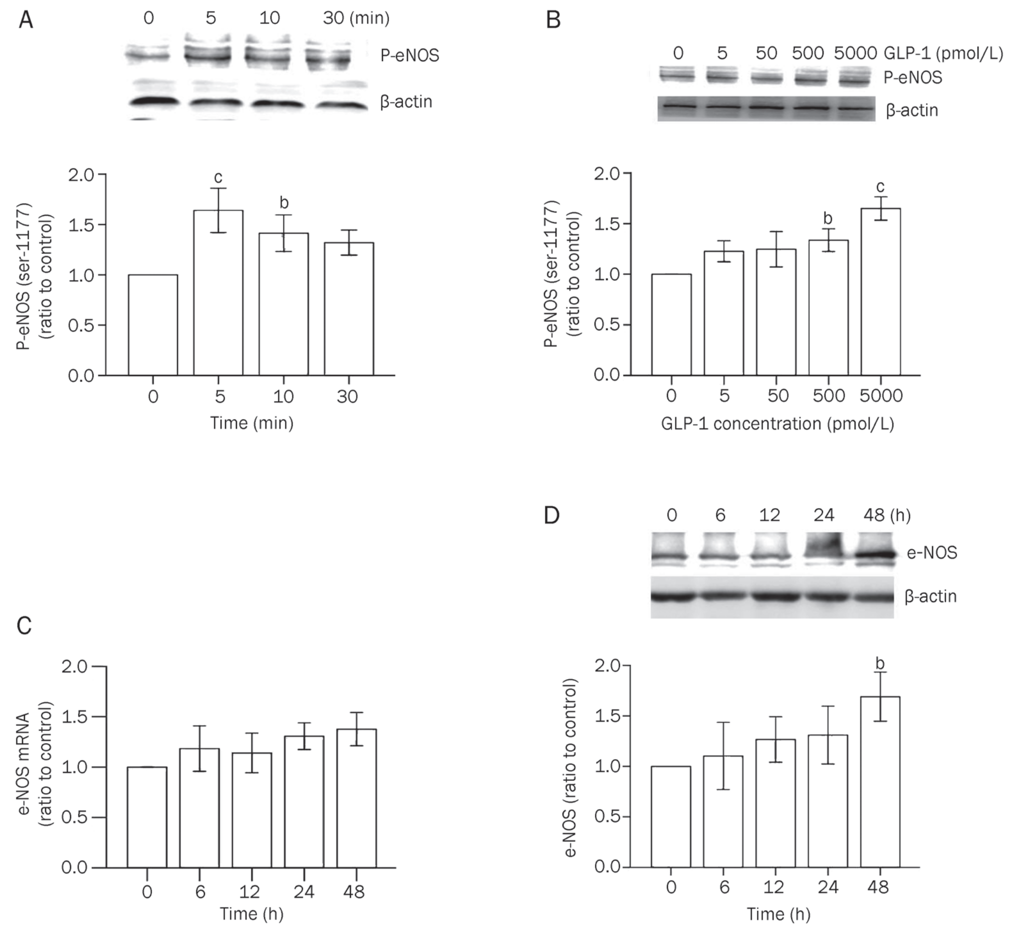

Figure 2. Effects of GLP-1 on eNOS Ser-1177 phosphorylation, mRNA and protein expression in HUVECs. (A) Cells were incubated in the presence of GLP-1 (5000 pmol/L) for 0 (control), 5, 10, and 30 min to investigate the time course of the effect on eNOS phosphorylation. (B) Cells were incubated in the absence (control) or presence of GLP-1 (5–5000 pmol/L) for 5 min to investigate the dose-dependence of the effect. eNOS phosphorylated at ser-1177 (P-eNOS 1177) was examined by Western blot analysis. Representative experiments are both shown in the upper parts. Band intensities, after normalization to β-actin, are expressed as ratios of control. Mean±SD. *n*=4. $^{b}P<0.05$, $^{c}P<0.01$ compared with control. (C and D) Before being harvested, cells underwent 0- (as control), 6-, 12-, 24-, and 48-h exposure to GLP-1 (5000 pmol/L). (C) eNOS mRNA levels, determined by real-time RT-PCR and normalized to β-actin mRNA , were expressed as mean±SD. (D) Total eNOS protein levels, determined by Western blot analysis and normalized to β-actin protein, are expressed as mean±SD. Representative experiment is shown in the upper part. *n*=4. $^{b}P<0.05$ compared with control.

min in HUVECs. After a 48-h incubation, GLP-1 elevated total eNOS protein but had no effect on eNOS mRNA levels. Both exenatide and GLP-1(9–36) increased eNOS activity, phosphorylation and total protein expression. In addition, GLP-1(9–36) elevated eNOS mRNA levels. Exendin(9–39) and sitagliptin, alone or in combination, partially blocked the GLP-1-induced enhancement of eNOS activity, phosphorylation and total protein levels. Taken together, our results suggest that GLP-1 upregulates eNOS activity and protein expression through the GLP-1R-dependent and GLP-1(9–36)-related pathways in HUVECs.

The concentration of 5–5000 pmol/L covers the physiological and pharmacological concentrations of GLP-1, thus this study seeks to observe the effects of GLP-1 within this range of concentration. Figure 1 shows that 50–5000 pmol/L of GLP-1 can increase the concentration of NO. In addition, we observed the effect of GLP-1 on eNOS phosphorylation, mRNA and protein expression (Figures 2 and 3). The observation of these three changes needs to explore the right time point. Taking into account that the relative high concentration of treatment factors may more easily produce the effects, we thus selected the 5000 pmol/L concentration for the experiment. After clarifying that this concentration could enhance eNOS phosphorylation and protein levels and determining the appropriate time point, we further observed the effect of other concentrations of GLP-1. Figure 2B shows that within 5–5000 pmol/L range, only 500–5000 pmol/L of GLP-1 can cause elevated levels of phosphorylation. However, a lower concentration (5–500 pmol/L) of GLP-1 does not cause changes in protein levels (data not shown), suggesting that only high concentrations of GLP-1 can result in eNOS expression upregulation. As indicated in Figure 1, 5000 pmol/L of GLP-1 did not cause eNOS mRNA change in the time period we observed, thus we did not further observe the effect of other concentrations.

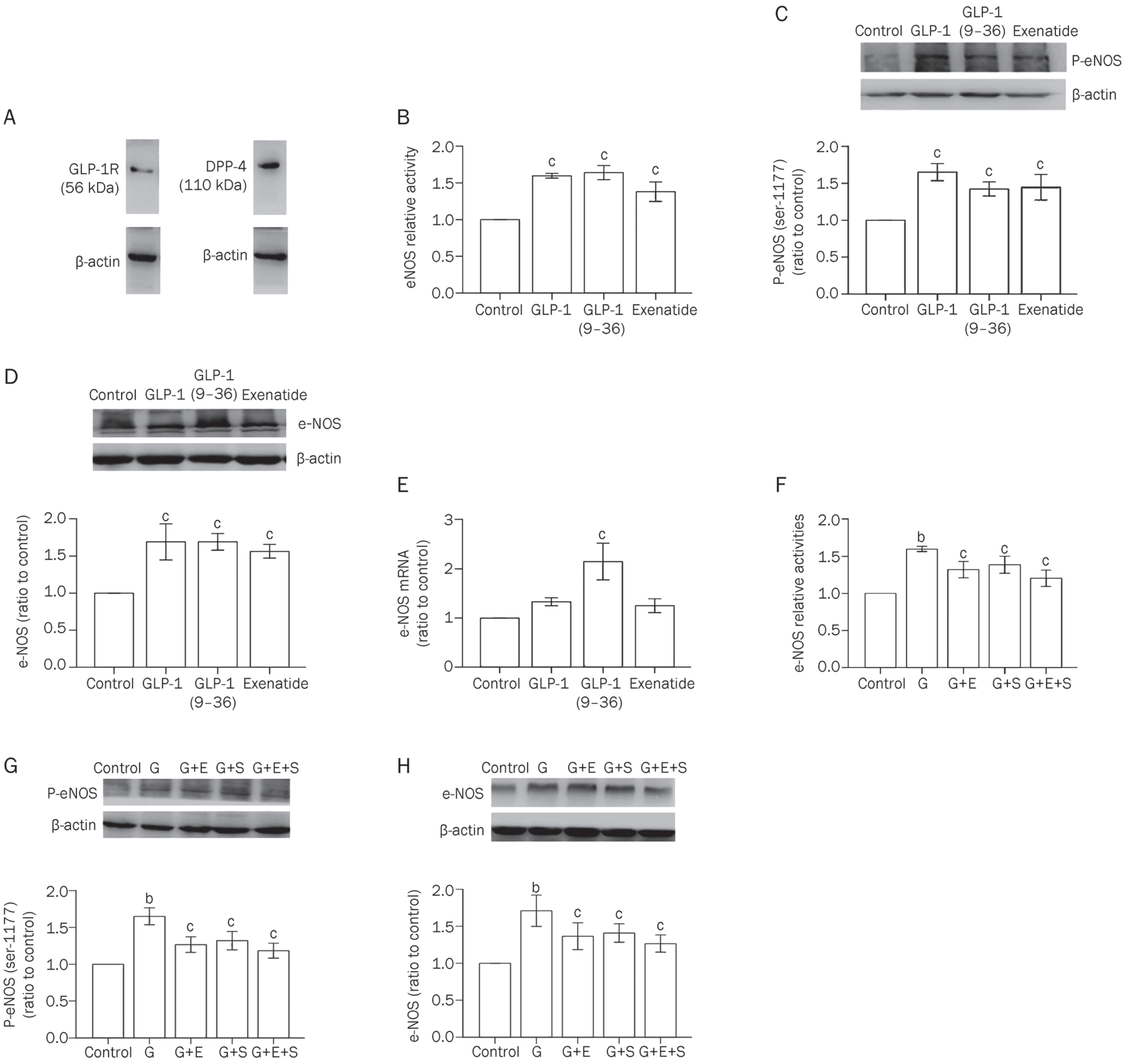

Figure 3. GLP-1R-dependent pathway and GLP-1(9–36)-related pathway are involved in effects of GLP-1 on eNOS levels in HUVECs. (A) GLP-1R and DPP-4 proteins were detected in HUVECs by Western blot analysis. Cells were incubated in the presence or absence (control) of GLP-1, GLP-1(9–36) or exenatide (GLP-1R agonist) (all at 5000 pmol/L) for the following times (B, C, D, E). Cells were incubated with GLP-1 in the presence of exendin (9–39) (G+E) or sitaglipin (G+S) or both (G+E+S) for the following times (F, G, H). (B, F) After 30-min incubation, eNOS activity was determined by NO content in cells. (C, G) After 5-min incubation, phosphorylation of eNOS at ser-1177 was examined by Western blot analysis. (D, H) After 48-h incubation, total eNOS protein level was measured by Western blot analysis. The upper parts of C, D, G, and H show representative experiments. Data are mean±SD after normalization to β-actin level. (E) After 48-h incubation, eNOS mRNA level was quantified by real-time RT-PCR. Data are mean±SD after normalization to β-actin level. $^{b}P<0.05$, $^{c}P<0.01$ compared to control.

Previous research has suggested that a 30-s infusion of GLP-1 can induce pulmonary vasodilation in isolated rat lungs that can be blocked by *L*-NAME, an eNOS inhibitor[9]. Thus, GLP-1 may increase NO release by directly increasing eNOS activity rather than protein levels in a short time. In this study, to understand the effect of GLP-1 on eNOS activity, we observed intracellular NO levels in HUVECs incubated with GLP-1 for 30 min and found that GLP-1 (50–5000 pmol/L) could increase eNOS activity. In normal individuals, the concentration of GLP-1 during the fasting state is 5–10 pmol/L and can increase to 20-40 pmol/L after meals whereas pharmacological concentrations of GLP-1 can be more than 100 pmol/L[21, 22]. Thus, GLP-1 may increase eNOS activity at both physiological and pharmacological concentrations. Among the rapid regulatory mechanisms of eNOS activity, eNOS ser-1177 phosphorylation is the most important pathway and is most frequently investigated. In the present study, GLP-1-induced eNOS ser-1177 phosphorylation was time dependent, *ie*, phosphorylated eNOS levels increased rapidly in a few minutes and then decreased within a short amount of time. Thus, GLP-1-induced eNOS activation may be restricted by negative feedback mechanisms, thereby limiting NO synthesis within an appropriate range to avoid adverse effects of excessive NO in endothelium.

GLP-1-induced NO synthesis and release via the activation of eNOS can explain the direct vasodilation by GLP-1. Moreover, GLP-1 can facilitate the effects of other vasodilator stimuli, such as fluid shear stress and acetylcholine[9–14]. However, in Daul salt-sensitive rats, after continuous infusion of GLP-1 for 14 d, the vasorelaxing reaction of the isolated thoracic aorta ring in response to acetylcholine was twice that in non-GLP-1-infused rats[12], indicating that GLP-1 has a long-term effect on eNOS, especially at the mRNA and protein levels. Here, our results reveal that a 48-h incubation of GLP-1 increases eNOS protein but not mRNA levels in HUVECs. Thus, GLP-1 regulates eNOS expression at the translational level and has no effects on gene transcription or mRNA stability.

GLP-1R mediates the main effect of GLP-1 on its target tissues, such as pancreatic islets, and plays an important role in maintaining glucose homeostasis. Indeed, GLP-1R is also expressed in endothelial cells[11, 13, 15]; thus, we hypothesize that the GLP-1R-dependent pathway may be involved in the endothelial effects of GLP-1. On the other hand, evidence indicates that an unknown signal pathway, which is independent of GLP-1R but is related to GLP-1(9–36), may exist and mediate certain biological effects of GLP-1. The half-life of GLP-1 *in vivo* is very short (only several minutes), and the cycling GLP-1 is usually present in the form of GLP-1(9–36)[23]. GLP-1(9–36) has a weak affinity with GLP-1R but cannot activate GLP-1R. Thus, it was considered either to have no biological activity or to antagonize GLP-1R to some extent[24]. Recent studies have found that GLP-1 can protect myocardium and relax blood vessels in mutagenic mice without GLP-1R. GLP-1(9–36) has a similar effect in normal and GLP-1R$^{-/-}$ mice. DPP-4 inhibitors, which block the conversion of GLP-1 to GLP-1(9–36), can weaken the above effects of GLP-1[11]. Studies have also found that GLP-1(9–36) has a more intense relaxing effect on isolated mouse femoral artery rings compared with GLP-1 and that single GLP-1R agonists have no relaxing effect[10, 11]. Together, these studies indicate that a GLP-1(9–36)-related, non-GLP-1R-dependent signaling pathway may mediate the biological effect of GLP-1. However, whether a GLP-1R-dependent or GLP-1(9–36)-related pathway mediates the effects of GLP-1 on eNOS was unknown. We thus treated HUVECS with GLP-1, exenatide (a GLP-1R agonist) and GLP-1(9–36) at the same concentrations and found that all of them could increase the activity and phosphorylation of eNOS as well as the total eNOS protein levels. In addition, like GLP-1, exenatide had no effect on eNOS mRNA levels, but GLP-1(9–36) could increase eNOS mRNA expression after a 48-h incubation. Thus, both the GLP-1R-dependent and GLP-1(9–36)-related pathways may be involved in the effect of GLP-1 on eNOS in HUVECs. Moreover, both the GLP-1R antagonist and the DPP-4 inhibitor that abolishes GLP-1(9–36) formation partially suppressed the GLP-1-induced eNOS activation, ser-1177 phosphorylation and upregulation of eNOS protein levels, further confirming the involvement of these two signaling pathways.

GLP-1 can upregulate eNOS in HUVECs, implying that, as a physiological hormone, it is involved in maintaining normal endothelial function. Thus, decreased GLP-1 levels may be a mechanism underlying the endothelial dysfunction in T2DM patients. Previous studies have demonstrated that GLP-1 and GLP-1(9–36) can lead to the vasodilation of femoral and mesenteric arteries in rats, but the GLP-1R agonist exendin-4 and exenatide has no such effects[12, 13]. This observation can be explained by the lack of GLP-1R expression in mesenteric artery intima[13]. Thus, the increased GLP-1(9–36) may be necessary to improve the pathophysiological changes caused by the decreased secretion of GLP-1 in T2DM patients, especially in tissues without GLP-1R expression. To date, there are few studies on the GLP-1(9–36)-related signaling pathway. Further research can provide a better understanding of the physiological functions and pharmacological actions of GLP-1(9–36).

In summary, GLP-1 can increase eNOS activity and protein levels in HUVECs via both the GLP-1R-dependent and GLP-1(9–36)-related pathways. New antidiabetic drugs, including GLP-1 analogues, GLP-1R agonists and DPP-4 inhibitors, improve glucose control in T2DM patients and have direct cardiovascular-protective effects. In addition, close attention should also be paid to the difference between the cardiovascular effects of GLP-1R agonists, GLP-1 analogues and DPP-4 inhibitors.

Acknowledgements

We thank Mu-li ZHAO for her assistance in cell culture. We are grateful to editors at BiomedWorld Bioscience Limited for their assistance in preparing this article.

Author contribution

Li DING and Jin ZHANG designed and performed the research and analyzed the data; and Li DING wrote the paper.

References

1 Yang Z, Ming XF. Recent advances in understanding endothelial dysfunction in atherosclerosis. Clin Med Res 2006; 4: 53–65.

2 Bauer V, Sotnikova R. Nitric oxide — the endothelium-derived relaxing factor and its role in endothelial functions. Gen Physiol Biophys 2010; 29: 319–40.

3 Stankevicius E, Kevelaitis E, Vainorius E, Simonsen U. Role of nitric oxide and other endothelium-derived factors. Medicina (Kaunas) 2003; 39: 333–41.

4 Drucker DJ. The biology of incretin hormones. Cell Metab 2006; 3: 153–65.

5 Drucker DJ, Nauck MA. The incretin system: glucagon-like peptide-1 receptor agonists and dipeptidyl peptidase-4 inhibitors in type 2 diabetes. Lancet 2006; 368: 1696–705.

6 Meier JJ, Nauck MA. Incretins and the development of type 2

diabetes. Curr Diab Rep 2006; 6: 194–201.

7 Toft-Nielsen MB, Damholt MB, Madsbad S, Hilsted LM, Hughes TE, Michelsen BK, *et al*. Determinants of the impaired secretion of glucagon-like peptide-1 in type 2 diabetic patients. J Clin Endocrinol Metab 2001; 86: 3717–23.

8 Briones M, Bajaj M. Exenatide: a GLP-1 receptor agonist as novel therapy for Type 2 diabetes mellitus. Expert Opin Pharmacother 2006; 7: 1055–64.

9 Golpon HA, Puechner A, Welte T, Wichert PV, Feddersen CO. Vasorelaxant effect of glucagon-like peptide-(7–36)amide and amylin on the pulmonary circulation of the rat. Regul Pept 2001; 102: 81–6.

10 Nathanson D, Erdogdu O, Pernow J, Zhang Q, Nystrom T. Endothelial dysfunction induced by triglycerides is not restored by exenatide in rat conduit arteries *ex vivo*. Regul Pept 2009; 157: 8–13.

11 Ban K, Noyan-Ashraf MH, Hoefer J, Bolz SS, Drucker DJ, Husain M. Cardioprotective and vasodilatory actions of glucagon-like peptide 1 receptor are mediated through both glucagon-like peptide 1 receptor-dependent and -independent pathways. Circulation 2008; 117: 2340–50.

12 Yu M, Moreno C, Hoagland KM, Dahly A, Ditter K, Mistry M, *et al*. Antihypertensive effect of glucagon-like peptide 1 in Dahl salt-sensitive rats. J Hypertens 2003; 21: 1125–35.

13 Nystrom T, Gutniak MK, Zhang Q, Zhang F, Holst JJ, Ahren B, *et al*. Effects of glucagon-like peptide-1 on endothelial function in type 2 diabetes patients with stable coronary artery disease. Am J Physiol Endocrinol Metab 2004; 287: E1209–15.

14 Basu A, Charkoudian N, Schrage W, Rizza RA, Basu R, Joyner MJ. Beneficial effects of GLP-1 on endothelial function in humans: dampening by glyburide but not by glimepiride. Am J Physiol Endocrinol Metab 2007; 293: E1289–95.

15 Ishibashi Y, Matsui T, Takeuchi M, Yamagishi S. Glucagon-like peptide-1 (GLP-1) inhibits advanced glycation end product (AGE)-induced up-regulation of VCAM-1 mRNA levels in endothelial cells by suppressing AGE receptor (RAGE) expression. Biochem Biophys Res Commun 2010; 391: 1405–8.

16 Ban K, Kim KH, Cho CK, Sauve M, Diamandis EP, Backx PH, *et al*. Glucagon-like peptide (GLP)-1(9–36)amide-mediated cytoprotection is blocked by exendin(9-39) yet does not require the known GLP-1 receptor. Endocrinology 2010; 151: 1520–31.

17 Chen ZP, Mitchelhill KI, Michell BJ, Stapleton D, Rodriguez-Crespo I, Witters LA, *et al*. AMP-activated protein kinase phosphorylation of endothelial NO synthase. FEBS Lett 1999; 443: 285–9.

18 Dimmeler S, Fleming I, Fisslthaler B, Hermann C, Busse R, Zeiher AM. Activation of nitric oxide synthase in endothelial cells by Akt-dependent phosphorylation. Nature 1999; 399: 601–5.

19 Fulton D, Gratton JP, McCabe TJ, Fontana J, Fujio Y, Walsh K, *et al*. Regulation of endothelium-derived nitric oxide production by the protein kinase Akt. Nature 1999; 399: 597–601.

20 Liu H, Hu Y, Simpson RW, Dear AE. Glucagon-like peptide-1 attenuates tumour necrosis factor-alpha-mediated induction of plasminogen [corrected] activator inhibitor-1 expression. J Endocrinol 2008; 196: 57–65.

21 Hojberg PV, Vilsboll T, Rabol R, Knop FK, Bache M, Krarup T, *et al*. Four weeks of near-normalisation of blood glucose improves the insulin response to glucagon-like peptide-1 and glucose-dependent insulinotropic polypeptide in patients with type 2 diabetes. Diabetologia 2009; 52: 199–207.

22 Vilsboll T, Krarup T, Madsbad S, Holst JJ. Both GLP-1 and GIP are insulinotropic at basal and postprandial glucose levels and contribute nearly equally to the incretin effect of a meal in healthy subjects. Regul Pept 2003; 114: 115–21.

23 Mentlein R. Mechanisms underlying the rapid degradation and elimination of the incretin hormones GLP-1 and GIP. Best Pract Res Clin Endocrinol Metab 2009; 23: 443–52.

24 Owji AA, Khoshdel Z, Sanea F, Panjehshahin MR, Shojaee Fard M, Smith DM, *et al*. Effects of intracerebroventricular injection of glucagon like peptide-1 and its related peptides on serotonin metabolism and on levels of amino acids in rat hypothalamus. Brain Res 2002; 929: 70–5.

npg
Acta Pharmacologica Sinica (2012) 33: 82–90
© 2012 CPS and SIMM All rights reserved 1671-4083/12 $32.00
www.nature.com/aps

Original Article

AVE8134, a novel potent PPARα agonist, improves lipid profile and glucose metabolism in dyslipidemic mice and type 2 diabetic rats

Hans Ludwig SCHÄFER, Wolfgang LINZ*, Eugen FALK, Maike GLIEN, Heiner GLOMBIK, Marcus KORN, Wolfgang WENDLER#, Andreas W HERLING, Hartmut RÜTTEN

Diabetes Division, Sanofi-Aventis Deutschland GmbH, Frankfurt am Main, Germany

Aim: AVE8134 is a structurally novel potent PPARα agonist. The aim of this study is to investigate the efficacy of AVE8134 on lipid profile and glucose metabolism in dyslipidemic mice and type 2 diabetic rats.
Methods: A cell based PPAR Gal4 transactivation assay was constructed for testing the activities of AVE8134 at 3 different PPAR isoforms *in vitro*. Transgenic human Apo A1 (hApo A1) mice and insulin-resistant ZDF rats were used to evaluate the effects of AVE8134 *in vivo*.
Results: AVE8134 was a full PPARα dominated PPAR agonist (the values of EC_{50} for human and rodent PPARα receptor were 0.01 and 0.3 μmol/L, respectively). AVE8134 was not active at PPARδ receptor. In female hApo A1 mice, AVE8134 (1–30 $mg\cdot kg^{-1}\cdot d^{-1}$, po for 12 d) dose-dependently lowered the plasma triglycerides, and increased the serum HDL-cholesterol, hApo A1 and mouse Apo E levels. In female ZDF rats, AVE8134 (3–30 $mg\cdot kg^{-1}\cdot d^{-1}$ for 2 weeks) improved insulin-sensitivity index. In pre-diabetic male ZDF rats (at the age of 7 weeks), AVE8134 (10 $mg\cdot kg^{-1}\cdot d^{-1}$ for 8 weeks) produced an anti-diabetic action comparable to rosiglitazone, without the PPARγ mediated adverse effects on body weight and heart weight. In male ZDF rats (at the age of 6 weeks), AVE8134 (20 $mg\cdot kg^{-1}\cdot d^{-1}$ for 12 weeks) increased mRNA levels of the target genes LPL and PDK4 about 20 fold in the liver, and there was no relevant effect with rosiglitazone.
Conclusion: AVE8134 improves lipid profile and glucose metabolism in dyslipidemic mice and type 2 diabetic rats.

Keywords: AVE8134; peroxisome proliferator-activated receptor; type 2 diabetes; glucose; serum lipids; rosiglitazone; transgenic human Apo A1 (hApo A1) mouse; insulin-resistant ZDF rat

Acta Pharmacologica Sinica (2012) 33: 82–90; doi: 10.1038/aps.2011.165

Introduction

Type 2 diabetes (T2D) is an increasing health problem in all western and developing countries[1, 2]. The disease is slow progressing and is characterized by disregulated glucose and lipid metabolism. Insulin resistance is a hallmark of early stage type 2 diabetes and at a more progressed stage partial or absolute β-cell failure leads to a relative or absolute lack of insulin[1, 3, 4], with the metabolic consequences of overt type 2 diabetes.

The morbidity and mortality of type 2 diabetes is caused by micro- as well as by macrovascular damage as consequences of the complex metabolic dysfunction. Whereas the microvascular complications are mainly correlated with high plasma glucose levels, the macrovascular damage and related cardiovascular mortality are associated with an atherogenic lipid profile[1, 5]. Lipid profiles in type 2 diabetes are usually characterized by high triglycerides and low HDL-C[6, 7]. An ideal treatment for T2D would need to improve both, glucose and lipid control[6, 8].

Glitazones (rosiglitazone, or pioglitazone) are insulin-sensitizing agents in clinical use for improving glucose control by activation of PPARγ receptors. They have little or no positive effect on the lipid profile[9]. Their clinical efficacy is limited by the mechanism-based side effects, mainly the risk of edema, heart failure and weight gain but probably also by other complications[10–12].

Fibrates (*eg*, fenofibrate) are weak PPARα agonists in clinical use for the treatment of mixed dyslipidemia. They decrease high plasma triglycerides and elevate low HDL-levels[13, 14]. The increase of serum Apo A1 and Apo A2 are less pronounced in clinical trials[15], but could be more distinctly shown in several transgenic animal models[16–18]. The effect of fenofibrate and other fibrates on insulin sensitivity has not

---

This paper is dedicated to the memory of Wolfgang WENDLER.
* To whom correspondence should be addressed.
E-mail wolfgang.linz@sanofi-aventis.com
Received 2011-07-25 Accepted 2011-11-08

been clearly demonstrated in humans[19, 20] and only moderate efficacy on glucose control has been demonstrated in animal models of T2D at high doses[18]. In contrast to the results reported with the weak PPARα activator fenofibrate, a few studies with more potent PPARα compounds have demonstrated stronger effects in animal models of T2D[21].

In this paper we report the efficacy of AVE8134, a potent structurally novel PPARα agonist in established pharmacological models for dyslipidemia, insulin resistance and T2D. The efficacy and markers of side effects were compared to the clinically used PPARγ agonist rosiglitazone and to the PPARα agonist fenofibrate.

Materials and methods

Test compounds

AVE8134 (Figure 1) was synthesized by Sanofi-Aventis Deutschland GmbH. Rosiglitazone was used from commercially available tablets (8 mg/tablet). Fenofibrate was purchased from Sigma-Aldrich (Steinheim, Germany).

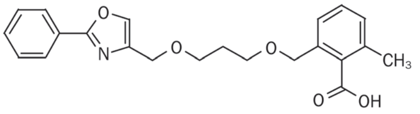

Figure 1. Chemical structure of AVE8134.

Compounds were pre-dissolved in ethanol and then transferred into 50 °C heated Solutol® and finally suspended or dissolved in 0.5% methylcellulose (*w*/*v*) to the final volume of 5 mL for rats and 10 mL for mice to achieve doses as indicated in the Results section. Drugs were administered once daily by oral gavage between 07:00 and 08:00 AM.

Gal4 assay

To test the PPAR activities of AVE8134 on the 3 different PPAR isoforms, human embryo kidney cells (HEK 293) were transfected with two genetic elements: 1) a luciferase reporter gene plasmid, containing five GAL4 binding sites upstream of the firefly luciferase reporter gene and 2) a PPAR expression plasmid, encoding a fusion protein of the N-terminus of the glucocorticoid receptor (GR), the DNA binding domain of the yeast GAL4 protein (GAL4) and the respective PPAR ligand binding domain (PPAR-LBD). HEK 293 cells transfected with both, the reporter plasmid and the PPAR expression plasmid produce a GR-GAL4-PPAR-LBD fusion protein which binds to the GAL4 binding sites located upstream of the firefly luciferase reporter gene. If a cell permeable PPAR agonist such as AVE8134 binds to and activates the respective PPAR-LBD, the expression of the firefly luciferase reporter gene is induced. This induction is dose-dependent and is measured as a chemiluminescence signal after addition of an appropriate firefly luciferase substrate.

Animals

Female C57BL/6-Tg(APO A1)1Rub/J mice were purchased from Charles River Germany (Sulzfeld, Germany) and treatment started at the age of 11–13 weeks. Male lean (ZDF/Crl-Fa/?) and obese (ZDF/Crl-fa/fa) Zucker Diabetic fatty (ZDF) rats were obtained from Charles River Belgium (Brussels, Belgium) and treatment started at the age of 7 and 10 weeks for male and female rats, respectively. They were housed in a temperature-controlled room at 23±2 °C with controlled humidity at 55%±5%. They were kept on a 12:12-h light-dark cycle (light on 06:00). All animals had free access to water and to a standard pellet rodent chow (mice and female ZDF rats: ssniff® Soest, Germany; male ZDF rats: Purina rat chow 5008), unless otherwise indicated. Mice and rats were acclimatized at minimal for 1 week before start of the treatment period and randomly allocated into study groups using a stratification method based on body weight. Animal studies were performed according to the German animal protection law as well as according to international animal welfare legislation and rules.

Experimental procedure

For analysis of blood glucose and HbA1c blood was drawn from tail tip from conscious animals using glass capillaries. For all other parameters blood was drawn from the retroorbital vein plexus during short-term isoflurane anesthesia or at the end of the study after laparotomy from the abdominal aorta during deep isofluran/nitric oxide anesthesia. Serum was obtained after centrifugation using Sarstedt® Serum-Gel tubes (Sarstedt, Nümbrecht, Germany).

Mice were treated for 12 d. At the end of the study blood was collected terminally from abdominal aorta during terminal anaesthesia from non-fasted animals.

Female ZDF rats were treated for 14 d. On the last day of the study after an overnight fast blood was collected retroorbitally in short-term isoflurane anesthesia for measuring of fasting blood glucose and fasting insulin levels and subsequent calculation of the insulin resistance index (HOMA^{IR}=fasted-glucose [mmol/L] × fasted-insulin [mU/L]/22.5).

Male ZDF rats were treated for 8 weeks. Food consumption and body weight were measured twice a week. The amount of diet for an additional control group was restricted to levels below the estimated consumption of the AVE8134 group: the starting value was 7 g chow/100 g body weight for the first week and than adapted to 8 g/100 g body weight. The chow for that control group was divided into two portions and was offered twice daily when light was switched on and off, all other groups had free access to food, except before measurements of fasted blood glucose, insulin and before oral glucose tolerance test. After two weeks of treatment an oral glucose tolerance test (oGTT) was performed. Briefly, after an overnight fast, the animals were treated with the drugs or vehicle between 06:30 and 07:00, glucose (2 g/kg) was administered orally 2 h later in a volume of 5 mL/kg, blood was drawn from the tip of the tail from using glass capillaries at 0, 30, 60, 90, 120, and 180 min after glucose administration. The glycemic index (GI) was calculated as area under the curve (AUC) of glucose response during oGTT. Blood glucose concentration before oral glucose load (0 min) was defined as baseline of AUC calculation.

Hepatic gene expression

Male 6-week old ZDF (*n*=5) rats were treated for 12 weeks, at the end of the study livers were dissected. Liver tissue samples (40–50 mg) were homogenized and lysed in RLT buffer (Qiagen, Hilden, Germany) with an UltraTurrax homogenizer (IKA Labortechnik, Staufen, Germany). Total RNA was isolated from the tissue lysate and cleaned up with the Qiagen Rneasy kit according to the manufacturers protocol. The isolated total RNA from 5 rats were pooled and subsequently analysed in a microarray experiment. Synthesis of labeled cRNA, hybridization, washing and staining of Affymetrix GeneChip arrays (Affymetrix, Santa Clara, CA, USA) were carried out as described[22]. Briefly, 10 µg of total RNA was utilized to generate cDNA, using the Superscript Choice System for cDNA synthesis (Life Technologies, Karlsruhe, Germany). After purification and subsequent precipitation, the cDNA was used as template for an *in vitro* transcription reaction (Enzo BioArray High Yield RNA Transcript Labeling Kit, distributed by Affymetrix, Santa Clara, CA, USA) according to the manufacturers protocol. At each case 15 µg of the labeled cRNAs was then fragmented and hybridized overnight onto RG U34A GeneChip arrays (Affymetrix, Santa Clara, CA, USA). The RG U34A GeneChip array contains probes for ~8000 rat mRNA transcripts and EST clusters. After hybridization and washing, the GeneChip arrays were stained using the antibody amplification protocol provided by Affymetrix (Affymetrix, Santa Clara, CA, USA). Finally, the GeneChip arrays were scanned with a confocal laser scanner (Hewlett Packard). GeneChip 4.0 software (Affymetrix, Santa Clara, CA, USA) was used for quantitative analysis of the scanned images. Further data analysis including estimation of regulation (comparison vehicle treated *versus* compound treated) and weighting of the statistical significance of those regulations was performed using proprietary software GECKO2 developed within Aventis[23].

Clinical chemistry

Serum levels of cholesterol, triglycerides, and safety variables: aspartate transaminase (AST), alanine transaminase (ALT), alkaline phosphatase (AP), as well as blood glucose and HbA1c were determined on a Hitachi 912 analyzer, using the respective Roche clinical chemistry kits for human diagnostics. Serum insulin concentrations were determined using a commercial rat and mouse ELISA kit (MERCODIA, Upsala, Sweden). Serum adiponectin concentrations were measured using a commercial mouse RIA kit (LINCO, USA). Assays were performed according to the instructions from the suppliers.

Statistical analysis

Data are presented as mean±SEM. Depending on the homogeneity of variances (Levene test), significant differences were calculated by a one-way ANOVA followed by a *post hoc* Dunnett´s test. Kruskal-Wallis test was used, if variances were not homogeneous. When testing for differences between repeated measured parameters, a two-way ANOVA (for repeated measures) followed by a *post hoc* Dunnett´s test was used. For repeated measured parameters, a rank transformation was performed if variances were not homogeneous. For all statistical calculations software Everstat V5 [(Sanofi-Synthelabo) based on SAS 8]) was used. A $P<0.05$ was considered to be statistically significant.

Results

In vitro activity

AVE8134 is a full PPARα dominated PPAR agonist, more potent on human than on rodent PPARα receptor. AVE8134 is not active on PPARδ (Table 1) and other nuclear receptors (data not shown) and has only partial activity on PPARγ (≅40%). In humans AVE8134 is PPARα selective, in rodents the split between PPARα and PPARγ is more than 20 fold lower (Table 1).

Effects on lipid metabolism *in vivo*: AVE8134 lowers serum triglycerides and increases HDL-cholesterol and Apo A1

In hApo A1 transgenic mice 12 d of treatment with AVE8134 decreased serum triglycerides, increased dose-dependently serum total cholesterol, as well as human Apo A1 (hApo A1) and mouse Apo E. Mouse Apo A1 was unchanged (Figure 2 and Table 2). Lipoprotein pattern showed that more than 90% of serum cholesterol was in the HDL fraction and the measured total cholesterol reflected predominantly HDL cholesterol. Treatment with AVE8134 further decreased the VLDL and LDL fraction and increased the HDL fraction (Figure 3). AVE8134 was already maximal effective on serum triglycerides at the medium dose (3 mg/kg). Higher doses were needed to increase hApo A1. Fenofibrate had comparable effects on serum lipids and hApo A1 but at 10 fold higher doses. Both PPARα agonists, AVE8134 as well as fenofibrate had no effect on serum adiponectin and heart weight (Figure 2 and Table 2). In contrast rosiglitazone did not change serum lipids, but increased serum adiponectin and heart weight

Table 1. EC_{50} values of AVE8134 in cell based PPAR Gal4 transactivation assays, relative to fenofibrate, rosiglitazone, or GW501516 for PPARα, PPARγ, or PPARδ, respectively.

Species	PPARα EC_{50}	PPARγ EC_{50}	PPARδ EC_{50}	PPARγ/α EC_{50} ratio
Human	0.01 (µmol/L) full activation	4 (µmol/L) partial activation (≅40%)	>10 (µmol/L)	400
Rat	0.3 (µmol/L) full activation	5 (µmol/L) partial activation (≅40%)	>10 (µmol/L)	17

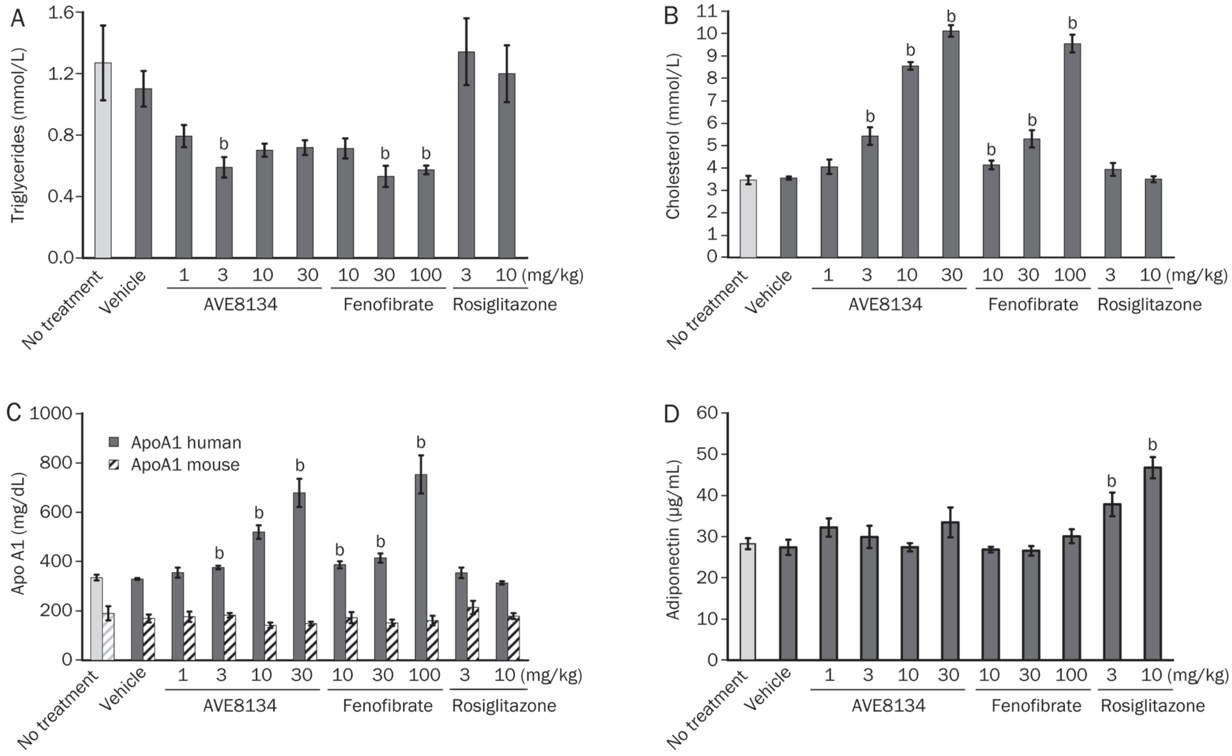

Figure 2. Effects of AVE8134, fenofibrate and rosiglitazone on serum triglycerides (A), serum cholesterol (B), serum Apo A1 (C), and adiponectin (D) in female Apo A1 mice after multiple administrations for 12 d. Mean±SEM (*n*=6). $^{b}P<0.05$ *vs* vehicle control.

Table 2. Effects of AVE8134, fenofibrate, and rosiglitazone in female hApo A1 mice on body weight (bw), relative liver weight, relative heart weight, and Apo E. $^{b}P<0.05$ *vs* vehicle control.

Treatment	Dose (mg/kg)	Weight gain (g)	Food consumption (g/d)	Liver weight (% bw)	Heart weight (% bw)	Apo E (mg/L)
Control	No treatment	1.28±0.25	3.52±0.08	4.34±0.07	0.45±0.01	0.95±0.07
	Vehicle	0.57±0.18	3.19±0.14	4.58±0.12	0.45±0.01	1.04±0.09
AVE8134	1	0.89±0.43	3.24±0.23	4.69±0.06	0.44±0.01	1.25±0.10
	3	0.96±0.55	3.29±0.03	5.40±0.11	0.44±0.01^{b}	2.00±2.20^{b}
	10	0.96±0.13	3.38±0.15	6.95±0.13	0.45±0.01^{b}	3.22±0.17^{b}
	30	1.48±0.31	3.23±0.05	7.73±0.13	0.45±0.01^{b}	3.53±0.08^{b}
Fenofibrate	10	0.76±0.16	3.40±0.10	5.09±0.06	0.47±0.01^{b}	1.49±0.07
	30	-0.14±0.43	3.15±0.09	6.12±0.16	0.46±0.01^{b}	2.32±0.29^{b}
	100	1.49±0.23	3.25±0.05	7.46±0.20	0.43±0.01^{b}	3.18±0.14^{b}
Rosiglitazone	3	0.81±0.26	3.49±0.17	4.60±0.09	0.47±0.02	1.29±0.09
	10	0.57±0.23	3.25±0.15	4.68±0.11	0.49±0.02	1.31±0.16

dose-dependently.

AVE8134 improves insulin resistance in female ZDF rats

The effect of AVE8134 on glucose control was first investigated in insulin-resistant female, obese ZDF rats after 2 weeks of treatment and the effects were compared to fenofibrate and rosiglitazone. Compared to lean control animals, the fasted blood glucose and non-fasted free fatty acids (FFA) levels in 10–12 weeks old female obese ZDF rats were slightly elevated. However, the fasted insulin levels in the obese animals were several-fold above the level of the lean control animals.

Treatment with AVE8134 dose-dependently decreased

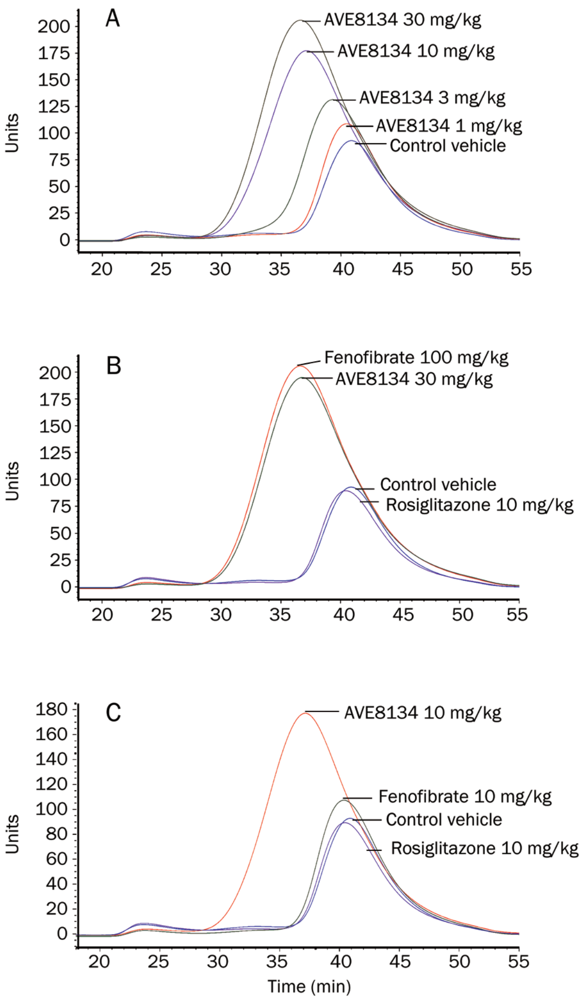

Figure 3. Effects of AVE8134, fenofibrate and rosiglitazone on serum FPLC lipoprotein pattern in female Apo A1 mice after multiple administrations for 12 d. (A) AVE8134 dose response: 1, 3, 10, and 30 mg·kg^{-1}·d^{-1} *vs* vehicle control. (B) Fenofibrate 100 mg·kg^{-1}·d^{-1} and AVE8134 30 mg·kg^{-1}·d^{-1} *vs* vehicle control. (C) Fenofibrate 10 mg·kg^{-1}·d^{-1}, rosiglitazone 10 mg·kg^{-1}·d^{-1} and AVE8134 10 mg·kg^{-1}·d^{-1} *vs* vehicle control.

fasted serum insulin levels resulting in an improved HOMA IR (homeostasis model assessment test). AVE8134 decreased dose-dependently serum FFA but has no additional effect on fasted blood glucose in female ZDF rats. Rosiglitazone decreased insulin and FFA levels and additionally slightly decreased fasted blood glucose resulting in an improved HOMA IR. The effect of AVE8134 at 30 mg/kg was comparable to the effect with an optimal efficacious dose of rosiglitazone. In contrast to AVE8134, the weak PPARα agonist fenofibrate had no significant effect on fasted insulin, fasted blood glucose and HOMA IR (Figure 4), but was still effective on serum FFA levels. AVE8134 and rosiglitazone (only) slightly increased the food consumption, while fenofibrate had no influence on food consumption in the female ZDF rat (data not shown), because altered food consumption could be a cause for improved glucose control.

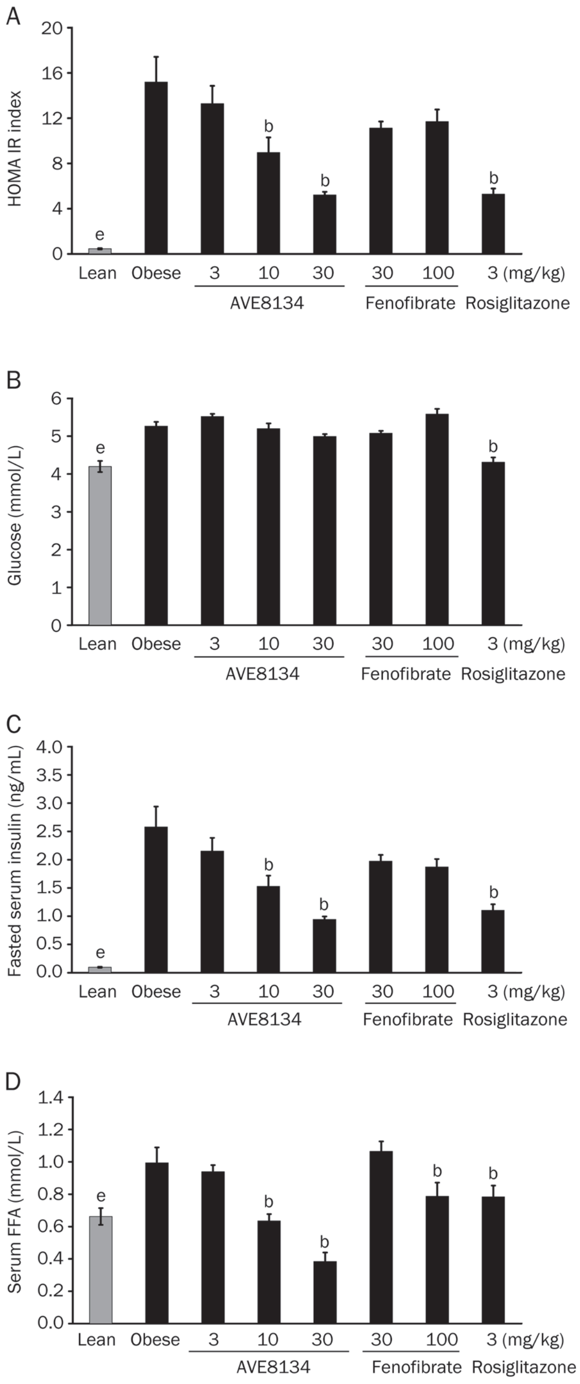

Figure 4. Effects of AVE8134, fenofibrate and rosiglitazone treatment on HOMA IR (A), fasted blood glucose (B), fasted Insulin (C), and non-fasted free fatty acids (FFA) (D) in female ZDF rats after multiple administration for 2 weeks. Mean±SEM (n=8). $^{b}P<0.05$ *vs* obese control. $^{e}P<0.05$ lean control *vs* obese control.

AVE8134 has anti-diabetic effects comparable to rosiglitazone without PPARγ side effects in male ZDF rats

Treatment of male ZDF rats was started at the age of 7 weeks when animals were in a pre-diabetic state. Blood glucose

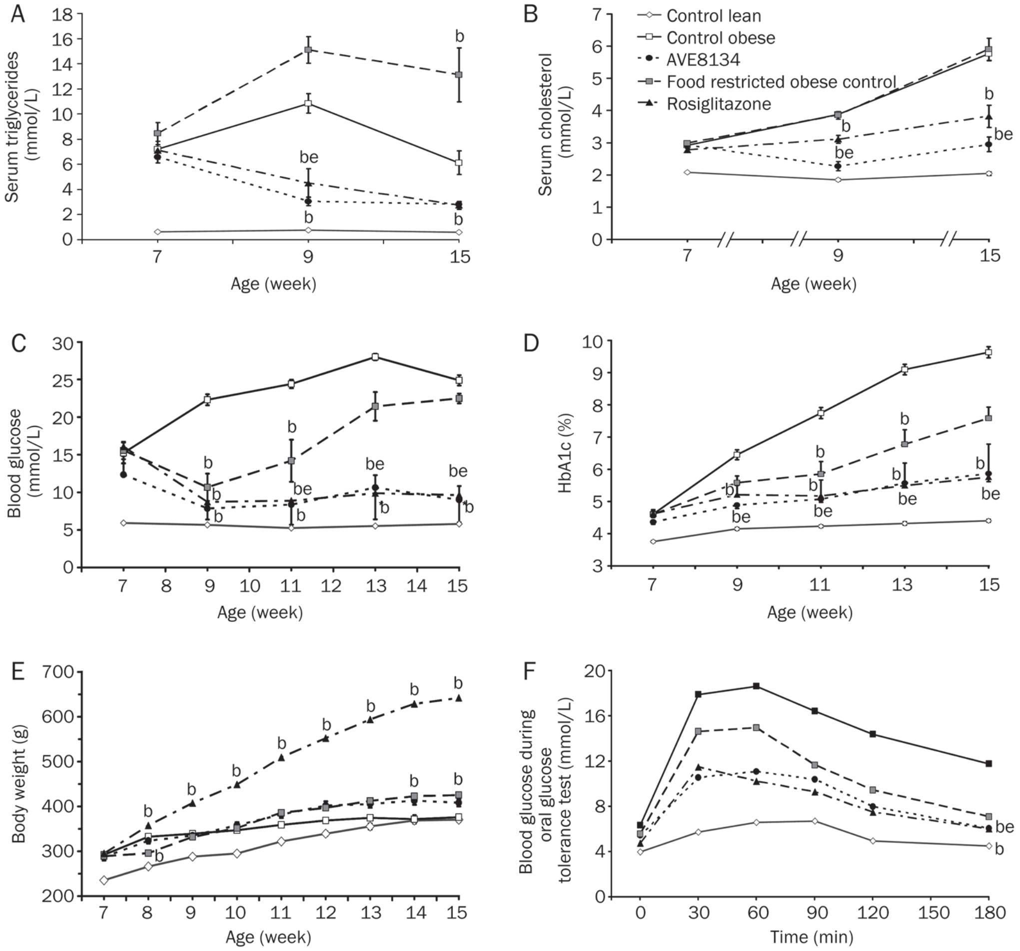

Figure 5. Effects of AVE8134 (10 mg·kg^{-1}·d^{-1}), and rosiglitazone (3 mg·kg^{-1}·d^{-1}) on serum triglycerides (A), serum cholesterol (B), blood glucose (C), HbA1c (D), body weight (E), and oral glucose tolerance test (F) in male ZDF rats after 8 weeks treatment. Mean±SEM (n=6). $^{b}P<0.05$ *vs* obese control. $^{e}P<0.05$ *vs* food restricted obese control.

was already significantly elevated and further increased in untreated animals during the 8 weeks of the study.

AVE8134 lowered blood glucose, serum triglycerides and cholesterol, improved HbA1c and glucose tolerance. From results of a pilot study as well as from published reports with PPARα agonists[21], it was known that potent PPARα agonists decreased food intake in male ZDF rats. Therefore, a second control group received same amount of food as calculated for AVE8134 treated animals. AVE8134 was more effective in glucose control than the effect achieved with partial food restriction. Rosiglitazone showed the expected anti-diabetic effect in male ZDF rats, lowered serum triglycerides, increased weight gain and prevented further increase of serum cholesterol. The efficacy of AVE8134 on glucose control was comparable to rosiglitazone, but unlike rosiglitazone, AVE8134 did not significantly increase the body weight gain or heart weight (Figure 5 and 6). Serum adiponectin, a biomarker for PPARγ activation was 5-fold increased by rosiglitazone after 8 weeks of treatment, while it was not influenced by AVE8134.

Food restriction alone (to amounts consumed by the AVE8134 group) decreased blood glucose and improved glucose tolerance during the first 2 weeks of the study, however, during the following 6 weeks on restricted food blood glucose, and HbA1c increased, at the end of the study blood glucose reached the level of the *ad libitum* fed control group. Food restriction increased the serum triglycerides (Table 3, Figure 5 and 6).

AVE8134 was well tolerated and no relevant changes in serum safety parameters were seen, no increase in serum transaminases activity, only increase in serum alkaline phosphate activity was observed (Table 3). As in mice the rodent specific PPARα effect on liver weight was also seen in male and female ZDF rats, the liver weight was 2 fold increased with AVE8134 (data not shown).

Hepatic gene induction of lipoprotein lipase (LPL) and PDK4

In a pilot study in male ZDF rats the *in vivo* effect on PPARα target genes was investigated. Treatment was started at the age of 6 weeks, animals were sacrificed after 12 weeks treatment. AVE8134 increased mRNA levels for LPL and PDK4 about 20 fold in the liver, there was no relevant effect with rosiglitazone (Figure 7).

Discussion

In humans, treatment with PPARα agonists like fenofibrate increases HDL and Apo A1 and decreases serum triglycerides. The effect on HDL and Apo A1 in rats and mice is not present, because the human – but not the mouse – Apo A1 promoter

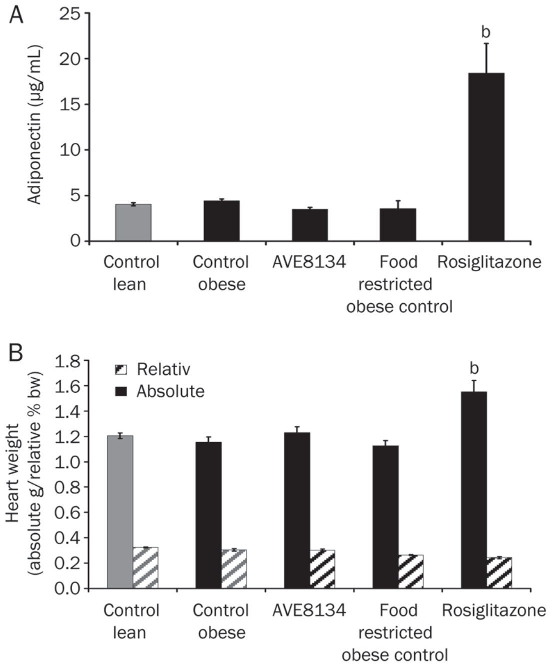

Figure 6. Effects of AVE8134 (10 mg·kg^{-1}·d^{-1}) and rosiglitazone (3 mg·kg^{-1}·d^{-1}) on serum adiponectin (A), relative and absolute heart weight (B), in male ZDF rats after 8 weeks treatment. Mean±SEM (*n*=6). $^{b}P<0.05$ *vs* obese control.

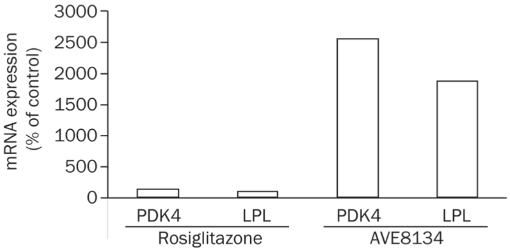

Figure 7. Relative mRNA levels for PDK4 or LPL in liver after treatment of male ZDF rats with rosiglitazone (3 mg·kg^{-1}·d^{-1}) or AVE8134 (20 mg·kg^{-1}·d^{-1}). Data are obtained in a microarray experiment described in Materials and methods and expressed as relative expression values in comparison to the vehicle treated control group.

has a positively regulated element that responds to the PPARα receptor[16, 17]. To investigate the effects of PPARα agonists on Apo A1 and HDL in rodents a transgenic mouse model that expresses the human Apo A1 gene was used[16]. As expected in that mouse model, AVE8134 and fenofibrate increased only the human Apo A1 and had no relevant effect on mouse Apo A1. Before treatment and in vehicle treated control mice, HDL cholesterol accounted for more than 90% of total cholesterol. Treatment with the PPARα agonists AVE8134 and fenofibrate decreased the Apo E carrying fractions low-density lipoprotein (LDL) and very low-density lipoprotein (VLDL) below the limit of detection. In mice and humans, Apo E is present in the HDL and also in non-HDL lipoprotein particles[24]. The increase of Apo E in the hApo A1 mouse indicates that the activation of the human Apo A1 promoter and subsequent increase in hApo A1 resulted in an increase in HDL particle number. The qualitative effects of a PPARα agonist on serum triglycerides, HDL and Apo A1 in the hApo A1 transgenic mice can be expected in humans, however the effect size can not be translated in humans, therefore the *in vivo* effect of AVE8134 on serum lipids was investigated by direct comparison to fenofibrate to estimate the relative *in vivo* potency of AVE8134. Data from the study in hApo A1 mice demonstrated that *in vivo*, AVE8134 is a potent PPARα agonist with 10-fold higher potency than fenofibrate. AVE8134 and fenofibrate were effective on triglycerides in the lowest tested dose, whereas effects on HDL and Apo A1 were seen with both drugs only with 10-fold higher doses. That corresponds with clinical observations with fenofibrate. The drug is very effective on triglycerides but has in clinical doses only moderate effects on HDL and Apo A1. PPARγ agonists improve insulin-sensitivity in insulin-resistant models and type 2 diabetic

Table 3. Effect of AVE8134 and rosiglitazone in male ZDF rats on food consumption during 8 weeks treatment. Glycemic index (GI) after 2 weeks treatment, calculated as AUC of blood glucose during oGTT. Non-fasted insulin before and after treatment. Safety parameter: serum activity of transaminases (AST and ALT) and alkaline phosphatase (AP) after 8 weeks treatment. $^{b}P<0.05$ *vs* obese control.

		Lean control	Obese control	AVE8134 10 mg/kg	Food restricted	Rosiglitazone 3 mg/kg
Food consumption (g·animal^{-1}·d^{-1})		21±0.3	41±1.3	29±0.8^{b}	30±1.4^{b}	44±1.3
	Age/treatment (week)					
Insulin (μg/L)	7/0	0.41±0.01	11.46±1.89	13.44±3.29	10.30±1.24	9.17±1.28
	9/2	0.56±0.07	3.87±0.33	3.84±0.36	10.30±1.31	4.79±0.54
	13/6	0.76±0.12	2.68±0.24	5.17±0.39	11.32±3.07	7.29±1.24
	15/8	<0.40	1.08±0.37	0.44±0.11	1.93±0.51	2.64±0.68
AUC oGTT (mmol·L^{-1}·min)		272±24	1541±50	601±30	954±137	663±100
AST (U/L)		135±4	109±8	125±9	151±17	105±4
ALT (U/L)		52±2	102±10	42±4	149±30	81±3
AP (U/L)		87±2	253±13	990±52	223±11	156±33

patients. An effect in an insulin-sensitive hApo A1 mouse can not be expected, nevertheless the known effect on serum adiponectin and side effects of rosiglitazone were already seen in that model, even after a short treatment period. Rosiglitazone increased serum adiponectin and heart weight. It is still under discussion whether or not a potent PPARα agonist will improve glycaemic control by improving insulin sensitivity, the effect of PPARγ agonists like rosiglitazone on glycaemic control and insulin sensitivity in humans is proven, but linked to the side effects edema, weight gain, and potential cardiovascular risk. In type 2 animal models, fenofibrate has moderate effects, but it is much less effective than rosiglitazone. These findings with fenofibrate and rosiglitazone could be confirmed in an insulin-resistance model, the female ZDF rat. On normal chow, female ZDF rats are not diabetic, but insulin resistant. The female animals have massive but stable hyperinsulinemia starting from age of 8 weeks for further several weeks. So the HOMA IR index is a predictive parameter for insulin sensitivity in that model. AVE8134 dose dependently improved the HOMA IR index and was as effective as rosiglitazone, whereas fenofibrate has no significant effect, only a trend without correlation to dose was observed, which fits to clinical observations. Based on results in female ZDF rats, the anti-diabetic effect of AVE8134 was investigated in a diabetes model, the male ZDF rat. In male ZDF rats, fenofibrate and other PPARα agonists have only a minor effect and part of the reported effects of PPARα agonists on glucose control in male ZDF rats could be related to decreased food intake, which is typical for these drugs in male ZDF rats[21]. PPARγ agonist rosiglitazone could prevent the onset of diabetes, despite the increased food intake under rosiglitazone treatment. In the male ZDF rat, non-fasted blood glucose together with HbA1c value are predictive and robust parameters to monitor the diabetes progression. With rosiglitazone, a daily dose of 3 mg/kg is established as the optimal dose in male ZDF rats. It could be demonstrated that not only did AVE8134 have an anti-diabetic effect comparable to rosiglitazone but also that the anti-diabetic effect of AVE8134 was not solely a result of decreased food intake. At start of treatment, the male ZDF rats were in an early diabetic state with already elevated blood glucose and both AVE8134 and rosiglitazone decreased blood glucose and prevented the onset of overt diabetes for the following weeks of treatment. Food restriction delayed only the onset of diabetes, at the end of the study blood glucose and HbA1c of food restricted control were at the same level than *ad libitum* fed obese control. Adiponectin is a validated *in vivo* biomarker for PPARγ activation[25] and increased body weight gain and elevated heart weight are the PPARγ mediated side effects in ZDF rats. *In vitro* results demonstrate that AVE8134 is a PPARα dominated PPAR agonist but never the less AVE8134 is also a weak partial PPARγ agonist.

In a pilot study in male ZDF rats it was observed that AVE8134 is *in vivo* a very potent PPARα agonist. Treatment with AVE8134 increased the PPARα target genes LPL and PDK4 about 20 fold in the liver. With the investigated dose of 10 mg/kg in male ZDF rats no PPARγ activation was detectable, no increase in serum adiponectin or PPARγ-mediated side effects on weight gain or absolute heart weight were seen, food restriction has also no influence on heart weight nor serum adiponectin. The absolute heart weight is more predictive than relative heart weight as PPARγ mediated side effect. We observed in several studies with male ZDF that there is no difference in absolute heart weight between lean and obese ZDF rats, the heart increased in growing lean and obese animals in parallel with age and reached a plateau of about 1.2 g in adult animal. Effects on relative heart weight are masked by PPARγ mediated increase in visceral body fat pad mass. In contrast to rosiglitazone, AVE8134 was shown to attenuate the progression of heart failure and to increase survival in rats[26].

The increase in serum alkaline phosphatise activity is a typical biomarker of PPARα activation, seen with several PPARα agonists in rats and the dose related increase of alkaline phospahtase was observed with fenofibrate[27]. This is not relevant in humans since in humans fibrates decrease serum alkaline activity[28] and the decrease in serum alkaline phosphatase activity has been used to monitor compliance of fibrates in clinical trials[29].

Conclusion

With the observed lipid lowering and anti-diabetic effects in animal models it can be expected that AVE8134 is a potent PPARα agonist which will improve an atherogenic lipid profile with the potential to optimize glucose homeostasis without PPARγ side effects in clinical trials.

Acknowledgements

We thank Thomas HENNIG, Carolin JOERG, Kerstin KLEINSCHMIDT, Manfred SCHMALZ, Pierre WENSKI and Gabriele BIEMER-DAUB for helpful support in conducting animal studies, animal care and serum clinical chemistry. We thank Marion SCHNEIDER for performance of the cellular assays and Gertraud JERABEK-SANDOW for performance of the gene expression studies.

We thank David CROWTHER for reviewing the manuscript.

Author contribution

Hans-Ludwig SCHÄEFER and Wolfgang LINZ designed and performed the studies and wrote the paper. Eugen FALK designed and performed the serum lipoproteine and lipid analysis. Marcus KORN designed and performed gene expression experiments. Maike GLIEN designed and performed the *in vivo* glucose tolerance tests. Heiner GLOMBIK designed and synthesized the test compound. Wolfgang WENDLER designed and performed the *in vitro* assays. Andreas W HERLING and Hartmut RÜTTEN designed research.

References

1 Kiess W, Bottner A, Bluher S, Raile K, Galler A, Kapellen TM. Type 2 diabetes mellitus in children and adolescents — the beginning of a renal catastrophe? Nephrol Dial Transplant 2004; 19: 2693–6.

2 Wild S, Roglic G, Green A, Sicree R, King H. Global prevalence of diabetes: estimates for the year 2000 and projections for 2030.

Diabetes Care 2004; 27: 1047–53.

3 Rhodes CJ. Type 2 diabetes–a matter of beta-cell life and death? Science 2005; 307: 380–4.

4 Rhodes CJ, White MF. Molecular insights into insulin action and secretion. Eur J Clin Invest 2002; 32: 3–13.

5 Agrawal RP, Sharma P, Pal M, Kochar A, Kochar DK. Magnitude of dyslipedemia and its association with micro and macro vascular complications in type 2 diabetes: a hospital based study from Bikaner (Northwest India). Diabetes Res Clin Pract 2006; 73: 211–4.

6 Rader DJ. Effect of insulin resistance, dyslipidemia, and intra-abdominal adiposity on the development of cardiovascular disease and diabetes mellitus. Am J Med 2007; 120: S12–8.

7 Valabhji J, Watson M, Cox J, Poulter C, Elwig C, Elkeles RS. Type 2 diabetes presenting as diabetic ketoacidosis in adolescence. Diabet Med 2003; 20: 416–7.

8 Cziraky MJ. Management of dyslipidemia in patients with metabolic syndrome. J Am Pharm Assoc 2004; 44: 478–88.

9 Buse JB, Tan MH, Prince MJ, Erickson PP. The effects of oral anti-hyperglycaemic medications on serum lipid profiles in patients with type 2 diabetes. Diabetes Obes Metab 2004; 6: 133–56.

10 Berlie HD, Kalus JS, Jaber LA. Thiazolidinediones and the risk of edema: a meta-analysis. Diabetes Res Clin Pract 2007; 76: 279–89.

11 Nissen SE, Wolski K. Effect of rosiglitazone on the risk of myocardial infarction and death from cardiovascular causes. N Engl J Med 2007; 356: 2457–71.

12 Patel C, Wyne KL, McGuire DK. Thiazolidinediones, peripheral oedema and congestive heart failure: what is the evidence? Diab Vasc Dis Res 2005; 2: 61–6.

13 Fruchart JC, Duriez P. Mode of action of fibrates in the regulation of triglyceride and HDL-cholesterol metabolism. Drugs Today (Barc) 2006; 42: 39–64.

14 Sharpe M, Ormrod D, Jarvis B. Micronized fenofibrate in dyslipidemia: a focus on plasma high-density lipoprotein cholesterol (HDL-C) levels. Am J Cardiovasc Drugs 2002; 2: 125–32.

15 Nissen SE, Nicholls SJ, Wolski K, Howey DC, McErlean E, Wang MD, *et al*. Effects of a potent and selective PPAR-alpha agonist in patients with atherogenic dyslipidemia or hypercholesterolemia: two randomized controlled trials. JAMA 2007; 297: 1362–73.

16 Berthou L, Duverger N, Emmanuel F, Langouet S, Auwerx J, Guillouzo A, *et al*. Opposite regulation of human versus mouse apolipoprotein A-I by fibrates in human apolipoprotein A-I transgenic mice. J Clin Invest 1996; 97: 2408–16.

17 Hennuyer N, Poulain P, Madsen L, Berge RK, Houdebine LM, Branellec D, *et al*. Beneficial effects of fibrates on apolipoprotein A-I metabolism occur independently of any peroxisome proliferative response. Circulation 1999; 99: 2445–51.

18 Nadeau KJ, Ehlers LB, Aguirre LE, Reusch JE, Draznin B. Discordance between intramuscular triglyceride and insulin sensitivity in skeletal muscle of Zucker diabetic rats after treatment with fenofibrate and rosiglitazone. Diabetes Obes Metab 2007; 9: 714–23.

19 Rosenson RS, Wolff DA, Huskin AL, Helenowski IB, Rademaker AW. Fenofibrate therapy ameliorates fasting and postprandial lipoproteinemia, oxidative stress, and the inflammatory response in subjects with hypertriglyceridemia and the metabolic syndrome. Diabetes Care 2007; 30: 1945–51.

20 Rosenson RS. Effects of peroxisome proliferator-activated receptors on lipoprotein metabolism and glucose control in type 2 diabetes mellitus. Am J Cardiol 2007; 99: 96B–104B.

21 Bergeron R, Yao J, Woods JW, Zycband EI, Liu C, Li Z, *et al*. Peroxisome proliferator-activated receptor (PPAR)-alpha agonism prevents the onset of type 2 diabetes in Zucker diabetic fatty rats: A comparison with PPAR gamma agonism. Endocrinology 2006; 147: 4252–62.

22 Voss MD, Beha A, Tennagels N, Tschank G, Herling AW, Quint M, *et al*. Gene expression profiling in skeletal muscle of Zucker diabetic fatty rats: implications for a role of stearoyl-CoA desaturase 1 in insulin resistance Diabetologia 2005; 48: 2622–30.

23 Theilhaber J, Ulyanov A, Malanthara A, Cole J, Xu D, Nahf R, *et al*. GECKO: a complete large-scale gene expression analysis platform. BMC Bioinformatics 2004; 5: 195.

24 Ishida BY, Blanche PJ, Nichols AV, Yashar M, Paigen B. Effects of atherogenic diet consumption on lipoproteins in mouse strains C57BL/6 and C3H. J Lipid Res 1991; 32: 559–68.

25 Yang B, Brown KK, Chen L, Carrick KM, Clifton LG, McNulty JA, *et al*. Serum adiponectin as a biomarker for *in vivo* PPARgamma activation and PPARgamma agonist-induced efficacy on insulin sensitization/lipid lowering in rats. BMC Pharmacol 2004; 4: 23.

26 Linz W, Wohlfart P, Baader M, Breitschofpf K, Falk E, Schäfer HL, *et al*. The peroxisome proliferator-activated receptor-α (PPAR- α) agonist, AVE8134, attenuates the progression of heart failure and increases survival in rats. Acta Pharmacol Sin 2009; 30: 935–46.

27 Nishimura J, Dewa Y, Muguruma M, Kuroiwa Y, Yasuno H, Shima T, *et al*. Effect of fenofibrate on oxidative DNA damage and on gene expression related to cell proliferation and apoptosis in rats. Toxicol Sci 2007; 97: 44–54.

28 Day AP, Feher MD, Chopra R, Mayne PD. The effect of bezafibrate treatment on serum alkaline phosphatase isoenzyme activities. Metabolism 1993; 42: 839–42.

29 Elisaf M. Effects of fibrates on serum metabolic parameters. Curr Med Res Opin 2002; 18: 269–76.

Acta Pharmacologica Sinica (2012) 33: 91–100
© 2012 CPS and SIMM All rights reserved 1671-4083/12 $32.00
www.nature.com/aps

Original Article

Autophagy counteracts apoptosis in human multiple myeloma cells exposed to oridonin *in vitro* via regulating intracellular ROS and SIRT1

Rong ZENG[#], Yan CHEN[#], Shuai ZHAO, Guo-hui CUI[*]

Department of Hematology, Union Hospital, Tongji Medical College, Huazhong University of Science and Technology, Wuhan 430022, China

Aim: To explore the mechanisms underlying the oridonin-induced apoptosis and autophagy in human multiple myeloma cells *in vitro*.
Methods: Human multiple myeloma RPMI8266 cells were used. The cell viability was assessed using MTT assay. Morphological changes of apoptosis and autophagy were observed under transmission electron microscope. TUNEL and annexin V-FITC/PI dual staining assays were used to measure apoptosis. Autophagy was analyzed using Western blot analysis and immunofluorescence staining with a $QDs_{605\ nm}$-Anti-LC3 fluorescent probe. Intracellular ROS was estimated with flow cytometry using DCFH-DA fluorescent probe. Protein levels of active caspase 3, Beclin 1 and SIRT1 were determined with Western blot analysis.
Results: Exposure to oridonin (1–64 μmol/L) inhibited the proliferation of RPMI8266 cells in a concentration-dependent manner with an IC_{50} value of 6.74 μmol/L. Exposure to oridonin (7 μmol/L) simultaneously induced caspase 3-mediated apoptosis and Beclin 1-dependent autophagy of RPMI8266 cells. Both the apoptosis and autophagy were time-dependent, and apoptosis was the main effector pathway of cell death. Exposure to oridonin (7 μmol/L) increased intracellular ROS and reduced SIRT1 nuclear protein in a time-dependent manner. The blockade of intracellular generation of ROS by NAC (5 mmol/L) abrogated apoptosis, autophagy and the decrease of SIRT1 in the cells exposed to oridonin (7 μmol/L). The inhibition of autophagy by 3-MA (5 mmol/L) sensitized the cells to oridonin-induced apoptosis, which was accompanied by increased intracellular ROS and decreased SIRT1.
Conclusion: Oridonin simultaneously induces apoptosis and autophagy of human multiple myeloma RPMI8266 cells via regulation of intracellular ROS generation and SIRT1 nuclear protein. The cytotoxicity of oridonin is mainly mediated through the apoptotic pathway, whereas the autophagy protects the cells from apoptosis.

Keywords: oridonin; autophagy; apoptosis; ROS; SIRT1; human multiple myeloma cells

Acta Pharmacologica Sinica (2012) 33: 91–100; doi: 10.1038/aps.2011.143; published online 12 Dec 2011

Introduction

Oridonin, an active diterpenoid compound isolated from *Rabdosia rubescens*, has various pharmacological and physiological effects (*eg*, anti-tumor, anti-inflammation, and anti-bacterial), and it has been widely used for the treatment of various human diseases[1–3]. Both apoptosis and autophagy are essential cellular homeostatic mechanisms, which are important in multicellular organisms for development, tissue turnover, and host defense. Autophagy is a conserved, genetically controlled process that leads to the degradation of cytoplasmic components within lysosomes and has recently gained much attention for its paradoxical relationship with apoptosis. Some studies suggest that the inhibition of autophagy enhances apoptosis. In contrast, others have suggested that autophagy acts as a cell death pathway, termed programmed cell death (PCD) type II, in cooperation with apoptosis[4–7]. Although oridonin has been shown to induce apoptosis and autophagy in some types of tumor cells in both *in vitro* and *in vivo* studies[8-10], the relationship between the two processes is unclear. Furthermore, the molecular mechanisms underlying oridonin-induced apoptosis and autophagy in RPMI8266 cells remain to be determined.

Multiple myeloma (MM) is an untreatable hematological disease characterized by the synthesis of excess immunoglobulin (Ig), which forms endoplasmic reticulum-localized unfolded or misfolded proteins that are potentially toxic to MM cells. Hoang *et al*[11] found that the level of autophagy that occurs in MM cells was significantly higher than that in normal plasma cells. Additionally, the inhibition of autophagy

---

[#] The first two authors contributed equally to this work.
[*] To whom correspondence should be addressed.
E-mail ghcui@medmail.com.cn
Received 2011-05-08 Accepted 2011-09-23

in MM cells using chloroquine or Beclin 1-siRNA leads to cell death. This observation suggests that autophagy has a protective effect on MM cell viability. Furthermore, the proteasome inhibitor bortezomib, a clinical drug used for the treatment of myeloma, can induce MM cell death and autophagy. However, the treatment of MM cells with an autophagy inhibitor in combination with bortezomib resulted in an antagonistic response *in vitro*[11]. Consequently, the relationship between autophagy and cell death remains complicated and requires further investigation in multiple myeloma.

Reactive oxygen species (ROS) are generally small, short-lived and highly reactive molecules. While ROS generation is a consequence of basal cellular respiration, increased ROS generation is associated with several pathological conditions (*eg*, hypoxia, ischemia, and anti-tumor agents). Some studies have demonstrated that ROS generation activated caspase cascades through the mitochondrial permeability transition to mediate apoptosis[12, 13]. In addition to apoptosis, ROS generation has recently been reported to mediate autophagy under certain conditions[14–16]. Sirtuin1 (SIRT1) is a NAD$^+$-dependent deacetylase that is involved in a diverse set of physiological functions, including gene silencing, stress resistance, apoptosis, inflammation, senescence, and aging. Studies have indicated that SIRT1 activity can be positively or negatively regulated by intracellular oxidative stress[17–19]. SIRT1 was suggested to have anti-apoptotic functions by a wide range of *in vivo* and *in vitro* studies[20, 21]. However, SIRT1 was shown to promote autophagy[22, 23]. Therefore, we hypothesized that the generation of intracellular ROS and SIRT1 activity could underlie the effects of oridonin treatment in RPMI8226 cells.

Methods and materials

Reagents and antibodies

Oridonin, thiazolyl blue tetrazolium bromide (MTT), the 2′, 7′-dichlorofluorescein diacetate (DCFH-DA) fluorescent probe, dimethyl sulfoxide (DMSO), the 3-methyladenine (3-MA) autophagy inhibitor and the N-acetylcysteine (NAC) free radical scavenger were purchased from Sigma-Aldrich. The purity of oridonin was confirmed by HPLC to be greater than 99%. Oridonin was dissolved in DMSO to make a stock solution. The DMSO concentration was kept maintained 0.1% in all cell cultures, and it did not exert any detectable effect on cell growth or cell death. Anti-active caspase 3 (Abcam, ab2302) and anti-LC3 (Abcam, ab48394) were purchased from Abcam. Anti-Beclin 1 (sc11427) and anti-SIRT1 (sc74504) were purchased from Santa Cruz Biotechnology.

Cell culture and treatments

Human multiple myeloma RPMI8226 cells were purchased from American Type Culture Collection (ATCC). The cells were maintained in RPMI-1640 medium (GIBCO, 31800-022) supplemented with 10% fetal bovine serum (FBS) (TBD Biotechnology Development, TBD0022HLY) without antibiotics at 37 °C in a 5% CO_2 humidified atmosphere. After the cells reached a steady-state of exponential growth in normal media, they were exposed to oridonin for 0, 6, 12, or 24 h prior to the analysis. To inhibit intracellular ROS generation and autophagy, cells were pre-incubated with NAC or 3-MA, respectively, at a concentration of 5 mmol/L for 1 h prior to oridonin treatment.

MTT assay

A 100-μL suspension of RPMI8226 cells were seeded on 96-well plates with or without oridonin at various concentrations (1, 2, 4, 8, 16, 32, and 64 μmol/L) at a density of 1×10^5 cells per well. After incubation for a designated period of time, MTT was added to each well at a final concentration of 0.5 mg/mL for 3 h, and the resulting formazan crystals were dissolved in DMSO. Optical density was measured at 490 nm with background subtraction at 630 nm using a plate microreader (TECAN SPETRA). The growth inhibitory ratio was calculated as follows:

$$\text{Growth inhibitory ratio (\%)} =[(A_{\text{control}}-A_{\text{blank of control}})-(A_{\text{sample}}-A_{\text{blank of sample}})]/(A_{\text{control}}-A_{\text{blank of control}})\times100\%$$

Transmission electron microscopy (TEM) analysis

After treatment, cell pellets were fixed with 2.5% glutaraldehyde in 0.1 mol/L cacodylate buffer, pH 7.4 at 4 ºC for at least 30 min. After fixation, the specimens were thoroughly washed in 0.1 mol/L cacodylate buffer and then fixed with 1% osmium tetroxide in the same buffer at room temperature (RT) for 1 h. The specimens were dehydrated in a graded series of ethanol and then embedded in Epon. Thin sections (0.1 μm) were cut, stained with uranyl acetate/lead citrate and viewed using a Hitachi H-300 TEM.

Analysis of apoptosis using the TUNEL assay and FCM of AV/PI dual staining

In this study, several approaches were used to detect apoptosis quantitatively and qualitatively, including (I) the terminal deoxynucleotidyl transferase mediated X-dUTP nick end labeling (TUNEL) assay and (II) annexin V-FITC (fluorescein isothiocyanate)/PI (propidium iodide) staining for FCM. The TUNEL assay was performed using a commercial kit (BOSTER Biological Technology, MK1020) according to the manufacturer's protocol. Briefly, 1×10^6 cells/mL that were treated with 7 μmol/L oridonin for 0 h or 24 h were collected and fixed in 4% paraformaldehyde at 4 ºC. The fixed cells were then incubated with the TUNEL reaction mixture for 1 h at 37 ºC, followed by the addition of a peroxidase-conjugated detection antibody. DNA fragments were stained using diaminobenzidine (DAB) as a substrate for the peroxidase. Positive staining was identified using a light microscope as brown granules. The apoptosis rate was calculated as follows: apoptotic rate (%)=number of positively stained cells/total number of cells×100% (at least 500 cells were counted under a light microscope). For annexin V-FITC/PI dual staining, cells were processed with an Annexin V-FITC kit (Keygene, KGA108) following treatment according to the manufacturer's instructions. Next, the samples were analyzed using the FACScan flow cytometer

(Becton Dickinson) to quantify the apoptotic rate. Different subpopulations were distinguished using the following criteria: Q1, annexin V-negative, but PI-positive (*ie*, necrotic cells) indicating autophagic cell death in this study; Q2, annexin V/PI-double positive (*ie*, late apoptotic cells); Q3, annexin V/PI-double negative (*ie*, live cells); Q4, annexin V-positive, but PI-negative (*ie*, early apoptotic cells). The apoptotic rate was determined as the percentage of Q2+Q4.

Immunofluorescence analysis of LC3 localization using a QDs$_{605\text{ nm}}$ (quantum dots 605 nm)-Anti-LC3 fluorescent probe

To prepare the QDs$_{605\text{ nm}}$-Anti-LC3 fluorescent probe, core-shell QDs (ZnS-capped CdSe) were synthesized by the College of Chemistry and Molecular Sciences, Wuhan University. We used a 1.5-mL solution of high-quality oil-soluble core-shell QD$_{605\text{ nm}}$ to synthesize water-soluble QDs according to a previously developed procedure[24]. These activated dots modified with thioglycolic acid were dissolved in PBS (0.08 mol/L, pH 7.4) containing 50 mmol EDC (1-(3-dimethyl-aminopropyl)-3-ethylcarbodiimide hydrochloride, >98%) and 5 mmol NHS (N-hydroxy-succinimide, >98%). Next, the QDs were incubated with 20 μL of a mouse anti-human monoclonal LC3 antibody at RT in a shaking incubator for 2–4 h. The final QD bioconjugates were purified by centrifugation at 6000×*g* for 10 min, and the suspension was dialyzed for 8–12 h. The resulting QD$_{605\text{ nm}}$-Anti-LC3 probes were stored at 4 ºC. For the immunofluorescence analysis, cells were collected following treatment and fixed in 4% paraformaldehyde for 1 h at 4 ºC. Next, the fixed cells were immobilized on a gelatin-covered (0.1% gelatin and 0.01% chromium potassium sulfate) slide and dried under sterile conditions at RT for 1 h. The specimen was permeabilized in phosphate buffer solution (PBS) containing 0.1% Triton X-100 and sodium citrate at RT for 10 min. Then, the specimen was incubated with the QD$_{605\text{ nm}}$-Anti-LC3 probes at a final concentration of 1×10^7 mol/L at RT for 4 h. After incubation, the slides were washed three times with PBS and observed using fluorescence microscopy (Olympus) with an excitation wavelength of 605 nm to determine LC3 localization. Under normal conditions, LC3-II is uniformly distributed and has a diffuse localization pattern. During autophagy, LC3-I is processed to LC3-II and translocates to autophagosome membranes, which appear as red fluorescent punctae. Because LC3-II localization is used as a marker for autophagy, the percentage of fluorescent punctae-positive cells compared with the total number of cells was calculated as follows to quantify the amount of autophagy: the percentage of fluorescent punctae-positive cells (%)=(the number of fluorescent punctae-positive cells/the total number of cells)×100% (at least 500 cells were counted using a fluorescence microscope).

Measurement of intracellular ROS generation

Intracellular ROS generation was estimated by FCM using the DCFH-DA fluorescent probe. Briefly, the treated cells were collected and washed twice with RPMI-1640. The level of intracellular ROS was determined by incubating the cells with the DCFH-DA working solution (25 μmol/L) at 37 ºC for 30 min. After incubation, cells were washed twice with RPMI-1640 and then analyzed using FCM to determine the DCF fluorescence intensity at excitation and emission wavelengths of 488 nm and 525 nm, respectively.

Protein extraction and Western blot analysis

Total cellular protein was harvested by washing cells with ice-cold PBS and incubating them in lysis buffer (10 mmol/L Tris, pH 7.4, 20 mmol/L NaCl, 5 mmol/L $MgCl_2$, 0.5% NP-40, and 0.1 mmol/L PMSF). The extracts were centrifuged, and the clear supernatants containing total protein were collected. Cellular nucleic proteins were extracted using a commercial kit (DBI Bioscience, DBI1017) according to the manufacturer's protocol. After isolation, the protein concentration was determined using the Bio-Rad protein assay, and an equal amount of protein was subjected to SDS-polyacrylamide gel electrophoresis and transferred to nitrocellulose membranes (Hybond-C extra, GE Healthcare Life Sciences, RPN203E). After blocking with 5% non-fat milk, the membranes were probed with the designated primary and secondary antibodies, developed with the enhanced chemiluminescence method (Pierce, 32106) and visualized using the Kodak Image Station. The band density was quantified using the Image J image processing program. Because the extent of LC3 conversion is correlated with the level of autophagy[25], LC3-I and LC3-II were detected by Western blot analysis.

Statistical analysis

All data are presented as mean±standard deviation (SD). Statistical significance was determined using Student's *t*-test with *P*-values <0.05 representing significance.

Results

Oridonin inhibits the proliferation of RPMI8226 cells

RPMI8226 cells were treated with oridonin at various concentrations (1, 2, 4, 8, 16, 32, and 64 μmol/L) for 6, 12, or 24 h. As shown in Figure 1, oridonin induces remarkable inhibition of cell proliferation in a time- and dose-dependent manner with an IC_{50} of 6.74 μmol/L in RPMI8226 cells at 24 h.

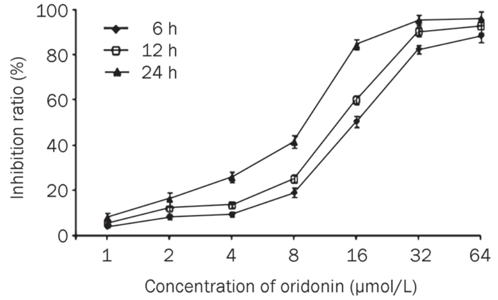

Figure 1. Assessment of the proliferation inhibition induced by oridonin in RPMI8226 cells. The cells were treated with oridonin at various doses for 6, 12, and 24 h. Viable cells were detected by MTT assay and proliferation inhibitory ratio (%) was calculated. The data were represented as mean±SD from three independent experiments.

Oridonin induces caspase 3-mediated apoptosis in RPMI8226 cells

The TUNEL assay, FCM analysis of annexin V-FITC/PI dual staining and TEM were performed to detect apoptosis in cells treated with 7 μmol/L oridonin for 0, 6, 12, or 24 h. As shown in Figure 2A, a significant increase in the number of TUNEL-positive apoptotic cells was detected in cells treated with oridonin for 24 h. The apoptotic rate of cells exposed to oridonin was increased to 41.4%±1.42% while the apoptotic rate of the control group was only 5.78%±0.56%. Annexin V-FITC/PI dual staining demonstrated that oridonin induces a significant time-dependent increase in the apoptotic rate [(Q2+Q4)%]. As shown in Figure 2C, the apoptotic rates of cells at the indicated time points were 5.00%±1.55% (0 h), 10.47%±0.68% (6 h), 14.70%±0.60% (12 h), and 17.53%±0.68% (24 h). Apoptotic morphology was also observed using TEM in cells treated with oridonin for 24 h (Figure 3B).

To explore the mechanism underlying the time-dependent increase in apoptosis induced by oridonin, the level of active caspase 3 was determined using Western blot analysis of cells treated with 7 μmol/L oridonin for 0, 6, 12, or 24 h. As shown in Figure 2B, oridonin also results in a time-dependent activation of caspase 3. These results indicate that oridonin induces caspase 3-mediated apoptosis in RPMI8226 cells.

Oridonin induces Beclin 1-mediated autophagy in RPMI8226 cells

Detection of autophagosomes, in addition to LC3 conversion and localization in cells treated with 7 μmol/L oridonin for 0, 6, 12, or 24 h was performed using TEM, Western blot analysis, and immunofluorescence using the $\text{QDs}_{605\ \text{nm}}$-Anti-LC3 fluorescent probe, respectively. There were a greater number of autophagosomes, which is indicative of autophagy, in cells exposed to oridonin for 24 h as compared with untreated controls (Figure 3C). LC3-II was detected using Western blot analysis. As shown in Figure 4A, the level of LC3-II protein increased in a time-dependent manner after treatment with oridonin. As shown in Figure 4B, oridonin induces a remarkable increase in red fluorescent punctae at 6, 12, and 24 h, which is indicative of LC3-II localization in autophagosomes in cells. The percentage of red fluorescent punctae-positive cells increased in a time-dependent manner during treatment with oridonin for 24 h. The percentages of red fluorescent punctae-positive cells at the indicated time points were 14.33%±4.04% (0 h), 35.67%±4.16% (6 h), 61.00%±3.61% (12 h) and 91.00%±2.65% (24 h) (Figure 4B). These results suggest that oridonin induces autophagy in a time-dependent manner in RPMI8226 cells.

Because Beclin 1-independent autophagy has been reported, the levels of Beclin 1 in cells treated with 7 μmol/L oridonin for 0, 6, 12, or 24 h were determined using Western blot analysis to investigate its role in autophagy induced by oridonin. As shown in Figure 4C, Beclin 1 expression followed the same time-dependent pattern as LC3 conversion and localization. These data indicate that autophagy induced by oridonin is canonical Beclin 1-mediated macro-autophagy.

Intracellular ROS generation mediates apoptosis and autophagy induced by oridonin through negative regulation of SIRT1 activity

To investigate whether ROS and SIRT1 are involved in oridonin-induced apoptosis and autophagy, the levels of intracellular ROS and SIRT1 nuclear protein in cells treated with 7 μmol/L oridonin for 0, 6, 12, or 24 h were assessed by the FCM analysis of DCF fluorescence intensity and Western blot analysis, respectively. As shown in Figure 5A, oridonin-induced apoptosis and autophagy, was associated with a time-dependent increase in DCF fluorescence intensity. DCF fluorescence intensities at the indicated time points were 23154.67±1332.90 (0 h), 28150.00±716.45 (6 h), 32574.33±1908.46 (12 h), and 44410.67±2478.12 (24 h). In contrast, oridonin treatment results in decreased nuclear SIRT1 protein in a time-dependent manner (Figure 5B). These results suggest that the induction of apoptosis and autophagy by oridonin may be positively regulated by intracellular ROS generation and negatively regulated by SIRT1 activity.

NAC, a general free radical scavenger, was used to block ROS generation to further confirm the roles of intracellular ROS generation and SIRT1 activity in the induction of apoptosis and autophagy by oridonin. RPMI8226 cells were pre-incubated with 5 mmol/L NAC for 1 h prior to exposure to 7 μmol/L oridonin for 24 h, and then, the apoptosis, autophagy, and the SIRT1 activity analyses were repeated. As shown in Figures 5A and 6A, NAC completely inhibited the oridonin-induced increase in DCF fluorescence intensity (22932.67±2715.65 *versus* 44410.67±2478.12, $P<0.01$). An analysis of apoptosis and autophagy, including the FCM analysis of annexin V-FITC/PI dual staining, Western blot analysis of active caspase 3 and LC3-II, localization of LC3-II, and Western blot analysis of Beclin 1, were repeated in cells pre-incubated with NAC. While exposure to NAC alone for 24 h did not affect apoptosis and autophagy in cells ($P>0.05$), NAC completely abrogated the oridonin-induced increase in apoptosis (Figures 2B, 2C, 6B, and 6C, $P<0.01$) and autophagy (Figures 4, 6D, 6E, and 6F, $P<0.01$). The SIRT1 nuclear protein level of cells pre-incubated with NAC was measured and compared with cells treated with oridonin alone. As shown in Figure 5B and Figure 6G, NAC reversed the oridonin-induced decrease in SIRT1 nuclear protein levels ($P<0.01$).

These data suggest that SIRT1 activity was negatively regulated by intracellular ROS generation. Therefore, we conclude that intracellular ROS generation mediates the induction of apoptosis and autophagy by oridonin, possibly through the negative regulation of SIRT1 activity.

Inhibition of autophagy sensitizes RPMI8226 cells exposed to oridonin to apoptosis mediated by intracellular ROS generation and SIRT1 downregulation

We used 3-MA, a well-known inhibitor of autophagy, to explore the role of autophagy in cell death and the relationship between autophagy and apoptosis. Autophagy and apoptosis of cells pre-treated with 5 mmol/L 3-MA for 1 h and then exposed to 7 μmol/L oridonin for 24 h were analyzed using above mentioned methods.

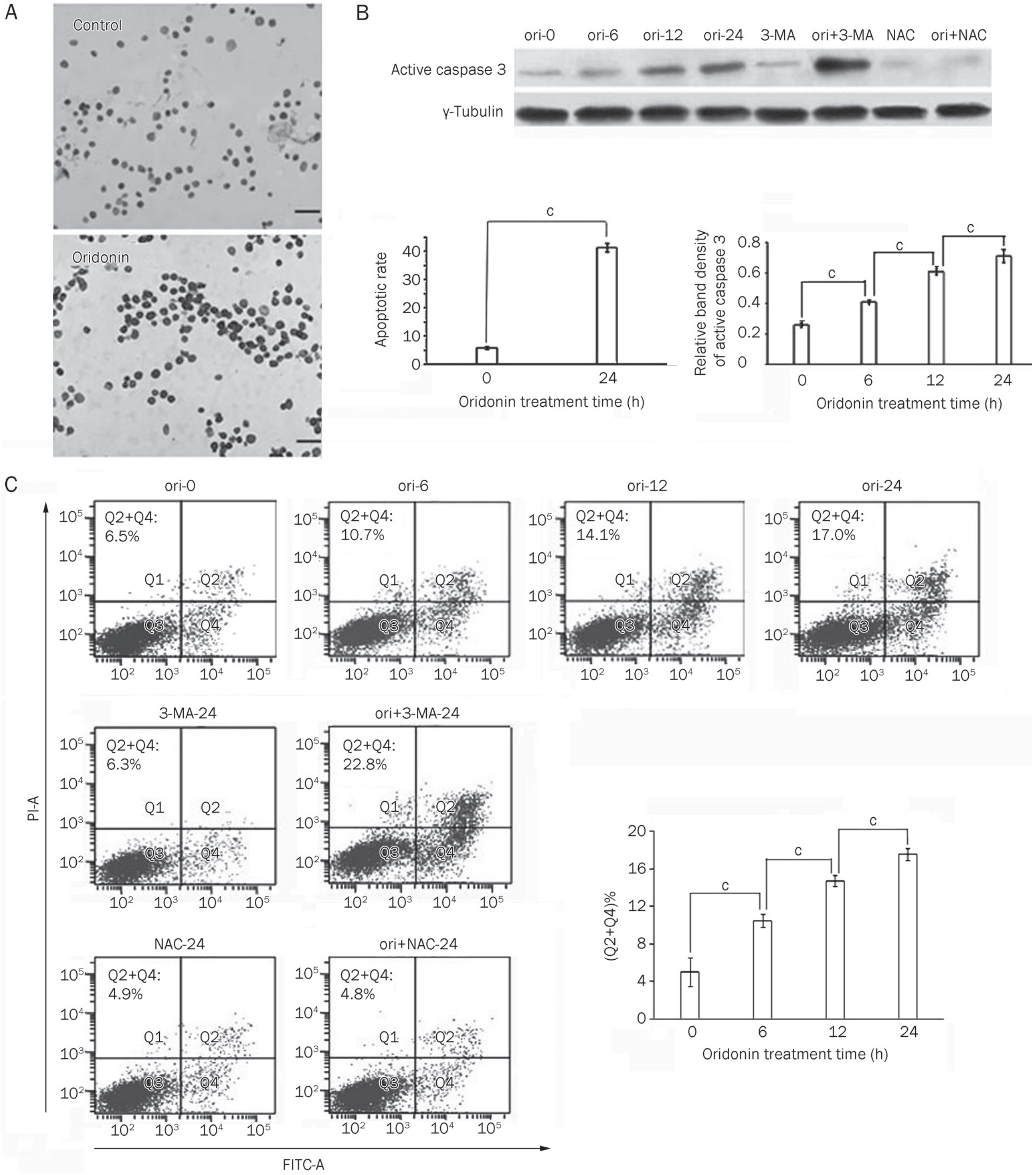

Figure 2. Assessment of apoptosis in cells treated with oridonin (ori) alone, cells pre-incubated with NAC, and cells pre-incubated with 3-MA. (A) The cells were treated with 7 μmol/L oridonin for 24 h, and apoptosis was determined using TUNEL assay. The cells cultured under normal media were used as control. The positive staining was identified under the light microscope at ×400 magnification as brown granules. Apoptotic rate was calculated as follows: apoptotic rate (%)=number of positive staining cells/number of total cells×100% (at least 500 cells were counted under a light microscope). (B) The cells were treated with 7 μmol/L oridonin for 0, 6, 12, and 24 h, or treated with 7 μmol/L oridonin in the presence or absence of 5 mmol/L NAC, or treated with 7 μmol/L oridonin in the presence or absence of 5 mmol/L 3-MA for 24 h. The active caspase 3 protein levels were detected using Western blot assay. γ-Tubulin was used as an equal loading control. The bands were quantified by densitometric analysis. The values for active caspase 3 were corrected relative to the γ-tubulin and shown in histogram. (C) The cells were treated with 7 μmol/L oridonin for 0, 6, 12, and 24 h, or treated with 7 μmol/L oridonin in the presence or absence of 5 mmol/L NAC, or treated with 7 μmol/L oridonin in the presence or absence of 5 mmol/L 3-MA for 24 h. The apoptotic rates were detected by FCM of annxin V-FITC/PI dual staining. Q1 quadrant (annexin V–, PI+) represented dead cells; Q2 quadrant (annexin V+, PI+) represented late apoptotic cells; Q4 quadrant (annexin V+, PI–) represented early apoptotic cells; Q4 quadrant (annexin V-, PI–) represented live cells. The percentage of total apoptotic cells (Q2+Q4) was calculated and shown in histogram. All statistical significance was determined by Student's *t*-test. Columns, mean of three independent experiments; Mean±SD; $^{c}P<0.01$.

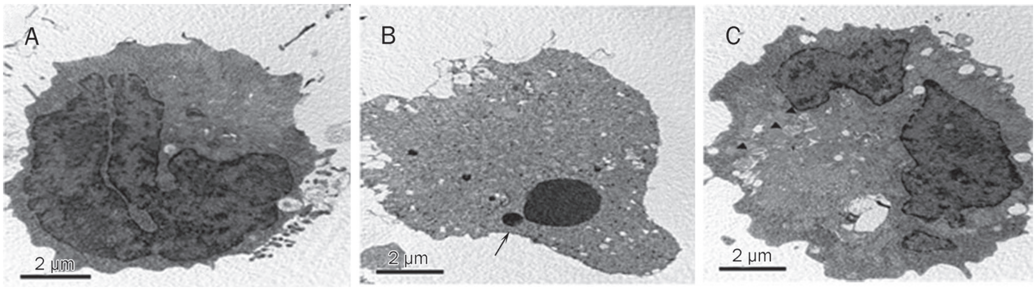

Figure 3. Assessment of the ultra-structure morphology of apoptosis and autophagy in RPMI8226 cells exposed to oridonin. The cells cultured under normal media were used as control (A). The cells were treated with 7 μmol/L oridonin for 24 h (B, C). The representative images are shown. The magnification was labeled in each image. (A) Normal morphology. (B) Apoptotic morphology. Arrow depicts apoptotic chromatin condensation. (C) Autophagic morphology. Arrowheads indicate autophagosomes.

3-MA suppresses oridonin-induced autophagy, but not baseline autophagy. As shown in Figures 4A, 7A, 7B, and 7C, the amount of LC3-II, the percentage of red fluorescent punctae-positive cells and Beclin 1 protein expression in cells pre-treated with 3-MA decreased markedly compared with cells treated with oridonin alone ($P<0.01$). In contrast, a comparison of these autophagic parameters between cells exposed to 3-MA alone and cells under normal conditions showed no significant differences ($P>0.05$). In addition, 3-MA enhances oridonin-induced apoptosis. As shown in Figures 2B and 7D, 3-MA augments the oridonin-induced increase in the apoptotic rate (24.30%±1.80% *versus* 17.53%±0.68%, $P<0.01$). Measurement of active caspase 3 levels in cells pre-treated with 3-MA revealed the same results as the analysis of the apoptotic rate (Figure 2C and Figure 7E). In conclusion, apoptosis, but not autophagy, is the major effector pathway of oridonin-induced cytotoxicity and autophagy protects cells against apoptosis.

Because the results above demonstrated that intracellular ROS generation mediates oridonin-induced apoptosis through negatively regulating SIRT1 activity, we determined whether intracellular ROS generation and SIRT1 were also involved in the pro-survival effect of autophagy. The intracellular ROS generation and SIRT1 protein level in the nuclei of cells pre-treated with 5 mmol/L 3-MA for 1 h and then exposed to 7 μmol/L oridonin for 24 h was detected by an FCM analysis of DCF fluorescence density and Western blot analysis, respectively. As shown in Figures 5B, 7F, and 7G, pre-treatment with 3-MA further increases DCF fluorescence intensity (57385.55±3935.33 *versus* 44410.67±2478.12, $P<0.01$) and decreases SIRT1 nuclear protein level ($P<0.01$) compared with cells treated with oridonin alone for 24 h.

In conclusion, we propose that intracellular ROS generation contributes to the autophagic pro-survival mechanism. Inhibition of autophagy sensitizes cells to apoptosis through promotion of ROS generation and SIRT1 downregulation induced by oridonin.

Discussion

Oridonin, a potential drug for tumor treatment, has been reported to simultaneously induce apoptosis and autophagy in some tumor cell lines, including HeLa and A431 cells, among others[9, 26]. Studies investigating the relationship between autophagy and apoptosis are complicated and depend on the cellular context and stimulus. Jia and colleagues demonstrated that the induction of autophagy was essential to TNF-α-induced apoptosis in a T-lymphoblastic leukemia cell line, which indicated that execution of apoptosis is preceded by and depends upon autophagy in this context[27]. In other cellular settings, autophagy antagonized or delayed apoptosis, and the inhibition of autophagy increased the sensitivity of the cells to apoptotic signals[26, 28]. In our study, we found that oridonin could simultaneously induce caspase 3-mediated apoptosis and Beclin 1-dependent autophagy in RPMI8226 cells. The inhibition of autophagy by 3-MA sensitized the cells to apoptosis, which suggests that oridonin cytotoxicity is mainly the result of apoptosis and that autophagy acts as a pro-survival mechanism in cells exposed to oridonin.

Intracellular ROS generation plays a significant role in physiological and pathological processes, and a high level of ROS is closely associated with apoptotic cell death. Recently, many studies have reported that ROS could induce apoptosis in a variety of malignant cells[12, 13]. Additionally, other studies have shown that oxidative stress could induce autophagy under certain conditions. H_2O_2 and 2-methoxyestradiol, a well-known generator of ROS, could induce autophagy, which contributed to cell death in HEK293, U87, and HeLa cells[29]. Our study demonstrated that oridonin induces a time-dependent increase in intracellular ROS generation accompanied by increases in apoptosis and autophagy. The complete inhibition of intracellular ROS generation by NAC abrogated oridonin-induced apoptosis and autophagy. These data indicate that intracellular ROS generation is required for the induction of autophagy and apoptosis by oridonin.

Hasegawa *et al* originally demonstrated that excess ROS positively regulates SIRT1 activity and serves as a compensatory mechanism to protect cells against apoptosis[18]. Recently, some studies have shown that SIRT1 activity was negatively regulated by intracellular ROS generation in lung epithelial cells, endothelial cells, and macrophages in response to cigarette smoke extract *in vitro* and in the lungs of patients with COPD (chronic obstructive pulmonary disease)[19, 30, 31]. In this study, we demonstrate that oridonin induces a time-dependent

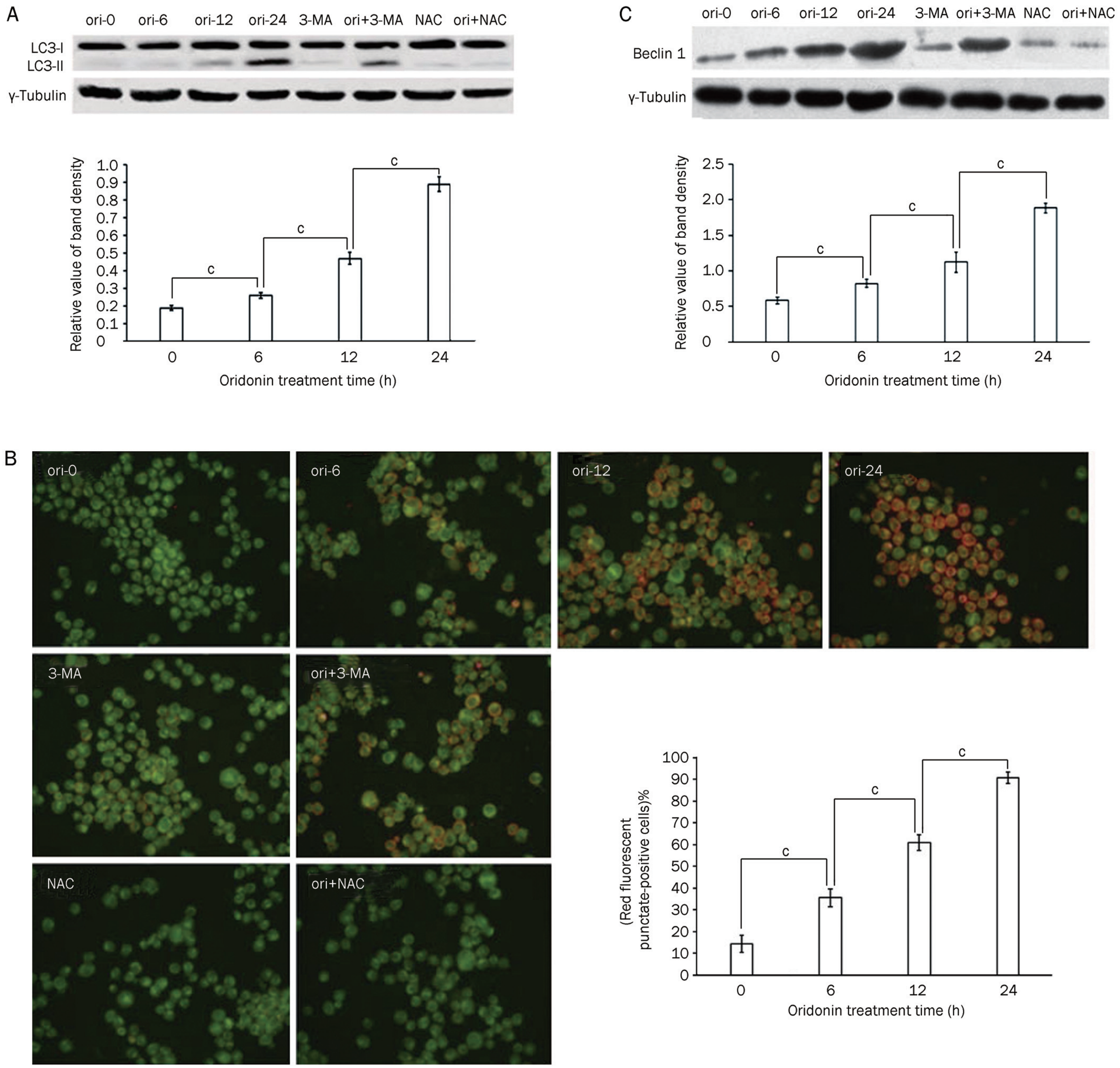

Figure 4. Autophagy of cell treated with oridonin (ori) alone, cells pre-incubated with NAC, and cells pre-incubated with 3-MA. The cells were treated with 7 μmol/L oridonin for 0, 6, 12, and 24 h, or treated with 7 μmol/L oridonin in the presence or absence of 5 mmol/L NAC, or treated with 7 μmol/L oridonin in the presence or absence of 5 mmol/L 3-MA for 24 h. (A) The LC3-II and LC3-I protein levels of treated cells were detected using Western blot assay. γ-Tubulin was used as an equal loading control. The bands were quantified by densitometric analysis. The LC3-II were corrected relative to γ-tubulin. (B) After designed experiment measures, the LC3 localization in cells was determined by immunofluorcesence using a fluorescent probe of $QDs_{605\ nm}$-Anti-LC3, and the localization of LC3-II at autophagosome membrane were indicated as red fluorescent punctate dots. The representative images are shown. Autophagy was quantitated by the percentage of fluorescent punctate-positive cells in total cells. the percentage of fluorescent punctate-positive cells was calculated as follows: the percentage of fluorescent punctate-positive cells (%)=number of fluorescent punctate-positive cells/number of total cells×100% (at least 500 cells were counted under a fluorescence microscope). (C) The protein level of Beclin 1 of treated cells was detected using Western blot assay. γ-Tubulin was used as an equal loading control. The bands were quantified by densitometric analysis. The values for Beclin 1 were corrected relative to theγ-tubulin and shown in histogram. All statistical significance was determined by Student's *t*-test. Columns, mean of three independent experiments; Mean±SD; $^{c}P<0.01$.

decrease in SIRT1 nuclear protein levels accompanied by an increase in intracellular ROS generation while NAC completely reverses this decrease. This observation suggests that SIRT1 activity is negatively regulated by intracellular

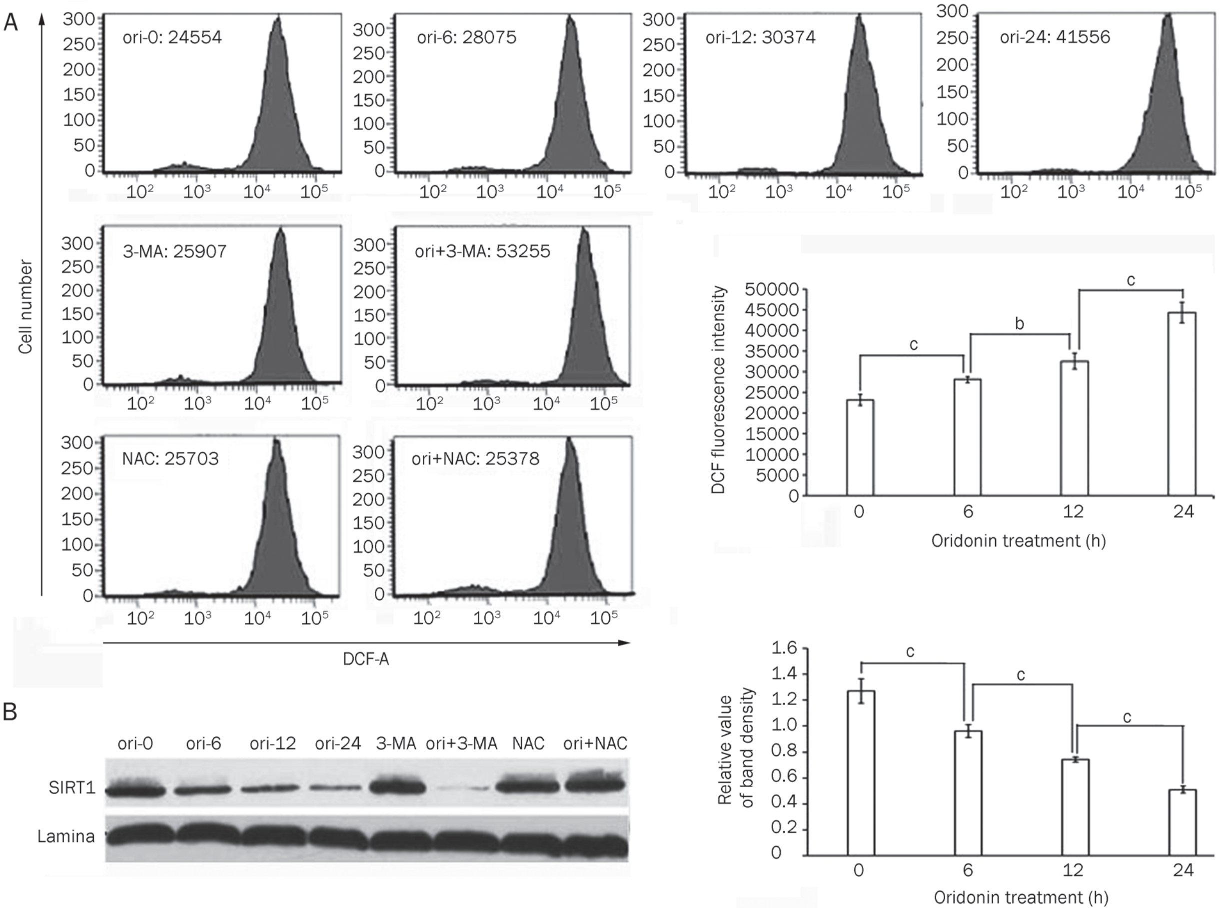

Figure 5. Assessment of the level of intracellular ROS generation and SIRT1 nucleic protein in cells treated with oridonin (ori) alone, cells pre-incubated with NAC and cells pre-incubated with 3-MA. The cells were treated with 7 μmol/L oridonin for 0, 6, 12, and 24 h, or treated with 7 μmol/L oridonin in the presence or absence of 5 mmol/L NAC, or treated with 7 μmol/L oridonin in the presence or absence of 5 mmol/L 3-MA for 24 h. (A) DCF fluorescent intensity was assessed by FCM analysis and shown in the histogram. (B) The levels of SIRT1 protein in nuclei were determined using Western blot assay. Nuclear lamina was used as an equal loading control. The bands were quantified by densitometric analysis and shown as histogram. All statistical significance was determined by Student's *t*-test. Columns, mean of three independent experiments; Mean±SD; $^{c}P<0.01$.

ROS generation in RPMI8226 cells exposed to oridonin. The anti-apoptotic function of SIRT1 was self-explanatory[20, 21, 32]. Accordingly, we demonstrated that oridonin decreases SIRT1 nuclear protein levels and increased apoptosis whereas 3-MA enhances oridonin-induced apoptosis and the decrease in SIRT1 nuclear protein levels. However, the role of SIRT1 in autophagy is controversial. Some studies have shown that SIRT1 promotes autophagy by down-regulating mTOR signaling[23]; however, other studies have shown that the inhibition of SIRT1 activity augmented autophagy[22]. In this study, we found that the increase in autophagy was associated with a decrease in SIRT1 nuclear protein levels and that the inhibition of autophagy by 3-MA further reduces SIRT1 nuclear protein levels and increases intracellular ROS generation. This result suggests that autophagy is negatively regulated by SIRT1 activity.

In summary, generation of intracellular ROS mediates apoptosis and autophagy in RPMI8226 cells exposed to oridonin and may be associated with a negative regulation of SIRT1 activity. Apoptosis, but not autophagy, was the major effector of oridonin-induced cytotoxicity. Autophagy protects against apoptosis mediated by intracellular ROS generation and SIRT1 activity. Our results provide new mechanistic information related to oridonin-induced apoptosis and autophagy, in addition to new MM therapeutic targets to enhance oridonin cytotoxicity.

Acknowledgements

This work was supported by grants from the National Natural Science Foundation of China (№ 30871036 and 81070429).

Author contribution

Yan CHEN, Rong ZENG, and Guo-hui CUI designed research; Rong ZENG and Shuai ZHAO performed research; and Rong ZENG analyzed data and wrote the paper.

References

1 Ikezoe T, Chen SS, Tong XJ, Heber D, Taguchi H, Koeffler HP. Oridonin

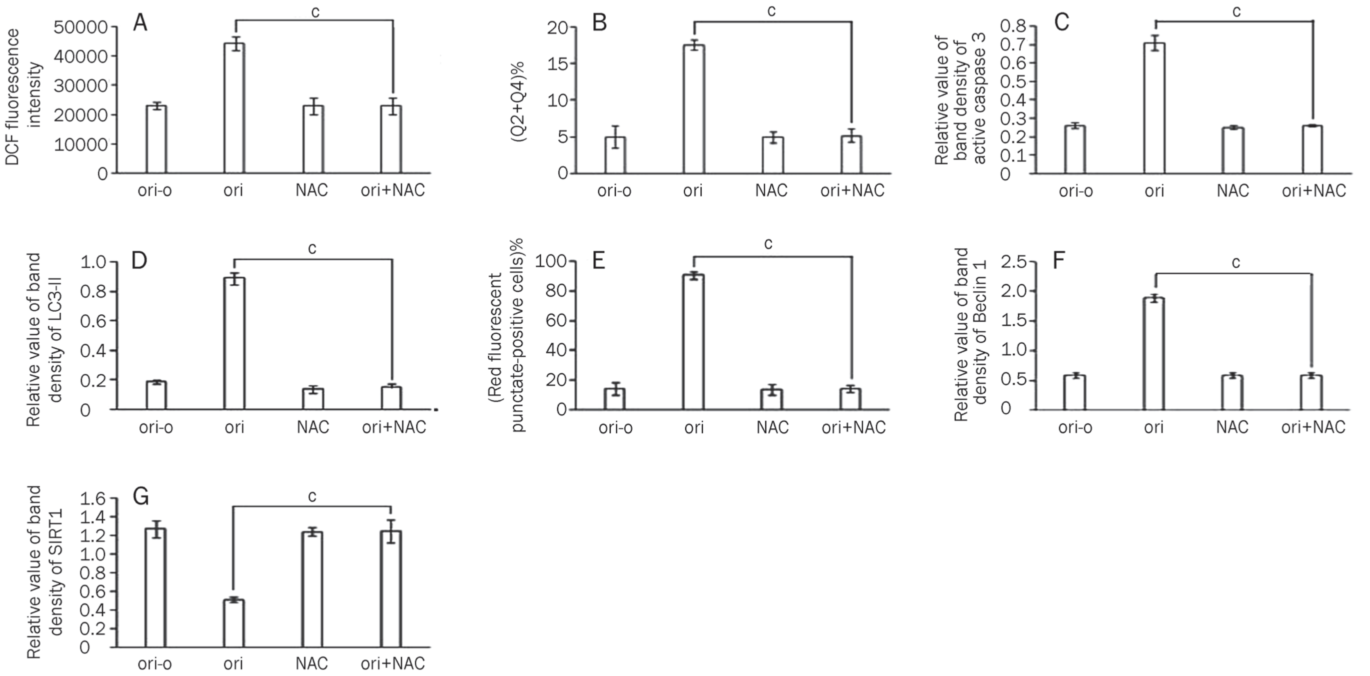

Figure 6. The effect of NAC on intracellular ROS generation, apoptosis, autophagy and SIRT1 activity in cells exposed to oridonin (ori). The data from the cells treated with 7 μmol/L oridonin in the presence and absence of 5 mmol/L NAC for 24 h were analyzed and compared with each other. Also data from the cells treated with 5 mmol/L NAC for 24 h and cells treated in the normal media were analyzed and compared. The histograms demonstrated the data mentioned above. (A) The DCF fluorescent intensity; (B) The apoptotic rate [(Q2+Q4)%]; (C) The protein levels of active caspase3; (D) The LC3-II/γ-tubulin ratio; (E) The percentage of red fluorescent punctate-positive cells; (F) The protein levels of Beclin 1; and (G) The SIRT1 nucleic protein levels. All statistical significance was determined by Student's *t*-test. Columns, mean of three independent experiments; Mean±SD; $^{c}P<0.01$.

induces growth inhibition and apoptosis of a variety of human cancer cells. Int J Oncol 2003; 23: 1187–93.

2 Osawa K, Yasuda H, Maruyama T, Morita H, Takeya K, Itokawa H. Antibacterial trichorabdal diterpenes from *Rabdosia trichocarpa*. Phytochemistry 1994; 36: 1287–91.

3 Han QB, Li ML, Li SH, Mou YK, Lin ZW, Sun HD. Ent-kaurane diterpenoids from *Isodon rubescens* var lushanensis. Chem Pharm Bull (Tokyo) 2003; 51: 790–3.

4 Bursch W, Ellinger A, Gerner C, Frohwein U, Schulte-Hermann R. Programmed cell death (PCD). Apoptosis, autophagic PCD, or others? Ann N Y Acad Sci 2000; 926: 1–12.

5 Shintani T, Klionsky DJ. Autophagy in health and disease: a double-edged sword. Science 2004; 306: 990–5.

6 Tsujimoto Y, Shimizu S. Another way to die: autophagic programmed cell death. Cell Death Differ 2005; 12: 1528–34.

7 Yang ZJ, Chee CE, Huang S, Sinicrope FA. The role of autophagy in cancer: therapeutic implications. Mol Cancer Ther 2011; 10: 1533–41.

8 Cui Q, Tashiro S, Onodera S, Minami M, Ikejima T. Oridonin induced autophagy in human cervical carcinoma HeLa cells through Ras, JNK, and P38 regulation. J Pharmacol Sci 2007; 105: 317–25.

9 Li D, Cui Q, Chen SG, Wu LJ, Tashiro S, Onodera S, *et al*. Inactivation of ras and changes of mitochondrial membrane potential contribute to oridonin-induced autophagy in a431 cells. J Pharmacol Sci 2007; 105: 22–33.

10 Cheng Y, Qiu F, Huang J, Tashiro S, Onodera S, Ikejima T. Apoptosis-suppressing and autophagy-promoting effects of calpain on oridonin-induced L929 cell death. Arch Biochem Biophys 2008; 475: 148–55.

11 Hoang B, Benavides A, Shi Y, Frost P, Lichtenstein A. Effect of autophagy on multiple myeloma cell viability. Mol Cancer Ther 2009; 8: 1974–84.

12 Hou DX, Tong X, Terahara N, Luo D, Fujii M. Delphinidin 3-sambubioside, a *Hibiscus anthocyanin*, induces apoptosis in human leukemia cells through reactive oxygen species-mediated mitochondrial pathway. Arch Biochem Biophys 2005; 440: 101–9.

13 Chipuk JE, Bouchier-Hayes L, Green DR. Mitochondrial outer membrane permeabilization during apoptosis: the innocent bystander scenario. Cell Death Differ 2006; 13: 1396–402.

14 Lisanti MP, Martinez-Outschoorn UE, Chiavarina B, Pavlides S, Whitaker-Menezes D, Tsirigos A, *et al*. Understanding the "lethal" drivers of tumor-stroma co-evolution: emerging role(s) for hypoxia, oxidative stress and autophagy/mitophagy in the tumor micro-environment. Cancer Biol Ther 2010; 10: 537–42.

15 Essick EE, Sam F. Oxidative stress and autophagy in cardiac disease, neurological disorders, aging and cancer. Oxid Med Cell Longev 2010; 3: 168–77.

16 Scherz-Shouval R, Elazar Z. Regulation of autophagy by ROS: physiology and pathology. Trends Biochem Sci 2011; 36: 30–8.

17 Grimsrud PA, Xie H, Griffin TJ, Bernlohr DA. Oxidative stress and covalent modification of protein with bioactive aldehydes. J Biol Chem 2008; 283: 21837–41.

18 Hasegawa K, Wakino S, Yoshioka K, Tatematsu S, Hara Y, Minakuchi H, *et al*. Sirt1 protects against oxidative stress-induced renal tubular cell apoptosis by the bidirectional regulation of catalase expression. Biochem Biophys Res Commun 2008; 372: 51–6.

19 Caito S, Hwang JW, Chung S, Yao H, Sundar IK, Rahman I. PARP-1

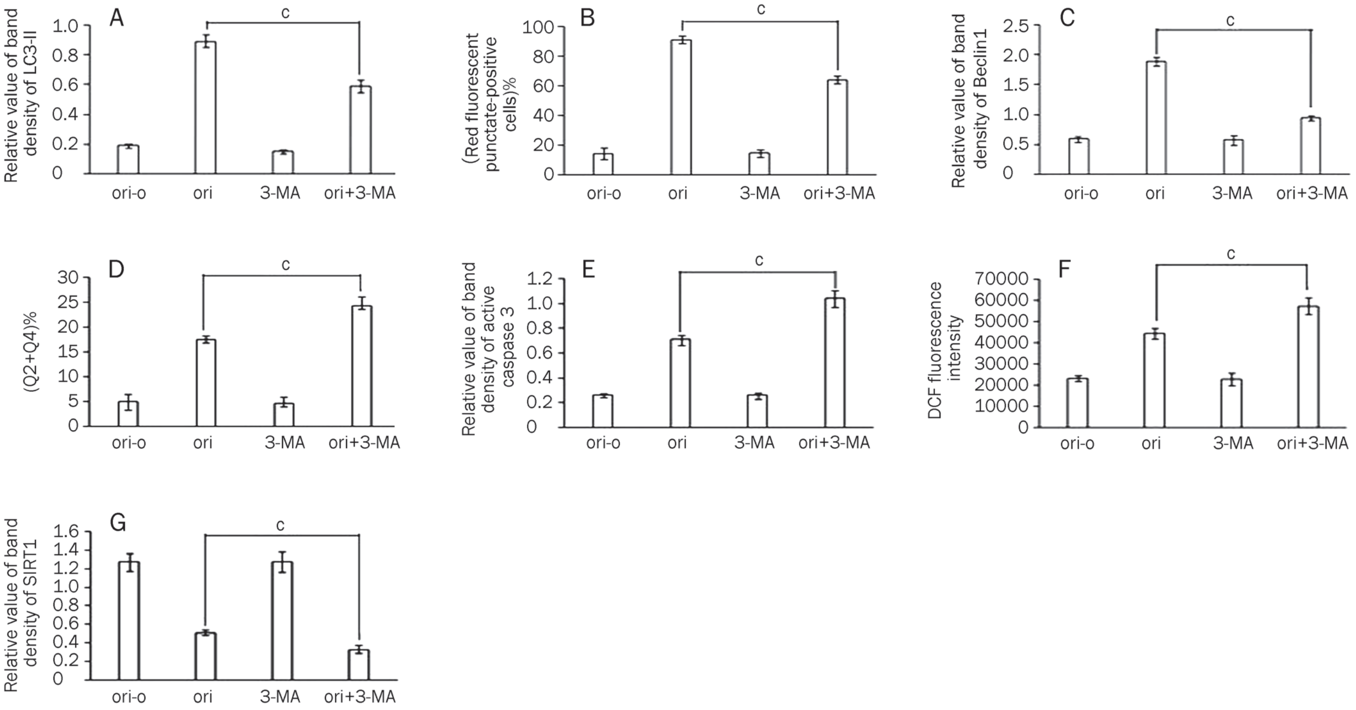

Figure 7. The effect of 3-MA on apoptosis, autophagy, intracellular ROS generation and SIRT1 activity in cells exposed to oridonin (ori). The data from the cells treated with 7 μmol/L oridonin in the presence and absence of 5 mmol/L 3-MA for 24 h were analyzed and compared with each other. Also data from the cells treated with 5 mmol/L 3-MA for 24 h and cells treated in the normal media were analyzed and compared. The histograms demonstrated the data mentioned above. (A) The LC3-II/γ-tubulin ratio; (B) The percentage of red fluorescent punctate-positive cells; (C) The protein levels of Beclin 1; (D) The apoptotic rate [(Q2+Q4)%]; (E) The protein levels of active caspase 3; (F) The DCF fluorescent intensity; and (G) The SIRT1 nucleic protein levels. All statistical significance was determined by Student's *t*-test. Columns, mean of three independent experiments; Mean±SD; $^{c}P<0.01$.

inhibition does not restore oxidant-mediated reduction in SIRT1 activity. Biochem Biophys Res Commun 2010; 392: 264–70.

20 Ford J, Jiang M, Milner J. Cancer-specific functions of SIRT1 enable human epithelial cancer cell growth and survival. Cancer Res 2005; 65: 10457–63.

21 Kojima K, Ohhashi R, Fujita Y, Hamada N, Akao Y, Nozawa Y, *et al*. A role for SIRT1 in cell growth and chemoresistance in prostate cancer PC3 and DU145 cells. Biochem Biophys Res Commun 2008; 373: 423–8.

22 Hwang JW, Chung S, Sundar IK, Yao H, Arunachalam G, McBurney MW, *et al*. Cigarette smoke-induced autophagy is regulated by SIRT1-PARP-1-dependent mechanism: implication in pathogenesis of COPD. Arch Biochem Biophys 2010; 500: 203–9.

23 Chung S, Yao H, Caito S, Hwang JW, Arunachalam G, Rahman I. Regulation of SIRT1 in cellular functions: role of polyphenols. Arch Biochem Biophys 2010; 501: 79–90.

24 Xie HY, Liang JG, Liu Y, Zhang ZL, Pang DW, He ZK, *et al*. Preparation and characterization of overcoated II–VI quantum dots. J Nanosci Nanotechnol 2005; 5: 880–6.

25 Kabeya Y, Mizushima N, Ueno T, Yamamoto A, Kirisako T, Noda T, *et al*. LC3, a mammalian homologue of yeast Apg8p, is localized in autophagosome membranes after processing. EMBO J 2000; 19: 5720–8.

26 Cui Q, Tashiro S, Onodera S, Ikejima T. Augmentation of oridonin-induced apoptosis observed with reduced autophagy. J Pharmacol Sci 2006; 101: 230–9.

27 Jia L, Dourmashkin RR, Allen PD, Gray AB, Newland AC, Kelsey SM. Inhibition of autophagy abrogates tumour necrosis factor alpha induced apoptosis in human T-lymphoblastic leukaemic cells. Br J Haematol 1997; 98: 673–85.

28 Zhu JH, Horbinski C, Guo F, Watkins S, Uchiyama Y, Chu CT. Regulation of autophagy by extracellular signal-regulated protein kinases during 1-methyl-4-phenylpyridinium-induced cell death. Am J Pathol 2007; 170: 75–86.

29 Chen Y, McMillan-Ward E, Kong J, Israels SJ, Gibson SB. Oxidative stress induces autophagic cell death independent of apoptosis in transformed and cancer cells. Cell Death Differ 2008; 15: 171–82.

30 Yang SR, Wright J, Bauter M, Seweryniak K, Kode A, Rahman I. Sirtuin regulates cigarette smoke-induced proinflammatory mediator release via RelA/p65 NF-kappaB in macrophages *in vitro* and in rat lungs *in vivo*: implications for chronic inflammation and aging. Am J Physiol Lung Cell Mol Physiol 2007; 292: L567–76.

31 Rajendrasozhan S, Yang SR, Kinnula VL, Rahman I. SIRT1, an anti-inflammatory and antiaging protein, is decreased in lungs of patients with chronic obstructive pulmonary disease. Am J Respir Crit Care Med 2008; 177: 861–70.

32 Kim EJ, Um SJ. SIRT1: roles in aging and cancer. BMB Rep 2008; 41: 751–6.

Acta Pharmacologica Sinica (2012) 33: 101–108
© 2012 CPS and SIMM All rights reserved 1671-4083/12 $32.00
www.nature.com/aps

Original Article

Inhibition of the STAT3 signaling pathway is involved in the antitumor activity of cepharanthine in SaOS2 cells

Zan CHEN, Chen HUANG, Yan-ling YANG, Yi DING, Han-qiang OU-YANG, You-yi ZHANG, Ming XU*

Institute of Vascular Medicine, Medical Research Center, Peking University Third Hospital, and Key Laboratory of Cardiovascular Molecular Biology and Regulatory Peptides, Ministry of Health, Beijing 100191, China

Aim: To investigate the molecular mechanisms underlying the antitumor activity of cepharanthine (CEP), an alkaloid extracted from *Stephania cepharantha* Hayata.
Methods: Human osteosarcoma cell line SaOS2 was used. MTT assay, Hoechst 33342 nuclear staining, flow cytometry, Western blotting and nude mouse xenografts of SaOS2 cells were applied to examine the antitumor activity of CEP *in vitro* and *in vivo*. The expression levels of STAT3 and its downstream signaling molecules were measured with Western blotting and immunochemistry analysis. The activity of STAT3 was detected based on the phosphorylation level of STAT3, luciferase gene reporter assay and translocation of STAT3 to the nucleus.
Results: Treatment of SaOS2 cells with CEP (2.5–20 μmol/L) inhibited the cell growth in a concentration- and time-dependent manner. CEP (10 μmol/L) caused cell cycle arrest at G_1 phase and induced apoptosis of SaOS2 cells. CEP (10 and 15 μmol/L) significantly decreased the expression of STAT3 in SaOS2 cells. Furthermore, CEP (5 and 10 μmol/L) significantly inhibited the expression of target genes of STAT3, including the anti-apoptotic gene Bcl-xL and the cell cycle regulators c-Myc and cyclin D1. In nude mouse xenografts of SaOS2 cells, CEP (20 $mg\cdot kg^{-1}\cdot d^{-1}$, ip for 19 d) significantly reduced the volume and weight of the tumor.
Conclusion: Our findings suggest that inhibition of STAT3 signaling pathway is involved in the anti-tumor activity of CEP.

Keywords: cepharanthine; anticancer drug; human osteosarcoma cell; SaOS2; cell cycle arrest; apoptosis; STAT3; nude mice

Acta Pharmacologica Sinica (2012) 33: 101–108; doi: 10.1038/aps.2011.164

Introduction

Cepharanthine (CEP) is a natural occurring small molecule, derived from the plant *Stephania cepharantha* Hayata, and has been used to treat diseases such as venomous snakebite, alopecia areata, exudative otitis media and endotoxic shock[1–4]. The pharmacological activities of CEP include the reversal of multidrug resistance[5–7], antitumor activity[8–10] and inhibiting the production of inflammatory mediators[11–14].

The mechanisms underlying the antitumor activity of CEP have drawn increasing attention. Although accumulating evidence has shown that CEP plays a potential role in inhibiting cell growth and inducing apoptosis in many tumors[3], the underlying mechanism remains elusive. Because CEP is primarily an anti-inflammatory agent, the antitumor activity of CEP is associated with inhibition of inflammation-related signaling pathways, among which NF-κB inactivation is important[8, 15, 16]. In addition to NF-κB, the signal transducer and activator of transcription protein 3 (STAT3) is another critical inflammatory mediator that links inflammation and cancer[17]. Constitutive activation of STAT3, as observed in multiple human cancers, plays a crucial role in cancer cell proliferation, differentiation, and survival by upregulating several genes. These genes include anti-apoptotic genes such as Bcl-xL, and cell cycle regulators such as cyclin D1 and c-Myc. As a critical mediator of oncogenic signaling, STAT3 is a promising target for cancer therapy and anti-cancer drug design[18].

It has been reported that the collaboration and crosstalk of STAT3 and NF-κB signaling are important for carcinogenesis associated with inflammation[19]. Genes that play vital roles in angiogenesis, anti-apoptosis and cell cycle regulation are regulated by both STAT3 and NF-κB in a cooperative and interdependent manner[19, 20]. In addition, although both STAT3 and NF-κB are recognized as promising targets for cancer therapy, disruption of the STAT3 or NF-κB signaling pathways

---

* To whom correspondence should be addressed.
E-mail xuminghi@bjmu.edu.cn
Received 2011-07-04 Accepted 2011-11-08

independently does not result in cell death[19]. We believe that inhibition of NF-κB activation alone cannot explain the antitumor activity of CEP. Our previous study demonstrated that CEP could downregulate the expression of the STAT3 gene at the transcriptional level[21]. Thus, we hypothesized that inhibition of STAT3 signaling is involved in CEP-induced cell death.

In this study, cell cycle arrest and apoptosis were observed in CEP-treated SaOS2 cells, an osteosarcoma cell line with constitutive STAT3 activation[22]. Downregulation of STAT3 gene expression was observed in SaOS2 cells after treatment with CEP. Further analysis of the STAT3 signaling pathway demonstrated that CEP inhibited the target genes of STAT3, including the anti-apoptotic gene Bcl-xL and cell cycle regulators c-Myc and cyclin D1. *In vivo* experiments were performed using nude mouse xenografts of SaOS2 cells. The antitumor activity and inhibitive effect on STAT3 expression and activation by CEP were further confirmed by animal experiments. Our findings provide the first evidence that CEP can inhibit the STAT3 signaling pathway, which helps us to better understand the anti-inflammatory and anti-tumor activity of CEP.

Materials and methods

Cells lines and cell culture

The SaOS2 human osteosarcoma cell line was obtained from the Global Bioresource Center (ATCC, USA). Cells were cultured in DMEM supplemented with 10% fetal bovine serum (FBS), penicillin (100 units/mL), and streptomycin (100 μg/mL) in the presence of 5% CO_2 in an incubator at 37 °C.

Materials

Cepharanthine (CEP) was purchased from the National Institute for the Control of Pharmaceutical and Biological Products (Beijing, China). MTT and Hoechst 33342 were purchased from Sigma.

Cell viability analysis

MTT assays were used to test cell viability as previously described[8]. In brief, 2.5×10^3 cells were seeded in each well of a 96-well plate. Cells were serum starved for 24 h and then incubated with different concentrations of CEP for 12, 24, and 48 h. After incubation, MTT (0.5 mg/mL final concentration) was added to each well. After 4 h of additional incubation, the medium was removed, and 200 μL of dimethyl sulfoxide (DMSO) was used to dissolve the resultant crystals. Absorption at 570 nm was determined for each sample using an automatic ELISA plate reader.

Hoechst 33342 staining

To observe morphological changes in the nucleus, cells were stained with 40 mg/L Hoechst 33342 after incubation with CEP (10 μmol/L) for 0, 24, and 48 h. Cells were visualized under a fluorescence microscope with a blue filter. Apoptotic cells were defined as those that showed cytoplasmic and nuclear shrinkage, and chromatin condensation or fragmentation.

Flow cytometry

Cell cycle progression and apoptosis were analyzed by flow cytometry. For cell cycle analysis, SaOS2 cells were treated with CEP (10 μmol/L) for 0, 24, and 48 h. After incubation, cells were trypsinized, counted, washed, fixed by dropwise addition of 70% ethanol and stored at 4 °C until analysis. Cells were washed with PBS, resuspended in 50 μg/mL propidium iodide (PI) solution and analyzed by flow cytometry. For apoptosis analysis, cells were incubated with CEP (15 μmol/L) for 0, 24, and 48 h followed by Annexin V-FITC and propidium iodide (PI) double staining performed according to the manufacturer's instructions (Biosea, Beijing, China).

Western blotting

Protein expression was examined by Western blot analysis as previously described[23]. Briefly, protein was harvested and quantified at different time points after SaOS2 cells were incubated with or without CEP at different concentrations. An amount of 40 μg of total protein per sample was separated by 10% or 15% sodium dodecyl sulfate polyacrylamide gel electrophoresis (SDS-PAGE) and then transferred by electroblotting onto a nitrocellulose membrane. The membrane was blocked in 5% bovine serum albumin and then incubated with antibodies against caspase 3 (Cell Signaling, USA), STAT3 (Santa Cruz, USA), phospho-STAT3 (Y705) (Cell Signaling, USA), c-Myc (Cell Signaling, USA), cyclin D1 (Cell Signaling, USA), Bcl-xL (Cell Signaling, USA) and β-actin (Cell Signaling, USA) in 5% BSA overnight at 4 °C. The membrane was then washed and incubated with horseradish peroxidase-labeled secondary antibodies for 1 h at room temperature. Bands were visualized by use of a Western super-sensitive chemiluminescence detection system (Pierce, USA). Autoradiographs were quantitated by densitometry (Science Imaging System, Bio-Rad). β-actin was used as the internal control for protein normalization.

Vector construction and luciferase gene reporter assay

Firefly luciferase reporter plasmids (APRE plasmids) with STAT3-driven promoters (2×APRE) were constructed as previously described[23]. Briefly, the STAT3-driven promoter (the 2×APRE sequence) was cloned into the multiple cloning site of the pGL3-TATA plasmid, which encodes a firefly luciferase gene containing a basic upstream TATA element. The internal control Renilla luciferase reporter plasmid was purchased from Promega (USA).

The luciferase gene reporter assay was performed as previously described[23]. Briefly, SaOS2 cells were transfected with APRE plasmids and the internal control Renilla luciferase reporter plasmid using Lipofectamine™ 2000 (Invitrogen, USA) in accordance with the manufacturer's instructions. After 6 h of transfection, cells were treated with 0, 5, or 10 μmol/L of CEP. For the time course, cells were treated with 10 μmol/L CEP for 0, 12, and 24 h. After CEP treatment, cell extracts were prepared and assayed according to the manufacturer's instructions (Dural Luciferase Assay System, Promega, USA). The measured firefly luciferase activity was normalized to the activity of Renilla luciferase in the same well.

Nude mice experiment

Eighteen four-week-old nude mice (T cell deficient nude mice) were housed and monitored in the Department of Laboratory Animal Science at the Peking University Health Science Center. The mice were randomly divided into a control group (CON) and a CEP-treated group (CEP), with nine mice in each group. Each mouse was injected subcutaneously in the right axilla with 2×10^6 SaOS2 cells. After the longest axis of the tumors grew to between 5 and 8 mm, the nude mice were intraperitoneally (ip) injected with DMSO or CEP (20 $mg\cdot kg^{-1}\cdot d^{-1}$) for 19 d. The mice were also weighed, and the longest axis (*L*) and vertical axis (*R*) of the tumors were measured every two days after starting ip injections. Tumor volumes (*V*) were estimated using the following formula: $V=0.5\times L\times R^2$. On the 20th d, the tumors were removed, weighed and fixed in 4% paraformaldehyde overnight for immunohistochemistry studies.

Immunohistochemistry

Immunohistochemistry assays were performed using the peroxidase-antiperoxidase technique after a microwave antigen retrieval procedure. Coverslips with mouse graft tissue sections were exposed to antibodies against STAT3 and phospho-STAT3-Y705 (Bioworld Technology, USA) and incubated overnight at 4 °C. Secondary antibody (Dako, Germany) incubation was performed at room temperature for 30 min. 3,3′-Diaminobenzidine (DAB) staining showed that the STAT3-positive cells were brown.

Statistical analysis

Values are expressed as the mean±SEM. The statistical significance was calculated using one-way ANOVA with a Bonferroni *post-hoc* test as applicable or a *t*-test for the comparison of two groups. A P value <0.05 was considered statistically significant.

Results

CEP inhibited SaOS2 cell viability in a dose- and time-dependent manner

The effects of CEP on the viability of SaOS2 cells were determined using an MTT assay (Figure 1). The result revealed that the growth of SaOS2 cells was inhibited after treatment with CEP in a time- and dose-dependent manner, with IC_{50} at 48 h of 3.18 μmol/L.

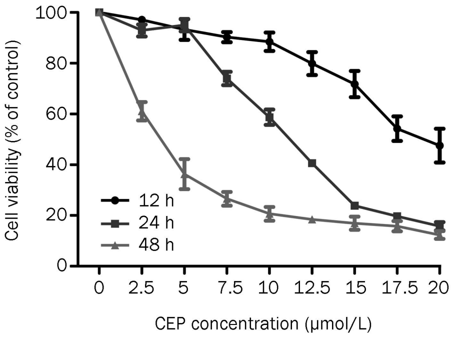

Figure 1. Growth inhibitive effects of CEP on SaOS2 cell line determined by MTT assay. SaOS2 cells were seeded in 96-well plates and treated with different concentrations of CEP for 12, 24, and 48 h, respectively. Relative cell viability was indicated as the percentage compared to control group (cells treated without CEP).

Cell cycle arrest and apoptosis of SaOS2 cells induced by CEP

To assess the effect of CEP on SaOS2 cells, we conducted Hoechst 33342 staining to observe morphological changes in the nucleus. As the results demonstrate (Figure 2A), a significant proportion of untreated SaOS2 cells showed mitotic phase features (indicated with the red arrow), while cells in the mitotic phase were rarely observed in the group treated with CEP for 24 h. This indicates that cell proliferation may have been inhibited by CEP. Furthermore, cells treated with CEP for 48 h contained significant morphological changes, including rippled nuclei, folded cell membranes and condensed and cracked chromatin in fragmented nuclei, resembling the appearance of apoptotic bodies (Figure 2A).

Flow cytometry further indicated that cell cycle arrest was induced after 24 h of treatment with CEP (Figure 2B). Cells remaining in the G_1 phase significantly increased after 24- and 48-h treatments with CEP. Flow cytometry using Annexin V-FITC and PI double staining revealed that the fraction of apoptotic cells in the group treated with CEP for 48 h was significantly higher than that of the control group (Figure 2C).

The effect of CEP on the activation of caspase 3 was examined to confirm the apoptotic effect of CEP. As shown in Figure 2D, cleaved caspase 3 protein was increased significantly by treatment with CEP.

Inhibition of STAT3 expression by CEP

To investigate whether the inhibition of STAT3 gene expression was involved in apoptosis induced by CEP, Western blotting was performed. STAT3 protein levels in SaOS2 cells were significantly downregulated after incubation for 24 h with 10 μmol/L and 15 μmol/L CEP (Figure 3A). Furthermore, when treated with CEP (10 μmol/L) for 0–48 h, the level of STAT3 decreased as the incubation time increased (Figure 3B).

Inhibition of STAT3 signaling pathway by CEP

Because inhibition of the STAT3 protein was observed by Western blotting, we further investigated whether activation of the STAT3 signaling pathway was inhibited by CEP. Phosphorylation of STAT3 is a vital step in the activation of STAT3, and therefore, we first quantified the levels of phosphorylated STAT3 in SaOS2 cells after treatment with CEP using Western blotting. As the results demonstrate, phosphorylation of STAT3 was inhibited by CEP (Figure 4A). The expression of some STAT3 target genes, including c-Myc, cyclin D1, and Bcl-xL, were also assessed by Western blotting. The results demonstrate that these target genes were also significantly downregulated by treatment with CEP, indicating that the

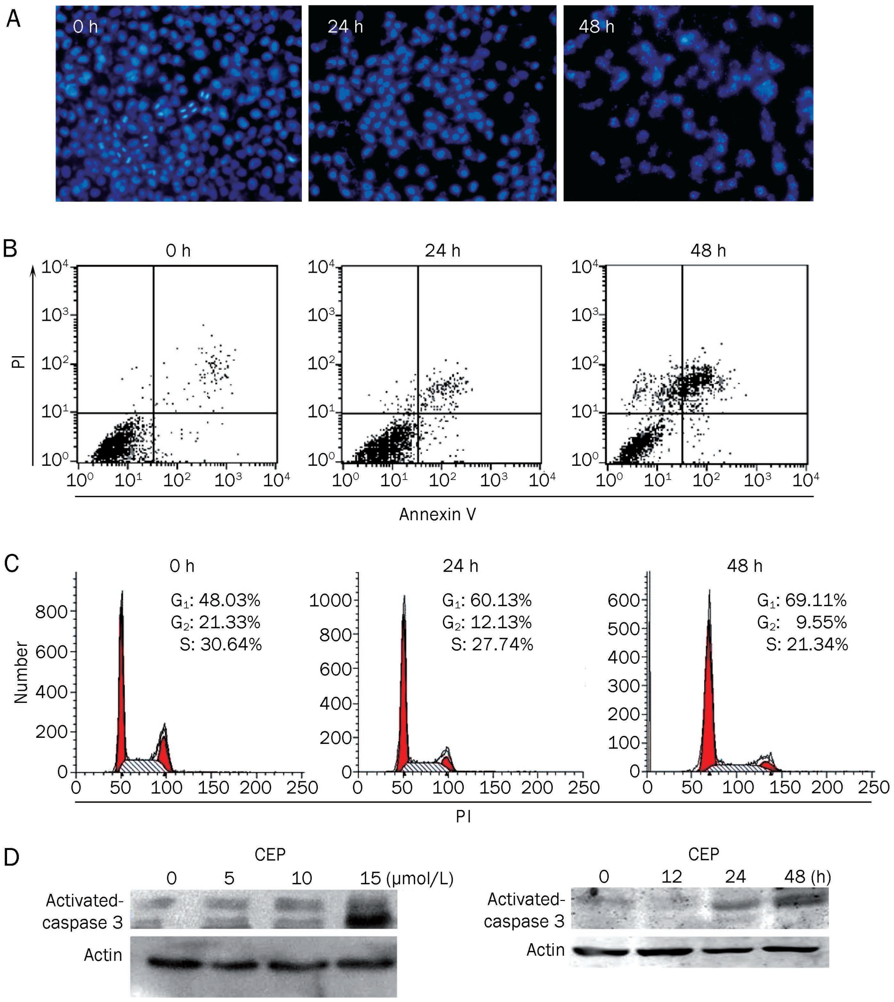

Figure 2. Cell cycle arrest and apoptosis of SaOS2 cells induced by CEP. (A) Nucleus staining by Hoechst 33342. SaOS2 cells were stained with Hoechst 33342 after incubation with CEP (10 μmol/L) for 0, 24, and 48 h. The red arrow indicates cells in mitotic phase. (B) Cell cycle arrest of SaOS2 cells induced by CEP. Cells were incubated with CEP at 10 μmol/L for 0, 24, and 48 h, and then treated with PI (50 μg/mL). Cell cycle was analyzed by flow cytometry. (C) Apoptosis-inducing effect of CEP on SaOS2 cells. After treatment with CEP (15 μmol/L) for 0, 24, and 48 h, the apoptotic rate of SaOS2 cells was determined by Annexin V-FITC and PI double staining using flow cytometry. (D) Activation of caspase 3 induced by CEP treatment. SaOS2 cells were treated with 0, 5, 10, and 15 μmol/L CEP for 48 h, and for 0, 12, 24, and 48 h at the concentration of 15 μmol/L. The level of caspase 3 was detected by Western blotting. The house-keeping gene β-actin was used as the internal control.

transcriptional activating activity of STAT3 was inhibited (Figure 4A). To further confirm the inhibitive effect of CEP on the activation of STAT3, luciferase reporter gene assays were performed. SaOS2 cells were transfected with APRE plasmids, which contained STAT3-driven promoters and encoded firefly luciferase, and were treated with different concentrations of CEP for 0, 12, and 24 h. APRE luciferase activities were significantly attenuated by treatment with CEP in a time- and dose-dependent manner (Figure 4B).

Antitumor effect of CEP and inhibition of STAT3 activation *in vivo*

The *in vivo* antitumor activity of CEP was assessed using nude mouse xenografts of SaOS2 cells. After subcutaneous injection tumors were established in the axilla of each mouse, the mice were randomly divided into a control group treated with vehicle DMSO and a CEP group treated with CEP (20 $mg \cdot kg^{-1} \cdot d^{-1}$, ip). Tumor volumes and body weights were recorded every two days. On the twentieth day, all the mice were euthanized and tumors were weighed. The volume growth curve showed that tumors from the CEP-treated group grew significantly slower than those from the control group (Figure 5A). Moreover, after treatment with CEP for 20 d, the tumor weights and volumes of the CEP-treated group were significantly lower than those of the control group (Figure 5B and 5C). However, the body weights of the mice were not significantly influenced by treatment with CEP (Figure 5D).

We determined whether the expression of STAT3 protein was decreased and STAT3 activity was suppressed by CEP administration in the nude mouse model. SaOS2 tumors were resected and processed for immunohistochemical analyses of STAT3 and phosphorylated STAT3. As shown in Figure 6, lower levels of STAT3 and phospho-STAT3 were found in CEP-treated tumor lesions than in untreated control tumors. In addition, we observed that nuclear localization of STAT3 in the CEP-treated group was inhibited (indicated by red arrows in Figure 6), suggesting that CEP may also have affected the translocation of STAT3 to the nucleus.

Discussion

Cepharanthine (CEP) is a promising, natural occurring small molecule for medical applications. As an anti-inflammatory agent, CEP has been used to treat many inflammatory diseases such as exudative otitis media and endotoxic shock[3, 4]. Similar to other widely studied natural products such as curcumin[24, 25], CEP has multiple targets and multiple effects. In recent years, the antitumor activity of CEP has drawn the

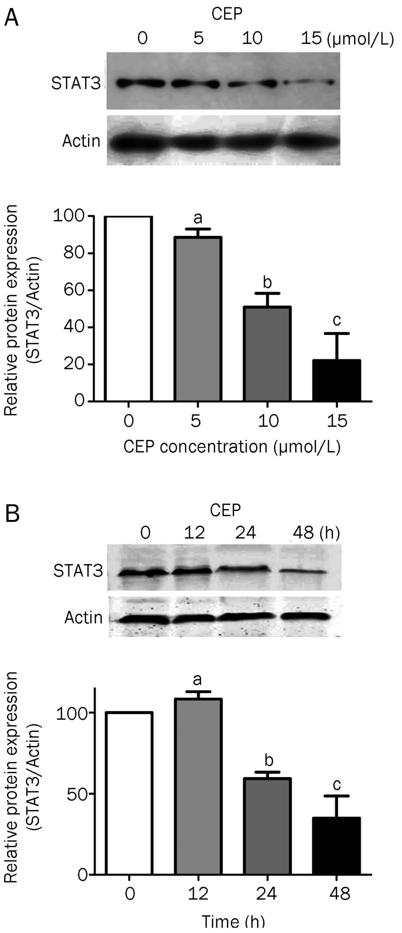

Figure 3. Western blotting for total STAT3 protein. (A) SaOS2 cells were incubated with CEP at the concentrations of 0, 5, 10, and 15 μmol/L for 24 h and protein was collected and analyzed with Western blotting. (B) SaOS2 cells were treated by CEP (10 μmol/L) for 0, 12, 24, and 48 h. Then the STAT3 expression level was determined by Western blotting using β-actin as the internal control. The graphs shown represent mean±SEM of three separate experiments. Results are expressed as percentage of the control (^{a}P>0.05, ^{b}P<0.05, ^{c}P<0.01 *vs* control).

most attention among its multiple pharmacological activities. CEP has shown the potential to inhibit growth and induce apoptosis in many tumors such as leukemia, lymphoma, lung carcinoma, myeloma, cholangiocarcinoma, oral squamous cell carcinoma and hepatocellular carcinoma[8–10, 15, 26–28]. In this study, treatment with CEP induced cell growth inhibition and apoptosis in SaOS2 cells, an osteosarcoma cell line (Figure 1 and 2). Notably, cell cycle arrest occurred earlier and at a lower dose than apoptosis in SaOS2 cells treated with CEP. This indicates that the antitumor activity of CEP is attributed to both cell cycle arrest and apoptosis, and cell cycle arrest might play a more important role (Figure 2). The ip administration of CEP in nude mouse grafts of SaOS2 cells demonstrated the tumor-suppressing activity of CEP (Figure 5).

According to previous studies, the mechanisms underlying the antitumor activity of CEP include the following. First, CEP stabilizes the cell membrane by interacting with

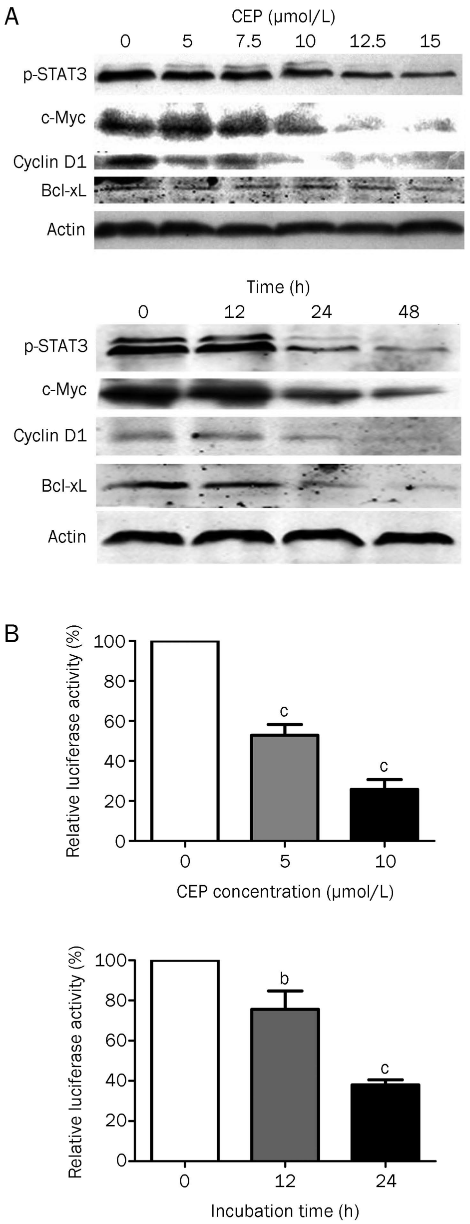

Figure 4. Inhibition of STAT3 signaling pathway by CEP. (A) Western blotting for p-STAT3, c-Myc, cyclin D1, and Bcl-xL. SaOS2 cells were treated with different concentrations of CEP from 0 to 15 μmol/L for 24 h. For the time course, cells were incubated with CEP (10 μmol/L) for 0, 12, 24, and 48 h. β-actin was used as the internal control. (B) Luciferase assay of APRE plasmids in SaOS2 cells under CEP treatment in different concentrations and at different time points. Cell extracts were prepared and luciferase activities were assayed according to the manufacturer's instruction. Each measured activity of firefly luciferase was normalized by the activity of Renilla luciferase in the same well. The data presents mean relative luciferase activity of three individual experiments (^{b}P<0.05, ^{c}P<0.01 *vs* control).

P-glycoprotein and increases the intracellular accumulation of anticancer drugs, thus reversing multidrug resistance in cancer cells[5–7]. Second, CEP might indirectly inhibit tumor growth by enhancing the immunological responses of the host[29, 30].

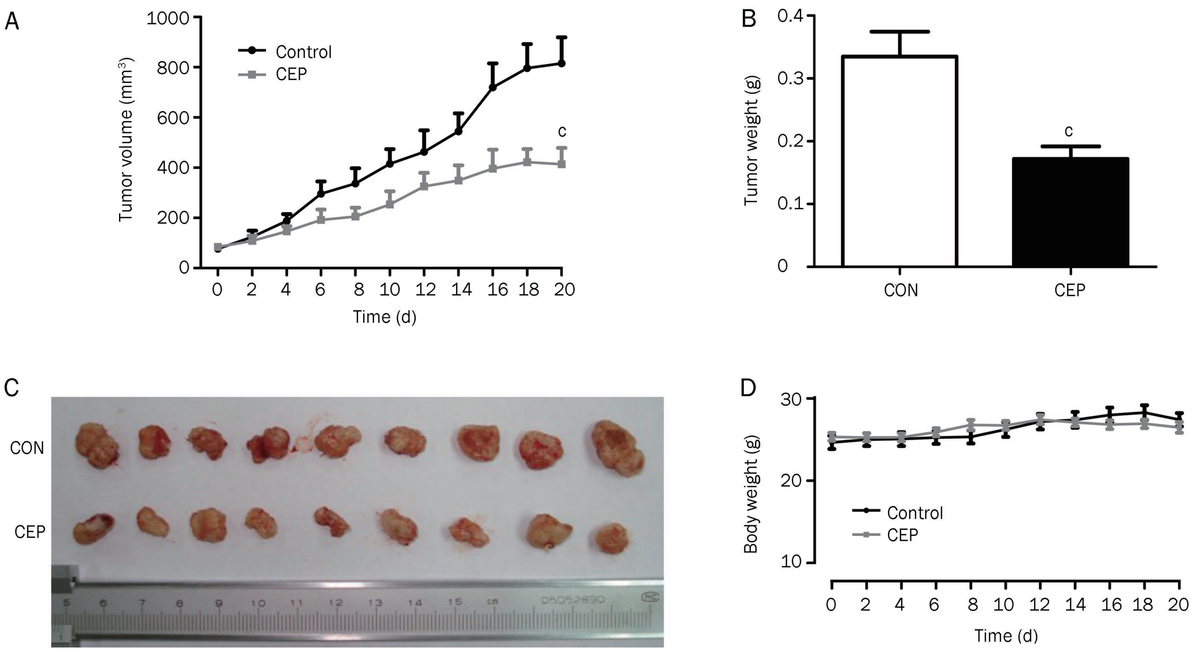

Figure 5. *In vivo* experiments. Eighteen nude mice were randomly grouped as a control group (CON) and a CEP-treated group (CEP). When the xenograft model of SaOS2 cells was established, mice in CON group were injected with DMSO while those in CEP group with CEP (20 mg·kg^{-1}·d^{-1}, ip). Body weight, long axon (L) and vertical axon (R) of each mouse were measured every two days. (A) Tumor volume growth curve of SaOS2 grafts in mice. The volumes of tumors were estimated using the formula: V=0.5×L×R^2. $^c P<0.01$. (B) The tumor weights of the two groups. On the twentieth day of CEP treatment, mice were sacrificed and the tumors were weighed after being sected. $^c P<0.01$ *vs* control. (C) Photograph of the tumors. (D) Record of body weights of mice.

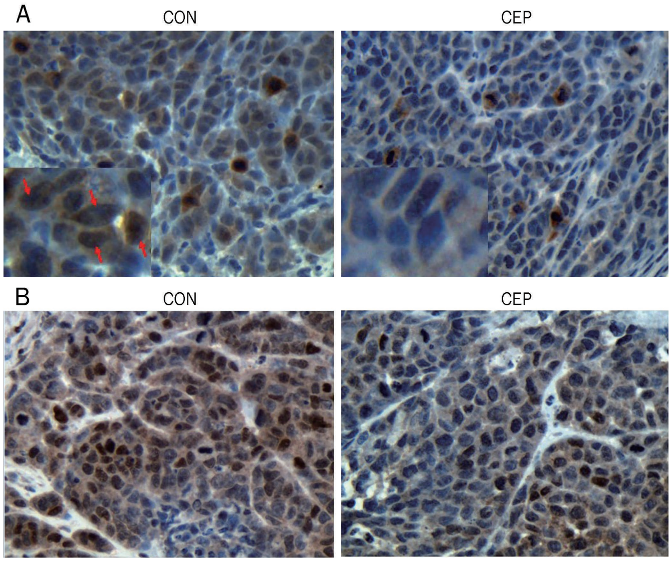

Figure 6. Immunohistochemical analyses of STAT3. After treatment of CEP for 20 d, the tumor samples were taken from the sacrificed mice and immunostained with antibodies against total and phosphorylated STAT3. (A) Immunohistochemical staining of total STAT3. STAT3 nuclear localization in control group was indicated with the red arrows. (B) Immunohistochemical staining of phospho-STAT3. Original magnification: ×400.

Third, CEP could induce tumor cell apoptosis by interfering with vital signaling pathways such as the nuclear factor kappa B (NF-κB) and JNK1/2 signaling pathways[8–10]. Because CEP is primarily an anti-inflammation agent, the mechanisms underlying its antitumor activity are closely related to the inhibition of inflammatory signaling[3]. The inflammatory pathways that are important in carcinogenesis include NF-κB, STATs and COX$^-$, and they are promising targets for cancer therapy[31, 32]. Previous studies have shown that inactivation of NF-κB is an important mechanism for the antitumor activity of CEP[8, 15, 16].

SaOS2 is an osteosarcoma cell line in which STAT3 is constitutively activated and plays a crucial role in cell proliferation and survival[10, 22, 33]. STAT3 is a critical inflammatory mediator that links inflammation and cancer[17, 32]. It relays signals from the cell membrane directly to the nucleus and activates the transcription of many important genes, including anti-apoptotic genes such as Bcl-xL, and cell cycle regulators such as cyclin D1 and c-Myc[34]. According to Western blotting results, STAT3 expression in SaOS2 cells was suppressed by CEP (Figure 4). Because downregulation of STAT3 expression was observed, we asked whether the inactivation of the STAT3 signaling pathway was involved in the antitumor activity of CEP. The activation of STAT3 requires many steps. Briefly, to be activated, cytoplasmic STAT3 protein is first phosphorylated by JAK. Phosphorylated STAT3 forms homodimers that translocate to the cell nucleus where they bind to the promoters of target genes and activate the transcription of oncogenes[34]. In our study, we showed that the phosphorylation of STAT3 was inhibited, the vital target genes of STAT3 such as c-Myc, cyclin D1 and Bcl-xL were downregulated, and the luciferase activity of APRE plasmids were attenuated by CEP (Figure 4). Immunohistochemistry further demonstrated that the expression of STAT3 was inhibited by CEP treatment (Figure 6A). It also indicated that activation of STAT3 was blocked by CEP because the phospho-STAT3 level in the CEP group significantly decreased compared to the control group (Figure 6B), and STAT3 translocation to the nucleus decreased with the administration of CEP (Figure 6A, indicated by red arrows). We showed through these results that inhibition of the STAT3 signaling pathway might play an important role in the antitumor activity of CEP. Our results also indicated that CEP inhibited STAT3 signaling by downregulating the expression of the STAT3 gene. However, further experiments are necessary to determine how STAT3 gene expression is downregulated by CEP, and to confirm the causal relationship between inhibition of the STAT3 signaling pathway and cell death.

In summary, CEP is an anti-inflammation and antitumor agent with multiple targets and effects. NF-κB signaling aside, our findings demonstrated that inhibition of another vital signaling pathway, the STAT3 signaling pathway, is involved in the antitumor activity of CEP. This helps us to better understand the anti-inflammation and antitumor activity of CEP. Moreover, our discovery of STAT3 signaling as a new mediator of the antitumor activity of CEP provides novel insight into the treatment of tumors with multi-target, naturally occurring small molecules.

Acknowledgements

This project was supported by the National Natural Science Foundation (81070196), the Natural Science Foundation of Beijing (7082101), and Program for New Century Excellent Talents in University and Beijing Talents Foundation (BMU20100012).

Author contribution

Ming XU and You-yi ZHANG designed the research; Zan CHEN performed the research and analyzed the data; Zan CHEN, Chen HUANG, Yan-ling YANG, Yi DING, and Han-qiang OU-YANG contributed new analytical tools; and Zan CHEN and Ming XU wrote this paper.

References

1 Kimoto T, Suemitsu K, Nakayama H, Komori E, Ohtani M, Ando S. Therapeutic experience of venomous snakebites by the Japanese viper (*Agkistrodon halys* Blomhoffii) with low dose of antivenin: report of 43 consecutive cases. Nippon Geka Hokan 1997; 66: 71–7.

2 Morita K, Nakamura M, Nagamachi M, Kishi T, Miyachi Y. Seventeen cases of alopecia areata: combination of SADBE topical immunotherapy with other therapies. J Dermatol 2002; 29: 661–4.

3 Furusawa S, Wu J. The effects of biscoclaurine alkaloid cepharanthine on mammalian cells: implications for cancer, shock, and inflammatory diseases. Life Sci 2007; 80: 1073–9.

4 Goto M, Zeller WP, Hurley RM. Cepharanthine (biscoclaurine alkaloid) treatment in endotoxic shock of suckling rats. J Pharm Pharmacol 1991; 43: 589–91.

5 Mukai M, Che XF, Furukawa T, Sumizawa T, Aoki S, Ren XQ, *et al.* Reversal of the resistance to STI571 in human chronic myelogenous leukemia K562 cells. Cancer Sci 2003; 94: 557–63.

6 Shiraishi N, Akiyama S, Nakagawa M, Kobayashi M, Kuwano M. Effect of bisbenzylisoquinoline (biscoclaurine) alkaloids on multidrug resistance in KB human cancer cells. Cancer Res 1987; 47: 2413–6.

7 Fujimura T, Shibata H, Maekawa I, Furusawa S, Kawauchi H, Sasaki K, *et al.* Reversal of resistance to doxorubicin with cepharanthine in murine P388 leukemia cells. Jpn J Pharmacol 1990; 54: 464–7.

8 Seubwai W, Vaeteewoottacharn K, Hiyoshi M, Suzu S, Puapairoj A, Wongkham C, *et al.* Cepharanthine exerts antitumor activity on cholangiocarcinoma by inhibiting NF-kappaB. Cancer Sci 2010; 101: 1590–5.

9 Wu J, Suzuki H, Zhou YW, Liu W, Yoshihara M, Kato M, *et al.* Cepharanthine activates caspases and induces apoptosis in Jurkat and K562 human leukemia cell lines. J Cell Biochem 2001; 82: 200–14.

10 Biswas KK, Tancharoen S, Sarker KP, Kawahara K, Hashiguchi T, Maruyama I. Cepharanthine triggers apoptosis in a human hepatocellular carcinoma cell line (HuH-7) through the activation of JNK1/2 and the downregulation of Akt. FEBS Lett 2006; 580: 703–10.

11 Murakami K, Okajima K, Uchiba M. The prevention of lipopolysaccharide-induced pulmonary vascular injury by pretreatment with cepharanthine in rats. Am J Respir Crit Care Med 2000; 161: 57–63.

12 Murakami K, Cox RA, Hawkins HK, Schmalstieg FC, McGuire RW, Jodoin JM, *et al.* Cepharanthin, an alkaloid from *Stephania cepharantha*, inhibits increased pulmonary vascular permeability in an ovine model of sepsis. Shock 2003; 20: 46–51.

13 Okamoto M, Ono M, Baba M. Potent inhibition of HIV type 1 replication by an antiinflammatory alkaloid, cepharanthine, in chronically infected monocytic cells. AIDS Res Hum Retroviruses 1998; 14: 1239–45.

14 Azuma M, Aota K, Tamatani T, Motegi K, Yamashita T, Ashida Y, *et al.* Suppression of tumor necrosis factor alpha-induced matrix metalloproteinase 9 production in human salivary gland acinar cells by cepharanthine occurs via down-regulation of nuclear factor kappaB: a possible therapeutic agent for preventing the destruction of the acinar structure in the salivary glands of Sjogren's syndrome patients. Arthritis Rheum 2002; 46: 1585–94.

15 Harada K, Ferdous T, Itashiki Y, Takii M, Mano T, Mori Y, *et al.* Cepharanthine inhibits angiogenesis and tumorigenicity of human oral squamous cell carcinoma cells by suppressing expression of vascular endothelial growth factor and interleukin-8. Int J Oncol 2009; 35: 1025–35.

16 Tamatani T, Azuma M, Motegi K, Takamaru N, Kawashima Y, Bando T. Cepharanthin-enhanced radiosensitivity through the inhibition of radiation-induced nuclear factor-kappaB activity in human oral squamous cell carcinoma cells. Int J Oncol 2007; 31: 761–8.

17 Bollrath J, Greten FR. IKK/NF-kappaB and STAT3 pathways: central signalling hubs in inflammation-mediated tumour promotion and metastasis. EMBO Rep 2009; 10: 1314–9.

18 Jing N, Tweardy DJ. Targeting Stat3 in cancer therapy. Anticancer Drugs 2005; 16: 601–7.

19 Grivennikov SI, Karin M. Dangerous liaisons: STAT3 and NF-kappaB collaboration and crosstalk in cancer. Cytokine Growth Factor Rev

2010; 21: 11–9.
20 Yang J, Liao X, Agarwal MK, Barnes L, Auron PE, Stark GR. Unphosphorylated STAT3 accumulates in response to IL-6 and activates transcription by binding to NFkappaB. Genes Dev 2007; 21: 1396–408.
21 Lin S, Li S, Chen Z, He X, Zhang Y, Xu X*, et al*. Formation, recognition and bioactivities of a novel G-quadruplex in the STAT3 gene. Bioorg Med Chem Lett 2011; 21: 5987–91.
22 Ryu K, Susa M, Choy E, Yang C, Hornicek FJ, Mankin HJ*, et al*. Oleanane triterpenoid CDDO-Me induces apoptosis in multidrug resistant osteosarcoma cells through inhibition of Stat3 pathway. BMC Cancer 2010; 10: 187.
23 Zhang H, Feng W, Liao W, Ma X, Han Q, Zhang Y. The gp130/STAT3 signaling pathway mediates beta-adrenergic receptor-induced atrial natriuretic factor expression in cardiomyocytes. FEBS J 2008; 275: 3590–7.
24 Fu S, Kurzrock R. Development of curcumin as an epigenetic agent. Cancer 2010; 116: 4670–6.
25 Lin JK, Pan MH, Lin–Shiau SY. Recent studies on the biofunctions and biotransformations of curcumin. Biofactors 2000; 13: 153–8.
26 Takahashi-Makise N, Suzu S, Hiyoshi M, Ohsugi T, Katano H, Umezawa K*, et al*. Biscoclaurine alkaloid cepharanthine inhibits the growth of primary effusion lymphoma *in vitro* and *in vivo* and induces apoptosis via suppression of the NF-kappaB pathway. Int J Cancer 2009; 125: 1464–72.
27 Ito H, Amano H, Noda H. Inhibitory effect of a biscoclaurine alkaloid, cepharanthin, on lung metastasis of Lewis lung carcinoma. Jpn J Pharmacol 1991; 56: 195–202.
28 Kikukawa Y, Okuno Y, Tatetsu H, Nakamura M, Harada N, Ueno S*, et al*. Induction of cell cycle arrest and apoptosis in myeloma cells by cepharanthine, a biscoclaurine alkaloid. Int J Oncol 2008; 33: 807–14.
29 Ono M. Antitumor effect of cepharanthin — mechanism of the antimetastatic effect on Lewis lung carcinoma (3LL). Gan To Kagaku Ryoho 1988; 15: 249–55.
30 Ebina T, Ishikawa K, Murata K. Antitumor effect of Cepharanthin in the double grafted tumor system. Gan To Kagaku Ryoho 1990; 17: 1165–71.
31 Deorukhkar A, Krishnan S. Targeting inflammatory pathways for tumor radiosensitization. Biochem Pharmacol 2010; 80: 1904–14.
32 Yu H, Pardoll D, Jove R. STATs in cancer inflammation and immunity: a leading role for STAT3. Nat Rev Cancer 2009; 9: 798–809.
33 Ryu K, Choy E, Yang C, Susa M, Hornicek FJ, Mankin H*, et al*. Activation of signal transducer and activator of transcription 3 (Stat3) pathway in osteosarcoma cells and overexpression of phosphorylated-Stat3 correlates with poor prognosis. J Orthop Res 2010; 28: 971–8.
34 Bowman T, Garcia R, Turkson J, Jove R. STATs in oncogenesis. Oncogene 2000; 19: 2474–88.

Acta Pharmacologica Sinica (2012) 33: 109–119
© 2012 CPS and SIMM All rights reserved 1671-4083/12 $32.00
www.nature.com/aps

Original Article

Triptolide induces cell-cycle arrest and apoptosis of human multiple myeloma cells *in vitro* via altering expression of histone demethylase LSD1 and JMJD2B

Lu WEN[1, #], Yan CHEN[1, #], Ling-lan ZENG[2], Fei ZHAO[1], Rui LI[1], Yuan LIU[1], Chun ZHANG[1, *]

[1]Department of Hematology, Union Hospital, Tongji Medical College, Huazhong University of Science and Technology, Wuhan 430022, China; [2]Department of Central Laboratory, Union Hospital, Tongji Medical College, Huazhong University of Science and Technology, Wuhan 430022, China

---

Aim: To elucidate the relationship between triptolide-induced changes in histone methylation and its antitumor effect on human multiple myeloma (MM) cells *in vitro*.
Methods: Human multiple myeloma cell line RPMI8226 was used. Apoptosis was evaluated using Annexin-V-FITC/PI-labeled flow cytometry, Hoechst 33258 staining, and transmission electron microscopy. Flow cytometry was used to detect the cell cycle distribution of the apoptotic cells. The presence of the LSD1, JMJD2B, H3K4me2, H3K9me2, and H3K36me2 proteins was verified by Western blot analysis. Semi-quantitative real-time PCR was performed to examine the expression of LSD1 and JMJD2B.
Results: Triptolide (10–160 nmol/L) suppressed the proliferation of MM cells in a dose- and time-dependent manner with an IC_{50} value of 99.2±9.0 nmol/L at 24 h. Triptolide (50 nmol/L) induced G_0/G_1 cell cycle arrest in MM cells. The agent (50–150 nmol/L) induced apoptosis of MM cells in a dose-dependent manner. The same concentrations of triptolide suppressed the expression of dimethylated H3K4, dimethylated H3K9 and dimethylated H3K36 by altering the expression of histone demethylase LSD1 and JMJD2B without affecting the expression of histone demethylase LSD1.
Conclusion: Triptolide potently inhibits the growth of MM cells via regulating the expression of histone demethylase LSD1 and JMJD2B, which lead to abnormal histone methylation.

Keywords: triptolide; multiple myeloma; apoptosis; cell cycle arrest; LSD1; JMJD2B

Acta Pharmacologica Sinica (2012) 33: 109–119; doi: 10.1038/aps.2011.145; published online 28 Nov 2011

Introduction

Tripterygium wilfordii is a perennial vine-like member of the Celastraceae plant family[1]. Extracts from this plant have recently been shown to possess anti-tumor effects against cancers, such as leukemia and lymphoma[2–6]. Triptolide induces apoptosis in AML cells via the downregulation of XIAP and upregulation of DR5 mediated by p53[1, 7]. Furthermore, triptolide upregulates the expression of glucocorticoid receptor and enhances PS-341-induced apoptosis via the PI3k/Akt/NF-kappaB pathway in multiple myeloma (MM) cells[8]. Although the development of chemotherapy regimens has improved the remission rate of MM, relapse is still inevitable.

Considerable evidence indicates that epigenetics is involved in the changes in gene expression that contribute to the pathogenesis of MM. The death-associated protein kinase (DAPK) promoter has been reported to be methylated in MM[9, 10]. MM patients with DAPK hypermethylation respond relatively poorly to treatment[11]. DNA methylation-mediated gene silencing is a frequent event in MM and disrupts the cell cycle, cell invasion and adhesion, DNA repair, and apoptotic pathways[12].

Histone methylation modulates the structure and function of chromatin[13]. These modifications are regulated by two classes of enzymes with opposing activities: histone methyltransferases and demethylases. The balance between the methylation and demethylation of specific histone residues is critical for regulating gene expression. Aberrant expression of histone-modifying enzymes has been implicated in the initiation and progression of tumors[14]. Our previous studies showed that histone-trimethylated H3K9 and H3K27 and the methyltransferases SUV39H1 and EZH2 were highly

---

[#] These two authors contributed equally to this work.
[*] To whom correspondence should be addressed.
E-mail Zhangchun23@yahoo.com.cn
Received 2011-08-12 Accepted 2011-09-29

expressed in triptolide-treated MM cells, which was the first evidence that triptolide induced epigenetic changes by regulating histone lysine methylation[15].

LSD1 was the first histone lysine demethylase to be discovered and is highly specific for di- and mono-methylated H3K4 and H3K9; LSD1 has been identified as a component of transcriptional repressor complexes comprising transcriptional corepressor protein (CoREST) and HDAC1/2. ChIP-DSL analyses revealed that LSD1 targets the promoters of an array of genes that are involved in several important cellular processes, including cellular growth, proliferation, apoptosis and fate specification. JMJD2B, a member of the JMJD2 family, which mainly consists of oncogenes, demethylates di- and trimethylated H3K9 and H3K36[14]. Compared with studies examining DNA methylation, studies on histone methylation, histone demethylases and their mechanisms of action in MM are scarce.

In this study, we aimed to investigate changes in the expression of the histone demethylases LSD1 and JMJD2B induced by triptolide in the MM cell line RPMI8226. We analyzed H3K4 dimethylation, H3K9 and H3K36 dimethylation states and examined the connections between apoptosis, histone methylation changes and demethylase regulation by triptolide to determine whether triptolide exerts its anti-myeloma effects through the regulation of histone demethylases in MM cells.

Materials and methods

Reagents

Triptolide (empirical formula: $C_{20}H_{24}O_6$, molecular weight: 360.40, purity: >98%; Figure 1) was purchased from Sigma-Aldrich (St Louis, MO, USA). Triptolide was dissolved in dimethylsulfoxide (DMSO), stored at -20 °C, and thawed before use. RPMI-1640 medium was purchased from Gibco (Gaithersburg, MD, USA). Propidium iodide (PI), DMSO and 3-(4,5-dimethylthiazol-2-yl)-2,5-diphenyltetrazoliumbromide (MTT) were purchased from Sigma-Aldrich (St Louis, MO, USA). TRIzol for RNA extraction was purchased from Invitrogen (Carlsbad, CA, USA), and the cDNA synthesis kit was obtained from Toyobo Biologics. SYBR Green PCR master mix was purchased from Applied Biosystems (Foster City, CA, USA).

Cell lines and culture

The human MM cell line RPMI8226 was purchased from Biomart Co Ltd (Shanghai, China); peripheral blood mononuclear cells (PBMCs) were isolated from the heparinized blood of healthy donors (after informed consent had been obtained) by Ficoll-Hypaque density gradient centrifugation. The two kinds of cells were maintained in RPMI-1640 medium supplemented with 10% (*v/v*) heat-inactivated fetal bovine serum, penicillin-streptomycin (100 IU/mL, 100 μg/mL, respectively), 2 mmol/L glutamine, and 10 mmol/L HEPES buffer at 37 °C in a humidified 5% CO_2 atmosphere. During the expansion phase, RPMI8226 cells were maintained at a concentration of 0.5–1×10^6 cells/mL in culture medium. The appropriate number of cells for use in the experiments was determined. RPMI8226 cells were treated with 50, 100, or 150 nmol/L triptolide for 48 h, except where otherwise specified.

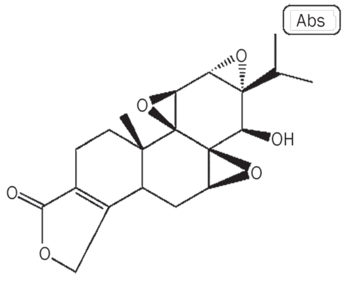

Figure 1. Chemical structure of triptolide.

Cell proliferation assay

The anti-proliferative effect of triptolide in RPMI8226 cells was determined by MTT assay. RPMI8226 cells (5×10^4 per well) were exposed to various concentrations of triptolide (0–160 nmol/L) for 24, 48, and 72 h in 96-well plates. The experiments were performed in triplicate. After incubation with triptolide, 20 μL MTT solution (5 mg/mL in PBS) was added to each well, the plates were incubated for 4–6 h, the supernatants were discarded and 150 μL of DMSO was added. Once the blue crystals were dissolved, the optical density (*OD*) was measured at 570 nm using a 96-well multiscanner autoreader (Biotech Instruments, NY, USA). The inhibition of cell proliferation was determined using the following formula: inhibition of cell proliferation (%)=[1–(*OD* of the experimental samples/*OD* of the control)]×100% (*n*=3, mean±SD). The triptolide concentration that caused 50% inhibition of cell proliferation was defined as half of the maximal inhibitory concentration (IC_{50}).

Cell cycle distribution analysis

RPMI8226 cells (1×10^6 cells/well) were treated with different concentrations of triptolide (0 or 50 nmol/L) for 48 h and were harvested. After being washed, the cells were fixed with 75% ice-cold ethanol and were maintained overnight at 4 °C. The cells were collected and resuspended in PBS containing 40 μg/mL PI, 0.1 mg/mL RNase, and 5% Triton X-100 and were incubated at 37 °C for 30 min. The cells were evaluated by flow cytometry (BD, San Diego, CA, USA). Data was collected from at least 10000 cells for each sample. The distribution of cells across the cell-cycle phases was analyzed using CELL-Quest.

Annexin-V/PI staining assay

An immunofluorescent flow cytometry assay was used to evaluate the ability of triptolide to induce apoptosis in RPMI8226 cells. The cells were seeded in 6-well plates (1×10^6 cells/well) and treated with varying concentrations of triptolide. PBMCs from 12 healthy donors were treated with 150 nmol/L triptolide for 48 h. The cells were harvested, washed with cold PBS, and were resuspended in 100 μL binding buffer. Subsequently, phosphatidyl serine on the surface of apoptotic cells was detected using Annexin V/FITC and a PI apoptosis detection kit according to the manufacturer's instructions (Bender Med Systems Inc, Burlingame, CA, USA). The number of apoptotic cells was evaluated by flow cytometry (BD, San Diego, CA, USA). At least 10 000 cells were analyzed.

Hoechst 33258 staining assay

Nuclear fragmentation was visualized by staining apoptotic nuclei with Hoechst 33258. Cells treated with varying concentrations of triptolide were collected and washed and were fixed with a mixture of acetic acid:ethanol (1:3) for 10 min before deposition onto polylysine-coated cover slips. The samples were subsequently permeabilized with 0.25% Triton X-100 for 5 min and stained with 1 μg/mL Hoechst 33258 for 30 min at 37 °C. The slides were mounted with glycerol-PBS, and the images were visualized and captured using a FV500 confocal microscope (Olympus, Tokyo, Japan).

Morphological observation by transmission electron microscopy

The ultrastructural appearance of the apoptotic cells was examined by transmission electron microscopy. After incubation with 150 nmol/L triptolide for 48 h, the cells were harvested and pre-fixed with 2% glutaraldehyde, post-fixed with 1% osmic acid, dehydrated in graded ethanol, embedded in resin, and cut into sections on an ultramicrotome. The ultrathin sections were doubly stained with uranyl acetate and lead citrate and were examined by transmission electron microscopy using a Hitachi H-7500 instrument (Hitachi, Tokyo, Japan).

Western blot analysis

Western blot analysis was used to evaluate the levels of LSD1, JMJD2B, and histones (dimethylated H3K4, dimethylated H3K9, and dimethylated H3K36) present in RPMI8226 cells exposed to triptolide.

Cells were treated with varying concentrations of triptolide and collected. The sample lysates (25 μg of protein per lane) were prepared, and the proteins were separated by sodium dodecyl sulfate polyacrylamide gel electrophoresis on 10% polyacrylamide gels. The proteins were electro-transferred onto polyvinylidene difluoride membranes, and the blots were incubated with a blocking solution (5% non-fat dry milk in Tris-buffered saline with 0.1% Tween-20) for 1 h at 25 °C. The membranes were subsequently incubated with diluted primary antibodies (1:500–1:1000, Table 1) for 2 h. The membranes were washed and incubated with horseradish peroxidase-conjugated secondary antibodies (Pierce Biotechnology, Rockford, IL, USA) for 1 h at 25 °C. The immune complexes were visualized using the enhanced chemiluminescence reagent Super Signal Substrate (Pierce Biotechnology, Rockford, IL, USA). The band intensity was measured and quantified with a chemiluminescence detection system (ChemiDoc XRS, Bio-Rad, USA). The protein levels were normalized relative to β-actin, and each group was subsequently normalized to the control (100%).

Real-time PCR analysis

Total RNA was isolated from each group using TRIzol according to the manufacturer's instructions. For each sample, 3 μg total RNA was reverse transcribed into cDNA. Real-time quantitative PCR was performed with SYBR Green PCR master mix in an ABI Prism 7900 Sequence Detection System (Applied Biosystems, Foster City, CA, USA).

All mRNA expression levels are expressed as a ratio relative to the control in each experiment, and β-actin was used as internal reference. The following primers for human genes were used: LSD1 forward, 5'-GTGTCTCGTTGGCGTGCT-3', reverse, 5'-CCCGCAAAGAAGAGTCGTG-3'; JMJD2B forward, 5'-GGAAGCGGATGAAGAAGGTG-3', reverse, 5'-GGTAGTACAGCCCGTTGCG-3'; β-actin forward, 5'-GCCCAGTCCTCTCCCAAGTC-3', reverse, 5'-GGCACGAAGGTCATCATTC-3'.

Immunofluorescence staining

An immunofluorescence staining assay was performed to evaluate the effects of triptolide on LSD1 expression in MM cells. The cells were fixed with 4% paraformaldehyde for 10 min and were permeabilized with 0.25% Triton X-100 for 5 min. The cells were subsequently washed twice with PBS and blocked in 3% bovine serum albumin. The rabbit monoclonal anti-LSD1 antibody was diluted 1:100 and incubated with 1×10^6 cells in a total volume of 100 μL for 1 h; non-immunoreactive IgG was used as a negative control. After being washed, the cells were incubated for 1 h with a TRITC-labeled goat anti-rabbit secondary antibody (Pierce, Rockford, USA), diluted in PBS and were stained with Hoechst 33258 (10 μg/mL) for 10 min. Images were visualized and captured using a FV500 confocal microscope (Olympus, Tokyo, Japan). The LSD1 levels were estimated as the mean fluorescence intensity after subtracting the fluorescence of the negative control cells. The

Table 1. Information about the primary antibodies used for Western blot and immunofluorescence staining.

Antibody	Company	Catalog	Source	Molecular weight
Anti-H3K4me2	Upstate	#07-436	Rabbit polyclonal antibody	17 kDa
Anti-H3K9me2	Upstate	#07-212	Rabbit polyclonal antibody	17 kDa
Anti-H3K36me2	Cell Signaling	#2901S	Rabbit polyclonal antibody	17 kDa
Anti-LSD1	Cell Signaling	#2139	Rabbit monoclonal antibody	150 kDa
Anti-JMJD2B	Cell Signaling	#2898	Rabbit monoclonal antibody	110 kDa
Anti-β-actin	Santa Cruz	sc-47778	Mouse monoclonal antibody	43 kDa

anti-JMJD2B antibody cannot be used for immunofluorescence staining.

Statistical analysis

The data are expressed as the mean±SD of three independent experiments. Also, *t*-tests were used to evaluate the differences between treated samples and controls. A *P* value <0.05 was considered to be significant.

Results

Effects of triptolide on the proliferation of RPMI8226 cells

The inhibitory effect of triptolide on MM cell proliferation was examined in RPMI8226 cells. Figure 2 shows that triptolide had a dose- and time-dependent anti-proliferative effect on RPMI8226 cells at 0–160 nmol/L after exposure for 24, 48, and 72 h. The number of viable cells decreased as the concentration of triptolide increased. The IC_{50} value at 24 h was 99.2±9.0 nmol/L. As the exposure time increased, the IC_{50} values gradually decreased. The IC_{50} values after 48 and 72 h of treatment were 61.6±5.8 nmol/L and 23.3±2.6 nmol/L, respectively.

Triptolide induced RPMI8226 cell-cycle arrest

To investigate whether triptolide was able to inhibit DNA synthesis, the effect of triptolide on cell-cycle progression in RPMI8226 cells was measured by flow cytometry. After incubation with triptolide at 50 nmol/L for 48 h, RPMI8226 cells were analyzed for alterations in their cell-cycle distribution (Figure 3); the proportion of G_0/G_1 phase cells significantly increased following the treatment with triptolide, with the G_2 phase cells also increasing slightly. Meanwhile, the fraction of cells in S phase decreased accordingly. This result indicates that triptolide-induced apoptosis is cell cycle-dependent (Table 2).

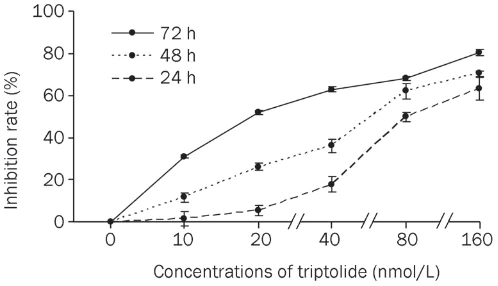

Figure 2. Anti-proliferation effect of triptolide on RPMI8226 cells. RPMI8226 were treated for 24, 48, 72 h, respectively with increasing concentrations of triptolide (0, 10, 20, 40, 80, 160 nmol/L). Inhibition rate was measured by MTT assay which is described in Materials and methods. Mean±SD. *n*=3.

Table 2. The cell cycle distribution was quantified in triptolide (50 nmol/L, 48 h) -treated and control cells. Mean±SD. *n*=3.

Triptolide	RPMI8226			
	G_1 (%)	S (%)	G_2 (%)	G_2/G_1
Control	29.2±0.5	69.7±0.7	1.2±0.2	1:1.88
50 nmol/L (48 h)	60.2±0.5	31.6±0.8	8.2±0.5	1:1.89

Triptolide induced apoptosis in RPMI8226 cells and PBMCs

Apoptosis induction by triptolide was observed in RPMI8226 cells using various methods. In Figure 4, the degree of apoptosis, as measured by flow cytometry, is quantitatively expressed as the percentage of cells that were Annexin V-positive in the presence of triptolide. For the triptolide concentrations in the range 50–150 nmol/L, the total percentage of apoptotic cells, designated as Annexin V-positive and PI-negative cells, gradually increased from 26.0%±0.6% to 40.3%±0.9%, which was statistically different from the control (2.9%±0.3%).

In addition, we observed the effects of triptolide on apoptosis in RPMI8226 cells by visualizing the Hoechst 33258 staining of live cell nuclei using laser scanning confocal microscopy. Nuclei in the control cells were regular in shape. However, the cells became shrunken and dark after treatment with 50 nmol/L triptolide, and the nuclei showed chromatin condensation and marginalization or nuclear beading. The number of apoptotic cells gradually increased as the triptolide concentration increased, and at high concentrations (100 or 150 nmol/L),

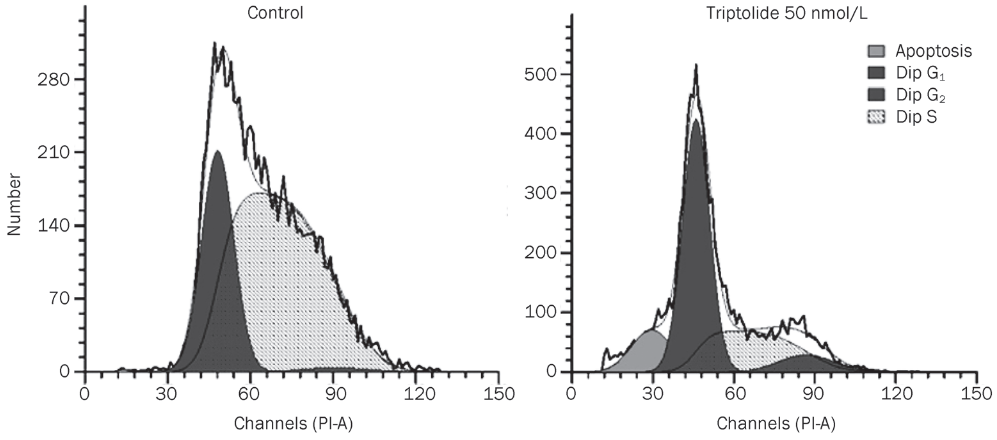

Figure 3. Effects of triptolide on cell cycle distribution in RPMI8226 cells. Cells were treated for 48 h with triptolide (50 nmol/L). The distribution of cell cycle was detected by PI staining.

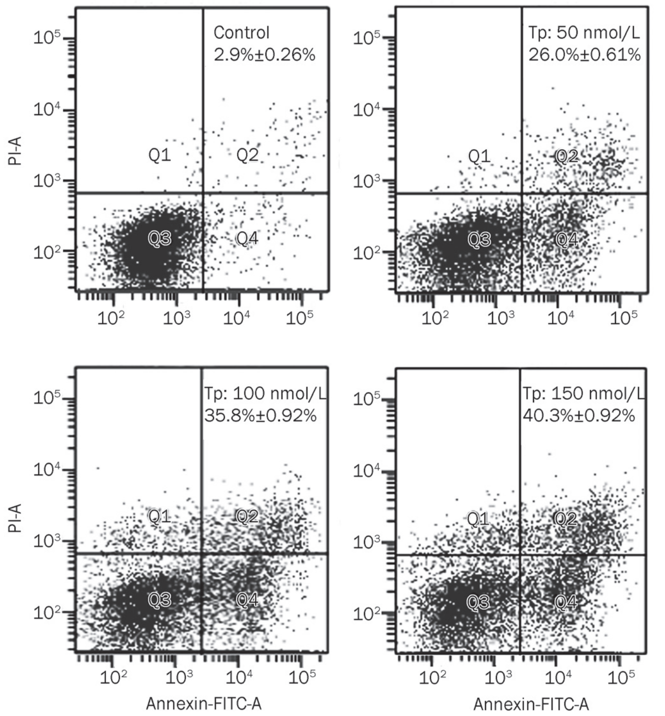

Figure 4. Effects of apoptosis induced by triptolide (Tp) on RPMI8226 cells. RPMI8226 cells were treated for 48 h with increasing triptolide (50, 100, 150 nmol/L) and suspended in 100 μL binding buffer and Annexin V/PI double staining solution. Apoptosis was then measured by flow cytometry. The figure showed the percentage of apoptosis cells increased in a dose-dependent manner. These figures are one representative experiment of three with similar results.

the cells showed morphological features typical of apoptotic cells (Figure 5).

To confirm further the induction of apoptosis by triptolide and to visualize better the ultrastructural changes occurring in MM apoptotic cells, we also used electron microscopy. Apoptotic bodies were observed in triptolide-treated cells; these bodies are spherical protuberances containing fragmented and segregated chromatin clumps separating from the cell surface (Figure 6). Conversely, the untreated RPMI8226 cells had intact plasma membranes and ordered chromatin folding (Figure 6).

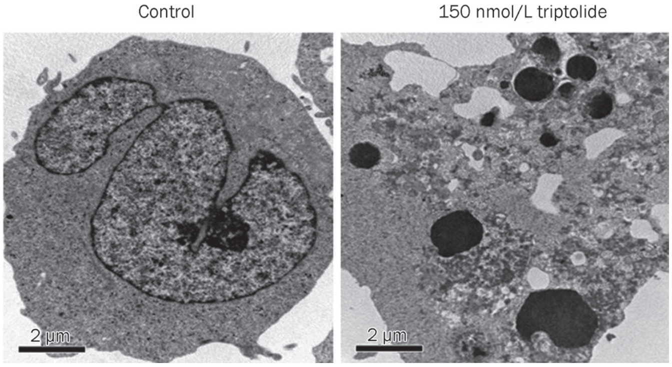

Figure 6. Apoptotic cells ultrastructural changes were viewed by transmission electron microscope with triptolide (150 nmol/L) treatment. The typical apoptotic bodies in triptolide-treated cells were spherical protuberances containing fragmentation and segregation of chromatin clumps separated from cell surface. However, the untreated RPMI8226 cells presented intact plasma membrane and orderly chromatin folding.

The experiments to detect apoptosis by flow cytometry were also performed on PBMCs isolated from 12 healthy donors after the cells had been treated with 150 nmol/L triptolide for 48 h. The amount of apoptosis induced by triptolide increased in 8 of the 12 donors (75%), but only 2 donors (17%) showed an increase of more than 30%, and 5 donors (41.7%) showed an increase of more than 20% (Table 3).

Triptolide decreased dimethylated H3K4 expression

H3K4 methylation is generally associated with active transcription[16]. RPMI8226 cells were treated with triptolide concentrations of 50, 100, or 150 nmol/L for 48 h. The levels of dimethylated H3K4 were measured by Western blot analysis. As shown in Figure 7B, the expression of dimethylated H3K4 decreased in a dose-dependent manner, and the rates of inhibition by 50, 100, and 150 nmol/L of triptolide were 17.5%, 53.6%, and 70.3%, respectively ($P<0.05$ *vs* untreated control). We also found that the global trimethylated H3K4 level decreased in a dose-dependent manner after treatment with

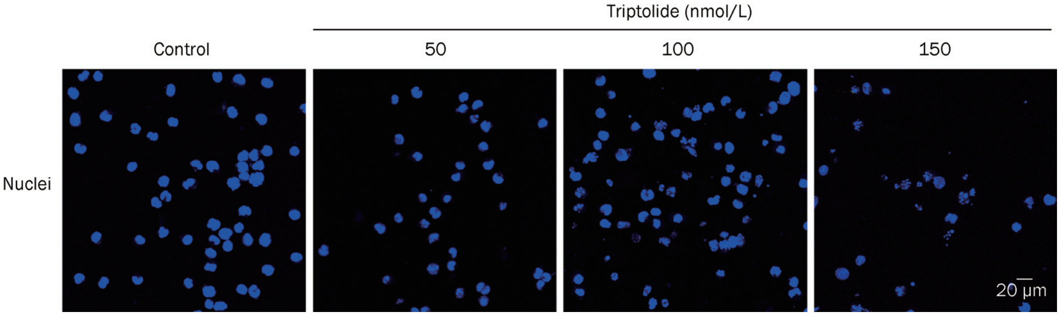

Figure 5. Triptolide induced apoptosis in RPMI8226 cell lines. Apoptotic cell death was revealed by Hoechst 33258 staining with increasing triptolide (50, 100, 150 nmol/L) treatment. Apoptotic cells exhibited highly condensed and fragmented nuclei morphology. Results showed that number of apoptotic cells increased with the increasing concentrations.

increasing triptolide concentrations in another MM cell line, U266[17].

Table 3. Apoptosis of PBMC from 12 healthy persons treated with triptolide (150 nmol/L, 48 h).

	Gender	Age (year)	Control (%) Early apoptosis	Control (%) Late apoptosis	T-treated (%) Early apoptosis	T-treated (%) Late apoptosis
1	M	26	3.9	3.2	3.5	3.6
2	M	53	7.1	1.3	38.3	10.1
3	F	48	5.1	2.9	30.8	15.6
4	M	40	22.3	3.5	45.8	6.5
5	M	56	53.3	3.1	54.7	3.6
6	M	55	30.9	5.9	36.6	10.2
7	M	58	3.6	12.2	14.4	26.4
8	F	61	8.9	16.2	19.3	33.5
9	F	24	10.9	4.5	19.1	3.6
10	M	31	21.8	3.9	36.1	2.9
11	M	26	8.9	2.3	7.8	3.5
12	M	27	7.9	3.9	3.9	3.5

Triptolide decreased dimethylated H3K9 expression

To date, H3K9 methylation has been examined primarily at repressed promoter regions and is thought to act as a docking site for the chromodomain of HP1. H3K9 methylation and HP1 were also found to be associated with the transcribed regions of all active genes examined[13]. RPMI8226 cells were treated with triptolide concentrations of 50, 100, or 150 nmol/L for 48 h. After triptolide treatment, the levels of dimethylated H3K9 were measured by Western blot analysis. The global levels of dimethylated H3K9 significantly decreased after exposure to triptolide. The rates of inhibition by 50, 100, and 150 nmol/L triptolide were 34.7%, 29.4%, and 39.6%, respectively; ($P<0.05$ *vs* untreated control) (Figure 7B). We also found that the expression of trimethylated H3K9 decreased in RPMI8226 cells, and monomethylated H3K9 was elevated in U266 cells in a dose-dependent manner following treatment with increasing concentrations of triptolide[15, 18].

Triptolide decreased dimethylated H3K36 expression

H3K36 methylation has primarily been characterized as an active mark that facilitates transcriptional elongation[19]. RPMI8226 cells were treated with triptolide concentrations of

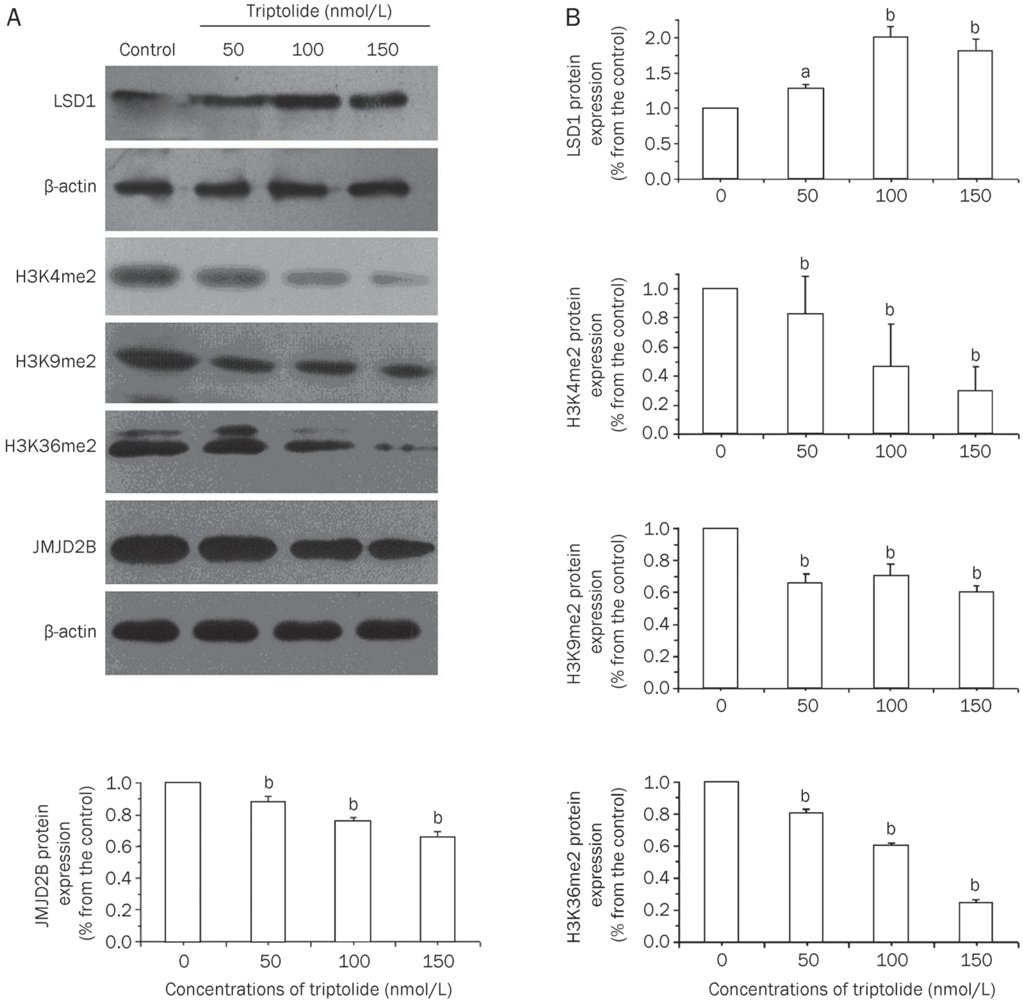

Figure 7. (A) Effects on the protein expression of H3K4me2, H3K9me2, H3K36me2, histone demethylase LSD1 and JMJD2B. RPMI8226 cells were treated with various concentrations (50, 100, 150 nmol/L) triptolide for 48 h, then cell lysates were subjected to SDS-PAGE followed by Western blotting with anti-H3K4me2, anti-H3K9me2, anti-H3K36me2, anti-LSD1, anti-JMJD2B antibodies. Each membrane was then stripped and reprobed with anti-β-actin antibody to confirm equal protein loading. (B) The statistical results of protein expression of H3K4me2, H3K9me2, H3K36me2, LSD1 and JMJD2B. Mean±SD. $n=3$. [a]$P>0.05$.[b]$P<0.05$ *vs* control.

50, 100, or 150 nmol/L for 48 h. Western blot analysis with an antibody against H3K36me2 was used to measured histone H3K36 dimethylation. Triptolide treatment for 48 h led to a significant reduction in the level of H3K36me2 in a dose-dependent manner. The rates of inhibition by 50, 100, and 150 nmol/L triptolide for H3K36me2 were 13.9%, 25.2%, and 35.8%, respectively (Figure 7B). In addition, H3K36 trimethylation was also found to be reduced by triptolide in U266 cells in a dose-dependent manner[17].

Triptolide altered the expression of the histone demethylase LSD1 in RPMI8226 cells

LSD1 is a flavin-dependent monoamine oxidase that demethylates both di- and mono-methylated H3K4 and H3K9, which is a post-translational modification that is associated with gene activation[20–22]. To investigate the potential mechanisms by which triptolide downregulates dimethylated H3K4 and dimethylated H3K9, RPMI8226 cells were treated with triptolide (50, 100, or 150 nmol/L), and LSD1 protein levels were analyzed using an antibody against human LSD1. As shown in Figure 7A, triptolide-treated cells showed significantly higher levels of LSD1 compared with the control (P<0.05 *vs* untreated control), which could be responsible for the decrease in dimethylated H3K4 and dimethylated H3K9. Consistent with the Western-blot results, immunofluorescence analysis showed that there was a significant increase in LSD1 in cells exposed to triptolide (shown in Figure 8).

We extracted total RNA from triptolide-treated RPMI8226 cells and analyzed LSD1 mRNA by real-time PCR to investigate the effects of triptolide on the transcriptional expression of LSD1. As shown in Figure 9A, the levels of LSD1 mRNA in RPMI8226 cells were increased slightly after exposure to triptolide for 48 h compared with the control, but this change was not statistically significant. Therefore, triptolide could not regulate the activity of LSD1 at the transcriptional level (P>0.05).

Triptolide decreased the expression of the histone demethylase JMJD2B in RPMI8226 cells

Unlike LSD1, JMJD2B actively mediates the removal of chromosomal tri- and dimethylated H3K36 and H3K9 well before the replication of chromatin[23]. We examined whether JMJD2B played a role in the triptolide-mediated induction of H3K36 and H3K9 dimethylation. RPMI8226 cells were treated with triptolide (50, 100, or 150 nmol/L), and JMJD2B protein levels were analyzed using an antibody against human JMJD2B. As shown in Figure 7A, JMJD2B levels declined as the concentration of triptolide increased (P<0.05 *vs* untreated control). The rates of inhibition by 50, 100, and 150 nmol/L triptolide at 48 h were 5.5%, 16.8%, and 66.5%, respectively, compared with the control (P<0.05 *vs* untreated control) (Figure 7B).

To determine whether triptolide affected the transcriptional expression of the JMJD2B gene, we extracted total RNA from triptolide-treated RPMI8226 cells and amplified JMJD2B by semiquantitative real-time PCR. As shown in Figure 9B, triptolide inhibited the mRNA expression of JMJD2B in a dose-dependent manner (P<0.05). A low concentration of triptolide

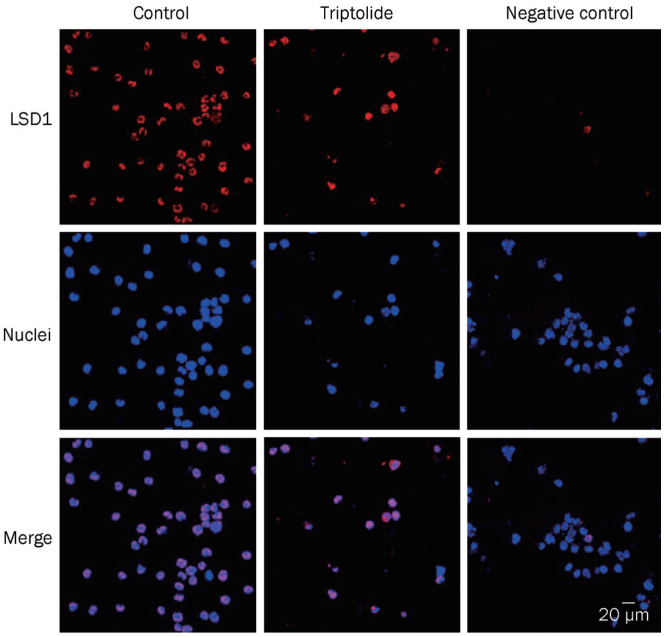

Figure 8. Effect of triptolide on the subcellular localization of LSD1 in RPMI8226 cells. Cells were treated with triptolide 150 nmol/L for 48 h, and Hoechst 33258 was used to visualize the DNA (which appeared as blue). The expression and subcellular location of LSD1 in control and triptolide-treated groups were visualized via confocal microscope (which appeared red) (×1000). LSD1 was distributed in nucleus completely in control group. While in triptolide-treated group a little part of LSD1 was redistributed to the cytoplasm, and distributed in nucleus principally.

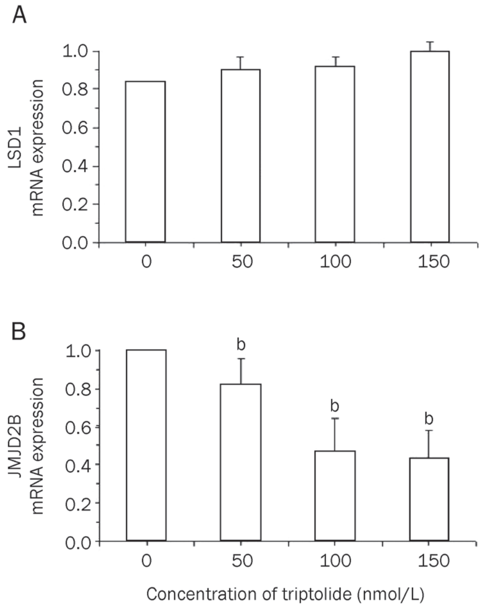

Figure 9. Histone demethylases LSD1 and JMJD2B expression were regulated by triptolide on mRNA level. RPMI8226 cells were treated for 48 h with increasing triptolide (50, 100, 150 nmol/L). Expression of mRNA was then measured by real-time PCR. (A) LSD1 gene expression profile. (B) JMJD2B gene expression profile. Mean±SD of at least three independent experiments (^bP<0.05).

(50 nmol/L) inhibited the expression of JMJD2B mRNA by 18%. However, the difference in inhibition rates between the 100 and 150 nmol/L triptolide treatments, which were 53% and 56%, respectively, was not significant ($P>0.05$). This result indicates that triptolide regulates JMJD2B activity at the transcriptional level.

Discussion

MM is a plasma cell neoplasm characterized by the accumulation of terminally differentiated monoclonal plasma cells in the bone marrow and, usually, the presence of monoclonal immunoglobulin in the blood and/or urine[24]. MM accounts for approximately 1% of malignant diseases and is the second most commonly diagnosed hematological malignancy[25]. The outcome for patients with MM is highly variable. The median overall survival time is 3–4 years[25]. Despite major improvements in treatments including high dose chemotherapy and autologous bone marrow transplantation, the disease remains incurable. Myelomas with no response to initial chemotherapy, incomplete response rates and the eventual emergence of drug resistance remain major obstacles, indicating an urgent need for novel therapeutic agents.

Cancer has traditionally been viewed as primarily a genetic disorder. However, it has become apparent that, in addition to genetic mutations, epigenetic abnormalities also play important roles in the pathogenesis of tumors[26]. Epigenetic control mechanisms involve changes in gene expression patterns, due to the modification of DNA and/or histones[15]. Modifications to histone N-terminal tails affect chromatin structure, gene transcription, and DNA replication and repair.

Highly specific histone modifications are enriched in target tumor genes and work together with other components to form a complex that interacts with the target genes to induce or inhibit DNA methylation, thereby causing transcriptional repression or activation[27, 28]. The N-terminal tails of histones undergo several types of post-translational modifications, including methylation, acetylation, phosphorylation and ubiquitination. Unlike other histone modifications, such as acetylation, phosphorylation and ubiquitination, histone methylation is important because of its highly specific effects on gene regulation[14]. These modifications remain stable between methylation and demethylation events, which are dynamically regulated by histone methyltransferases and demethylases. It has been demonstrated that abnormalities affecting histone methylation-modifying enzymes lead to aberrant histone modifications, which may occur at gene promoters and induce the improper expression or repression of individual genes that play important roles in tumorigenesis. Recently, the overexpression, amplification and mutation of several histone demethylases have been linked to cell proliferation, cell apoptosis, gene expression, genome stability, and the genesis of cancer.

Triptolide has multiple pharmacological activities, including anti-inflammatory, immunosuppressive, male anti-fertility and anticancer effects[29]. Research into its mechanisms of action has revealed that it potently inhibits monocyte activation, activates caspases and other proapoptotic signaling cascades, inhibits angiogenesis and reverses drug resistance[30, 31]. Triptolide is able to induce cell apoptosis by inhibiting nuclear factor κB activation through the downregulation of Bcl-2 expression and the inhibition of p53 transcriptional activity in p53-wild type human tumors and by upregulating nuclear factor κB inhibiting protein (IκBα) and Bax[32–35]. Moreover, triptolide has been shown to downregulate various proteins, including heat shock protein 70, Bcr-Abl, survivin, Mcl-1, Akt, c-Myc, cyclin A/cdk2, cyclin B/cdc2, cyclin D1, and pRb, which may contribute to its anticancer activities under specific conditions[4, 36, 37]. Recently, research has shown that triptolide enhances PS-341-induced apoptosis via the P13k/Akt/NF-kappaB pathways in human MM cells[8]. Our previous study also suggested that triptolide inhibits proliferation and cell-cycle progression by upregulating p21$^{\text{wap1/cip1}}$ and p27$^{\text{kip1}}$ in RPMI8226 cells[38]. Nevertheless, the anticancer mechanisms of triptolide remain unclear.

In this study, we found that triptolide inhibited the proliferation of RPMI8226 cells, and its pharmacological effects on cell growth changes occurred in a dose- and time-dependent manner. Triptolide predominantly arrested RPMI8226 cells at G_0/G_1; however, the proportion of cells in G_2 phase also slightly increased.

Flow cytometric analysis of apoptosis suggested that the extent of apoptosis induced by triptolide varied in relation to the duration of the exposure. The fraction of apoptotic RPMI8226 cells was significantly upregulated following exposure to 50, 100, or 150 nmol/L triptolide compared with the control ($P<0.01$).

However, the experiments showed that triptolide had toxic effects on human PBMCs. After staining with Hoechst 33258, RPMI8226 cells treated with triptolide showed typical morphological features of apoptosis. As the drug dose increased, the number of apoptotic cells increased, as indicated by the presence of fragmented nuclei and apoptotic bodies. Ultrastructural changes associated with apoptosis were also visualized by electron microscopy, which showed spherical protuberances containing fragmented and segregated chromatin clumps.

Translocations involving the Ig heavy chain gene locus have been found in approximately 60% of MM cases with a hypodiploid karyotype, but no common pattern of genetic aberrations characterizes the disease[39]. Highly specific histone modifications and methylation-modifying enzymes work together with other components to form a complex that interacts with tumor target genes and is recognized as having a primary role in the control of gene expression and chromatin structure[40].

LSD1, also known as AOF2 and KDM1, was the first histone lysine demethylase to be discovered and belongs to the flavin adenine dinucleotide-dependent enzyme family[41]. LSD1 can interact with nuclear receptors; it specifically demethylates H3K4me2/1 and H3K9me2/1 and functions as a transcriptional co-activator or co-repressor[42, 43]. Whether LSD1 has a tumor suppressive or tumor promoting effect depends on many factors, including the cellular context[14]. Amanda has shown that SPR-5 (a Caenorhabditis elegans orthologue of

LSD1) could increase p53-dependent germ cell apoptosis and plays a unique role in meiotic DNA double-strand break (DSB) repair[44]. In addition, knockdown of LSD1 delays the initial induction of p53 in response to DNA damage, which leads to reduced activation of p21 and MDM2, resulting in a decrease in p53-mediated apoptosis. Likewise, in p53-deficient cells, LSD1 can regulate DNA-damage-induced cell death by promoting E2F1 accumulation during DNA damage and the activation of its proapoptotic target gene p73, a major mediator of p53-independent apoptosis[45]. In contrast, Huang *et al* found that knockdown of LSD1 increases the transcriptional activation of p21 and MDM2 by p53[46, 47]. However, the LSD1 complex has been shown to be required for the repressive activity of an oncogenic I kappa B protein, and a functional link has been established between the E3 ligase TBLR1 and NF-kappaB[48].

In our study, triptolide promoted the expression of LSD1 at the translational level in a dose-dependent manner. LSD1 could exert its proapoptotic effects by directly demethylating non-histone proteins, such as p53 and E2F1 in multiple myeloma cells. LSD1 can also induce apoptosis through its H3K4 demethylase activity. H3K4me2 is highly enriched at transcriptionally competent or active gene promoters. According to the ENCODE pilot project, GM12878 and K562 show significant enrichment for H3K4me2, including large subsets of pluripotency-related or developmentally regulated gene promoters and enhancers[49]. For instance, c-Myc expression is downregulated after the loss of H3K4me2 in the c-Myc promoter[46]. We have consistently found high H3K4me2 expression in multiple myeloma cells, and triptolide was observed to downregulate H3K4me2 protein expression in a dose-dependent manner. The reduction in H3K4me2 promoted by LSD1 strongly inhibited the epigenetic control of anti-apoptotic gene transcription in RPMI8226 cells, which is probably one of the most important anti-MM mechanisms of triptolide.

Another family of histone lysine demethylases that are structurally different from LSD1 has been described, all of which share a conserved jumonji C (JmjC) domain[50]. The JMJD2 family of histone demethylases is amplified in human cancers[51]. However, little is known about the physiological or tumorigenic roles of these proteins. The depletion of JMJD2 has previously been demonstrated to increase DNA double-strand breaks in the adult germ line, resulting in ATR/p53-dependent apoptosis[51]. Hypoxia-inducible factor-1 alpha (HIF-1 alpha) may cooperate with estrogen receptor alpha (ER alpha) to regulate JMJD2B, which drives breast cancer cell proliferation under hypoxic conditions and regulates the expression of cell-cycle genes, such as CCND1, CCNA1, and WEE1[52]. Moreover, JMJD2B has been suggested as a potential novel target gene for p53 that can mediate the DNA damage response and may be protective against apoptosis[53]. As a member of the JMJD2 family, JMJD2B is capable of reversing the lysine trimethylation of H3K9me3 at pericentric heterochromatin in mammalian cells[54]. In addition, the removal of H3K9me3 marks by JMJD2B may prevent the induction of senescence, which is a specific form of irreversible growth arrest and an important process for the suppression of tumorigenesis[23, 55]. Therefore, cancer cells that highly express JMJD2B may evade this important tumor suppression mechanism[55].

Our experiments demonstrated that histone H3K9 and H3K36 dimethylation were dose-dependently reduced by triptolide, as were JMJD2B mRNA and protein levels. These results suggest that the downregulation of H3K9me2 was partly due to the decrease in JMJD2B in RPMI8226 cells because the levels of H3K9me2 formed by the demethylation of H3K9me3 were significantly reduced. Triptolide may exert its proapoptotic effects partly by directly downregulating JMJD2B in multiple myeloma cells.

In addition, JMJD2B could demethylate trimethylated H3K36 to dimethylated H3K36. H3K36me2/me3 are enriched mostly in the transcribed region of active genes and are associated with the later stages of transcription in actively transcribed regions[18]. However, a direct association between H3K36me2 and proapoptotic genes has not been proven; further investigation will be required to clarify this relationship. In our study, the downregulation of JMJD2B may be partially responsible for the reduction in H3K9me2 and H3K36me2 in triptolide-treated cells. LSD1 and JMJD2B are assumed to be two targets for triptolide as an anti-MM drug.

In summary, our experiments showed that triptolide inhibited proliferation and induced apoptosis and G_0/G_1 cell cycle arrest in the MM cell line RPMI8226 in a dose-dependent manner. Moreover, this study provided the first evidence that triptolide could restore epigenetic changes by regulating the histone demethylases LSD1 and JMJD2B, thereby offering a novel view of the anti-MM mechanism of triptolide.

Abbreviations

MM, multiple myeloma; BM, bone marrow; PI, propidium iodide; DMSO, dimethylsulfoxide; MTT, 3-(4,5-dimethylthiazol-2-yl)-2, 5-diphenyltetrazoliumbromide; PBMC, peripheral blood mononuclear cells; SDS, sodium dodecylsulfate; TBS, Tris-buffered saline; H3K4me2, dimethyl-lysine 4 on histone H3; H3K9me2, dimethyl-lysine 9 on histone H3; H3K36me2, dimethyl-lysine 36 on histone H3; ECL, enhanced chemiluminescence; BSA, bovine serum albumin; LSD1, lysine-specific demethylase 1; JMJD2B, the second member of the Jumonji domain 2 family of proteins. PBS, phosphate-buffered saline.

Acknowledgements

This work was supported by two grants from the National Natural Sciences Foundation of China (No̲ 30700882 and No̲ 81070429).

Author contribution

Yan CHEN, Ling-lan ZENG, and Chun ZHANG designed the research; Lu WEN, Rui LI, Fei ZHAO, and Yuan LIU performed the experiments; Lu WEN analyzed the data and wrote the paper.

References

1 Carter BZ, Mak DH, Schober WD, McQueen T, Harris D, Estrov Z, *et al*. Tliptolide induces caspase-dependent cell death mediated via the mitochondfial pathway in leukemic cells. Blood 2006; 108: 630–7.

2 Kiviharju TM, Lecane PS, Sellers RG, Peehl DM. Antiproliferative and proapoptotic activities of triptolide (PG490), a natural product entering clinical trials, on primary cultures of human prostatic epithelial cells. Clin Cancer Res 2002; 8: 2666–74.

3 Pigneux A, Mahon FX, Uhalde M, Jeanneteau M, Lacombe F, Milpied N, *et al*. Triptolide cooperates with chemotherapy to induce apoptosis in acute myeloid leukemia cells. Exp Hematol 2008; 36: 1648–59.

4 Yang SM, Chen JG, Guo Z, Xu XM, Wang LP, Pei XF, *et al*. Triptolide inhibits the growth and metastasis of solid tumors. Mol Cancer Ther 2003; 2: 65–72.

5 Zhang C, Cui GH, Liu F, Wu QL, Chen Y. Inhibitory effect of triptolide on lymph node metastasis in patients with non-Hodgkin lymphoma by regulating SDF-1/CXCR4 axis *in vitro*. Acta Pharmacol Sin 2006; 27: 1438–46.

6 Zhang C, Cui GH, Liu F, Wu QL, Chen Y. Effects of triptolide on cell proliferation and CXCR4 expression in Burkitt's lymphoma Raji cells *in vitro*. Chin J Cancer Res 2007; 19: 27–31.

7 Carter BZ, Mak DH, Schober WD, Dietrich MF, Pinilla C, VassileV LT, *et al*. Triptolide sensitizes AML cells to TRAIL-induced apoptosis via decrease of XIAP and p53-mediated increase of DR5. Blood 2008; 111: 3742–50.

8 Yang M, Huang J, Pan HZ, Jin J. Triptolide overcomes dexamethasone resistance and enhanced PS-341-induced apoptosis via PI3k/Akt/NF-kappa B pathways in human multiple myeloma cells. Int J Mol Med 2008; 22: 489–96.

9 Ng MHL, To KW, Lo KW, Chan S, Tsang KS, Cheng SH, *et al*. Frequent death-associated protein kinase promoter hypermethylation in multiple myeloma. Clin Cancer Res 2001; 7: 1724–9.

10 Galm O, Wilop S, Reichelt J, Jost E, Gehbauer G, Herman JG, *et al*. DNA methylation changes in multiple myeloma. Leukemia 2004; 18: 1687–92.

11 Chim CS, Pang R, Fung TK, Choi CL, Liang R. Epigenetic dysregulation of Wnt signaling pathway in multiple myeloma. Leukemia 2007; 21: 2527–36.

12 Lohrum M, Stunnenberg HG, Logie C. The new frontier in cancer research: Deciphering cancer epigenetics. Int J Biochem Cell Biol 2007; 39: 1450–61.

13 Vakoc CR, Mandat SA, Olenschock BA, Blobel GA. Histone H3 lysine 9 methylation and HP1 gamma are associated with transcription elongation through mammalian chromatin. Blood 2005; 106: 1734.

14 Lim S, Metzger E, Schule R, Kirfel J, Buettner R. Epigenetic regulation of cancer growth by histone demethylases. Int J Cancer 2010; 127: 1991–8.

15 Zhao F, Chen Y, Li R, Liu Y, Wen L, Zhang C. Triptolide alters histone H3K9 and H3K27 methylation state and induces G_0/G_1 arrest and caspase-dependent apoptosis in multiple myeloma *in vitro*. Toxicology 2010; 267: 70–9.

16 Eissenberg JC, Shilatifard A. Histone H3 lysine 4 (H3K4) methylation in development and differentiation. Dev Biol 2010; 339: 240–49.

17 Zhao F, Chen Y, Zeng LL, Li R, Zeng R, Wen L, *et al*. Role of triptolide in cell proliferation, cell cycle arrest, apoptosis and histone methylation in multiple myeloma U266 cells. Eur J Pharmacology 2010; 646: 1–11.

18 Zhao F, Chen Y, Zeng LL, Li R, Zeng R, Wen L, *et al*. Effects of triptolide on RIZ1 expression, proliferation, and apoptosis in multiple myeloma U266 cells. Acta Pharmacol Sin 2010; 31: 733–40.

19 Strahl BD, Grant PA, Briggs SD, Sun ZW, Bone JR, Caldwell JA, *et al*. Set2 is a nucleosomal histone H3-selective methyltransferase that mediates transcriptional repression. Mol Cell Biol 2002; 22: 1298–306.

20 Forneris F, Battaglioli E, Mattevi A, Binda C. New roles of flavoproteins in molecular cell biology: Histone demethylase LSD1 and chromatin. FEBS J 2009; 276: 4304–12.

21 Sharma A, Heuck CJ, Fazzari MJ, Mehta J, Singhal S, Greally JM, *et al*. DNA methylation alterations in multiple myeloma as a model for epigenetic changes in cancer. Wiley Interdiscip Rev Syst Biol Med 2010; 2: 654–69.

22 Wang GG, Allis CD, Chi P. Chromatin remodeling and cancer, part I: covalent histone modifications. Trends Mol Med 2007; 13: 363–72.

23 Fodor BD, Kubicek S, Yonezawa M, O'Sullivan RJ, Sengupta R, Perez-Burgos L, *et al*. Jmjd2b antagonizes H3K9 trimethylation at pericentric heterochromatin in mammalian cells. Genes & Development 2006; 20: 1557–62.

24 Moreaux J, Hose D, Bonnefond A, Reme T, Robert N, Goldschmidt H, *et al*. MYEOV is a prognostic factor in multiple myeloma. Exp Hematology 2010; 38: 1189–98.

25 Lopez-Otero A, Ruiz-Delgado GJ, Hernandez-Arizpe A, Ruiz-Arguelles A, Ruiz-Arguelles GJ. The flow-cytometric DNA content of the plasma cells of patients with multiple myeloma is a prognostic factor: a single institution experience. Hematology 2010; 15: 378–81.

26 Feinberg AP, Ohlsson R, Henikoff S. The epigenetic progenitor origin of human cancer. Nat Rev Genet 2006; 7: 21–33.

27 Ballestar E, Wolffe AP. Methyl-CpG-binding proteins –– Targeting specific gene repression. Eur J Biochem 2001; 268: 1–6.

28 Schlesinger Y, Straussman R, Keshet I, Farkash S, Hecht M, Zimmerman J, *et al*. Polycomb-mediated methylation on Lys27 of histone H3 pre-marks genes for de novo methylation in cancer. Nat Genet 2007; 39: 232–6.

29 Shen JA, He CH. Isolation and purification of triptolide from the leaves of tripterygium wilfordii Hook F. Chin J Chem Engineering 2010; 18: 750–4.

30 Liu QY, Chen TY, Chen GY, Shu XL, Sun A, Ma PC, *et al*. Triptolide impairs dendritic cell migration by inhibiting CCR7 and COX-2 expression through PI3-K/Akt and NF-kappa B pathways. Mol Immunol 2007; 4: 2686–96.

31 Zhou B, Miao Z, Deng G, Ding J, Yang Y, Feng H, *et al*. Synthesis and biological evaluation of novel triptolide analogues for anticancer activity. Bioorg Med Chem Lett 2010; 20: 6217–21.

32 Jiang XH, Wong BCY, Lin MCM, Zhu GH, Kung HF, Jiang SH, *et al*. Functional p53 is required for triptolide-induced apoptosis and AP-1 and nuclear factor-kappa B activation in gastric cancer cells. Oncogene 2001; 20: 8009–18.

33 Lin J, Chen LY, Lin ZX, Zhao ML. The effect of triptolide on apoptosis of glioblastoma multiforme (GBM) cells. J Int Med Res 2007; 35: 637–43.

34 Lou YJ, Jie J, Wang YG. Triptolide inhibits transcription factor NF-kappaB and induces apoptosis of multiple myeloma cells. Leukemia Res 2005; 29: 99–105.

35 Zhou GX, Ding XL, Huang LF, Zhang H, Wu SB, Cheng JP, *et al*. Apoptosis of human pancreatic cancer cells induced by Triptolide. World J Gastroenterol 2008; 14: 1504–9.

36 Lou YJ, Jin J. Triptolide down-regulates bcr-abl expression and induces apoptosis in chronic myelogenous leukemia cells. Leukemia & Lymphoma 2004; 45: 373–6.

37 Phillips PA, Dudeja V, McCarroll JA, Borja-Cacho D, Dawra RK, Grizzle WE, *et al*. Triptolide induces pancreatic cancer cell death via inhibition of heat shock protein 70. Cancer Res 2007; 67: 9407–16.

38 Liu YA, Zeng LL, Chen Y, Zhao F, Li R, Zhang C, *et al*. Triptolide inhibits

cell growth and induces G_0–G_1 arrest by regulating $P21^{wap1/cip1}$ and $P27^{kip1}$ in human multiple myeloma RPMI-8226 cells. Chin J Cancer Res 2010; 22: 141–7.

39 Tshuikina M, Jernberg-Wiklund H, Nilsson K, Oberg F. Epigenetic silencing of the interferon regulatory factor ICSBP/IRF8 in human multiple myeloma. Exp Hematol2008; 36: 1673–81.

40 Yadav S, Singhal J, Singhal SS, Awasthi S. hSET1: A novel approach for colon cancer therapy. Biochem Pharmacol 2009; 77: 1635–41.

41 Shi YJ, Lan F, Matson C, Mulligan P, Whetstine JR, Cole PA, *et al*. Histone demethylation mediated by the nuclear arnine oxidase homolog LSD1. Cell 2004; 119: 941–53.

42 Garcia-Bassets I, Kwon YS, Telese F, Prefontaine GG, Hutt KR, Cheng CS, *et al*. Histone methylation-dependent mechanisms impose ligand dependency for gene activation by nuclear receptors. Cell 2007; 128: 505–18.

43 Metzger E, Wissmann M, Yin N, Muller JM, Schneider R, Peters A, *et al*. LSD1 demethylates repressive histone marks to promote androgen-receptor-dependent transcription. Nature 2005; 437: 436–9.

44 Nottke AC, Beese-Sims SE, Pantalena LF, Reinke V, Shi Y, Colaiacovo MP. SPR-5 is a histone H3K4 demethylase with a role in meiotic double-strand break repair. Proc Natl Acad Sci U S A 2011; 108: 12805–10.

45 Kontaki H, Talianidis I. Lysine methylation regulates E2F1-induced cell death. Mol Cell 2010; 39: 152–60.

46 Koche RP, Smith ZD, Adli M, Gu H, Ku M, Gnirke A, *et al*. Reprogramming factor expression initiates widespread targeted chromatin remodeling. Cell Stem Cell 2011; 8: 96–105.

47 Huang J, Sengupta R, Espejo AB, Lee MG, Dorsey JA, Richter M, *et al*. p53 is regulated by the lysine demethylase LSD1. Nature 2007; 449: 105–8.

48 Keutgens A, Shostak K, Close P, Zhang X, Hennuy B, Aussems M, *et al*. The repressing function of the oncoprotein BCL-3 requires CtBP, while its polyubiquitination and degradation involve the E3 ligase TBLR1. Mol Cell Biol 2010; 30: 4006–21.

49 Huda A, Bowen NJ, Conley AB, Jordan IK. Epigenetic regulation of transposable element derived human gene promoters. Gene 2011; 475: 39–48.

50 Lim S, Janzer A, Becker A, Zimmer A, Schule R, Buettner R, *et al*. Lysine-specific demethylase 1 (LSD1) is highly expressed in ER-negative breast cancers and a biomarker predicting aggressive biology. Carcinogenesis 2010; 31: 512–20.

51 Black JC, Allen A, Van Rechem C, Forbes E, Longworth M, Tschöp K, *et al*. Conserved antagonism between JMJD2A/KDM4A and HP1γ during cell cycle progression. Mol Cell 2010; 40: 736–48.

52 Yang J, Jubb AM, Pike L, Buffa FM, Turley H, Baban D, *et al*. The Histone Demethylase JMJD2B Is Regulated by Estrogen Receptor alpha and Hypoxia, and Is a Key Mediator of Estrogen Induced Growth . Cancer Res 2010; 70: 6456–66.

53 Adamsen BL, Kravik KL, Clausen OPF, De Angelis PM. Apoptosis, cell cycle progression and gene expression in TP53-depleted HCT116 colon cancer cells in response to short-term 5-fluorouracil treatment. Int J Oncol 2007; 31: 1491–500.

54 Palomera-Sanchez Z, Zurita M. Open, repair and close again: chromatin dynamics and the response to UV-induced DNA damage. DNA Repair (Amst) 2011; 10: 119–25.

55 Cloos PAC, Christensen J, Agger K, Maiolica A, Rappsilber J, Antal T, *et al*. The putative oncogene GASC1 demethylates tri- and dimethylated lysine 9 on histone H3. Nature 2006; 442: 307–11.

npg **Acta Pharmacologica Sinica** (2012) 33: 120–126
© 2012 CPS and SIMM All rights reserved 1671-4083/12 $32.00
www.nature.com/aps

Original Article

Epigallocatechin-3-gallate inhibits proliferation and migration of human colon cancer SW620 cells *in vitro*

Fang ZHOU[1, 2], Hong ZHOU[2, *], Ting WANG[2], Yuan MU[2], Biao WU[2], Dong-lin GUO[2], Xian-mei ZHANG[2], Ying WU[2]

[1]Department of Clinical Laboratory, Jiangsu Province Rongjun Hospital, Wuxi 214035, China; [2]Department of Clinical Laboratory and Hematology, Jiangsu University School of Medicine, Zhenjiang 212013, China

---

Aim: Epigallocatechin-3-gallate (EGCG) is the major polyphenolic constituent in green tea. The aim of this study is to investigate the effects of EGCG on proliferation and migration of the human colon cancer SW620 cells.
Methods: Proliferation and migration of SW620 cells were induced by the protease-activated receptor 2-agonist peptide (PAR2-AP, 100 μmol/L) or factor VIIa (10 nmol/L), and analyzed using MTT and Transwell assays, respectively. The cellular cytoskeleton was stained with rhodamine-conjugated phalloidin and examined with a laser scanning confocal fluorescence microscope. The expression of caspase-7, tissue factor (TF) and matrix metalloproteinase (MMP)-9 in the cells was examined using QT-PCR, ELISA and Western blot assays. The activation of extracellular signal-regulated kinase 1 and 2 (ERK1/2) and nuclear factor-kappa B (NF-κB) signaling pathways was analyzed with Western blot.
Results: Both PAR2-AP and factor VIIa promoted SW620 cell proliferation and migration, and caused cytoskeleton reorganization (increased filopodia and pseudopodia). Pretreatment with EGCG (25, 50, 75, and 100 μg/mL) dose-dependently blocked the cell proliferation and migration induced by PAR2-AP or factor VIIa. EGCG (100 μg/mL) prevented the cytoskeleton changes induced by PAR2-AP or factor VIIa. EGCG (100 μg/mL) counteracted the down-regulation of caspase-7 expression and up-regulation of TF and MMP-9 expression in the cells treated with PAR2-AP or factor VIIa. Furthermore, it blocked the activation of ERK1/2 and NF-κB (p65/RelA) induced by PAR2-AP or factor VIIa.
Conclusion: EGCG blocks the proliferation and migration of SW620 cells induced by PAR2-AP and factor VIIa via inhibition of the ERK1/2 and NF-κB pathways. The compound may serve as a preventive and therapeutic agent for colon cancers.

Keywords: epigallocatechin-3-gallate; polyphenol; protease-activated receptor 2; factor VIIa; tissue factor; colon cancer; ERK1/2; NF-κB

Acta Pharmacologica Sinica (2012) 33: 120–126; doi: 10.1038/aps.2011.139; published online 21 Nov 2011

Introduction

Recently, tissue factor (TF) has attracted considerable attention as a receptor capable of mediating intracellular signals closely involved in metastasis, angiogenesis and tumor growth[1]. TF is expressed in a wide variety of malignancies[2] and can induce a variety of non-coagulant cellular responses related to angiogenesis, metastasis, tumor growth, and cell migration[3, 4]. It has been found that TF binding to factor VII (hereafter factor VII) or factor VIIa can trigger cell signal transduction via activation of protease-activated receptor 2 (PAR2)[5]. The activation of PAR2 induced by the TF/factor VIIa complex may contribute to the malignant behavior of certain cancer cells[6].

PAR2 is a G-protein-coupled receptor activated by proteolytic cleavage of its amino terminal domain. Experimentally, PARs can also be activated by synthetic peptides [referred to as an agonist peptide (AP)] that mimic the neo-amino terminus of the cleaved receptors. Specific PAR-APs are important tools for investigating the roles of PAR activation[7]. In a previous study, we observed that TF and PAR2 are highly expressed in the colon cancer cell line SW620[8]. Treatment with factor VIIa (10 nmol/L) induced SW620 cell proliferation and migration. The effects of factor VIIa on cells are similar to that of the PAR2 agonist peptide, PAR2-AP, and could be inhibited by anti-TF or anti-PAR2 antibodies. Furthermore, some intracellular signaling molecules were activated in these processes[9]. These results led us to hypothesize that there is a TF/factor VIIa/PAR2 axis in SW620 cells, and this axis might be a potential therapeutic target for colon cancers.

Epigallocatechin-3-gallate (EGCG), the major polyphenolic constituent in green tea, is well known to possess remarkable

---

* To whom correspondence should be addressed.
E-mail hongzhou@ujs.edu.cn
Received 2011-07-06 Accepted 2011-09-22

cancer chemo-preventive activity and therapeutic potential against various cancers due to its ability to inhibit cell growth, arrest cell cycle and induce apoptosis in some human carcinoma cells. One mechanism by which EGCG exerts its antitumor effects is through the inhibition of cell signaling associated with tumor cell proliferation, apoptosis, invasion and metastasis[10, 11].

Although it has been known for several years that EGCG has potent anticancer effects, whether or not it can affect TF/factor VIIa/PAR2 axis-mediated proliferation and migration of SW620 cells remains unclear. In the current study, we investigated whether EGCG is capable of blocking the stimulating effects of the TF/factor VIIa/PAR2 axis on SW620 cells and the possible mechanisms involved in this process.

Materials and methods

Materials

Leibovitz's L-15 medium and fetal bovine serum (FBS) were obtained from Gibco BRL (Grand Island, NY, USA). EGCG (purity >98%) was purchased from Sigma (St Louis, MO, USA). The PAR2 agonist (SLIGKV-NH_2, PAR2-AP) was synthesized by Proteintech Group Inc (Wuhan, China). Recombinant human factor VIIa was obtained from Novo Nordisk (Maaloev, Denmark). All reagents (EGCG, PAR2-AP, and factor VIIa) were dissolved in distilled water and then diluted in medium. Trizol and RT-PCR reagents were purchased from Invitrogen (Carlsbad, CA, USA). MMP-9 ELISA assay kits were purchased from R&D Systems, Inc (Minneapolis, MN, USA). TF activity assay kits (Actichrome^{TM} TF) were purchased from American Diagnostica, Inc (Greenwich, CT, USA). Polyclonal anti-caspase-7, anti-ERK1/2 and anti-NF-κB (p65) antibodies were obtained from Cell Signaling Technology (Beverly, MA, USA). Polyclonal anti-histone H3 antibody was purchased from Biosynthesis Biotechnology Co, Ltd (Beijing, China). Nuclear and cytoplasmic extraction kits were purchased from KeyGen Biotech Co, Ltd (Nanjing, China). All other chemicals and reagents used in the experiments were commercially available.

Cell lines and cell culture

The human colon cancer cell line SW620 was obtained from Shanghai Institutes for Biological Sciences (Shanghai, China). The cells were cultured in Leibovitz's L-15 medium supplemented with 10% FBS. The cells were maintained at 37 °C in a humidified atmosphere of 5% CO_2 and were deprived of serum for 16 h before they were used in the experiments. All of the experimental data were obtained from cells passaged between 3 and 10 times.

Cell proliferation assay

The SW620 cells were seeded in 96-well plates at 5×10^4 cells per well and grown to 70% confluence in culture medium. The cells were pretreated with various concentrations of EGCG (0, 25, 50, 75, and 100 μg/mL) for 15 min and then stimulated with PAR2-AP (100 μmol/L) or factor VIIa (10 nmol/L) in the presence of EGCG for 24 h. Then, 20 μL of MTT solution (5 mg/mL in PBS) was added to each well, and the cells were incubated for another 4 h at 37 °C. Finally, the culture media were removed and the cells were solubilized with 100 μL dimethylsulfoxide (DMSO), and the absorbance of the cells was measured at 490 nm using a microtiter plate photometer (BioTek, USA).

Cell migration assay

Cell migration assays were performed using modified Boyden chambers with a 65 μm diameter and a porous (8 μm) polycarbonate membrane separating the two chambers (Transwell, Corning Inc, USA). The cells were harvested by brief exposure to trypsin/EDTA and neutralized with Leibovitz's L-15 medium. The cells were washed and resuspended in medium with 0.1% bovine serum albumin (BSA) in an adequate concentration. At the indicated times, cells (1.0×10^5 in 100 μL) were incubated with EGCG (100 μg/mL) for 15 min at 37 °C, then placed in the upper compartments in the continued presence of EGCG. Cells were placed in the upper compartment of the migration chamber with PAR2-AP (100 μmol/L) or factor VIIa (10 nmol/L) in both the upper and lower compartments. The cells without any agonists or inhibitors in the assay were used as a control. After 8 h of incubation, the cells that had migrated through the pores to the lower side of membrane were fixed with methanol and stained with Giemsa. The number of cells was counted in five randomly chosen fields using light microscopy (×200). For each triplicate, the number of cells in ten high power fields was determined, and the counts were averaged.

Cellular cytoskeleton detection

The SW620 cells were placed in 24-well culture dishes at a density of 3×10^4 cells per well in culture medium containing 10% FBS at 37 °C in 5% CO_2. After 12 h, the cells were serum-starved for 16 h prior to stimulation with PAR2-AP (100 μmol/L) or factor VIIa (10 nmol/L) for 1 h. The cells in some wells were pretreated with EGCG (100 μg/mL) for 15 min as described above. Then, the cells were fixed on glass coverslips with 4% paraformaldehyde and washed with PBS three times. The DNA was stained with Hoechst 33342 (Sigma), and the actin cytoskeleton was stained with rhodamine-conjugated phalloidin (Sigma). The samples were observed under a laser scanning confocal fluorescence microscope (Carl Zeiss, Germany).

Quantitative real-time PCR analysis

The SW620 cells were seeded at 1×10^6 cells/mL into 6-well plates and serum-starved for 16 h prior to stimulation with PAR2-AP (100 μmol/L) or factor VIIa (10 nmol/L) for 2 h. The cells in some wells were pretreated with EGCG (100 μg/mL) for 15 min. Then, the total cellular RNA was isolated, and first-strand cDNA was synthesized using SuperScript II reverse transcriptase (Life Technologies). Finally, Q-PCR was performed using a Rotor-Gene 2000 (Corbett Research, Australia). The caspase-7 forward primer was 5′-TGACCTATCCTGCCCTCA-3′, and the reverse primer was 5′-TCTCCTGC-

CTCACTGTCC-3′. Primers for the control housekeeping gene β-actin were 5′-CACGAAACTACCTTCAACTCC-3′ (forward) and 5′-CATACTCCTGCTTGCTGATC-3′ (reverse). Each pair of primers was shown to yield only one product. The Q-PCR parameters consisted of an initial hold at 95 °C for 5 min followed by 35 cycles of 95 °C for 30 s, 54.5 °C (caspase-7) or 56 °C (β-actin) for 30 s and 72 °C for 30 s. After each Q-PCR run, a melting curve was performed to ensure that only a single amplicon was generated. Caspase-7 mRNA levels were normalized to control values of β-actin (%).

Detection of MMP-9 secretion

The SW620 cells were seeded at 1×10^6 cells/mL into 6-well plates and serum-starved for 16 h prior to stimulation with PAR2-AP (100 μmol/L) or factor VIIa (10 nmol/L) for 24 h. The cells in some wells were pretreated with EGCG (100 μg/mL) for 15 min. The MMP-9 secreted into the cell supernatant was measured using MMP-9 ELISA assay kits following the manufacturer's instructions. The MMP-9 protein level was expressed as ng/mL.

TF activity measurement

The SW620 cells were seeded at 1×10^6 cells/mL into 6-well plates and treated as described above. Following stimulation, the cells were briefly trypsinized, suspended in Leibovitz's L-15/10% FBS, pelleted, and resuspended in Tris-buffered saline (TBS) at a density of 10^6 cells/mL. The cells were then pelleted again and lysed with 1 mL of lysate buffer (TBS/1% Triton X-100/1 mmol/L PMSF). The TF activity of the lysates was determined based on factor X activation by the TF/factor VIIa complex, and the resulting factor Xa was measured using a chromogenic assay (Actichrome^{TM} TF provided by ADI).

Western blotting analysis

For detection of NF-κB (p65/RelA) protein expression, SW620 cells were seeded at 1×10^7 cells per well into 10-cm plates and stimulated with PAR2-AP (100 μmol/L) or factor VIIa (10 nmol/L). The cells in some wells were pretreated with various concentrations of EGCG (0, 25, 50, 75, and 100 μg/mL) for 15 min, and EGCG was not removed. Following the manufacturer's protocol, nuclear proteins were accumulated. To assay the protein levels of phospho-ERK1/2 and caspase-7, SW620 cells (1×10^6) were seeded into 6-well plates and treated as above, followed by preparation of cell lysates. The protein concentrations of the samples were measured using a spectrophotometer (Thermo Scientific, USA). Sodium dodecyl sulfate (SDS)-polyacrylamide gel electrophoresis (PAGE) was used to separate 30 μg of protein per well, and the bands were transferred to PVDF membranes (Bio-Rad, CA, USA). The membranes were blocked with a blocking solution containing 5% defatted milk/Tris-buffered saline/0.05% Tween-20 (TBST) (pH 7.6) for 1 h at room temperature (RT). After being washed 3 times with TBST, the membranes were probed with anti-NF-κB (p65/RelA, 1:1000), anti-caspase-7 (1:1000), anti-phospho-ERK1/2 (1:1000), anti-total-ERK1/2 (1:1000), anti-β-actin (1:2500) or anti-histone H3 (1:500) antibodies with gentle agitation overnight (16 h) at 4 °C. The membrane was then washed with TBST three times and incubated for 1 h at RT with horseradish peroxidase (HRP)-conjugated secondary antibodies (1:2000, Cell Signaling Technology, Billerica, MA, USA). Finally, immunoreactive proteins were visualized using ECL Western blotting detection reagents (GE Healthcare, Buckinghamshire, UK) and quantitated using a Bio-Rad Fluor-S Multi Imager (Typhoon 9400, Amersham, Sweden).

Statistical analysis

The data were expressed as mean±SEM. The statistical significance of the differences was calculated by applying analysis of variance (ANOVA) using SPSS software (version 16.0). $P<0.05$ was considered statistically significant.

Results

EGCG inhibits PAR2-AP- or factor VIIa-induced proliferation and migration of SW620 cells

Our previous work indicated that PAR2-AP (100 μmol/L) and factor VIIa (10 nmol/L) promoted SW620 cell proliferation and migration[9]. In this study, we first investigated whether EGCG at various concentrations could decrease the effects of PAR2-AP and factor VIIa on cell proliferation (as assayed using the MTT reagent). As shown in Figure 1A, EGCG inhibited PAR2-AP- (100 μmol/L) or factor VIIa- (10 nmol/L) induced growth

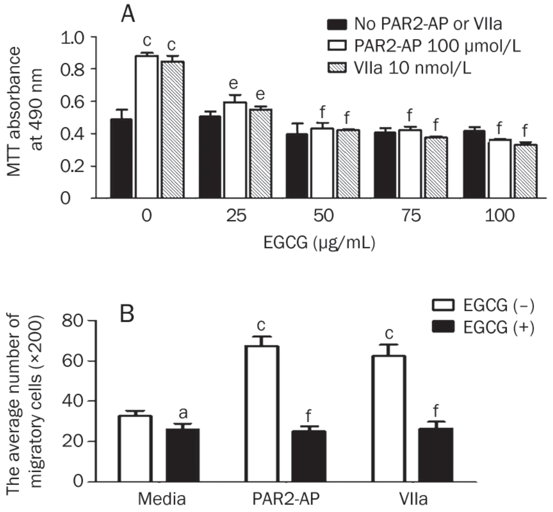

Figure 1. Effects of EGCG on PAR2-AP- and factor VIIa-induced proliferation and migration of SW620 cells. (A) SW620 cells were plated at 5×10^4 cells in 96-well plates and pretreated with different concentrations of EGCG (0, 25, 50, 75, and 100 μg/mL) for 15 min, then incubated with PAR2-AP (100 μmol/L) or factor VIIa (10 nmol/L) for 24 h. The above EGCG was kept in media. The cell proliferation was measured using MTT colorimetric assay. *n*=6. Mean±SEM. $^{e}P<0.05$, $^{f}P<0.01$ *vs* PAR2-AP- or factor VIIa-stimulated alone. (B) The cells were pretreated with or without EGCG (100 μg/mL) for 15 min as described above and then incubated with PAR2-AP (100 μmol/L) or factor VIIa (10 nmol/L) for 8 h. The cell migratory potential was measured by modified Boyden Chambers as described in Methods. *n*=3. Mean±SEM. $^{a}P>0.05$, $^{c}P<0.01$ *vs* media only; $^{e}P<0.05$, $^{f}P<0.01$ *vs* PAR2-AP- or factor VIIa-stimulated alone.

of SW620 cells. The inhibitory effects of EGCG were shown at concentrations as low as 25 μg/mL, with the maximal effects observed at 50 μg/mL (approximately 60% inhibition). Increasing the concentration of EGCG to 75 or 100 μg/mL did not further enhance its effects. In the absence of stimulation by PAR2-AP or factor VIIa, EGCG itself had no significant effects on the proliferation of cells. The inhibitory effects of EGCG were also confirmed with cell cycle analysis using flow cytometry, where a dose-dependent effect was observed from 25 to 100 μg/mL EGCG (Supplemental Figure 1). The difference between the dose effects observed in the MMT and cell cycle analyses may be due to different incubation times (24 h in MMT versus 8 h in the cell cycle analysis). EGCG itself was not toxic, based on a trypan blue exclusion assay (Supplemental Figure 2).

We next asked if EGCG was capable of inhibiting PAR2-AP- or factor VIIa-induced SW620 cell migration, as determined by Transwell chamber assays. The data showed that pre-incubation of cells with EGCG (100 μg/mL) prior to PAR2-AP (100 μmol/L) or factor VIIa (10 nmol/L) treatment resulted in decreases of 63% and 62% in the number of migratory cells, compared with the corresponding control (PAR2-AP or factor VIIa treatment without EGCG pre-treatment). EGCG alone had no significant effects on the migration of cells (Figure 1B) (cell migration images are shown in Supplemental Figure 3). These results demonstrated that EGCG inhibited both PAR2-AP- and factor VIIa-mediated migration of SW620 cells.

Effects of EGCG on the actin cytoskeleton in SW620 cells

Phalloidin staining, which labels actin filaments, was used to assess changes in the cytoskeleton following PAR2-AP and factor VIIa treatment in the presence and absence of EGCG. The cytoskeleton of untreated cells was found to have some homogeneous actin fibers, which were stained a moderate red color (Figure 2A). However, after exposure to PAR2-AP (100 μmol/L) or factor VIIa (10 nmol/L) for 1 h, the actin filaments were present at the cell cortex, in filopodia and pseudopodia and stained a strong red color (Figures 2B, 2C). Pre-treatment of cells with EGCG (100 μg/mL) significantly rescued the aberrant actin organization that was induced by PAR2-AP or factor VIIa (Figures 2E, 2F). EGCG alone had no effect on the actin cytoskeleton in SW620 cells (Figure 2D).

Effects of EGCG on the expression of caspase-7 in SW620 cells

Caspase-7 is one of the key effector caspases that induce cell apoptosis. In a previous study, we showed that caspase-7 was down-regulated by PAR2-AP or factor VIIa[9]. To examine whether EGCG could affect the regulatory effects of PAR2-AP or factor VIIa on caspase-7 expression in SW620 cells, the caspase-7 mRNA and protein levels in these cells were evaluated under different conditions. We found that both PAR2-AP (100 μmol/L) and factor VIIa (10 nmol/L) decreased the level of caspase-7 mRNA (Figure 3A, white column). However, pre-incubation of SW620 cells with EGCG (100 μg/mL) significantly increased caspase-7 mRNA expression, even though the cells were treated with similar concentrations of PAR2-AP and factor VIIa (Figure 3A, black column). Compared with the corresponding controls (PAR2-AP or factor VIIa treatment alone), EGCG increased caspase-7 mRNA levels to approximately 4.3- and 4-fold (Figure 3A). Similarly, the caspase-7 protein level also increased with treatment of EGCG prior to PAR2-AP or factor VIIa stimulation (Figure 3B). EGCG alone had a slight effect on the regulation of caspase-7 release compared with media alone, but it was not statistically significant.

Effects of EGCG on the expression of TF and MMP-9 in SW620 cells

It has been shown that TF and MMP-9 are closely associated with tumor growth, invasion and metastasis[12, 13]. Our previous data also showed that TF levels were elevated in SW620 cells stimulated with PAR2-AP or factor VIIa[9]. In this study, we found that both PAR2-AP (100 μmol/L) and factor VIIa (10 nmol/L) enhanced the expression of TF and MMP-9 (Figure 4A and 4B, white column). When the cells were pre-incubated with EGCG (100 μg/mL), PAR2-AP- or factor VIIa-induced TF activity and MMP-9 expression were markedly decreased ($P<0.01$ *vs* PAR2-AP or factor VIIa alone), as shown in the black column in Figures 4A and 4B. EGCG alone seemed to

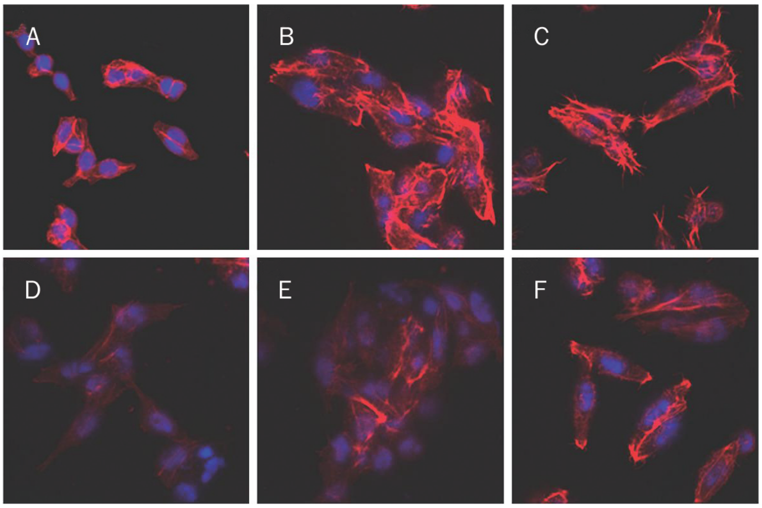

Figure 2. Fluorescence photomicrographs of SW620 cells with rhodamin-conjugated phalloidin and Hoechst 33342 staining (×400). SW620 cells were placed in 24-well culture dishes at 3×10^4 cells/well and treated with different conditions for 1 h. Then, the cells were fixed with 4% paraformaldehyde and washed with PBS three times. The DNA was stained with Hoechst 33342 (blue) and the actin cytoskeleton with rhodamin-conjugated phalloidin (red) which were observed under a laser scanning confocal fluorescence microscope. (A) Media only; (B) With 100 μmol/L of PAR2-AP; (C) With 10 nmol/L of factor VIIa; (D) With 100 μg/mL of EGCG; (E) With EGCG (100 μg/mL)/PAR2-AP (100 μmol/L); (F) With EGCG (100 μg/mL)/factor VIIa (10 nmol/L).

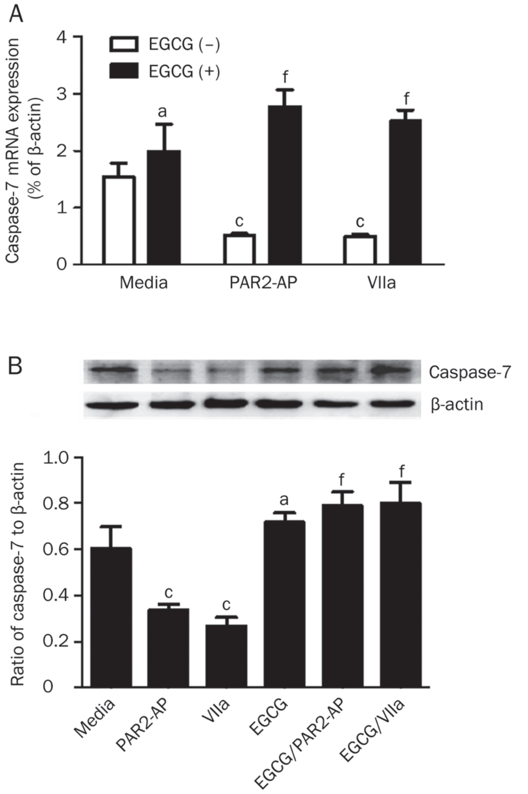

Figure 3. Effects of EGCG on caspase-7 expression in SW620 cells. SW620 cells (1×10^6–1×10^7) were stimulated with PAR2-AP (100 μmol/L) or factor VIIa (10 nmol/L) in the absence or presence of EGCG (100 μg/mL) for 2 h or 24 h. Then the total RNAs (2 h) and cell lysates (24 h) were collected for caspase-7 mRNA (A) and its protein (B) determination using QT-PCR and Western blot analysis, respectively. The caspase-7 mRNA levels were normalized to control values of β-actin and its protein levels were expressed as the ratio of caspase-7/β-actin bands density. *n*=3. Mean±SEM. $^aP>0.05$, $^cP<0.01$ *vs* media only; $^fP<0.01$ *vs* PAR2-AP- or factor VIIa-stimulated alone.

have a slight inhibitory effect on the MMP-9 level ($P<0.05$ *vs* media only).

Effects of EGCG on activation of ERK1/2 and NF-κB in SW620 cells

Previously, we found that PAR2-AP and factor VIIa stimulated the activation of ERK1/2 and NF-κB (p65/RelA) in SW620 cells within 30 min of treatment[14, 15]. In this study, we further investigated whether EGCG could influence the effects of PAR2-AP and factor VIIa on the levels of p-ERK1/2 and NF-κB (p65/RelA) in the cells. As the concentrations of EGCG increased (0–100 μg/mL), the levels of p-ERK1/2 (Figure 5A) and NF-κB (p65/RelA) (Figure 5B) in SW620 cells stimulated with factor VIIa (10 nmol/L) gradually decreased, indicating a dose-dependent inhibitory effect of EGCG. Similarly, the stimulatory effects of PAR2-AP (100 μmol/L) on p-ERK1/2 and NF-κB (p65/RelA) were also blocked by EGCG (100 μg/mL).

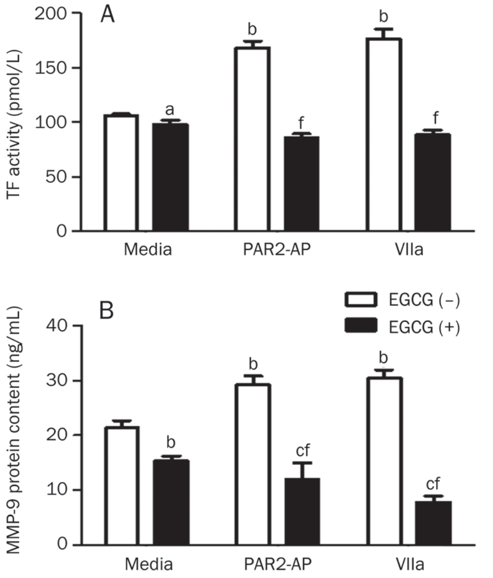

Figure 4. Effect of EGCG on the expression of TF and MMP-9 in SW620 cells. The cells (1×10^6) were incubated with PAR2-AP (100 μmol/L) or factor VIIa (10 nmol/L) in the absence or presence of EGCG (100 μg/L) for 24 h. The cell lysates were prepared and the TF activity (A) as well as MMP-9 levels (B) was measured by the specific kits, respectively. *n*=3. Mean±SEM. $^aP>0.05$, $^bP<0.05$, $^cP<0.01$ *vs* media only; $^fP<0.01$ *vs* PAR2-AP- or factor VIIa-stimulated alone.

Discussion

It is well known that factor VII can bind to TF on the cell surface and then activated by cleavage to generate factor VIIa. The formation of the TF/factor VIIa complex triggers the blood coagulation cascade. As a trypsin-like serine protease, factor VIIa by itself or in the TF/factor VIIa complex can trigger the cell signal transduction pathway in certain cells. It has been reported that factor VIIa or TF/factor VIIa might activate other receptors on the cell surface and cause a series of changes within the cell[16]. It was found that PAR2 was activated by factor VIIa and that TF/factor VIIa/PAR2 was involved in tumor growth and invasion in colorectal cancer and breast carcinoma. We previously demonstrated that both TF and PAR2 are highly expressed in the colon cancer cell line SW620. Factor VIIa can activate PAR2 and promote SW620 cell proliferation and migration in a TF-dependent manner. Some intracellular signaling molecules, such as ERK1/2 and NF-κB, are activated in these processes[9, 14, 15].

The anti-tumor properties of EGCG have received much attention in recent years. It has been shown that EGCG can induce apoptosis and inhibit proliferation in many tumor cell lines. Recent studies revealed that EGCG modulates the cell signaling pathways associated with angiogenesis, metastasis, and migration of prostate, liver and breast cancer cells[17]. Lim *et al* found that EGCG effectively inhibited HGF-induced invasion and metastasis of hypopharyngeal carcinoma cells via several intracellular signaling pathways[18]. In the current study, we investigated whether EGCG was able to interfere

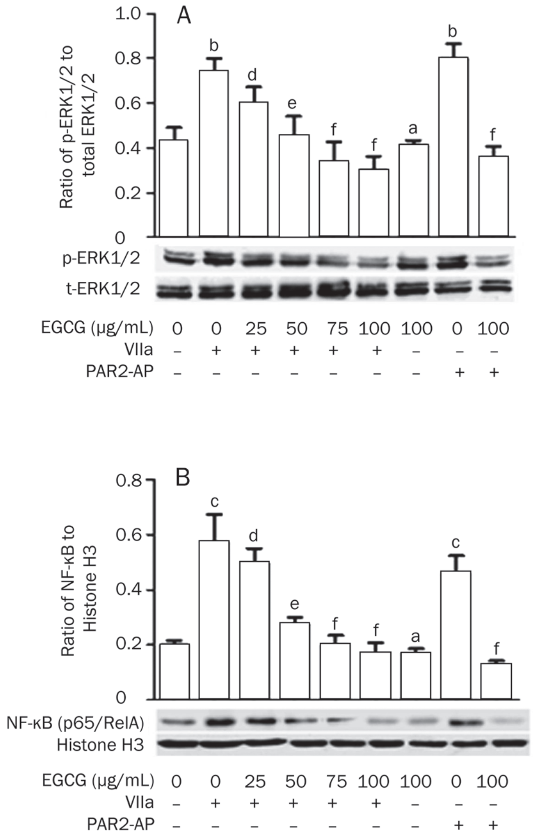

Figure 5. Effects of EGCG on activation of ERK1/2 and NF-κB pathway in SW620 cells. The cells were pretreated with or without the indicated concentrations of EGCG for 15 min and then incubated with PAR2-AP (100 μmol/L) or factor VIIa (10 nmol/L) for indicated time. The above EGCG was kept in media. The cytoplasmic and nuclear lysates of the cells were collected and subjected to Western analysis with antibodies to total and phosphorylated ERK1/2 (A) and to NF-κB/p65 as well as Histon H3 (B). *n*=3. Mean±SEM. $^{a}P>0.05$, $^{b}P<0.05$, $^{c}P<0.01$ *vs* control; $^{d}P>0.05$, $^{e}P<0.05$, $^{f}P<0.01$ *vs* PAR2-AP- or factor VIIa-stimulated alone.

with the effects of the TF/factor VIIa/PAR2 axis on SW620 cells.

Our results showed that PAR2 agonist- (PAR2-AP) or factor VIIa-induced SW620 cell proliferation was inhibited in a dose-dependent manner by EGCG. At a concentration of 100 μg/mL, EGCG decreased the number of migratory cells that were stimulated by PAR2-AP or factor VIIa by approximately 63% or 62%, respectively (Figure 1). These inhibitory effects of EGCG on PAR2-AP- and factor VIIa-induced proliferation and migration of SW620 cells led us to explore the changes in the actin cytoskeleton and to determine if these changes were closely associated with cell adhesion, invasion and signal transduction[19]. Indeed, both PAR2-AP and factor VIIa induced cytoskeleton reorganization, as indicated by increased filopodia and pseudopodia, and EGCG prevented this change. This result may partly elucidate the mechanism(s) of EGCG-mediated effects on cell proliferation and migration.

Caspase-7 has been defined as one of the key executioners involved in apoptosis induced by various stimuli, and it is necessary for apoptosis-associated nuclear changes, such as chromatin condensation[20]. It has been demonstrated that EGCG can mediate the activation of caspases by inhibition of the NF-κB pathway and subsequently induce apoptosis in human epidermoid carcinoma A431 cells[21]. In our present study, we further demonstrated that activation of PAR2 in SW620 cells by PAR2-AP or factor VIIa suppressed caspase-7 expression at both the mRNA and protein levels. EGCG reversed the down-regulating effects of PAR2-AP or factor VIIa on the expression of caspase-7 (Figure 3). These results suggested that EGCG might enhance cell apoptosis and thereby reduce cell proliferation. Whether EGCG can affect the expression of other molecules related to cell apoptosis (such as caspase-3) remains to be answered.

Over the past few years, several target molecules, including angiogenic growth factor, chemotactic factors, and some anti-apoptotic molecules, were found to be regulated by the activation of the TF/factor VIIa/PAR2 complex. Furthermore, TF has been implicated in angiogenesis, growth and metastasis of cancers[22]. Matrix metalloproteinases (MMPs) are closely related to cell invasion and migration. Our data shows that EGCG significantly suppressed both TF activity and MMP-9 secretion in SW620 cells induced by PAR2 activation with PAR2-AP or factor VIIa stimulation. These results are largely consistent with other reports. For example, Annabi *et al* demonstrated that EGCG directly and indirectly decreased MMP-9 secretion in macrophage-like HL-60 cells[23]. Lim *et al* showed that EGCG was able to inhibit the HGF-induced MMP-9 activity in hypopharyngeal carcinoma cells[18]. Taken together, these results suggest that EGCG is capable of blocking the expression of some key molecules in tumor cells and, therefore, it contributes to the suppression of cell proliferation, migration and metastasis.

It is well known that the ERK1/2 and NF-κB signaling pathways play a pivotal role in many cellular processes, such as proliferation, apoptosis, and differentiation[24–27]. PAR2 activation induced by the TF/factor VIIa complex can trigger cell signal transduction through different pathways, including ERK1/2 and NF-κB[15, 28]. This study investigated whether EGCG could reverse the activation of ERK-1/2 as well as NF-κB by PAR2 activation. As shown in Figure 5, PAR2-AP, and factor VIIa activated ERK-1/2, as indicated by increased ERK-1/2 phosphorylation and NF-κB (p65/RelA) expression in the nuclear fraction. However, EGCG dose-dependently inhibited both ERK-1/2 and NF-κB activation by factor VIIa. Similarly, EGCG at a concentration of 100 μg/mL obviously inhibited PAR2-AP-induced ERK-1/2 and NF-κB activation. These results indicate that the blockade of ERK-1/2 and NF-κB activation is the major mechanism for the inhibitory effects of EGCG on TF/factor VIIa/PAR2 axis-mediated cell proliferation and migration.

In summary, the present data, together with our previous studies, strongly indicate that PAR2 activation by PAR2-AP or the TF/factor VIIa complex triggers the phosphorylation of ERK1/2 and the activation of the NF-κB signaling pathway, thereby regulating the expression of caspase-7, TF, and

MMP-9, which further contributes to the proliferation and migration of colon cancer cells. EGCG, the major polyphenolic constituent in green tea, can target the axis of TF/factor VIIa/PAR2 and the ERK1/2/NF-κB signaling pathways and may serve as a preventive and therapeutic agent for colon cancers.

Acknowledgements

This project was supported by the Provincial Science Foundation of Jiangsu (No BK2010336) and the Student's Scientific Research of Jiangsu University (No 09A080).

Author contribution

Hong ZHOU designed the research; Fang ZHOU performed the research and analyzed the data; Ting WANG and Ying WU contributed new reagents; Dong-lin GUO and Xian-mei ZHANG contributed to the experiments; Yuan MU and Biao WU contributed analytic tools; and Fang ZHOU and Hong ZHOU wrote the paper.

Supplementary information

Supplementary tables are available at Acta Pharmacologica Sinica website of NPG.

References

1 Rak J, Milsom C, Magnus N, Yu J. Tissue factor in tumour progression. Best Pract Res Clin Haematol 2009; 22: 71–83.

2 Khorana AA, Ahrendt SA, Ryan CK, Francis CW, Hruban RH, Hu YC, *et al*. Tissue factor expression, angiogenesis, and thrombosis in pancreatic cancer. Clin Cancer Res 2007; 13: 2870–5.

3 Petersen LC. Microarray studies of factor VIIa-activated cancer cells. Thromb Res 2008; 122: S11–3.

4 Krishnan R, Kotian PL, Chand P, Bantia S, Rowland S, Babu YS. Probing the S2 site of factor VIIa to generate potent and selective inhibitors: the structure of BCX-3607 in complex with tissue factor-factor VIIa. Acta Crystallogr D Biol Crystallogr 2007; 63: 689–97.

5 Morris DR, Ding Y, Ricks TK, Gullapalli A, Wolfe BL, Trejo J. Protease-activated receptor-2 is essential for factor VIIa and Xa-induced signaling, migration, and invasion of breast cancer cells. Cancer Res 2006; 66: 307–14.

6 Zerbib P, Grimonprez A, Corseaux D, Mouquet F, Nunes B, Petersen LC, *et al*. Inhibition of tissue factor-factor VIIa proteolytic activity blunts hepatic metastasis in colorectal cancer. J Surg Res 2009; 153: 239–45.

7 Kirkland JG, Cottrell GS, Bunnett NW, Corvera CU. Agonists of protease-activated receptors 1 and 2 stimulate electrolyte secretion from mouse gallbladder. Am J Physiol Gastrointest Liver Physiol 2007; 293: G335–46.

8 Zhou H, Hu H, Shi W, Ling S, Wang T, Wang H. The expression and the functional roles of tissue factor and protease-activated receptor-2 on SW620 cells. Oncol Rep 2008; 20: 1069–76.

9 Zhou H, Shi W, Zhou B, Guo D, Wang T. Tissue factor-factor VIIa regulates interleukin-8, tissue factor and caspase-7 expression in SW620 cells through protease-activated receptor-2 activation. Mol Med Rep 2010; 3: 269–74.

10 Khan N, Mukhtar H. Multitargeted therapy of cancer by green tea polyphenols. Cancer Lett 2008; 269: 269–80.

11 Yamauchi R, Sasaki K, Yoshida K. Identification of epigallocatechin-3-gallate in green tea polyphenols as a potent inducer of p53-dependent apoptosis in the human lung cancer cell line A549. Toxicol *In Vitro* 2009; 23: 834–9.

12 Versteeg HH, Schaffner F, Kerver M, Petersen HH, Ahamed J, Felding-Harbermann B, *et al*. Inhibition of tissue factor signaling suppresses tumor growth. Blood 2008; 111: 190–9.

13 Ou YQ, Chen LH, Li XJ, Lin ZB, Li WD. Sinomenine influences capacity for invasion and migration in activated human monocytic THP-1 cells by inhibiting the expression of MMP-2, MMP-9, and CD147. Acta Pharmacol Sin 2009; 30: 435–41.

14 Zhou B, Zhou H, Ling S, Guo D, Yan Y, Zhou F, *et al*. Activation of PAR2 or/and TLR4 promotes SW620 cell proliferation and migration via phosphorylation of ERK1/2. Oncol Rep 2011; 25: 503–11.

15 Guo D, Zhou H, Wu Y, Zhou F, Xu G, Wen H, *et al*. Involvement of ERK1/2/NF-κB signal transduction pathway in TF/FVIIa/PAR2-induced proliferation and migration of colon cancer cell SW620. Tumor Biol 2011; 32: 921–30.

16 Albrektsen T, Sørensen BB, Hjortø GM, Fleckner J, Rao LVM, Petersen LC. Transcriptional program induced by factor VIIa-tissue factor, PAR1 and PAR2 in MDA-MB-231 cells. J Thromb Haemost 2007; 5: 1588–97.

17 Yang CS, Wang X, Lu G, Picinich SC. Cancer prevention by tea: animal studies, molecular mechanisms and human relevance. Nat Rev Cancer 2009; 9: 429–39.

18 Lim YC, Park HY, Hwang HS, Kang SU, Pyun JH, Lee MH, *et al*. Epigallocatechin-3-gallate (EGCG) inhibits HGF-induced invasion and metastasis in hypopharyngeal carcinoma cells. Cancer Lett 2008; 271: 140–52.

19 Houben F, Ramaekers FC, Snoeckx LH, Broers JL. Role of nuclear lamina-cytoskeleton interactions in the maintenance of cellular strength. Biochim Biophys Acta 2007; 1773: 675–86.

20 Walsh JG, Cullen SP, Sheridan C, Lüthi AU, Gerner C, Martin SJ. Executioner caspase-3 and caspase-7 are functionally distinct proteases. Proc Natl Acad Sci U S A 2008; 105: 12815–9.

21 Gupta S, Hastak K, Afaq K, Ahmad N, Mukhtar H. Essential role of caspases in epigallocatechin-3-gallate-mediated inhibition of nuclear factor kappaB and induction of apoptosis. Oncogene 2004; 23: 2507–22.

22 Belting M, Ahamed J, Ruf W. Signaling of the tissue factor coagulation pathway in angiogenesis and cancer. Arterioscler Thromb Vasc Biol 2005; 25: 1545–50.

23 Annabi B, Currie JC, Moghrabi A, B'eliveau R. Inhibition of HuR and MMP-9 expression in macrophage-differentiated HL-60 myeloid leukemia cells by green tea polyphenol EGCG. Leuk Res 2007; 31: 1277–84.

24 Chen Y, Wang J, Yao Y, Yuan W, Kong M, Lin Y, *et al*. CRP regulates the expression and activity of tissue factor as well as tissue factor pathway inhibitor via NF-kappaB and ERK 1/2 MAPK pathway. FEBS Lett 2009; 583: 2811–8.

25 Balmanno K, Cook SJ. Tumour cell survival signalling by the ERK1/2 pathway. Cell Death Differ 2009; 16: 368–77.

26 Lee YK, Ng KM, Lai WH, Man C, Lieu DK, Lau CP, *et al*. Ouabain facilitates cardiac differentiation of mouse embryonic stem cells through ERK1/2 pathway. Acta Pharmacol Sin 2011; 32: 52–61.

27 Wang S, Liu Z, Wang L, Zhang X. NF-kappB signaling pathway, inflammation and colorectal cancer. Cell Mol Immunol 2009; 6: 327–34.

28 Awasthi V, Mandal SK, Papanna V, Rao LV, Pendurthi UR. Modulation of tissue factor–factor VIIa signaling by lipid rafts and caveolae. Arterioscler Thromb Vasc Biol 2007; 27: 1447–55.

Acta Pharmacologica Sinica (2012) 33: 127–136
© 2012 CPS and SIMM All rights reserved 1671-4083/12 $32.00
www.nature.com/aps

npg

Original Article

A mechanism-based pharmacokinetic/pharmacodynamic model for CYP3A1/2 induction by dexamethasone in rats

Liang LI[2], Zai-quan LI[3], Chen-hui DENG[2], Miao-ran NING[2], Han-qing LI[2], Shan-shan BI[2], Tian-yan ZHOU[1, 2, *], Wei LU[1, 2, *]

[1]State Key Laboratory of Natural and Biomimetic Drugs, Peking University, Beijing 100191, China; [2]Department of Pharmaceutics, School of Pharmaceutical Sciences, Peking University Health Science Center, Beijing 100191, China; [3]Department of Radiation Medicine, School of Basic Medical Sciences, Peking University Health Science Center, Beijing 100191, China

Aim: To develop a pharmacokinetic/pharmacodynamic (PK/PD) model describing the receptor/gene-mediated induction of CYP3A1/2 by dexamethasone (DEX) in rats.
Methods: A group of male Sprague-Dawley rats receiving DEX (100 mg/kg, ip) were sacrificed at various time points up to 60 h post-treatment. Their blood sample and liver were collected. The plasma concentration of DEX was determined with a reverse phase HPLC method. CYP3A1/2 mRNA, protein levels and enzyme activity were measured using RT-PCR, ELISA and the testosterone substrate assay, respectively. Data analyses were performed using a first-order conditional estimate (FOCE) with INTERACTION method in NONMEM version 7.1.2.
Results: A two-compartment model with zero-order absorption was applied to describe the pharmacokinetic characteristics of DEX. Systemic clearance, the apparent volume of distribution and the duration of zero-order absorption were calculated to be 172.7 $mL \cdot kg^{-1} \cdot h^{-1}$, 657.4 mL/kg and 10.47 h, respectively. An indirect response model with a series of transit compartments was developed to describe the induction of CYP3A1/2 via PXR transactivation by DEX. The maximum induction of CYP3A1 and CYP3A2 mRNA levels was achieved, showing nearly 21.29- and 8.67-fold increases relative to the basal levels, respectively. The CYP3A1 and CYP3A2 protein levels were increased by 8.02-fold and 2.49-fold, respectively. The total enzyme activities of CYP3A1/2 were shown to increase by up to 2.79-fold, with a lag time of 40 h from the Tmax of the DEX plasma concentration. The final PK/PD model was able to recapitulate the delayed induction of CYP3A1/2 mRNA, protein and enzyme activity by DEX.
Conclusion: A mechanism-based PK/PD model was developed to characterize the complex concentration-induction response relationship between DEX and CYP3A1/2 and to resolve the drug- and system-specific PK/PD parameters for the course of induction.

Keywords: drug-drug interactions; dexamethasone; CYP induction; CYP3A1/2; pharmacokinetics; pharmacodynamics; NONMEM

Acta Pharmacologica Sinica (2012) 33: 127–136; doi: 10.1038/aps.2011.161

Introduction

Clinical drug-drug interaction (DDIs) is a major problem, largely resulting from the inhibition or induction of drug-metabolizing enzymes (DMEs), particularly cytochrome P450s (CYPs)[1]. Although CYP induction-mediated DDIs are less frequent and less of a safety concern than CYP inhibition-mediated DDIs[2], these interactions can nevertheless reduce both the exposure and the pharmacological effect of a drug; this can occur when the drug is cleared by an enzyme that is induced by a coadministered drug. The induction of CYP3A is particularly important because it is the major CYP isoform and has been estimated to be involved in the metabolism of approximately 50% of marketed drugs[3].

The induction of CYPs has been well known for decades. However, the underlying mechanisms of this induction still remain to be understood[3]. The major mechanism of rat CYP3A1/2 induction is via an increased rate of gene transcription mediated by the pregnane X receptor (PXR)[4]. Briefly, the mechanism of rat CYP3A1/2 induction involves the binding of an inducer to PXR, the formation of an inducer-bound PXR/RXR (retinoid X-receptor) complex, translocation of the complex to the nucleus, and binding of the complex to DNA-responsive elements in the 5′-regulatory region of target genes (*ie*, *CYP3A1/2*) thereby triggering the transcription of these genes. Many drugs that induce CYP3A1/2 are PXR ligands

---

* To whom correspondence should be addressed.
E-mail luwei_pk@hsc.pku.edu.cn (Wei LU);
tianyanzhou@bjmu.edu.cn (Tian-yan ZHOU)
Received 2011-04-30 Accepted 2011-09-27

and have demonstrated transactivation in the PXR reporter assay.

Dexamethasone (DEX) has been widely used to treat patients with inflammatory and autoimmune conditions[5–7], and it has been reported to be a remarkable inducer of both human CYP3A4 and rat CYP3A1/2[8–10]. Recently, multiple *in vitro* and *in vivo* studies have demonstrated that the pharmacodynamics (PD) of CYP3A1/2 induction by DEX are dose- and time-dependent[11–13]. However, none of these studies explored the quantitative relationship between DEX exposure and the resultant alterations in CYP3A1/2 mRNA levels, protein levels and enzyme activity using a pharmacokinetic/pharmacodynamic (PK/PD) modeling approach.

The objective of the present study was to develop a mechanism-based PK/PD model that could quantitatively characterize the time-dependent relationship among the multiple elements (CYP3A1/2 mRNA, protein and enzyme activity) of CYP3A1/2 induction in rats treated with DEX. The key element in mechanism-based PK/PD modeling is the explicit distinction between parameters that describe drug-specific properties and those that describe biological system-specific properties[14]. As a result, the potential of unknown compounds to induce CYP3A1/2 could be predicted and simulated by this mechanism-based PK/PD model solely by utilizing knowledge of the *in vitro* potency ($S_{\max}$ and SC_{50}) and single-dose *in vivo* pharmacokinetics of these compounds.

Materials and methods

Animals and treatments

Normal male Sprague-Dawley rats weighing 200–250 g were purchased from the Department of Laboratory Animal Science at the Peking University Health Science Center. The animals were housed and acclimatized in a temperature- (22 °C) and light-controlled (12 h/12 h light/dark) animal care unit for 10 d before experimentation. They were allowed food and water *ad libitum*. All of the experiments were conducted in accordance with the European Community guidelines for the use of experimental animals and were approved by the Peking University Committee on Animal Care and Use.

Rats weighing 200–250 g received DEX (Sigma-Aldrich Inc, USA, 100 mg/kg in 5 mL/kg of corn oil) intraperitoneally (ip) after fasting for 12 h prior to the experiments. For the PK analysis, serial blood samples were collected from three treated rats at various times after dosing (0.083, 0.25, 0.5, 0.75, 1, 2, 3, 4, 6, 8, 12, 16, 24, 30, 36, and 48 h). The collected blood was centrifuged at 3000×*g* at 4 °C for 10 min. Plasma samples were then stored at -80 °C until analysis. In the PD study, 84 rats were randomly sorted into DEX or control (corn oil only) treatment groups. The treated rats were anesthetized with 60 mg/kg pentobarbital sodium and sacrificed at 0, 1, 2, 4, 8, 12, 16, 24, 30, 36, 42, 48, 54, and 60 h (*n*=3 per time point). For the CYP3A1/2 enzyme activity assays, approximately 4 g of liver was rapidly excised for the preparation of liver microsomes. The remaining liver tissues were flash-frozen in liquid nitrogen and stored at -80°C for RNA extraction.

Plasma concentration assays

The DEX concentrations were determined by a reverse phase high performance liquid chromatography (HPLC) method[15]. The lower limit of quantification was 0.25 μg/mL. The variability of the assay was <15%, and the inter-day and intra-day coefficients of variation (CV) were less than 10%.

CYP3A1 and CYP3A2 mRNA measurements

RNA isolation and cDNA synthesis

Total RNA was extracted from the rat livers using the TRIzol reagent (Invitrogen, USA), according to the manufacturer's protocol. The amount of purified RNA was determined by UV spectroscopy measurements at 260 nm, and its purity was determined by calculating the ratio of UV activity at 260 nm/280 nm. cDNA was reverse-transcribed from 0.5 μg of total RNA using random primers (25 μmol/L), a dNTP mixture (10 mmol/L), RTase M-MLV (RNase H$^-$) (200 U/μL), M-MLV buffer (5×) and an RNase inhibitor (40 U/μL) (Takara, Dalian, China).

Construction of reference standards

The reference standards were constructed for the absolute quantification of CYP3A1, CYP3A2, and GAPDH (the latter used as a house-keeping control) by real-time PCR. Fragments of these three target genes were cloned by conventional PCR using the appropriate primer sets[16], as listed in Table 1. The presence of the specific amplified products was confirmed by electrophoresis using a 1.2% agarose gel with ethidium bromide. The purification of the amplification products was performed using an Agarose Gel DNA Purification Kit (Takara, Dalian, China), according to manufacturer's recommendations. The DNA manipulation techniques, which included the insertion of the amplification products into the pMD19-T vector (Takara, Dalian, China), the transformation of the vector into competent *Escherichia coli* (JM109) (Takara, Dalian, China), screening for positive clones, plasmid DNA preparation and so on, were performed according to standard protocols. The identity of the cloned insert was confirmed by direct sequenc-

Table 1. Primers used for real-time PCR.

Gene	Forward primer (5′–3′)	Reverse primer (5′–3′)	Genbank number
CYP3A1	GGAAATTCGATGTGGAGTGC	AGGTTTGCCTTTCTCTTGCC	NM_013105
CYP3A2	AGTAGTGACGATTCCAACATAT	TCAGAGGTATCTGTGTTTCCT	NM_153312
GAPDH	CTGTGGTCATGAGCCCCTCC	CGCTGGTGCTGAGTATGTCG	NM_017008

ing, which was performed using the universal sequencing primer M13F (-47) by GenScript Co (China).

Real-time PCR amplification and dissociation curve analysis

Real-time PCR was performed using an ABI PRISM 7300 real-time quantitative PCR system (ABI, USA), using SYBR® Premix Ex Taq™ (Takara, Dalian, China), according to the manufacturer's instructions. Following cycling, dissociation curves were obtained by heating and cooling the samples at the following conditions: 95 °C for 15 s, 60 °C for 30 s, and 95 °C for 15 s[17]. The standard curves for CYP3A1, CYP3A2, and GAPDH were constructed using standard values obtained by 10-fold serial dilutions, ranging from 1 attomol/μL to 1×10^6 attomol/μL, of the extract of plasmids harboring the target insert. Reference standard curves were generated for each assay, and the standards and unknown samples were run in triplicate. The controls, which consisted of water and the mRNA control, were used to determine the extent of primer-dimer formation and DNA contamination in the isolated samples, respectively. The amplification plots and dissociation curves of the controls did not show any signal or dissociation product, suggesting the lack of primer-dimer formation and genomic DNA contamination in the RNA samples. The slope, intercept, percent efficiency (E) and R^2 values from the three standard curves in each experiment were used to calculate the intra-assay CVs and the inter-assay reproducibility. Low CVs (less than 15%) for both inter- and intra-assay variability implied good reproducibility of the real-time PCR standard curves for CYP3A1, CYP3A2, and GAPDH.

CYP3A1 and CYP3A2 protein measurements

For the CYP3A1/2 protein measurements and the CYP3A1/2 enzyme activity assays, liver microsomes were prepared from fresh livers using a differential centrifugation method, as described previously[18]. The protein concentration of the microsomal suspension was determined using the BCA assay kit (Biomiga Inc, San Diego, USA), according to the manufacturer's protocol. After determining the protein concentration, the microsomal suspension was diluted with 0.25 mol/L sucrose solution to a final protein concentration of 10 mg/mL and was stored at -80 °C until use. The CYP3A1 and CYP3A2 protein concentrations were determined by a non-competitive enzyme-linked immunosorbent assay (ELISA)[19]. The amount of microsomal proteins used was 0.1 μg for CYP3A1 and 1 μg for CYP3A2. The isoform protein values are expressed as pmol per milligram of protein.

CYP3A1/2 enzyme activity

The CYP concentrations of rat liver microsomes were determined according to the spectrophotometric method described by Omura and Sato[20]. The CYP3A1/2 enzyme activities were evaluated by the testosterone substrate assay[21]. The separation and detection of testosterone and its metabolites were performed using a Bisep™-1100 HPLC system (Unimicro Technologies Inc, USA), according to a previously described method[22].

Pharmacokinetic/pharmacodynamic modeling

PK analysis

A two-compartment mammillary model with zero-order absorption was used to describe the plasma PK after administration of 100 mg/kg DEX. The equations describing the model were as follows:

$$V_c \cdot \frac{dC_p}{dt} = \frac{DOSE}{T_0} - \frac{CL}{V_c} \cdot X_c - \frac{Q}{V_c} \cdot X_c + \frac{Q}{V_p} \cdot X_p \tag{1}$$

$$\frac{dX_p}{dt} = \frac{Q}{V_c} \cdot X_c - \frac{Q}{V_p} \cdot X_p \tag{2}$$

where X_c and X_p are the amount of DEX in the central and peripheral compartments, respectively; T_0 is the duration of the zero-order phase of absorption; C_p is the plasma concentration; V_c is the central volume of distribution; V_p is the peripheral volume of distribution; CL is the systemic clearance and Q is the inter-compartmental clearance.

PK/PD analysis

A schematic for the PK/PD model for CYP3A1/2 induction is presented in Figure 1. This model included three elements: CYP3A1/2 mRNA dynamics, CYP3A1/2 protein dynamics and CYP3A1/2 enzyme activity.

CYP3A1 and CYP3A2 mRNA dynamics

Graphical analyses of the CYP3A1 and CYP3A2 mRNA concentrations *versus* time demonstrated a considerable time delay between CYP3A1/2 mRNA and drug concentration (Figures 2 and 3). Therefore, an indirect response model with a chain of transit compartments, as described previously[23, 24], was applied for the transduction of the DEX exposure to the mRNA response. In the absence of the drug, it was assumed that CYP3A1 and CYP3A2 mRNA were produced from their DNA according to a zero-order rate constant, k_{in}, and degraded according to a first-order rate constant, k_{out}. The effect of the DEX concentration on the transcription rates of mRNA was described as a PXR-mediated process. The fractional occupancy (FO) of the DNA responsive elements by the DEX-PXR complex was related to the DEX plasma concentration and was calculated from the DEX concentration using a Hill equation, as reported by Sarangapani[25]. The time delay accounting for the transcription process of CYP3A1 and CYP3A2 mRNA was characterized by two parallel chains of transit compartments, as shown in Figure 1. The optimal number of transit compartments was assessed by stepwise addition or deletion of one transit compartment and was selected from the inflection point on the objective function value (OFV) *versus* compartment number curve[26, 27]. The equations describing this chain of events are as follows:

$$FO_i = \frac{\text{DEX-PXR-DNA}_i}{\text{DNA}_{i,\text{total}}} = \frac{C_p^{\gamma_i}}{\text{SC}_{50,i}^{\gamma_i} + C_p^{\gamma_i}} \tag{3}$$

$$S_{i,0} = S_{\max,i} \cdot FO_i \tag{4}$$

$$\frac{dS_{i,1}}{dt} = \frac{1}{\tau_i} \cdot (S_{i,0} - S_{i,1}) \tag{5}$$

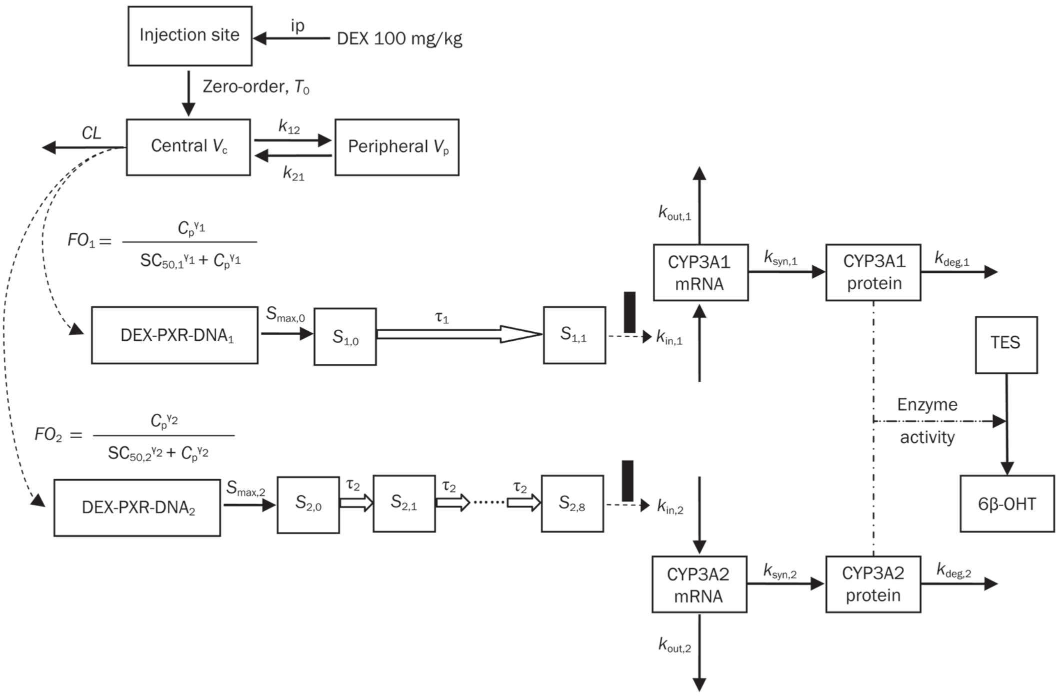

Figure 1. A schematic picture for the PK/PD model for CYP3A1/2 induction.

$$\frac{dS_{i,n_i}}{dt} = \frac{1}{\tau_i} \cdot (S_{i,n_i-1} - S_{i,n_i}) \tag{6}$$

$$\frac{dmRNA_i}{dt} = k_{in,i} \cdot (1+S_{i,n_i}) - k_{out,i} \cdot mRNA_i \tag{7}$$

The initial condition for CYP3A mRNA is as follows:

$$mRNA_{i,0} = \frac{k_{in,i}}{k_{out,i}} \tag{8}$$

where i is the identification for the CYP3A subtype: 1 for CYP3A1 and 2 for CYP3A2; DEX-PXR-DNA$_i$ is the concentration of the DNA ligand binding sites bound to the DEX-PXR complex; DNA$_{i,total}$ is the total concentration of binding sites for this complex; $S_{i,0}$ is the stimulation constant; $S_{max,i}$ is the maximum stimulation of the transcription rate of CYP3A mRNA ($k_{in,i}$); $k_{out,i}$ is the degradation rate constant for CYP3A mRNA; SC$_{50,i}$ is the DEX concentration required to reach 50% $S_{max,i}$; γ_i is the Hill coefficient; S_{i,n_i} is the n_i^{th} transit compartment of the stimulation and τ_i is the mean transit time between each transit compartment.

CYP3A1 and CYP3A2 protein dynamics

CYP3A1 and CYP3A2 mRNA induction was followed by an increase of CYP3A1 and CYP3A2 protein expression. This induction is described by the following equation:

$$\frac{dCYP3A_i}{dt} = k_{syn,i} \cdot mRNA_i^{m_i} - k_{deg,i} \cdot CYP3A_i \tag{9}$$

The initial condition for each CYP3A$_i$ protein is as follows:

$$CYP3A_{i,0} = \frac{k_{syn,i}}{k_{deg,i}} \cdot mRNA_{i,0}^{m_i} \tag{10}$$

where $k_{syn,i}$ is the synthesis rate constant, assuming that the translation of *CYP3A*$_i$ protein is proportional to its mRNA level; $k_{deg,i}$ is the first-order degradation rate constant of *CYP3A*$_i$ protein and m_i is the amplification factor, indicating that one copy of the mRNA can be translated into multiple copies of the protein.

CYP3A1/2 enzyme activity

Because the measurement of 6β-hydroxy testosterone (6β-OHT) formation is a reliable indicator of CYP3A1/2 activity levels[28] and all of the reactions were performed in the linear range, with respect to CYP concentration and incubation time, the formation of 6β-OHT (EA, enzyme activity) was described to be proportional to the CYP3A1 and CYP3A2 protein concentrations:

$$EA = \alpha \cdot CYP3A1 + \beta \cdot CYP3A2 \tag{11}$$

where α and β are the rates of formation of 6β-OHT for CYP3A1 and CYP3A2, respectively, and their values were expressed as pmol of 6β-OHT per min per pmol of CYP3A1 or CYP3A2.

Data analysis

The development of the PK/PD model was performed in two steps using a sequential process, as described previously[29]. First, the pharmacokinetic data were modeled. Then, the PK parameters were fixed, and the predicted DEX concentration-time profile was used as an input function for the entire PK/PD model. All of the three PD models described by Equations (3)–(11) were estimated simultaneously. This approach is computationally much faster than the simultaneous estimation of the PK and PD models and is not expected to compromise the precision and accuracy of the PD parameter estimates, unless the PK model is misspecified[29, 30]. All of the analyses were performed using a first-order conditional estimate (FOCE) with INTERACTION method in NONMEM version 7.1.2 (Icon Development Solutions, MD, USA).

The animals used in the PK study contributed to several measurements, and the population approach was used to compute the mean population estimates. An exponential error model was selected for modeling the between-subject variability (BSV). In contrast, the PD data were fit using the naïve pool approach because each animal contributed with a single measurement; therefore, it was not possible to distinguish between inter-animal and residual variability. The residual variability for both the PK and PD models was modeled initially with a combined error model; if one of the components (additive or proportional) of the residual was negligible, it was deleted from the model.

The goodness of fit was assessed by model convergence, precision in parameter estimates, decrease in objective function value (χ^2=10.83, *P*<0.001, *df*=1) and examination of the residuals. The ability of the PK/PD model to describe the observed data was evaluated by a visual predictive check (VPC) based on 1000 data sets that were simulated with the obtained final parameter estimates, and the median and 2.5th and 97.5th percentiles were calculated. Exploratory analyses, graphical displays and other statistical analyses, including the evaluation of the NONMEM outputs, were performed (version 2.12.1 for Windows).

Results

Pharmacokinetics

The time course of plasma DEX concentrations after 100 mg/kg ip administration is shown in Figure 2. During an early exploratory analysis, several models (*ie*, one-, two-, and three-compartment PK models with zero-order or first-order absorption processes were developed to fit to the time course of the DEX plasma concentration. The two-compartment model had a lower OFV than the one-compartment model (123.188 versus 142.226; *P*<0.001 by χ^2 test; *df*=2), and it showed a more favorable distribution of CWRES over time. The addition of an extra peripheral compartment did not yield a significantly lower OFV. Absorption of DEX from the peritoneal cavity was best characterized by a zero-order kinetic process because this yielded a significantly better fit than a first-order absorption rate constant. The OFV was 45.60 units lower with zero-order absorption. The estimates of the PK parameters are listed in Table 2. Only the BSV for inter-compartment clearance (*Q*) was included in the final PK model. The T_0 (the duration of the zero-order absorption) obtained was 10.47 h. The maximal plasma concentration ($C_{\max}$) of DEX was achieved within 8 h and declined bi-exponentially, with a terminal half-life ($T_{1/2}$) of 2.64 h. The volume of distribution at steady state (V_{ss}, equal to the sum of V_c and V_p) was very large, indicating that DEX has a significant extravascular distribution in rats. The PK profile for DEX was similar to that reported by a previous study[31].

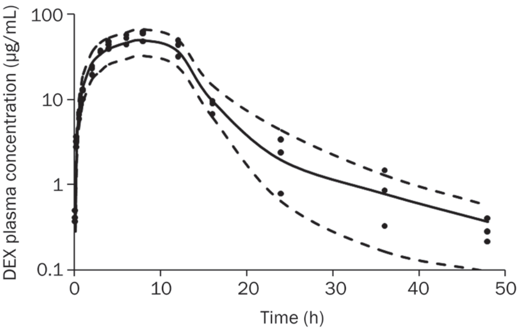

Figure 2. Time course of plasma DEX concentrations after 100 mg/kg ip administration. The symbols represent individual data from rats and the solid line represents the model fit lines. The dashed lines depict 95% prediction interval of the PK model.

CYP3A1 and CYP3A2 mRNA dynamics

The CYP3A1 and CYP3A2 mRNA levels in vehicle-treated animals remained relatively constant throughout the time course (data not shown), indicating that the baselines were stable. The model corresponding to Equations (3)–(8), with different numbers of transit compartments, was evaluated to describe the profiles of CYP3A1 and CYP3A2 mRNA concentrations *versus* time. The transit model using one transit compartment provided the lowest OFV and the best fit for the CYP3A1 mRNA induction profile. For CYP3A2 mRNA, an OFV of 1836.70 was obtained for the model with no transit compartment, whereas an OFV of 1794.16 was obtained for a transit compartment model using eight transit compartments. The OFV continued to decrease with the inclusion of additional transit compartments, but there was no further visual improvement in the model predictions.

Table 2. Pharmacokinetic parameters for dexamethasone.

Parameters	Definitions	Values (% RSE)	BSV (% RSE)
CL/F (mL·kg^{-1}·h^{-1})	Clearance	172.7 (6.70)	–
Q/F (mL·kg^{-1}·h^{-1})	Inter-compartmental clearance	14.32 (36.52)	0.655 (36.66)
V_c/F (mL/kg)	Central volume	657.4 (12.55)	–
V_p/F (mL/kg)	Peripheral volume	263.2 (31.95)	–
T_0 (h)	The duration of the zero-order absorption	10.47 (6.36)	–

BSV, between subject variability; RSE, relative standard error.

The results corresponding to the VPC, as shown in Figure 3, confirmed that the model fit the data and was appropriate to describe the mean tendency of the data and their dispersion. The estimated CYP3A1 and CYP3A2 mRNA baseline levels were 32.48 attomol/μg (total RNA) and 203.46 attomol/μg (total RNA), respectively. The CYP3A1 and CYP3A2 mRNA values increased gradually to their peak levels (21.29- and 8.67-fold increase, respectively, *vs* baseline) within 24 h and 36 h, respectively, and then returned to their baseline levels 60 h after drug administration. The estimated parameters for CYP3A1 and CYP3A2 mRNA dynamics are listed in Table 3. The estimated $S_{\max,i}$ values for CYP3A1 and CYP3A2 mRNA synthesis were 22.42- and 8.55-fold of the $k_{\text{in},i}$, respectively. The high Hill coefficient estimates (8.01 and 5.00 for CYP3A1 and CYP3A2 mRNA, respectively) could be explained by one of the following: 1) the CYP3A1/2 DNA responsive elements were initially saturated with the DEX-PXR complex because the plasma concentration was much higher than the $SC_{50,i}$ values (2.39 μg/mL for CYP3A1 mRNA and 2.82 μg/mL for CYP3A2 mRNA) within 18 h after DEX administration, or 2) the affinity of the DEX-PXR complex binding to CYP3A1/2 DNA responsive elements could be increased dramatically by heterodimerization with the nuclear hormone receptor RXR[32]. Subsequently, the two chains of transit compartments with different numbers of compartments and mean transit times resolved the delay of the mRNA transcription relative to the concentration of DEX. The first chain for CYP3A1 mRNA had one compartment and a τ_1 of 4.59 h, whereas the second chain for CYP3A2 mRNA had eight compartments and a τ_2 of 2.58 h.

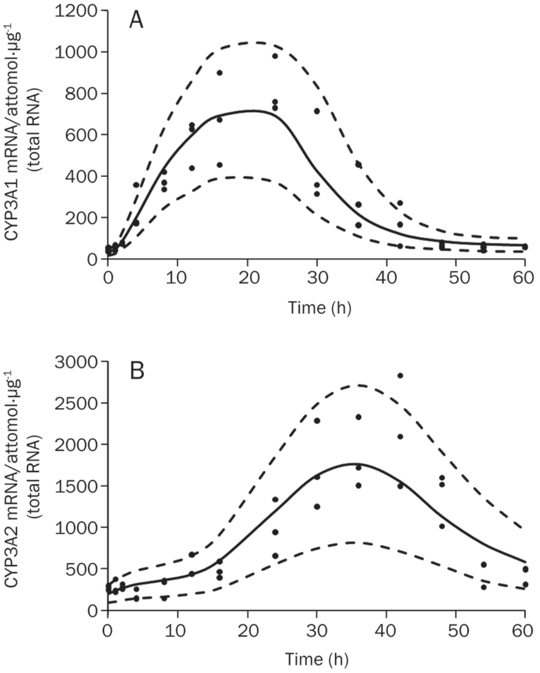

Figure 3. Time course of CYP3A1 (A) and CYP3A2 (B) mRNA expression. The symbols represent individual data from rats and the solid line represents the model fit lines. The dashed lines depict 95% prediction interval of the mRNA PD models.

CYP3A1 and CYP3A2 protein dynamics

The time courses of CYP3A1 and CYP3A2 protein expression were simulated by the model (Figure 4), and the lag time between mRNA and protein expression changes was approximately 12 h. The CYP3A1 protein exhibited an inductive potency in DEX-treated rats (from 31.92 to 256.03 pmol·mg^{-1} protein, an 8.02-fold increase), which was greater than that of the CYP3A2 protein (from 39.39 to 97.99 pmol·mg^{-1} protein, a 2.49-fold increase). The estimated parameters for Equation (9) are listed in Table 4. A visual predictive check indicated that the time courses of CYP3A1 and CYP3A2 protein dynamics were well described by the model.

CYP3A1/2 enzyme activity dynamics

The maximum induction of testosterone 6β-hydroxylation

Table 3. Dynamic parameters for CYP3A1 and CYP3A2 mRNA after DEX administration.

Parameters	Definitions	Values (% RSE)
$k_{\text{in},1}$ (attomol·h^{-1}·μg^{-1} total RNA)	Transcription rate for CYP3A1 mRNA	7.47 (4.65)
$k_{\text{out},1}$ (h^{-1})	Degradation rate for CYP3A1 mRNA	0.23 (6.45)
$S_{\max,1}$	Maximum stimulation of the transcription rate of CYP3A1 mRNA	22.42 (10.90)
$SC_{50,1}$ (μg/mL)	DEX concentration required to reach 50% $S_{\max,1}$	2.39 (15.89)
γ_1	Hill-type parameter for CYP3A1 mRNA	8.01 (6.92)
τ_1 (h)	Mean transit time of the stimulation of $k_{\text{in},1}$	4.59 (4.71)
n_1	Number of the transit compartments for CYP3A1 mRNA	1 (Fixed)
$k_{\text{in},2}$ (attomol·h^{-1}·μg^{-1} total RNA)	Transcription rate for CYP3A2 mRNA	40.00 (19.56)
$k_{\text{out},2}$ (h^{-1})	Degradation rate for CYP3A2 mRNA	0.197 (21.00)
$S_{\max,2}$	Maximum stimulation of the transcription rate of CYP3A2 mRNA	8.55 (11.72)
$SC_{50,2}$ (μg/mL)	DEX concentration required to reach 50% $S_{\max,2}$	2.82 (38.50)
γ_2	Hill-type parameter for CYP3A2 mRNA	5.00 (13.16)
τ_2 (h)	Mean transit time of the stimulation of $k_{\text{in},2}$	2.58 (12.79)
n_2	Number of the transit compartments for CYP3A2 mRNA	8 (Fixed)

RSE, relative standard error.

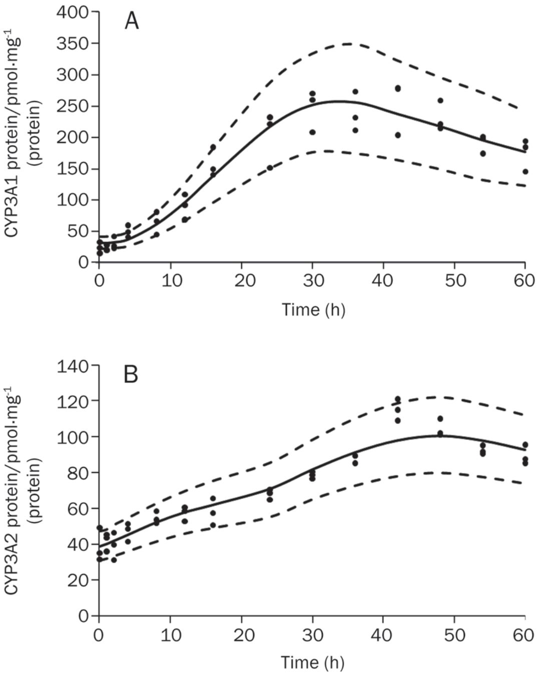

Figure 4. Time courses of CYP3A1 protein (A) and CYP3A2 protein (B) after DEX administration. The symbols represent individual data from rats and the solid line represents the model fit lines. The dashed lines depict 95% prediction interval of the protein PD models.

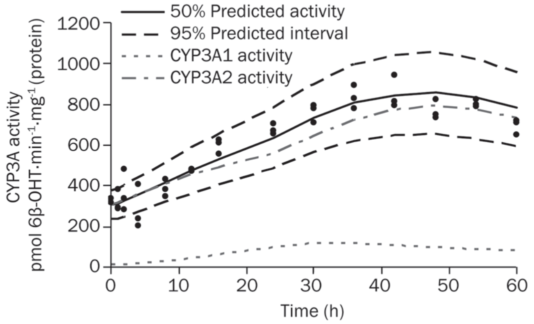

Figure 5. Time course of CYP3A1/2 enzyme activity after DEX administration. The symbols represents individual data from rats and the solid line represents the model fit lines. The black dashed lines depict 95% prediction interval of the enzyme activity dynamic model. The gray dashed line and the dotted line represent the simulated contributions of CYP3A1 and CYP3A2 to 6β-OHT formation, respectively.

activity was observed after DEX dosing, as depicted in Figure 5. Because both CYP3A1 and CYP3A2 proteins are capable of catalyzing 6β-hydroxylation of testosterone, the enzyme activities were composed of two parts, as described by Equation (12). The gray dashed line and the dotted line in Figure 5 show the contributions of CYP3A1 and CYP3A2, respectively, to 6β-OHT formation, which were generally parallel to their protein levels. The rates of formation of 6β-OHT for CYP3A1 and CYP3A2, as shown in Table 5, were estimated to be 0.463 pmol·min^{-1}·pmol^{-1} CYP3A1 and 7.49 pmol·min^{-1}·pmol^{-1} CYP3A2, respectively.

Discussion

In the present study, a mechanism-based PK/PD model was successfully developed to characterize the complex relationships between DEX PK and the time courses of CYP3A1/2 mRNA, protein and enzyme activity in male Sprague-Dawley rats.

We found that a conventional two-compartment model with a zero-order absorption process best described the pharmacokinetics of DEX in our study. Both one-compartment[33, 34] and two-compartment models[35] have been found to best describe DEX plasma concentration profiles

Table 4. Pharmacodynamic parameters for CYP3A1 and CYP3A2 protein after DEX administration.

Parameters	Definitions	Values (% RSE)
$k_{syn,1}$ (pmol·h^{-1}·mg^{-1} protein)/(attomol mRNA·μg^{-1} total RNA)	Synthesis rate for CYP3A1 protein	0.0359 (18.68)
$k_{deg,1}$ (h^{-1})	Degradation rate for CYP3A1 protein	0.0268 (15.99)
m_1	Amplification factor for CYP3A1 protein	0.911 (3.99)
$k_{syn,2}$ (pmol·h^{-1}·mg^{-1} protein)/(attomol mRNA·μg^{-1} total RNA)	Synthesis rate for CYP3A2 protein	0.486 (11.77)
$k_{deg,2}$ (h^{-1})	Degradation rate for CYP3A2 protein	0.0567 (11.79)
m_2	Amplification factor for CYP3A2 protein	0.287 (9.68)

RSE, relative standard error.

Table 5. Pharmacodynamic parameters for CYP3A1/2 enzyme activity after DEX administration.

Parameters	Definitions	Values (% RSE)
α (pmol·min^{-1}·pmol^{-1} CYP3A1)	Rate of formation of 6β-OHT for CYP3A1	0.463 (22.73)
β (pmol·min^{-1}·pmol^{-1} CYP3A2)	Rate of formation of 6β-OHT for CYP3A2	7.49 (5.51)

RSE, relative standard error.

in other research studies. Our ability to differentiate the bi-exponential elimination of DEX may have been facilitated by the relatively long sampling duration. The *CL* and V_c estimates for DEX obtained in our study were comparable to the values reported by Varma[34]. The first-order absorption of DEX has been reported previously[36]. However, first-order absorption was not an appropriate fit for our data because of the saturation of absorption from the peritoneal cavity when a high dosage of DEX was administered.

The PD data from this study demonstrated that a single dose of DEX could generate markedly elevated levels of CYP3A1 and CYP3A2 mRNA, protein and enzyme activities. The total plasma concentration of DEX was used as a forcing function in the PK/PD system, with the assumptions of rapid diffusion into hepatocytes, binding with PXR and translocation to the nucleus. Our mechanism-based PD model was developed based on the model introduced by Sarangapani[25], which described the time course of CYP2B1/2 proteins, their enzyme activities in the liver and increases in liver weight induced by octamethylcyclotetrasiloxane (D4). In this previous study, the authors did not investigate the relationship between CYP2B1/2 mRNA and the inducer. The resultant mRNA regulation serves as a key component of the signaling pathway downstream of CYP induction, and it has been widely used as an important indicator of CYP induction during drug development[3]. Thus, the CYP3A1/2 mRNA levels were incorporated into our mechanism-based PK/PD model to enhance the integrity and stability of the models and to provide a better understanding of the sequence of molecular events that cause CYP3A1/2 induction. The time course of CYP3A1/2 mRNA was described using an indirect response model, where the impact of DEX on the synthesis rate of CYP3A1/2 mRNA was introduced by a receptor-based sigmoidal induction model with $S_{\max}$, SC_{50}, and γ parameters. Several functions with an increase in complexity were also tested to select the optimal model for the effect of DEX on the rates of CYP3A1 and CYP3A2 mRNA synthesis. The sigmoid $S_{\max}$ model in Equations (3)–(4) was shown to better fit the data than the linear model (ΔOFV=-31.47, $P<0.0001$ for CYP3A1 mRNA; ΔOFV=-37.18, $P<0.0001$ for CYP3A2 mRNA) or the $S_{\max}$ model (ΔOFV=-41.54, $P<0.0001$ for CYP3A1 mRNA; ΔOFV=-23.28, $P<0.0001$ for CYP3A2 mRNA).

The indirect response model was found to adequately describe CYP2B1/2 protein profiles after D4 administration. However, the indirect response model was not appropriate for our study because significant time delays between DEX exposure and CYP3A1/2 mRNA induction (approximately 16 h for CYP3A1 mRNA and 28 h for CYP3A2 mRNA) were observed. These delayed onsets of induction are likely due to the complex series of events that are required to trigger an induction in transcription[37]. In our study, we applied a series of transit compartments, which explained the time spent by mRNA maturation, to account for this observed temporal delay between the DEX plasma concentration and the increase in mRNA levels. Our indirect response models, with a series of one transit compartment and eight transit compartments, adequately characterized the general trends of CYP3A1 and CYP3A2 mRNA dynamics, respectively.

Differential induction of CYP3A1 and CYP3A2 mRNA expression by DEX was observed; this disparity was likely a result of a difference in the rate of CYP3A1 and CYP3A2 transcription. The estimated maximum change in synthesis rates for CYP3A1 and CYP3A2 mRNA due to induction were 22.42- and 8.55-fold, respectively. As reported, the CYP3A1 and CYP3A2 promoters both contain HNF4-binding sites and two DEX response elements, referred to as DexRE-1 and DexRE-2[38]. The DR-3 sequence in DexRE-2, which can be bound by the heterodimer of PXR and RXR, plays a key role in CYP3A1/2 mRNA induction[4, 39]. The DexRE-1 of CYP3A2 is mainly occupied by COUP-TF, whereas the DexRE-1 of CYP3A1 is preferentially bound by protein complex B, which can stimulate the binding of PXR/RXR to DexRE-2[39]. Therefore, although the CYP3A1 and CYP3A2 genes share highly comparable promoter structures, small sequence differences in DexRE-1 may contribute to the apparent discrepancies in the transcription rates of CYP3A1 and CYP3A2 mRNA.

The baseline levels of CYP3A1 and CYP3A2 protein in liver microsomes were 28.95 pmol/mg and 48.60 pmol/mg, respectively, and this result was consistent with the values previously reported in the literature[40]. Experiments from previous studies showed significant induction of CYP3A1 and CYP3A2 proteins in rats treated with the same dose of DEX[41, 42], which is similar to the results obtained in the present study. Although CYP3A2 protein was less inducible than CYP3A1, the contribution of CYP3A2 protein to 6β-OHT formation was greater than that of CYP3A1 during the time course of induction (Figure 5 and Table 5). This phenomenon was likely observed because CYP3A2 has higher basal protein expression levels than CYP3A1.

Mechanism-based PK/PD models differ from conventional PK/PD models in that they contain specific expressions to characterize, in a quantitative manner, processes in the causal path between drug administration and effect[14]. In addition, mechanism-based PK/PD models can resolve drug-specific and biological system-specific parameters. Because the system-specific parameters (*ie*, k_{in}, k_{out}, τ, k_{syn}, k_{deg}, α, and β) characterize the physiological functioning of CYP3A1/2 mRNA, protein and enzyme activity in the rat, they should remain generally consistent within the Sprague-Dawley rat population. These values of system-specific parameters can only be estimated by *in vivo* analysis[14]. In contrast, drug-specific parameters (*ie*, $E_{\max}$ and EC_{50}) can often be predicted based on *in vitro* bioassays[43, 44]. As a result, this mechanism-based PK/PD approach may serve as a tool for predicting the extent of CYP3A1/2 induction by potential inducers and the magnitude of changes in the PK of a probe substrate, based on drug-specific parameters and the PK of the inducers.

In summary, the present study sought to establish a mechanism-based PK/PD model to characterize the effect of DEX on CYP3A1/2 induction as a function of time. The results of this study illustrate the relationships between the molecular events involved in CYP3A1/2 induction by a single dose of DEX. In addition, the system-specific parameters of this mechanism-based PK/PD model could help to design and conduct DDI studies with the aim of regulating the induction of CYP3A1/2.

Acknowledgements

The authors would like to express their appreciation to Dr Ma-gang SHOU for his valuable and constructive suggestions during the planning and development of this research work. The authors would like to thank Dr Feng GUO for his advice on model construction and validation.

Author contribution

Wei LU, Tian-yan ZHOU, and Liang LI designed the research; Liang LI, Zai-quan LI, Miao-ran NING, and Han-qing LI performed the research; Liang LI, Wei LU, Chen-hui DENG, and Shan-shan BI analyzed the data; and Liang LI, Wei LU, and Tian-yan ZHOU wrote the paper.

References

1 Shou M, Hayashi M, Pan Y, Xu Y, Morrissey K, Xu L*, et al.* Modeling, prediction, and *in vitro in vivo* correlation of CYP3A4 induction. Drug Metab Dispos 2008; 36: 2355–70.

2 Bjornsson TD, Callaghan JT, Einolf HJ, Fischer V, Gan L, Grimm S*, et al.* The conduct of *in vitro* and *in vivo* drug-drug interaction studies: a pharmaceutical research and manufacturers of America (PhRMA) perspective. Drug Metab Dispos 2003; 31: 815–32.

3 Dickins M. Induction of cytochromes P450. Curr Top Med Chem 2004; 4 : 1745–66.

4 Kliewer SA, Moore JT, Wade L, Staudinger JL, Watson MA, Jones SA*, et al.* An orphan nuclear receptor activated by pregnanes defines a novel steroid signaling pathway. Cell 1998; 92: 73–82.

5 van Schaik IN, Eftimov F, van Doorn PA, Brusse E, van den Berg LH, van der Pol WL, *et al.* Pulsed high-dose dexamethasone *versus* standard prednisolone treatment for chronic inflammatory demyelinating polyradiculoneuropathy (PREDICT study): a double-blind, randomised, controlled trial. Lancet Neurol 2010; 9: 245–53.

6 Leggas M, Kuo KL, Robert F, Cloud G, deShazo M, Zhang R*, et al.* Intensive anti-inflammatory therapy with dexamethasone in patients with non-small cell lung cancer: effect on chemotherapy toxicity and efficacy. Cancer Chemother Pharmacol 2009; 63: 731–43.

7 Rossignol J, Michallet AS, Oberic L, Picard M, Garon A, Willekens C*, et al.* Rituximab-cyclophosphamide-dexamethasone combination in the management of autoimmune cytopenias associated with chronic lymphocytic leukemia. Leukemia 2011; 25: 473–8.

8 Pascussi JM, Drocourt L, Fabre JM, Maurel P, Vilarem MJ. Dexamethasone induces pregnane X receptor and retinoid X receptor-alpha expression in human hepatocytes: synergistic increase of CYP3A4 induction by pregnane X receptor activators. Mol Pharmacol 2000; 58: 361–72.

9 Ejiri N, Katayama K, Doi K. Induction of CYP3A1 by dexamethasone and pregnenolone-16alpha-carbonitrile in pregnant rat and fetal livers and placenta. Exp Toxicol Pathol 2003; 54: 273–9.

10 Kostrubsky VE, Lewis LD, Wood SG, Sinclair PR, Wrighton SA, Sinclair JF. Effect of Taxol on cytochrome P450 3A and acetaminophen toxicity in cultured rat hepatocytes: comparison to dexamethasone. Toxicol Appl Pharmacol 1997; 142: 79–86.

11 Schmiedlinren P, Benedict PE, Dobbins WO, Ghosh M, Kolars JC, Watkins PB. Cultured adult-rat jejunal explants as a model for studying regulation of Cyp3a. Biochem Pharmacol 1993; 46: 905–18.

12 Hosoe T, Nakahama T, Inouye Y. Divergent modes of induction of rat hepatic and pulmonary CYP3A1 by dexamethasone and pregnenolone 16 alpha-carbonitrile. J Health Sci 2005; 51: 75–9.

13 Ronis MJJ, Chen Y, Liu XL, Blackburn ML, Shankar K, Landes RD*, et al.* Enhanced expression and glucocorticoid-inducibility of hepatic cytochrome P450 3A involve recruitment of the pregnane-X-receptor to promoter elements in rats fed soy protein isolate. J Nutr 2011; 141: 10–6.

14 Danhof M, de Jongh J, De Lange EC, Della Pasqua O, Ploeger BA, Voskuyl RA. Mechanism-based pharmacokinetic-pharmacodynamic modeling: biophase distribution, receptor theory, and dynamical systems analysis. Annu Rev Pharmacol Toxicol 2007; 47: 357–400.

15 Kumar V, Mostafa S, Kayo MW, Goldberg EP, Derendorf H. HPLC determination of dexamethasone in human plasma and its application to an *in vitro* release study from endovascular stents. Pharmazie 2006; 61 : 908–11.

16 Khan AA, Chow EC, van Loenen-Weemaes AM, Porte RJ, Pang KS, Groothuis GM. Comparison of effects of VDR versus PXR, FXR and GR ligands on the regulation of CYP3A isozymes in rat and human intestine and liver. Eur J Pharm Sci 2009; 37: 115–25.

17 Spandidos A, Wang X, Wang H, Dragnev S, Thurber T, Seed B. A comprehensive collection of experimentally validated primers for polymerase chain reaction quantitation of murine transcript abundance. BMC Genomics 2008; 9: 633.

18 Yao HT, Chang YW, Lan SJ, Yeh TK. The inhibitory effect of tannic acid on cytochrome P450 enzymes and NADPH-CYP reductase in rat and human liver microsomes. Food Chem Toxicol 2008; 46: 645–53.

19 Roe AL, Warren G, Hou GQ, Howard G, Shedlofsky SI, Blouin RA. The effect of high dose endotoxin on CYP3A2 expression in the rat. Pharm Res 1998; 15: 1603–8.

20 Omura T, Sato R. Carbon monoxide-binding pigment of liver microsomes. I. Evidence for its hemoprotein nature. J Biol Chem 1964; 239: 2370–8.

21 Chovan JP, Ring SC, Yu E, Baldino JP. Cytochrome P450 probe substrate metabolism kinetics in sprague dawley rats. Xenobiotica 2007; 37: 459–73.

22 Mills JB, Rose KA, Sadagopan N, Sahi J, de Morais SMF. Induction of drug metabolism enzymes and MDR1 using a novel human hepatocyte cell line. J Pharmacol Exp Ther 2004; 309: 303–9.

23 Hamberg AK, Dahl ML, Barban M, Scordo MG, Wadelius M, Pengo V*, et al.* A PK–PD model for predicting the impact of age, CYP2C9, and VKORC1 genotype on individualization of warfarin therapy. Clin Pharmacol Ther 2007; 81: 529–38.

24 Savic RM, Jonker DM, Kerbusch T, Karlsson MO. Implementation of a transit compartment model for describing drug absorption in pharmacokinetic studies. J Pharmacokinet Pharmacodyn 2007; 34: 711–26.

25 Sarangapani R, Teeguarden J, Plotzke KP, McKim JM Jr, Andersen ME. Dose-response modeling of cytochrome p450 induction in rats by octamethylcyclotetrasiloxane. Toxicol Sci 2002; 67: 159–72.

26 Florian JA, Tornoe CW, Brundage R, Parekh A, Garnett CE. Population pharmacokinetic and concentration-QTc models for moxifloxacin: pooled analysis of 20 thorough QT studies. J Clin Pharmacol 2011; 51: 1152–62.

27 Masui K, Kira M, Kazama T, Hagihira S, Mortier EP, Struys MM. Early phase pharmacokinetics but not pharmacodynamics are influenced by propofol infusion rate. Anesthesiology 2009; 111: 805–17.

28 Lu SK, Callahan SA, Jin RY, Brunner LJ. Cyclosporine and bromocriptine-induced suppressions of CYP3A1/2 and CYP2C11 are not mediated by prolactin. Eur J Pharmacol 2004; 501: 215–24.

29 Zhang LP, Beal SL, Sheiner LB. Simultaneous *vs* sequential analysis

for population PK/PD data I: best-case performance. J Pharmacokinet Phar 2003; 30: 387–404.

30 Zhang LP, Beal SL, Sheiner LB. Simultaneous *vs* sequential analysis for population PK/PD data II: robustness of methods. J Pharmacokinet Phar 2003; 30: 405–16.

31 Earp JC, Pyszczynski NA, Molano DS, Jusko WJ. Pharmacokinetics of dexamethasone in a rat model of rheumatoid arthritis. Biopharm Drug Dispos 2008; 29: 366–72.

32 Ourlin JC, Lasserre F, Pineau T, Fabre JM, Sa-Cunha A, Maurel P*, et al.* The small heterodimer partner interacts with the pregnane X receptor and represses its transcriptional activity. Mol Endocrinol 2003; 17: 1693–703.

33 Samtani MN, Jusko WJ. Comparison of dexamethasone pharmacokinetics in female rats after intravenous and intramuscular administration. Biopharm Drug Dispos 2005; 26: 85–91.

34 Varma DR, Yue TL. Influence of protein-calorie malnutrition on the pharmacokinetics, placental transfer and tissue localization of dexamethasone in rats. Br J Pharmacol 1984; 83: 131–7.

35 Hansen DK, LaBorde JB, Wall KS, Holson RR, Young JF. Pharmacokinetic considerations of dexamethasone-induced developmental toxicity in rats. Toxicol Sci 1999; 48: 230–9.

36 Yang L, Panetta JC, Cai X, Yang W, Pei D, Cheng C*, et al.* Asparaginase may influence dexamethasone pharmacokinetics in acute lymphoblastic leukemia. J Clin Oncol 2008; 26: 1932–9.

37 Raybon JJ, Pray D, Morgan DG, Zoeckler M, Zheng M, Sinz M*, et al.* Pharmacokinetic-pharmacodynamic modeling of rifampicin-mediated cyp3a11 induction in steroid and xenobiotic X receptor humanized mice. J Pharmacol Exp Ther 2011; 337: 75–82.

38 Hoen PA, Commandeur JN, Vermeulen NP, Van Berkel TJ, Bijsterbosch MK. Selective induction of cytochrome P450 3A1 by dexamethasone in cultured rat hepatocytes: analysis with a novel reverse transcriptase-polymerase chain reaction assay section sign. Biochem Pharmacol 2000; 60: 1509–18.

39 Huss JM, Wang SI, Kasper CB. Differential glucocorticoid responses of CYP3A23 and CYP3A2 are mediated by selective binding of orphan nuclear receptors. Arch Biochem Biophys 1999; 372: 321–32.

40 Aiba T, Yoshinaga M, Ishida K, Takehara Y, Hashimoto Y. Intestinal expression and metabolic activity of the CYP3A subfamily in female rats. Biol Pharm Bull 2005; 28: 311–5.

41 Eeckhoudt SL, Horsmans Y, Verbeeck RK. Differential induction of midazolam metabolism in the small intestine and liver by oral and intravenous dexamethasone pretreatment in rat. Xenobiotica 2002; 32: 975–84.

42 Yu LS, Lu SJ, Zhao NP, Ni SQ, Yao TW, Zeng S. Male-specific induction of CYP3A2 in rats by zolmitriptan. J Pharm Pharmacol 2008; 60: 1601–7.

43 Van Der Graaf PH, Van Schaick EA, Math-ot RA, Ijzerman AP, Danhof M. Mechanism-based pharmacokinetic–pharmacodynamic modeling of the effects of N6-cyclopentyladenosine analogs on heart rate in rat: estimation of *in vivo* operational affinity and efficacy at adenosine A1 receptors. J Pharmacol Exp Ther 1997; 283: 809–16.

44 Visser SA, Wolters FL, Gubbens-Stibbe JM, Tukker E, Van Der Graaf PH, Peletier LA*, et al.* Mechanism-based pharmacokinetic/pharmacodynamic modeling of the electroencephalogram effects of $GABA_A$ receptor modulators: *in vitro-in vivo* correlations. J Pharmacol Exp Ther 2003; 304: 88–101.

Acta Pharmacologica Sinica (2012) 33: 137–144
© 2012 CPS and SIMM All rights reserved 1671-4083/12 $32.00
www.nature.com/aps

Original Article

Pharmacokinetic and pharmacodynamic profiles of recombinant human erythropoietin-loaded poly(lactic-co-glycolic acid) microspheres in rats

Xiang-lian ZHOU[1], Jin-tian HE[1, *], Hui-juan DU[1], Yang-yang FAN[1], Ying WANG[2], Hong-xia ZHANG[2], Yang JIANG[2]

[1]College of Life Science, Hebei Normal University, Shijiazhuang 050016, China; [2]NCPC GeneTech Biotechnology Development Co, Ltd, Shijiazhuang 050000, China

---

Aim: To characterize the pharmacokinetic and pharmacodynamic profiles of the recombinant human erythropoietin (rhEPO)-loaded poly(lactic-co-glycolic acid) (PLGA) microspheres in rats.
Methods: The rhEPO-loaded microspheres were prepared using a solid-in-oil-in-water emulsion method. Pharmacokinetics and pharmacodynamics of the rhEPO-loaded microspheres were evaluated in male Sprague-Dawley rats. The serum rhEPO level was determined with ELISA. The level of anti-rhEPO antibody in the serum was measured to assess the immunogenicity of rhEPO released from the microspheres.
Results: rhEPO was almost completely released from the PLGA microspheres in vitro, following zero-order release kinetics over approximately 30 d. After intramuscular injection (10 000 or 30 000 IU rhEPO/kg) in the rats, the serum rhEPO concentration reached maximum levels on d 1, then decreased gradually and was maintained at nearly steady levels for approximately 4 weeks. Furthermore, the release of rhEPO from the PLGA microspheres was found to be controlled mainly by a dissolution/diffusion mechanism. A good linear correlation (R^2=0.98) was obtained between the *in vitro* and *in vivo* release data. A single intramuscular injection of the rhEPO-loaded PLGA microspheres (10 000 or 30 000 IU rhEPO/kg) in the rats resulted in elevated hemoglobin and red blood cell concentrations for more than 28 d. Moreover, the immunogenicity of rhEPO released from the PLGA microspheres was comparable with that of the unencapsulated rhEPO.
Conclusion: The results prove the feasibility of using the PLGA-based microspheres to deliver rhEPO for approximately 1 month.

Keywords: recombinant human erythropoietin; poly(lactic-co-glycolic acid); microspheres; pharmacokinetics; pharmacodynamics

---

Acta Pharmacologica Sinica (2012) 33: 137–144; doi: 10.1038/aps.2011.157; published online 5 Dec 2011

Introduction

Erythropoietin (EPO) is a hormone primarily produced by kidney cells and is the main regulator of red blood cell (RBC) production in mammals. Recombinant EPO is used to treat anemia resulting from renal failure, zidovudine treatment for HIV infection, bone marrow transplantation, and cancer chemotherapy[1–3]. Recombinant EPO is usually administered via two or three intravenous or subcutaneous injections per week for several years. Unfortunately, no patient-friendly administration routes exist other than these parenteral routes. To improve patient compliance and therapeutic efficacy, a sustained-release delivery system that permits EPO administration only once or twice a month is desirable.

Injectable, sustained-release biodegradable microspheres could control drug release for several days or even several months. The development of biodegradable polymeric microspheres as carriers has become a promising way to overcome problems with drug administration[4, 5]. Some poly(*D*,*L*-lactic-co-glycolic acid) (PLGA) depot products containing peptide hormones or other drugs have become commercially available, including LHRH agonists, somatostatin derivatives and estradiol[4]. Over the last decade, many attempts have been made to develop biodegradable microsphere systems for rhEPO. Morlock *et al* developed PLGA and PLGA–PEO–PLGA triblock copolymer microspheres using a water-in-oil-in-water (w/o/w), double-emulsion micro-encapsulation process[6–8]. EPO was continuously released from the microspheres for up to 2 weeks *in vitro*. However, rhEPO (recombinant human erythropoietin) was susceptible to the micro-encapsulation processes and easily aggregated. The amount of aggregated

---

* To whom correspondence should be addressed.
E-mail he_jintian@yahoo.com
Received 2011-07-08 Accepted 2011-10-19

rhEPO within the microspheres prepared using the w/o/w double-emulsion technique was higher than safety standards allow (≤2%) (for a solution from EPO)[8]. Geng *et al* reported a novel method to prepare erythropoietin-loaded PLGA microspheres[9]. EPO was first formulated with dextran to form EPO-dextran glassy particles. These particles were subsequently encapsulated into PLGA microspheres using a solid-in-oil-in-water (s/o/w) emulsion method. The stability of EPO was effectively preserved during this preparation process (aggregation of EPO <2%). An *in vitro* release study showed that EPO could be released from the composite PLGA microspheres in a sustained-release manner up to 60 d. However, the *in vivo* efficacy of EPO was maintained for only approximately 30 d. To achieve optimum therapeutic efficacy for the rhEPO-loaded microspheres, the relationship between *in vitro* drug release and *in vivo* pharmacokinetics and pharmacodynamics should be well characterized. However, the *in vivo* pharmacokinetics and pharmacodynamics of EPO-loaded microspheres has rarely been investigated in detail until now.

In the present study, PLGA microspheres loaded with rhEPO were fabricated by an s/o/w emulsion solvent evaporation method. The *in vitro* release kinetics, *in vivo* pharmacokinetics and pharmacodynamics of the rhEPO-loaded PLGA microspheres were evaluated. The correlation between *in vitro* release kinetics and *in vivo* pharmacokinetics of the microspheres was examined. In addition, the acute toxicity and immunogenicity of the rhEPO-loaded microspheres were investigated in rats.

Materials and methods

Materials

The rhEPO solution was obtained from NCPC GeneTech Biotechnology Development Co, Ltd (Shijiazhuang, China). Polyethylene glycol (PEG) with an average molecular weight of 6000 Da was purchased from Sigma (St Louis, MO, USA). Polyvinyl alcohol (PVA) with a molecular weight range of 31 000–50 000 Da was obtained from Aldrich Chemical Company Inc (USA). PLGA was purchased from the Ji-nan Daigang Biomaterial Co, Ltd (Ji-nan, China). PLGA is a copolymer with *DL*-lactide/glycolide ratio of 75:25 and an average molecular weight of approximately 23 kDa. Human serum albumin (HSA) was obtained from Shanghai RAAS Blood Products Co, Ltd (Shanghai, China). All other chemicals used were of analytical grade.

Preparation of the rhEPO-HSA microparticles

The rhEPO-HAS microparticles were prepared using a modified freezing-induced phase separation method[10]. In brief, a solution containing 0.1% rhEPO (*w/v*), 1% HSA (*w/v*), 5% PEG (*w/v*) and 0.02 mol/L sodium phosphate was frozen at -80 °C overnight. Subsequently, the solution was lyophilized using a Christ ALPHA 1-2 plus freeze-dryer at a pressure of 5.0×10^{-3} Pa for 20 h. The lyophilized powders were dispersed in 5 mL of dichloromethane with high-speed agitation. To remove the PEG within the particles, the mixtures were centrifuged at 8000 r/min for 10 min. This operation was repeated three times. The final precipitates were dried overnight under a vacuum.

Preparation of the rhEPO-loaded PLGA microspheres

The rhEPO-loaded PLGA microspheres were prepared using a modified s/o/w method[11]. Briefly, 10 mg of the rhEPO-HSA mixture microparticles was suspended in 2.5 mL of dichloromethane solution containing 180 mg/mL of PLGA. An IKA T25 ultra-turrax homogenizer was used at 20 000 r/min for 1.5 min. The resulting solid-in-oil (s/o) suspension was mixed with 75 mL of 2% (*w/v*) aqueous PVA solution containing 5% (*w/v*) NaCl. The mixture was then homogenized at 600 r/min for 1 min to form the s/o/w emulsion. For solvent extraction, the s/o/w emulsion was immediately diluted with 225 mL of 20 mmol/L phosphate buffer (PB; pH 7.4) containing 5% NaCl. The emulsion was stirred with a magnetic stirrer at 300 r/min for 6 h. The resulting rhEPO-loaded microspheres were collected by filtration and washed three times with distilled water to remove the PVA and NaCl. The microspheres were then lyophilized using a Christ ALPHA 1-2 plus freeze-dryer operating at a pressure of 5.0×10^{-3} Pa overnight. The samples were stored at -20 °C.

Microsphere characterization and determination of drug encapsulation efficiency

The rhEPO-HSA mixture microparticles and the rhEPO-loaded PLGA microspheres were examined for morphology and size by scanning electron microscopy (SEM) using a Hitachi S-520. The rhEPO-HSA mixture microparticles and the rhEPO-loaded PLGA microspheres were mounted onto metal stubs using double-sided adhesive tape and vacuum coated with a thin layer of gold. Then, the samples were examined by SEM. One hundred rhEPO-HSA mixture microparticles or PLGA microspheres were randomly selected and measured in diameter; the results were reported as an average value.

The protein content in the microspheres was determined using a previously described extraction method[12]. Thirty milligrams of dried microspheres were dissolved in methylene chloride and centrifuged at 10 000 r/min for 15 min to remove the polymer solution. The remaining protein pellet was dissolved in 0.2 mL of 20 mmol/L PB (pH 7.4). The rhEPO concentration was determined using a Quantikine *in vitro* diagnostic rhEPO ELISA kit purchased from R&D Systems (Minneapolis, MN, USA). The protein encapsulation efficiency in the microspheres was calculated as the ratio of actual to theoretical protein loadings.

In vitro release of proteins from PLGA microspheres

Thirty milligrams of dried microspheres were suspended in 1 mL of 0.02 mol/L phosphate buffered saline (PBS, pH 7.4) containing 0.05% (*w/v*) sodium azide. The samples were agitated in a rotating bottle apparatus at 50 r/min at 37 °C. Samples of 1 mL were removed at the following sampling times after centrifugation at 3000 r/min for 10 min: 0, 1, 3, 5, 8, 11, 14, 17, 21, 25, 29, and 33 d. The removed medium was immediately replaced with the same volume of fresh PBS solution. The rhEPO content in the supernatant was determined using a Quantikine *in vitro* diagnostic rhEPO ELISA kit purchased from R&D Systems (Minneapolis, MN, USA). The amount of rhEPO released within 24 h was defined as the initial burst.

Pharmacokinetics of the rhEPO-loaded PLGA microspheres in rats

In vivo release of the rhEPO-loaded PLGA microspheres was evaluated in male SD rats (male, 180–210 g, Grade II, Certificate N̲o̲ 06057) purchased from the Experimental Animal Center of Hebei Province in China. The rats were housed under conventional laboratory conditions in a room maintained at 24±1 °C and fed commercial rat food and water *ad libitum*. The rats were randomly divided into four groups of six rats each. One group was used for intramuscular injection of rhEPO solution at a dose of 30 000 IU/kg, the second and the third groups were used for intramuscular injection of the microspheres at a dose of 10 000 or 30 000 IU/kg of rhEPO, and the fourth group was used for intramuscular injection of the equivalent amount of blank microspheres (without rhEPO) as a control. The rhEPO-loaded microspheres were pre-suspended in the diluent containing 2% carboxymethylcellulose sodium and 0.9% (*w*/*v*) NaCl. One milliliter of the formulations was injected at multiple points into the gastrocnemius muscle of the hind legs. After injection, 0.4 mL of blood was withdrawn from the retro-orbital sinus through the eye canthus of anesthetized rats at 0.5, 1, 3, 6, 9, 12, 16, 20, and 24 h after injection of the rhEPO solution and at 1, 4, 8, 13, 18, 23, 28, 33, and 38 d after injection of the microsphere formulations. The obtained blood samples were centrifuged at 1500 r/min for 15 min. Approximately 0.2 mL of plasma samples was obtained and stored at -40 °C. All animal studies were performed in Hebei Normal University in accordance with Institutional Animal Care and Use Committee guidelines.

The content of rhEPO in plasma samples was determined using a Quantikine *in vitro* diagnostic rhEPO ELISA kit purchased from R&D Systems (Minneapolis, MN, USA). Pharmacokinetic parameters were calculated directly from the plasma concentration *versus* time plot[13]. The area under the curve (AUC) was calculated by the trapezoidal method. The apparent elimination rate constants (K_e) were determined from the semi-logarithmic plot of plasma concentration *versus* time. k was calculated from the terminal linear portion of the curve using linear regression analysis[13]. The terminal elimination half-lives ($t_{1/2}$) were calculated by dividing 0.693 by the elimination rate constant[13].

Pharmacodynamics of the rhEPO-loaded PLGA microspheres in rats

The pharmacodynamics of the rhEPO-loaded PLGA microspheres were also evaluated in male SD rats. The rats were randomly divided into 4 groups with 6 rats in each group. The drug administration method was the same as for the pharmacokinetic study. After intramuscular injection, 20 μL of blood was collected from the rats (at the tail vein) at each sampling time after starting the treatment. The blood sample was immediately mixed with 0.5 mL of dilution buffer provided by the manufacturer. The hemoglobin (HGB) concentration and red blood cell number (RBC) in the blood samples was determined using an XE-2100 automated hematology analyzer (Sysmex, Japan).

In vivo polymeric degradation in rats

To determine the sites of microspheres in rats, the injection site was marked with 3%–5% picric acid solution. At designated time points, the rats were sacrificed in an induction chamber filled with ether, the muscles at the injection site were cut, and the microspheres were removed. The degradation of the rhEPO-loaded PLGA microspheres in rats was observed with scanning electron microscopy (SEM, Hitachi S-520).

Acute toxicity test in rats

Forty SD rats (180–210 g, Grade II, Certificate N̲o̲ 06057), 20 males and 20 females, were used for the acute toxicity test. According to the maximum dosage method, the available maximum dose of the rhEPO-loaded PLGA microspheres was 2000 mg/kg, which is equivalent to approximately 50 times the normal clinical dose for humans. The lower doses were 500 mg/kg, 50 mg/kg, and 5 mg/kg, respectively and the medium was used as a control. After intramuscular injection into the hind limbs, the rats were observed for acute reactions including tachypnea, restlessness and stupor. In addition, the rats were weighed daily throughout the two-week observation period.

Detection of anti-rhEPO antibody

To examine the immune response to the rhEPO-loaded PLGA microspheres, 2000 IU/kg rhEPO in solution, 2000 IU/kg rhEPO in microsphere form, 2000 IU/kg rhEPO in denatured HSA-rhEPO mixture (heated at 100 °C for 10 min) and the equivalent amount of blank microspheres (without rhEPO) were injected intramuscularly into SD rats (5 rats per group). The amount of anti-rhEPO antibody in the blood samples taken at the 6th week was analyzed by ELISA. Briefly, polystyrene microtiter plates were coated overnight at 4 °C with 100 μL of 0.1 mg/mL rhEPO in coating buffer (50 mmol/L sodium carbonate buffer pH 9.6) and rinsed with PBST (0.01 mol/L PBS at pH 7.4 containing 0.1% Tween 20). After blocking with 5% (*w/v*) dried skimmed milk powder at 37 °C for 2 h, the microtiter plates were washed three times with PBST. One hundred microliters of the diluted serum samples (1/200) were loaded and incubated at 37 °C for 1 h. After the plates were washed three times with PBST, 100 μL of horseradish peroxidase-labeled rabbit anti-rat polyclonal immunoglobulin diluted 1:2000 was added and incubated with for 1 h at room temperature. The plate was again washed three times with PBST, and the bound enzyme conjugate was detected by adding 100 μL of 3,3,5,5-tetramethylbenzidine (substrate) to each well. The reaction was stopped 10–20 min later using 50 μL of 2 mol/L H_2SO_4. The absorbance at 450 nm was measured on a Bio-Rad 550 microplate reader.

Statistical analysis

The differences between two groups were evaluated statistically using analysis of variance (ANOVA) followed by the Newman-Keuls test. A *P* value of <0.05 was considered statistically significant. All data analysis was performed with the Statistica statistical software package (version 6.0, StatSoft Inc, Tulsa, OK, USA).

Results

Characterization of the rhEPO-HSA mixture microparticles and the rhEPO-loaded PLGA microspheres

Figures 1A and 1B show SEM images of the rhEPO-HAS microparticles and the rhEPO-loaded PLGA microspheres, respectively. The rhEPO-HSA microparticles possessed a spherical shape, smooth surface and diameters ranging between 200 and 600 nm. The rhEPO-loaded PLGA microspheres showed a spherical, smooth, nonporous and solid morphology, with sizes ranging between 40 and 100 μm in diameter. The rhEPO encapsulation efficiency and actual drug loading were 85.3% and 0.21%, respectively.

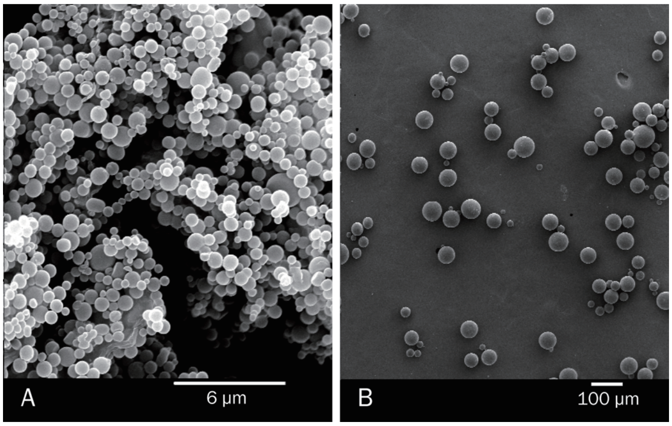

Figure 1. Scanning electron microscopic images of freeze-dried rhEPO-HSA mixture microparticles and rhEPO-loaded PLGA microspheres. (A) rhEPO-HSA mixture microparticles; (B) rhEPO-loaded PLGA microspheres.

In vitro drug release

The *in vitro* release profile of rhEPO from the PLGA microspheres is presented in Figure 2. The *in vitro* release profile exhibited a biphasic pattern. The first phase was an initial burst release of approximately 17% of the loaded rhEPO, which occurred within one day. After the initial burst, rhEPO release was sustained, following zero-order release kinetics for approximately 30 d. The linear regression equation was inserted into Figure 2. A good linear regression correlation was made between time and the percentage of drug released in PBS at 37 °C; the correlation coefficient was greater than 0.98, indicating that ideal zero-order kinetics was obtained. Furthermore, rhEPO was nearly completely released from the PLGA microspheres after 33 d.

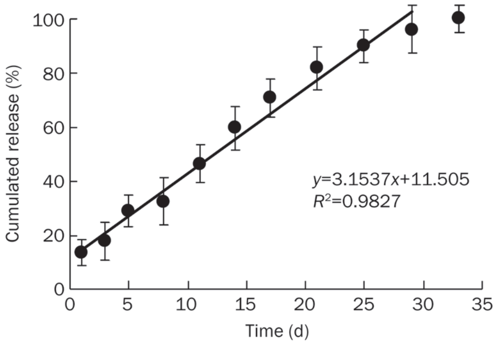

Figure 2. *In vitro* cumulative release profiles of rhEPO (●) from the rhEPO-loaded PLGA microsphere.

In vivo pharmacokinetic studies

Figure 3A shows the *in vivo* rhEPO concentration–time profile after intramuscular injection of rhEPO solution in rats. The peak plasma concentration (C_{max}) for the rhEPO solution was 17.85 mIU/mL, and the time to attain the peak concentration (T_{max}) was 0.3 h. The rapid decrease in rhEPO concentration indicated that the elimination of rhEPO was rapid. The fast decrease in rhEPO concentration suggested that frequent injections are needed to maintain a constant plasma rhEPO level. After analyzing the concentration–time profiles, the apparent elimination rate constant (K_e) and terminal elimination half-life ($t_{1/2}$) after intramuscular injection were determined to be 0.75 h^{-1} and 9.6 h, respectively (Table 1). These results are consistent with those from a previous report[3].

Figure 3B shows the rhEPO plasma concentration *versus* time profile after intramuscular injection of the rhEPO-loaded PLGA microspheres. The pharmacokinetic profiles for all

Table 1. Pharmacokinetic parameters for the rhEPO solution and the rhEPO-loaded microspheres (MS) after intramuscular injection in SD rats. Mean±SD. *n*=3.

Samples	$t_{1/2}$ (d)	k_e (d^{-1})	AUC_{0-t} (mIUd/mL)[a]	Relative bioavailability (%)
Solution containing 30 000 IU rhEPO	0.40±0.07	1.75±0.43	198.8±15.2	100
MS containing 10 000 IU rhEPO	8.66±0.53	0.080±0.005	135.4±12.5	204
MS containing 30 000 IU rhEPO	12.83±0.95	0.054±0.006	395.3±26.8	197

[a] The AUC was calculated from 0 to 24 h for the rhEPO solution and from 0 to 33 d for the rhEPO-loaded microspheres.

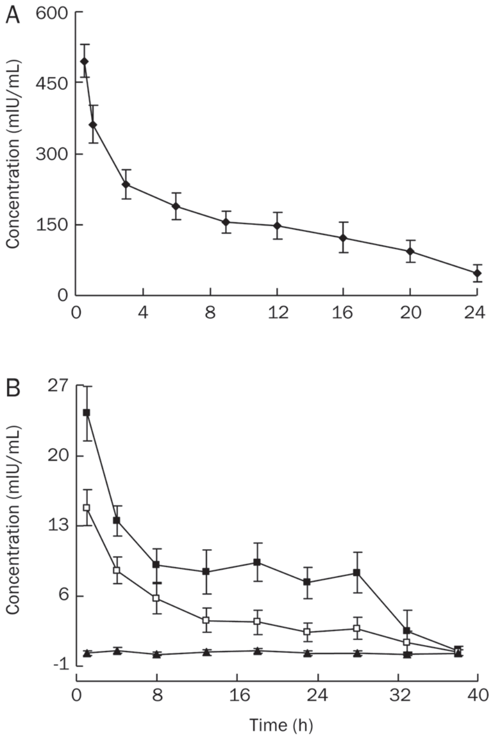

Figure 3. (A) The rhEPO plasma levels after intramuscular injection of rhEPO solution at a dose of 30 000 IU/kg rhEPO in rats. (B) The rhEPO plasma levels after intramuscular injection of PLGA microspheres in rats: 10 000 IU rhEPO/kg (□), 30 000 IU rhEPO/kg (■) and the equivalent amount of blank PLGA microspheres without rhEPO (▲). Mean±SD. *n*=6.

of the rhEPO-loaded microspheres showed that the rhEPO plasma concentrations peaked during the first day following injection. The concentrations then decreased gradually and were maintained at a stable level from d 1 to d 28, approaching zero at d 38. The plasma rhEPO concentrations were significantly higher than that of the control group at d 33 ($P<0.05$). The pharmacokinetic parameters estimated from the concentration–time profiles are summarized in Table 1. The areas under the curve ($AUC_{0–33}$) were 125.42 and 384.33 mIU/mL for the microsphere formulation at the doses of 10 000 IU rhEPO/kg and 30 000 IU rhEPO/kg, respectively. The elimination half-life of rhEPO release from PLGA microspheres was estimated to be 8.66 d and 12.83 d for the microsphere formulations at doses of 10 000 IU rhEPO/kg and 30 000 IU rhEPO/kg, respectively (Table 1). The apparent elimination rate constant K_e was determined to be 0.08 h^{-1} and 0.054 h^{-1} for the microsphere formulations at doses of 10 000 IU rhEPO/kg and 30 000 IU rhEPO/kg, respectively (Table 1).

The *in vivo* degradation of the rhEPO-loaded PLGA microspheres was observed with SEM after isolation from the injection site. The results are illustrated in Figure 4. The microspheres underwent progressive changes in surface morphology throughout the experimental period. One day after intramuscular injection, the microspheres exhibited a distorted, irregular shape (Figure 4A). The distortion of microspheres may result from microsphere shrinkage, which may be an artifact of dehydration during the sample preparation for SEM. Six days later, the microspheres began to lose their smooth surface morphology, and the number of small surface pores increased significantly (Figure 4B). The microspheres completely lost their shape and exhibited a porous bulky surface after 18 d (Figure 4C). Although the structure of PLGA microspheres was broken after 30 d, the residual structure could still be observed (Figure 4D).

Correlation between *in vitro* and *in vivo* data

The data obtained from the pharmacokinetic study after the intramuscular administration of the rhEPO-loaded microspheres at a dose of 30 000 IU/kg were used to develop the *in vitro-in vivo* correlation. A plot of the percent AUC *versus* the percent *in vitro* release is shown in Figure 5. The results illustrate a good linear regression relationship between the percent *in vitro* release in PBS at 37 °C and percent AUC after intramuscular administration of the rhEPO-loaded microspheres into the rats ($R^2=0.98$).

In vivo pharmacodynamics

In vivo pharmacodynamics of the rhEPO-loaded PLGA microspheres were examined based on elevated hemoglobin (HGB) concentrations and RBCs in male SD rats. The results are shown in Figure 6. RBCs and the HGB concentration reached a peak at 3.0 h after a single injection of the rhEPO solution at a dose of 30 000 IU/kg. Both levels declined rapidly to baseline at approximately 24 h ($P<0.05$) (Figure 6A and 6B). On the other hand, the RBCs and HGB concentration gradually increased to peaks at d 5 after a single injection of the rhEPO-loaded microspheres (Figure 6C and 6D). Then, the peak concentrations were maintained for approximately 10 d and subsequently decreased slowly toward baseline. The microsphere formulations at doses of 10 000 IU rhEPO/kg and 30 000 IU rhEPO/kg were sufficient to significantly increase RBCs and HGB concentrations for over 22 and 28 d, respectively ($P<0.05$).

Acute toxicity and immunogenicity of rhEPO-loaded microsphere formulations

A single injection of microspheres at different dosages did not induce any acute reactions or reduce body weight during the two-week observation period. No animals died.

The immunogenicity of rhEPO released from the microspheres was evaluated by measuring anti-rhEPO antibodies. A denatured rhEPO-HSA mixture and blank microspheres (without rhEPO) were used as controls. Anti-rhEPO antibodies from anti-sera taken at week 6 was analyzed by ELISA. The results are shown in Figure 7. The anti-rhEPO IgG titer induced by the rhEPO-loaded PLGA microspheres was comparable to the titer induced by the rhEPO solution ($P>0.05$). The titers induced by the rhEPO-loaded PLGA microspheres and the rhEPO solution were significantly higher than that elicited by the blank control ($P<0.05$) and significantly lower than that elicited by the denatured rhEPO-HSA mixture ($P<0.01$).

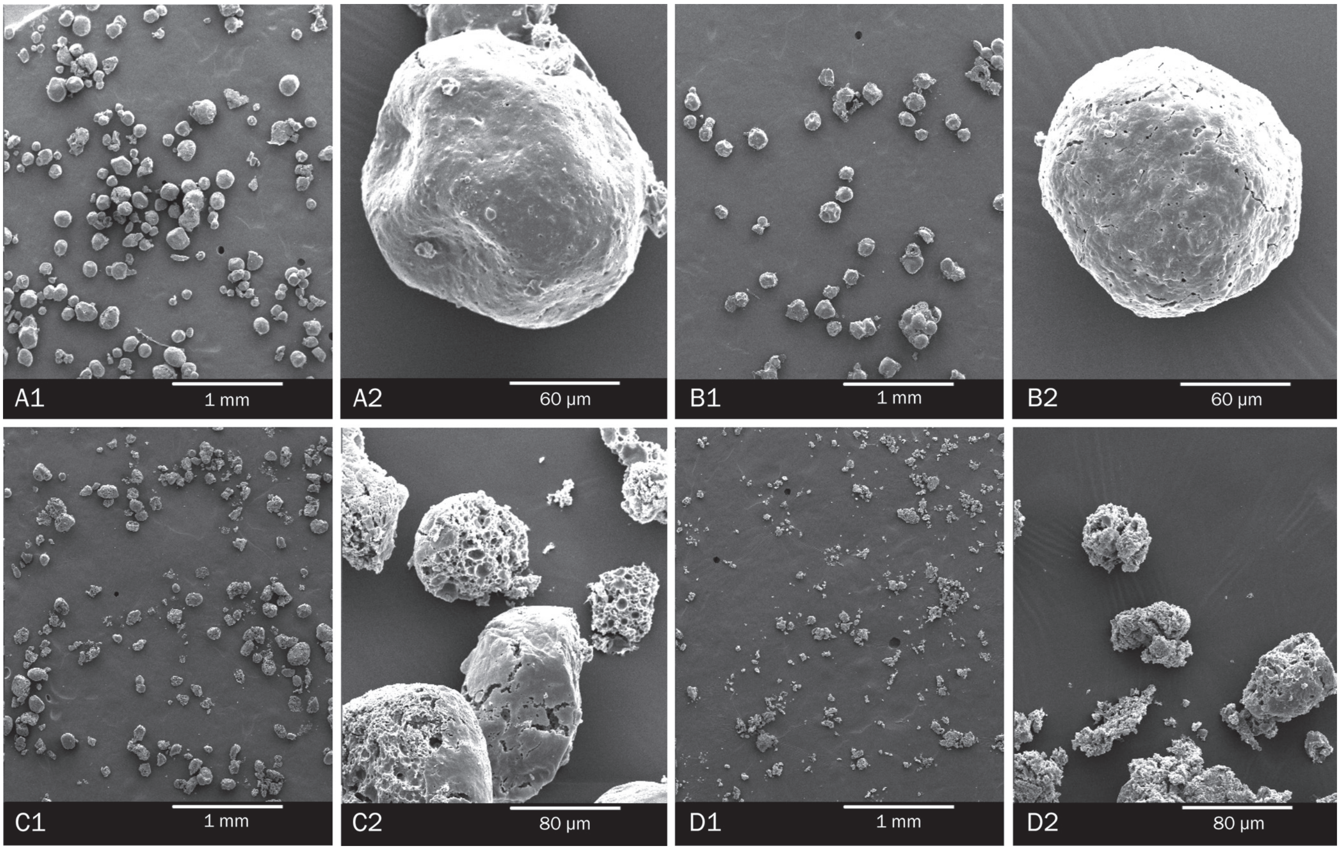

Figure 4. Scanning electron micrographs of PLGA microspheres recovered from injection site at different time. (A) One day after intramuscular injection; (B) Six days after injection; (C) Eighteen days after injection; (D) Thirty days after injection.

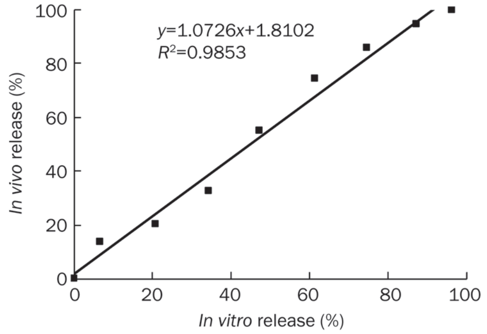

Figure 5. Correlation of *in vitro* and *in vivo* release of rhEPO from the rhEPO-loaded PLGA microsphere.

Discussion

In the present study, rhEPO-loaded PLGA microspheres were successfully prepared using a modified s/o/w emulsion solvent evaporation method. The microspheres were spherical in shape and had smooth surfaces under an electron microscope. The rhEPO recovered from PLGA microspheres was identical to that before encapsulation in our previous study[14]. An *in vitro* release test showed that rhEPO was released from PLGA microspheres following ideal zero-order kinetics for approximately 30 d after a low initial burst, and this release was nearly complete after 33 d. In SD rats, the pharmacokinetic parameters $t_{1/2}$ and $AUC_{0\text{–}t}$ for the rhEPO microsphere formulation were significantly higher than for the rhEPO solution. The elimination half-life $t_{1/2}$ was 21.7 and 32.1 times higher for rhEPO in microspheres than in solution at 10 000 IU rhEPO/kg and 30 000 IU rhEPO/kg, respectively. The relative bioavailability of the rhEPO released from PLGA microspheres was approximately 2.0 times that of the rhEPO solution. The rhEPO plasma concentration was sustained for 33 d, which was similar to the *in vitro* release data. The apparent elimination rate constant K_e was approximately 21.9 and 32.4 times lower for the rhEPO microspheres than the rhEPO solution at 10 000 IU rhEPO/kg and 30 000 IU rhEPO/kg, respectively.

Two possible mechanisms may be involved to explain the release of rhEPO from PLGA microspheres. Protein dissolution/diffusion from the microspheres and/or erosion of the matrix due to degradation/dissolution of PLGA polymers[15, 16] may be responsible. Because the degradation/dissolution of PLGA takes quite a long time, the polymer backbone probably retains integrity without significant degradation/dissolution at the early release stage. As a result, drug release from the microspheres is most likely controlled by a dissolution/diffusion mechanism during the early release stage. Polymer erosion would increase drug diffusion through the polymer

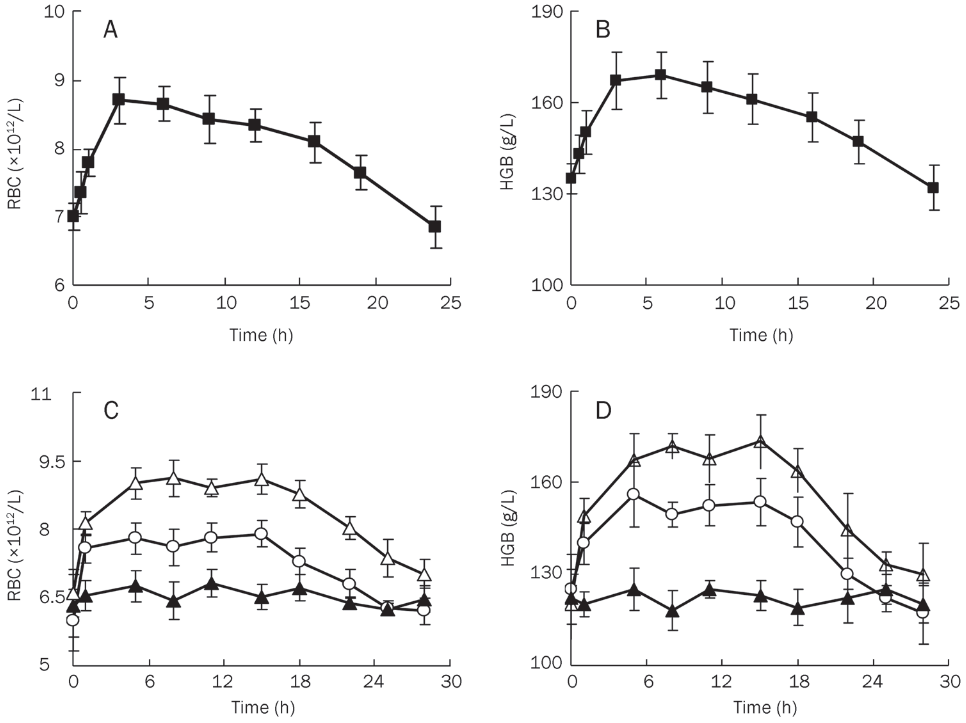

Figure 6. Profiles of red blood cell (RBC) and hemoglobin (HGB) levels in SD rats after intramuscular injection of different rhEPO formulation. (A) and (B): 3×10^4 IU rhEPO/kg in solution; (C) and (D): 1×10^4 IU/kg rhEPO within the rhEPO-loaded microspheres (○), 3×10^4 IU/kg rhEPO within the rhEPO-loaded microspheres (Δ) and blank microspheres without rhEPO (▲). Mean±SD. *n*=6.

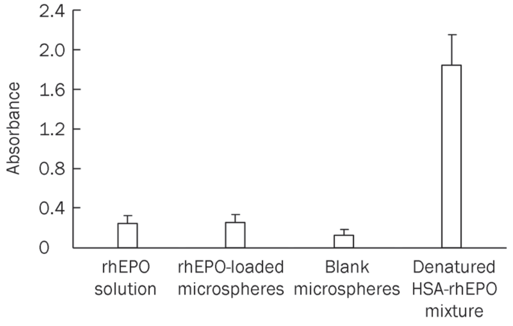

Figure 7. ELISA analysis of anti-EPO IgG within the serum from SD rats at 6th week after subcutaneous injection of various formulations. The serum samples were diluted 1/200 before ELISA analysis. Mean±SD. *n*=5.

matrix and increase the size of aqueous polymer pores, which facilitate the release of the entrapped proteins from the interior of PLGA microspheres[17]. We found that erosion of the polymer surface and bulk matrix occurred at later release stages in our system. Matrix erosion may contribute to rhEPO release from PLGA microspheres. However, the release rate of rhEPO from PLGA microspheres *in vivo* was not obviously faster than the *in vitro* release rate, although polymer degradation was generally faster *in vivo* than *in vitro* due to the presence of enzymes and other biological factors[18]. These results suggest that the release of rhEPO from the PLGA microspheres was not primarily controlled by matrix erosion but rather by a dissolution/diffusion mechanism.

The *in vitro* and *in vivo* correlation (IVIVC) is an important issue for parenteral biodegradable depot systems as well as for oral dosage forms[18, 19]. A proper IVIVC can be used to predict an *in vivo* release profile for parenteral biodegradable depot systems with the aid of an *in vitro* release profile conducted in PBS. For erosion-controlled sustained-release depot systems, the release of PLGA-based microspheres is often slower *in vitro* than *in vivo*. Thus, it is difficult to establish a good IVIVC for erosion-controlled depot systems. It has been reported that a proper IVIVC can usually be obtained for diffusion-controlled sustained-release depot systems[20]. The release of rhEPO from the PLGA microspheres was controlled mainly by dissolution/diffusion in our depot system. Therefore, good IVIVC for rhEPO-loaded PLGA microspheres was obtained, and the results confirmed our speculations.

The pharmacodynamic studies indicated that the rhEPO-loaded PLGA microspheres could maintain elevated RBC and HGB levels over 28 d, which was similar to the drug residence time in plasma. These results suggest that the released rhEPO was biologically active during sustained release.

PLGA microspheres have enhanced the immunogenicity of vaccines[21]. Whether the microsphere formulation increases the immunogenicity of rhEPO was investigated. An anti-rhEPO antibody was clearly elicited by the rhEPO solution in rats. The rat and human EPO sequences differ by thirty-five amino acids[22], and thus, rats may generate anti-rhEPO antibodies. The rhEPO released from the PLGA microspheres elicited a comparable amount of anti-rhEPO antibody to the solution formulation and significantly less antibody than was elicited from the denatured rhEPO-HAS mixture. These results suggest that the immunogenicity of the encapsulated rhEPO did not increase when the rhEPO-loaded microspheres were given as a depot. Our results are similar to a previous report on a sustained-release formulation of human growth hormone[23].

In conclusion, the PLGA microspheres containing rhEPO were successfully prepared with an s/o/w emulsion solvent evaporation method. An *in vitro* release test showed that rhEPO was released from PLGA microspheres following nearly zero-order kinetics for approximately 30 d. *In vivo*, after intramuscular injection, the plasma concentration of rhEPO reached a maximum at d 1, decreased gradually, and was maintained at a near constant level for approximately 4 weeks. Furthermore, the release of rhEPO from the PLGA microspheres was found to be controlled primarily by a dissolution/diffusion mechanism. A good linear correlation was also observed between the *in vitro* and the *in vivo* release data, suggesting that *in vitro* release data may be used to predict *in vivo* drug release performance. A single injection of rhEPO-loaded PLGA microspheres in SD rats resulted in elevated hemoglobin and red blood cell concentrations for over 28 d. Moreover, the immunogenicity of rhEPO released from this formulation, as assessed by the titer of anti-rhEPO antibody from SD rats, was comparable to that of the unencapsulated protein. No toxic effects were observed in an acute toxicity test in SD rats. Therefore, the present study demonstrates the feasibility of delivering rhEPO for approximately 1 month with injectable PLGA-based microspheres.

Acknowledgements

This project was supported by the Provincial Science and Technology Department of Hebei Province (09276418D-3) and the Science and Technology Project of the Provincial Education Department of Hebei (200645).

Author contribution

Xiang-lian ZHOU, Hui-juan DU, and Yang-yang FAN performed the main experiments; Jin-tian HE designed the experiment and drafted the manuscript; Ying WANG and Hong-xia ZHANG analyzed the data; Hui-juan DU and Yang JIANG aided in the design of the experiment and improved the manuscript.

References

1 Davis JM, Aralkawas T, Strickland TW, Yphantis DA. Characterization of recombinant human erythropoietin produced in Chinese hamster ovary cells. Biochemistry 1987; 26: 2633–8.

2 Eschbach JW, Egrie JC, Downing MR, Browne JK, Adamson JW. Correction of the anemia of end-stage renal disease with recombinant human erythropoietin. N Engl J Med 1987; 316: 73–8.

3 Markham A, Bryson H, Epoetin A. A review of its pharmacodynamic and pharmacokinetic properties and therapeutic use in non-renal applications. Drugs 1995; 49: 232–54.

4 Mundargi RC, Babu VR, Rangaswamy V, Patel P, Aminabhavi TM. Nano/micro technologies for delivering macromolecular therapeutics using poly(*D*,*L*-lactide-co-glycolide) and its derivatives. J Control Release 2008; 125: 193–209.

5 Pisal DS, Kosloski MP, Balu-Iyer SV. Delivery of therapeutic proteins. J Pharm Sci 2010; 99: 2557–75.

6 Morlock M, Koll H, Winter G, Kissel T. Microencapsulation of rh-erythropoietin, using biodegradable poly(*DL*,-lactide-co-glycolide): protein stability and the effects of stabilizing excipients. Eur J Pharm Biopharm 1997; 43: 29–36.

7 Morlock M, Kissel T, Li YX, Koll H, Winter G. Erythropoietin loaded microspheres prepared from biodegradable LPLG-PEO-LPLG triblock copolymers: protein stabilization and *in-vitro* release properties. J Control Release 1998; 56: 105–15.

8 Pistel KF, Bittner B, Koll H, Winter G, Kissel T. Biodegradable recombinant human erythropoietin loaded microspheres prepared from linear and star-branched block copolymers: Influence of encapsulation technique and polymer composition on particle characteristics. J Control Release 1999; 59: 309–25.

9 Geng Y, Yuan W, Wu F, Chen J, He M, Jin T. Formulating erythropoietin-loaded sustained-release PLGA microspheres without protein. J Control Release 2008; 130: 259–65.

10 Morita T, Horikiri Y, Yamahara H, Suzuki T, Yoshino H. Formation and isolation of spherical fine protein microparticles through lyophilization of protein-poly(ethylene glycol) aqueous mixture. Pharm Res 2000; 17: 1367–73.

11 Morita T, Sakamura Y, Horikiri Y, Suzuki T, Yoshino H. Protein encapsulation into biodegradable microspheres by a novel s/o/w emulsion method using poly(ethylene glycol) as a protein micronization adjuvant. J Control Release 2000; 69: 435–44.

12 Zhu G, Mallery SR, Schwendeman SP. Stabilization of proteins encapsulated in injectable poly(lactide-co-glycolide). Nat Biotechnol 2000; 18: 52–7.

13 El-Sayed YM, Niazy EM, Khidr SH. *In vivo* evaluation of sustained-release microspheres of metoclopramide hydrochloride in beagle dogs. Int J Pharm 1995; 123: 113–8.

14 He J, Feng M, Zhou X, Ma Sh, Jiang Y, Wang Y, *et al*. Stabilization and encapsulation of recombinant human erythropoietin into PLGA microspheres using human serum albumin as a stabilizer. Int J Pharm 2011; 416: 69–76.

15 Wischke C, Schwendeman SP. Principles of encapsulating hydrophobic drugs in PLA/PLGA microparticles. Int J Pharm 2008; 364: 298–327.

16 Sun Y, Wang J, Zhang X, Zhang Z, Zheng Y, Chen D, *et al*. Synchronic release of two hormonal contraceptives for about one month from the PLGA microspheres: *in vitro* and *in vivo* studies. J Control Release 2008; 129: 192–9.

17 Cohen S, Yoshioka T, Lucarelli M, Hwang LH, Langer R. Controlled delivery systems for proteins based on poly(lactic/glycolic acid) microspheres. Pharm Res 1991; 8: 713–20.

18 Zolnik BS, Burgess DJ. Evaluation of *in vivo-in vitro* release of dexamethasone from PLGA microspheres. J Control Release 2008; 127: 137–45.

19 Chu DF, Fu XQ, Liu WH, Liu K, Li YX. Pharmacokinetics and *in vitro* and *in vivo* correlation of huperzine A loaded poly(lactic-co-glycolic acid) microspheres in dogs. Int J Pharm 2006; 325: 116–23.

20 Van Dijkhuizen-Radersma R, Wright SJ, Taylor LM, John BA, De Groot K, Bezemer JM. *In vitro/in vivo* correlation for ^{14}C-methylated lysozyme release from poly(ether-ester) microspheres. Pharm Res 2004; 21: 484–91.

21 Tamber H, Johansen P, Merkle HP, Gander B. Formulation aspects of biodegradable polymeric microspheres for antigen delivery. Adv Drug Deliv Rev 2005; 57: 357–76.

22 Nagao M, Suga H, Okano M, Masuda S, Narita H, Ikura K, *et al*. Nucleotide sequence of rat erythropoietin. Biochim Biophys Acta 1992; 1171; 99–102.

23 Lee HJ, Riley G, Johnson O, Cleland JL, Kim N, Charnis M, *et al*. *In vivo* characterization of sustained-release formulations of human growth hormone. J Pharmacol Exp Ther 1997; 281: 1431–9.